UNIVERSITÀ DEGLI STUDI DI PADOVA

Sede Amministrativa: Università degli Studi di Padova
Dipartimento di Ingegneria Industriale

SCUOLA DI DOTTORATO DI RICERCA IN INGEGNERIA INDUSTRIALE
INDIRIZZO: INGEGNERIA METALLURGICA
XXIVº CICLO

SURFACE AND WEAR ANALYSES OF CERMET AND CERAMIC COATINGS

Direttore della Scuola : Ch.mo Prof. Paoli F. Bariani
Coordinatore d'indirizzo: Ch.mo Prof. Maurizio Magrini
Supervisore :Ch.mo Prof. Irene Calliari

Dottorando : Reyna Areli Vazquez Aguilar

Gennaio 2012

Para mi Abuela y
Mis Padres con amor

¡Quien, a través de la observación y el contacto
sensible con el maravilloso orden del universo
conducido por la sabiduría divina, no es llevado
a la admiración del constructor que todo lo ejecuta!
NICOLÁS COPÉRNICO (1473-1543)

PREFACE

The work presented in the present doctoral thesis was carried out during three years of full-time research and studies at the University of Padua from January 2009 to December 2011. The research and experimental work were developed and executed at the Engineering Department of the University of Ferrara (ENDIF), under the main supervision of Professor Gian Luca Garagnani; in the Department of Engineering's Chemical Processes (DPCI), Padua (Italy) under the main supervision of Professor Irene Calliari and at the Department of Mechanical, Energetic and Materials Engineering in Extremadura University, Badajoz (Spain) in collaboration with Professor Fernando Guiberteau Cabanillas.

The thesis consists of an introductory part and a research section that includes the following papers:

A. Effect of relative humidity and applied loads on the tribological behavior of a steel Cr2O3-Ceramic coupling.

M. Merlin, C. Soffritti, R. Vazquez

Preprint 2012

B. Friction and wear behavior of APS and HVOF advanced ceramic coatings Cr2O3-Ceramic coupling.

M. Merlin, C. Soffritti, R. Vazquez

Published in La Metallurgia Italiana, Consedit, Grado (GO), 11 (2011), p. 17-23, (ISSN 0026-0843). (Translated in English)

C. Amorphous phase considerations in wear resistant coatings

R. Vazquez, C. Soffritti, M.Merlin, G.L. Garagnani

Preprint 2012

D. Microstructural homogeneity between APS and HVO WC-12Co coatings.

R.Vazquez.

Preprint 2012

Other Related Papers and Activities not Included in the Thesis

In addition to the papers included in the thesis, further publications are listed below:

1. F. A REYES-VALDES, V. M. LOPEZ-CORTES, G. Y. PEREZ-MEDINA, H. F. LOPEZ, M. MERLIN, R. A. VAZQUEZ-AGUILAR, I. CALLIARI, **"Effect of welding on the mechanical integrity of a TRIP steel"**, International Congress "Super-High Strength Steels", Peschiera del Garda (VR), October 17-20 of 2010, AIM Ed., Milano, CD-ROM, (2010), (ISBN 978-88-85298-79-8). (ISBN 9781605112190)

2. M. MERLIN, C: SOFFRITTI, R: VAZQUEZ, V. MAZZANTI, G. L. GARAGNANI, **"Analytical treatment of uncertainties for a macroscopic tribology instrumentation"**, Atti del Convegno Internazionale "8th International Workshop on Progress in Analytical Chemistry &Materials Characterization in the Steel and Metal Industries ", Luxembourg, may 17-19 of 2011, (2011), p. 383-390.

3. M. MERLIN, R. VAZQUEZ, C. SOFFRITTI, A. REYES, **"Influence of heat input and solubilizing heat treatment on the impact properties of SAW joints in SAF 2205 duplex steel"**, Presented in XVIII International Materials Research Congress - Materials Welding and Joining Technologies, Cancun (Mexico) august 14-19 of 2011, Selected for the congress memoirs.

4. F. A. REYES-VALDES, M. MERLIN, V. H. LOPEZ-CORTES, R. A. VAZQUEZ-AGUILAR, G. L. GARAGNANI**, "Effetto delle condizioni di trattamento termico sulle proprietà microstrutturali e meccaniche di giunti saldati in**

acciaio ad alta resistenza (AHSS) per applicazioni automobilistiche", Presented at 22° Convegno Nazionale Trattamenti Termici, Salsomaggiore Terme (PR) may 6-7-8 of 2009, AIM Ed., Milano, CD-ROM, (2009) (ISBN 88-85298-68-0).

5. M. MERLIN, C. SOFFRITTI, R. VAZQUEZ, G.L. GARAGNANI, **"Comportamento tribologico di rivestimenti ceramici avanzati mediante tecniche APS e HVOF"**, Atti del 33° Convegno Nazionale AIM, Brescia, november 10-12 of 2010, AIM Ed., Milano, CD-ROM, (2010), (ISBN 978-88-85298-80-4).

6. M. MERLIN, C. SOFFRITTI, R. VAZQUEZ, G.L. GARAGNANI, **"Caratterizzazione tribologica di accoppiamenti bilanciere-valvola e bilanciere-asta di motori diesel per macchine industriali"**, Atti del 33° Convegno Nazionale AIM, Brescia, november 10 -12 of 2010, AIM Ed., Milano, CD-ROM, (2010), (ISBN 978-88-85298-80-4).

Another important role of my PhD was to supervise the following theses, performed at the Engineering Department of the University of Ferrara:

1. Andrea Artioli (2009), **"Analisi microstrutturale di un acciaio da cementazione sottoposto a prove d'usura"**, Supervisors: G.L. Garagnani, C. Soffritti, R. Vazquez.

2. Valentina Boccia (2009**), "Valutazione del comportamento tribologico di riporti termici in Cr2O3 e Al2O3-13%TiO2 ottenuti mediante spruzzatura al plasma"**,Supervisors: G.L. Garagnani, C. Soffritti, R. Vazquez.

3. Marco Vitali (2010), **"Comportamento ad usura di rivestimenti ceramici realizzati mediante spruzzatura termica"**, Supervisors: G.L.Garagnani, C. Soffritti, R. Vazquez.

4. Marcello Bertasi (2010), **"Caratterizzazione microstrutturale di rivestimenti in**

Al2O3-13%TiO2 e Cr2O3 ottenuti mediante APS (Air-Plasma-Spray)”, Supervisors: G.L. Garagnani, C. Soffritti, R. Vazquez.

5. Matteo Cisotto (2010), **“Caratterizzazione metallografica del rivestimento WC-12Co ottenuto mediante HVOF (High Velocity Oxygen-Fuel)”,** Supervisors: G.L. Garagnani, C. Soffritti, R. Vazquez.

6. Andrea Covizzi (2010), **“Caratterizzazione metallografica del rivestimento WC-12Co ottenuto mediante APS (Atmospheric Plasma Spraying)”**, Supervisors: G.L. Garagnani, C. Soffritti, R. Vazquez.

ACKNOWLEDGEMENTS

I would like to thank my supervisors Prof. Gian Luca Garagnani and Prof. Irene Calliari for the opportunity of this PhD research project, for their advice, guidance and for sharing their knowledge with me.

I want especially to thank my PhD colleagues and friends Mattia and Chiara for their invaluable support, expertise and advice.

A well merited thanks for Prof. Vincenzo Gabrieli for sharing such experience and knowledge without any reserve.

To Armando Saldivar Garcia† that still now his advices are considered.

To those without any interest friends who always helped me; Annalissa, Arge, Daniele, Fabio, Luis and….Monia.

To all the wonderful friends that I have the opportunity to know during this period and now is part of my life.

A special recognition to my Grandmother: for her love, patient and advices.

And for my parents, and my wonderful big family, because they believe in me.

All those people who in one way or another, gave me part of his force to continue. Laura, Irma, Sergio, Aniceto, Bertha, Viann, Vanne, Ruth, Eben, Rebe[2], Clara, Giezi etc… are so many… love you.

To Del Real Family because always help me with advices, phone calls, and translations… thanks Dr. del Real.

For my sister and brother, because you are blessings of God in my life.

Are many people to thanks and is impossible to write in this piece of paper but also if your names are not here you must be sure that are impressed in my heart, and without you this could not have been possible.

SUMMARY

This thesis presents the results obtained through characterization techniques and wear tests for diverse kinds of cermet and ceramic coatings applied by APS and HVOF techniques. The Al_2O_3-13TiO_2 and WC-12Co can be applied by high temperature spraying process allowing them to be deposited onto metallic surfaces with less tribological properties. The application of those coatings onto metallic surfaces of finished parts, increases their performance in industrial applications; reducing maintenance cost, and increasing its operating time.

The actual methods to characterize these coatings are usually destructive methods. But with non-destructive tests like XRD and XRF it is possible to obtain important information and establish a standard quality.

The most important characteristics of ceramic and cermet coatings are the crystal phase distribution, the amorphous bending phase and in the WC-12Co the decarburization. Depending on the application processes, the original powder particles are altered, changing their particle size, creating new phases and producing residual stress and deformation of crystal structures by the loss or substitution of atoms in the original crystal structures. Analyzing the diffraction patterns it is possible to observe which changes occur after spraying processes and evaluate the effect of those processes on the coating. A mapping via XRD allows to observe how homogeneous is the coating applied and if specific uneven zones exist that will present lower wear characteristics.

RIASSUNTO

Questo lavoro di tesi mostra il risultati ottenuti mediante tecniche di carcaterisazione e prove di usura per diversi tipi di material tipo ceramico e cermet applicati mediante tecniche di spruzzatura tipo APS e HVOF.

Il Al_2O_3-13TiO_2 e WC-12Co possono essere applicati mediante tecniche di spruzzatura ad alta temperatura permettendo di essere depositate sopra superfici metalliche, dove le sue proprietà tribologica sonno minori.

La applicazione di questi ricoprimenti sopra superficie metallica di pezzi già finite, aumenta la sua prestazione nel ambito industriale, riducendo I costi di manutenzione e anche un aumento nella durata della sua vita utile

Gli attuali metodi di caratterizzazione su questi rivestimenti sono di solito prove distruttivi. Ma ci sono delle prove non distruttive fatte con XRD e XRF, è anche possibile ottenere informazioni importanti e stabilire uno standard di qualità.

Le caratteristiche più importanti dei rivestimenti tipo ceramico e cermet sono la distribuzione di fase cristallina, la fase di incollaggio amorfo e nel WC e 12CO la decarburazione.

A seconda del processi di applicazione, le particelle di polvere originali sono alterati, cambiando le dimensioni delle particelle, creando nuove fasi e producendo tensioni residue e deformazione delle strutture cristalline dovuto alla perdita o sostituzione di atomi nelle strutture cristalline originale.

Analizzando il pattern di diffrazione è possibile osservare quali cambiamenti avvengono dopo i processi di spruzzatura e valutare l'effetto di tali processi sul rivestimento.

Una mappatura tramite XRD permette di osservare come omogeneo è il rivestimento applicato e se esistono specifiche zone irregolari che presentano caratteristiche di usura inferiore.

CONTENTS

I

INTRODUCTION

The study of the materials used as resistant coatings has been carried out for a long time. Cermet and ceramic coatings are an important sector of the wear resistant materials.

The cermet and ceramic coatings can protect surfaces against the wear produced by friction, abrasion, corrosion and their properties are improved by using diverse application processes. Usually, if the microstructure is similar to that of a sintered material, the wear behavior increases. But this compact characteristic is difficult to obtain with the actual coating processes, like APS and HVOF, which have many variables that can affect the final coating`s characteristics. The improvement of these processes, in the application of coatings from cermet and ceramic powders, is obtained by means of varying the application parameters such as distance, particle size, velocity, temperature, etc.

According to the final microstructural characteristics, residual stress and porosity of the coating the tribological behavior can present different mechanisms. In this study an exhaustive characterization of coatings, basically via XRD in different modalities, has been carried out. In particular for the case of the ceramic coating material, wear tests have been carried out in order to understand its tribological properties.

The studied materials were a ceramic coating: Al_2O_3-13TiO_2 applied with the APS technique that provides lower porosity levels and higher coating density. The coating adhesion to the substrate is usually improved through the use of a bonding coat, in this case Ni-20Cr. The Al_2O_3-13TiO_2 coating is used where wear resistance, good surface finish and precise dimensions are required.

The other coatings used were cermets: WC-12Co, usually applied on cutting tools for machining. Their high wear, temperature and friction resistance make the WC-12Co one of the principals materials for this kind of application. Two different processes have been evaluated: coatings applied by APS and HVOF techniques. The differences

between these two application techniques on microstructure are wide which allows a comparative study with solutions proposed for particular applications.

The thesis is divided in two main parts. The first one includes the State of the Art where the recent studies in Al_2O_3-$13TiO_2$ ceramic and WC-12Co cermet coatings applied wit APS and HVOF process are considered; and a brief description of wear mechanisms.

In the second part the main results of the research activity are reported in the form of scientific articles for publication.

II

STATE OF THE ART

2.1. - INTRODUCTION

2.1.1. - The Origin of Coatings

The need to create materials more and more resistant is an ever-present fact in man history, from the Stone Age, evolving into the Bronze Age, the Iron Age, etc. and with the arrival of the industrial revolution the current production processes require greater productivity, which means less dead time, for example for preventive maintenance or replacement of parts.

Modern equipment is highly sophisticated, mostly automated and expensive. This equipment is designed to sustain high production rates for a reasonable period of time. Advanced materials and surface engineering processes are used in manufacturing the equipment in order to minimize wear.

A particular sector in wear resistance of the materials is the finishing surface where the material if is a metal is treated with a mirror finish surface or a particular surface treatment as carburized. Another important process is the electroplating addition of another kind of material to protect the core from corrosion.

The coatings have been commercially used since 1920's [1].

The application processes, the materials used as a coating and substrate, the effects that are produced have been studied.

The development of these materials as coatings create ceramic and cermets coatings that usually been applied onto a metal, to improve its wear, corrosion and temperature resistance.

The application fields range from cutting tool inserts to the biomedical sector depending of the materials used. New applications have been found every day.

The materials used in this study are composites; according to ASM a composite material is a macroscopic combination of two or more distinct materials, having a

recognizable interface between them. The resulting composite material has a balance of structural properties that is superior to either constituent material alone. [2]

In this case a mix of powders and bond material are combined to create a coating to protect metal surfaces.

The studied coatings are Al_2O_3-13TiO_2 (ceramic coating), and WC-12Co (cermet coating) applied by APS or HVOF onto a steel surface. These techniques and the main characteristics of the bulk materials will be described.

However, the study of these coatings is very interesting due to the versatility of application surfaces and the wear and corrosion resistance. There are also many troubles been related to the process and use of coatings. The microstructure is usually inhomogeneous and totally different from that of cast, rolled or sintered material. Discontinuities, such as pores, thermal stresses, induced cracks, oxide lamellas or incomplete molten spray particles are commonly present.

2.2.- MATERIALS

2.2.1 Aluminum oxide, (Alumina, Al_2O_3).

It exists in many metastable polymorphs besides the thermodynamically stable α-Al_2O_3 (corundum form). The metastable Al_2O_3 structures can be divided into two broad categories: a face-centered cubic (fcc) or a hexagonal close-packed (hcp) arrangement of oxygen anions. It is the distribution of cations within each subgroup that results in the different polymorphs. The Al_2O_3 structures based on fcc packing of oxygen include γ, η (cubic), θ (monoclinic), and δ (either tetragonal or orthorhombic), whereas the Al_2O_3 structures based on hcp packing are represented by the α (trigonal), κ (orthorhombic), and χ (hexagonal) phases. Some additional monoclinic Al_2O_3 phases have been identified recently.

Because of their fine particle size, high surface area, and catalytic activity of their surfaces, the transition aluminas (especially the γ form) find applications in industry as adsorbents, catalysts or catalyst carriers, coatings, and soft abrasives. The excellent stoichiometry and stability of Al_2O_3 help to make it an important constituent of many protective oxide scales formed on the surface of high-temperature metals and alloys [3-4].

If the bulk material is the stable form α-Al_2O_3 (corundum form) the polymorphs can be obtained by dehydration of different alumina hydroxides, rapid quenching from the melt, vapor deposition, thermal spraying and crystallization [5]. The standard transitions [4] are showed in the figure 1.

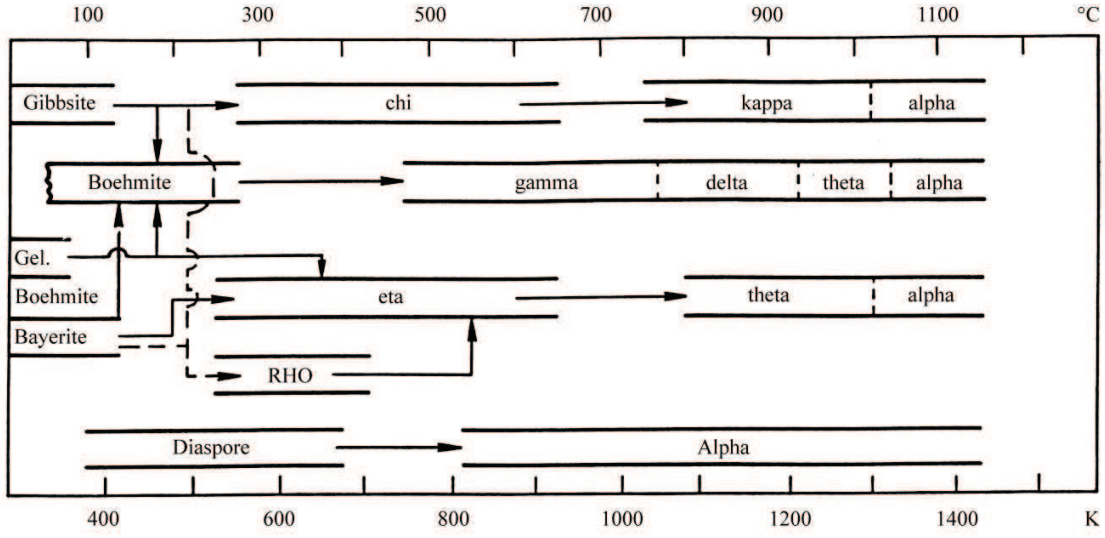

Figure 1. - Thermal transformation sequence of the aluminum hydroxides [4].

Flame sprayed alumina coatings were reported to contain predominantly metastable γ-Al_2O_3 in addition to the equilibrium α-Al_2O_3 phase. Plasma as-sprayed alumina coatings from commercial α-Al_2O_3 feedstock additionally showed presence of δ-Al_2O_3. Recent studies show the presence of new phases after HVOF or APS, this phase is called U phase [5].

2.2.2. - Titanium dioxide, (Titania, TiO_2).

Titania exists mainly in two polymorphic phases, anatase and rutile, which crystallize both in tetragonal lattice. The rutile is the stable form of TiO_2 and the other one is anatase (metastable), which irreversibly transforms to rutile during heating. Depending of the powders characteristics and application parameters it is possible to control the transformation between the anatase (low temperature) phase and the rutile (high temperature) phase [6-7].

The importance of control transformation is dependent on the applications; one application of TiO_2 is in photocatalysis where TiO_2 in the anatase phase has shown the greater photocatalytic efficiency compared with rutile phase. The photocatalytic efficiency of the material depends on the cristallinity of the material, surface area, shape of the particle, band gap and the amount of electrons around the Fermi energy. Depending of the application parameters it is also possible to dissolve all the crystal phase of TiO_2 [8-9].

2.2.3. - Tungsten carbide, (WC).

The tungsten carbide is relatively hard and brittle, has highly corrosion-resistant properties, and shows a high-temperature stability, chemical inertness and good electrical conductivity. The coatings of pure tungsten carbide, or alloyed with cobalt or iron tungsten carbide, exhibit high wear resistance and low friction. Furthermore, their hardness at high temperatures is outstanding [10].

According with S. Kim et al, the WC grains change their shape with the C content depending on the preferred growth of the crystal structure and it is responsible for the appearance of new crystallographic planes [11].

2.2.4. - Cobalt, (Co).

In coatings the Co is used as binder, based on considerations of strength, hardness, and toughness, cobalt is the best binder for tungsten carbide. The wetting of tungsten carbide by cobalt, the solubility of tungsten carbide in cobalt, the adhesion of cobalt to tungsten carbide and the strength characteristics of thin cobalt films containing carbon and tungsten all contribute to its performance [12].

2.3. - COMPOSITE MATERIALS FOR COATINGS.

The powders for coatings are mixed and fused or sintered and crushed with micrometric dimensions and in some cases nanometric size. The particle size selection is in order to improve the final properties, cost and use.

In the table I a summary of the material characteristics and the application technique is presented.

2.3.1 Al_2O_3-13TiO_2

Plasma sprayed ceramic coatings are used in the industry due to the high wear and corrosion resistance and thermal insulation.

The mechanical properties of the coating are usually strongly dependent on their microstructure such as phase composition, grain size, porosity and its distribution. Microhardness and toughness values of the Al_2O_3 coating can be amended by changing its composition with addition of TiO_2 in plasma spraying in a way that this contribute to increase the toughness and wear resistance values of the coating.

R. Yilmaz et al. find that Al_2O_3 with addition of TiO_2 lowered significantly the microhardness of the alumina coating. And a decrease in hardness values resulted in an increase in toughness values of the alumina coatings [13].

Depending of the material conditions process and composition a phase diagram for these composites is reported in figure 2, and tacked from a study where after APS of AL_2O_3-13TiO_2 the particles have been cooled at different cooling range the phase diagram present the possible structures that can be created at specific conditions.

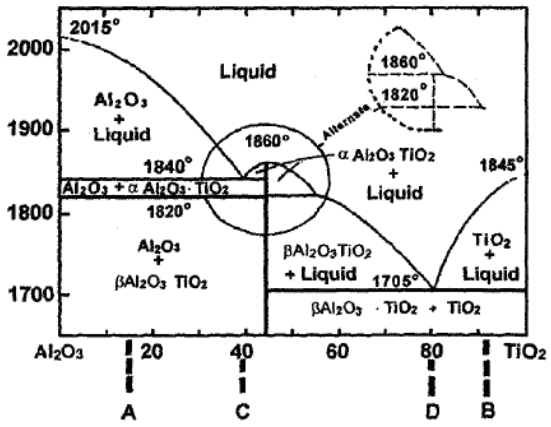

Figure 2.- Phase diagram for the system Al_2O_3-TiO_2

2.3.2. - WC-12Co

WC cermet carbides are used as tool and dies, depending of the application and cost the Co content has been controlled, but the effect about Co content on the cermet properties is still unclear [14]. The Co content and WC grain size influence the mechanical properties and wear behavior. Hsaito et al. find that increasing the Co content and WC grain size the specific wear rate increased [15].

The principal effect in the Co content is in the hardness of the material, increasing the Co content the hardness decrease. Also the sizes of the WC particles significantly affect the mechanical properties and wear behavior. The studies realized about the grain size and its effect tried to improve the parameters of the high temperature application techniques (APS and HVOF) to use particles with smaller dimensions and with adequate control of application parameters technique is possible obtain less decarburation of WC and change in properties.

Li et al. find that the relative abrasive wear of WC-Co coating is proportional to the square root of relative carbide size [16].

2.4. - THERMAL SPRAY TECHNOLOGIES

Thermal spray coating technologies have become indispensable in several high-tech areas such as aircraft and automobile manufacture, power engineering, heavy machinery manufacturing, electronics, the waste treatment industry, and medicine. Thermal spray technologies have bright prospects for the future as they have proved to be technically feasible and highly effective investments [17].

Materials applied with these techniques retain their properties, as in the case of ceramics low chemical reactivity and the thermal insulation capacity, or like cermet materials with super hardness, high temperature and wear resistance.

2.4.1 APS (Air Plasma Sprayed)

The Plasma Spray Process uses an electric arc that heats up to high temperature the flux or inert gas (pure Ar, and mixtures with He, H_2, etc.) to generate plasma. The addition of He and in particular of molecular gases results in a drastic increase in the enthalpy of the plasma. The temperatures reached with this source are around 8300°C

(15000°F) and the velocities around 300-550 m/s, where the maximum velocity and temperature are functions of the design and the operating parameters. The powder material is injected into the plasma flame, then the material impacts on the substrate surface and solidifies almost immediately, creating the coating. If the process is carried out correctly, the substrate temperature remains low during the process, preventing mechanical and metallurgical changes in the substrate material. In figure 3 a scheme of a Plasma spray operation is shown[18-19].

The control parameters as temperature and velocity and the particles size, shape, chemistry and the surface preparation for these depend on the finish surface. An example is the porosity control, for the lowest porosity, the particles should be relatively hot and not too fast. This ensures proper splat formation and flow of the splat material as individual thermal spray particles impact the surface. Once a coating is optimized in one location or with one gun, the temperature/velocity data can be transferred to other [19].

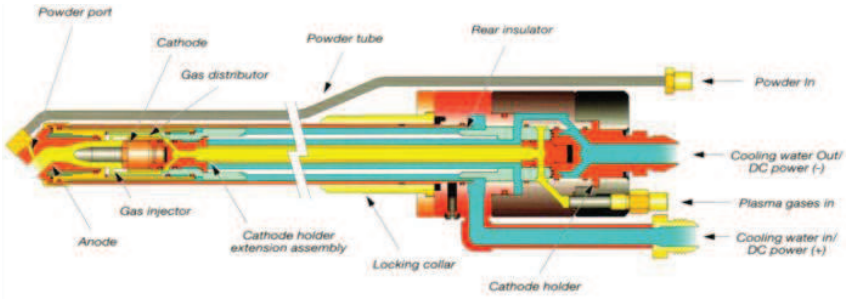

Figure 3. - Schematic illustration of Plasma Spray operation [18].

In the plasma spray torch a gas flows around the tungsten cathode and through a water-cooled copper anode which is shaped as a constricting nozzle. An electric arc is initiated between the two electrodes using a high-frequency discharge and then sustained using DC power. The arc ionizes the gas, creating high-pressure gas plasma. The resulting increase in gas temperature, which may exceed 30,000 °C, in turn increases the volume of the gas and, hence, its pressure and velocity as it exits the nozzle. Power levels in plasma spray torches are usually in the range of 30 to 80 kW, but they can be as high as 120 kW [19].

An important advantage of Plasma spray is that this process can be used to produce coatings of virtually any metallic, cermet, or ceramic material.

Disadvantages of the plasma spray process are a relative high cost and the complexity of the process.

2.4.2 HVOF (High Velocity Oxygen Fuel).

This system is a refined oxy-fuel burner which uses advanced nozzle design technology to accelerate the gas particle stream to achieve particle velocities in excess of 550m/s.

A torch for this process is shown in figure 4 Fuel (propane, propylene, MAPP, or hydrogen) is mixed with oxygen and burned in a chamber. The products of the combustion are allowed to expand through a nozzle where the gas velocities may become supersonic. Powder is introduced, usually axially into the nozzle, where it is heated and accelerated. The powder is usually fully or partially melted. Because the powder is exposed to the products of combustion, they may be melted in either an oxidizing or reducing environment, and significant oxidation of metal and carbides is possible.

With appropriate equipment, operating parameters, and choice of powder, coatings with high density and with bond strengths frequently exceeding 69 MPa (10,000 psi) can be achieved. Coating thicknesses are usually in the range of 0.05 to 0.50 mm (0.002 to 0.020 in.), but substantially thicker coatings can occasionally be used when necessary with some materials.

HVOF processes can produce coatings of virtually any metallic or cermet material and, for some HVOF processes, most ceramics. Those few HVOF systems that use acetylene as fuel are necessary to apply the highest-melting-point ceramics such as zirconium or some carbides. HVOF coatings have primarily been used for wear resistance to date, but their field of applications is expanding. [19]

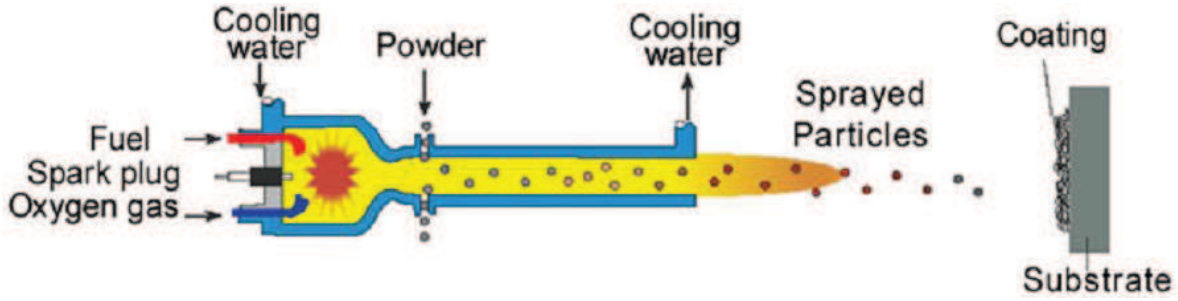

Figure 4. - Schematic illustration of HVOF Spray operation [20].

The coatings produced by HVOF are similar to those produced by the detonation process. HVOF coatings are very dense, strong and show low residual tensile stress or in some cases compressive stress, which enable the application of very much thicker coatings than those previously possible with the other processes.

The very high kinetic energy of particles striking the substrate surface does not require the particles to be fully molten to form high quality HVOF coatings. This is certainly an advantage for the carbide cermet type coatings and is where this process really excels.

HVOF coatings are used in applications requiring the highest density and strength not found in most other thermal spray processes.

2.4.3. - Differences between processes

Plasma and HVOF processes are different with regard to two principal aspects: the thermal and the kinetic engines of sprayed particles. A comparison of APS and HVOF spraying shows that the plasma processes offer higher plasma temperature at relative low velocities whereas in the HVOF process is the opposite. The temperature of the HVOF spray stream does have some dependence on the choice of fuel gas. In addition, it has to be taken into account that the HVOF spray distance exceeds the plasma spray distance and that when HVOF is used with at shorter spray distances it can lead to overheating of the substrate. But the HVOF process, because of the lower flame temperature and higher particle velocity, induces less phase transformation into the

starting material and produces denser coatings with lower porosity and higher cohesive strength in comparison to those obtained with the APS process [21-22].

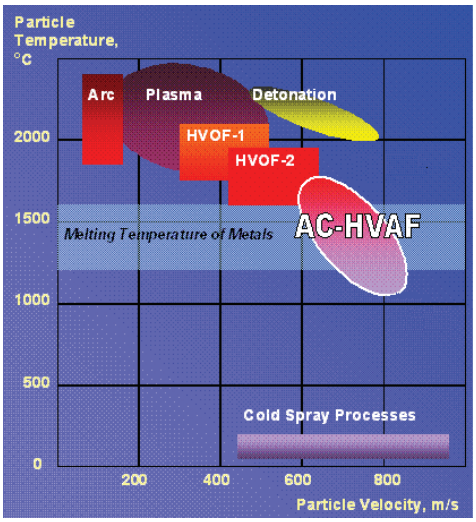

Figure 5. - Schematic illustration of differences in velocity and particle temperature in some spraying processes.

It is possible to better understand the process technique in the next image according from Goberman. He applies this model toAl_2O_3-13TiO_2 coating[9].

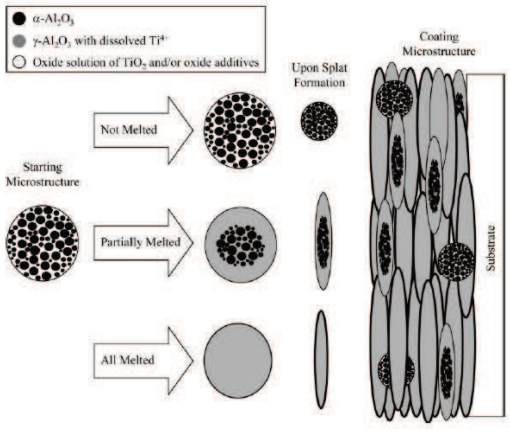

Figure 6. - A schematic illustration of phase transformations and microstructural development during the plasma spray deposition of reconstituted nanostructured Al_2O_3–13wt.%TiO_2 agglomerates [9].

Table I. - Material characteristics and application techniques.

Material	Particle Size(μm)	Application technique	Bond Coat
Al_2O_3-13TiO_2	-45+15	APS	---
WC-12Co	-88+44	APS	---
WC-12Co	-45+15	HVOF	Ni-19Cr

A review has been carried out on all the recent studies involving materials and application techniques in the field of characterization, microstructure and wear resistance properties of coatings,.

2.5. - WEAR

2.5.1. - General concepts of wear process.

The interaction of the surface with its interfacing environment produces damage and the progressive removal of material from surface; according to this concept is possible defines wear. The study of this phenomenon is fundamental in the study of tribology; this term comes from the Greek word tribos, or rubbing, and is defined as the science of friction-wear-lubrication of interacting surfaces in relative motion.

The study of tribology has an important effect in the industrial sector because the costs generated by degradation of materials are high, the industry invest an important part of resources in prevention and attenuation of its effects.

The wear is classified mainly in four types based on mechanisms, this are adhesion, abrasion, surface fatigue, and corrosion [23-25,30]. Even the mechanisms may vary slightly depending on the approach from the area of materials being studied. In this study a brief description of the main four mechanisms has been done. Wear is not an intrinsic property of the material but a system property classification. In a wear process normally more than one of these mechanisms is present.

The general form of the wear equation is based on the relationship:

The wear volume (V) is directly proportional to the sliding distance (d) and the applied normal force (FN) and inversely proportional to the hardness or yield stress (H) of the softer surface as follows:

$$V \propto \frac{F_N}{H} \cdot d \quad \text{(Eq. 2.5.1)}$$

$$V = K\frac{F_N}{H} \cdot d \quad \text{(Eq. 2.5.2)}$$

The wear coefficient K is a proportionality number equal to the wear volume per unit sliding distance with the applied normal force equal to the hardness or yield stress of the softer material, from eq. 2.5.1 adding the proportionality constant is obtained eq. 2.5.2.

To evaluate a wear process ASTM has standards to regulate the tests [26] as well as the results and some of them appear in Table II.

The amount of wear in any system will, in general, depend upon the number of system factors such as the applied load, machine characteristics, sliding speed, sliding distance, the environment, and the material properties.

Table II. - ASTM standards for wear and tribology tests.

ASTM standard designation:	**Method for:**
G 99	Standard Test Method for Wear Testing with a Pin-on-Disk Apparatus
D 4172	Standard Test Method for Wear Preventive Characteristics of Lubricating Fluid (Four-Ball Method)
G 40	Terminology Relating to Wear and Erosion
G 65	Standard Test Method for Measuring Abrasion Using the Dry Sand/Rubber Wheel Apparatus
G 76	Standard Test Method for Conducting Erosion Tests by Solid Particle Impingement Using Gas Jets
G 102	Standard Practice for Calculation of Corrosion Rates and Related Information from Electrochemical Measurements

2.5.2. - Test configuration for wear process.

Examples of some wear test geometries are briefly described bellow in order to have a general idea of the application and because is necessary to develop appropriate design systems to simulate the closest conditions to the real process. Fortunately, some work on the selection and standardization of wear test for coatings can be found in the literature[27].

a) Pin/ball/cylinder -on-disc test: two materials are tested under nominally non-abrasive conditions; pin-on-disk wear test system consists of a driven spindle and chuck for holding the revolving disk, a lever-arm device to hold the pin, and attachments to allow the pin specimen to be forced against the revolving disk specimen with a controlled load. Another type of system loads a pin revolving about the disk center against a stationary disk. In any case the wear track on the disk is a circle, involving multiple wear passes on the same track. The pin can be: flat, radiused tip, an sphere or a cylinder [26].
b) Block-on-ring test: A stationary block specimen is pressed with a constant force against a rotating ring specimen at 90° to the ring's axis of rotation. Friction between the sliding surfaces of the block and ring results in loss of material from both pieces [26].
c) Ball-on-balls/flat: Three balls are clamped together, a fourth ball, concerns to as the top ball is pressed into the cavity formed by the three clamped balls for three point contact, the top ball is rotated with a specific number of rpm. The contact surface formed by the three balls can be modified by three fixed flat surfaces and the track will be likewise circular [26].

The geometries discussed earlier are shown in figure 7 respectively.

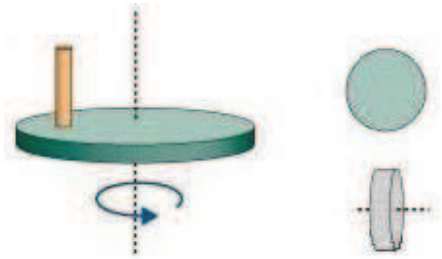

a) Pin-on disk/ball/cylinder

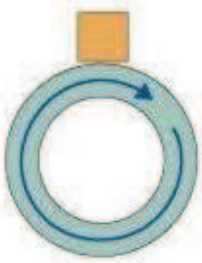

b) Block on ring

c) Ball on balls/flat

Figure 7. - Commonly wear test geometries.

2.5.3. - Wear Mechanisms.

2.5.3.1. - Adhesive wear

In adhesive wear, the sliding surfaces under load adhere together through solid phase welding of asperities, as the figure 8 showed. Subsequent detachment from either surface results in loss of materials. It is caused when the yield strength is exceeded, and the contacting surface asperities has been deformed plastically until break point of material, producing wear particles that can be cold-weld.

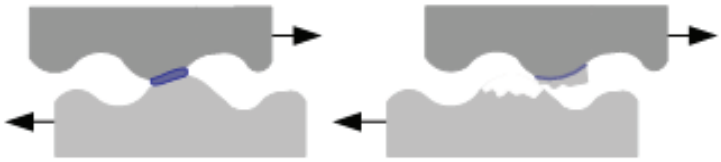

Figure 8. - Schematic of adhesive wear.

The adhesive wear equation (Eq. 2.5.3) is:

$$V = K_{adh} \frac{F_N}{H} \cdot d \text{ (Eq. 2.5.3)}$$

Where Kadh = K/3

This equation indicates that the wear volume for adhesion is proportional to the normal load and sliding distance and inversely proportional to the hardness of wear material.

Three different set of conditions help to cause low adhesive wear:

Mating Pairs with a low wear ratio

Suitable surface finis of the mating components

Suitable surface coating is provided to the surface to be protected from wear

2.5.3.2. - Abrasive wear

As defined by ASTM [23], is due to hard particles or hard protuberances that are forced against and move along a solid surface. Wear, in turn, is defined as damage to a solid surface that generally involves progressive loss of material and is due to relative motion between that surface and a contacting substance or substances.

Parallel grooves are formed on a wear surface. This means that hard abrasive asperities are formed on the wear surface because of e.g. such as work hardening, phase transitions and third body formation at the interface [28].

The abrasive wear can be sub divided in two body low stress abrasion, and three body or high stress abrasion:

Abrasive two-body wear occurs when a hard object ploughs through a softer object, due to an applied normal force and the relative movement of these objects, the stress involved normally does not cause fragmentation of abrasives[29].

During three-body abrasive wear, the abrasive particles are forced between two mating surfaces, high stress abrasion occurs, leading to loss of materials from both component surfaces. Under extreme high-stress conditions is known as gouging.

The schematic representation of two and three body abrasive process is represented in figure 9 a) and b) respectively.

A loss of material from the surface is caused by sliding abrasives under load. Both free-flowing particles and abrasive attached to the counterbody cause wear.

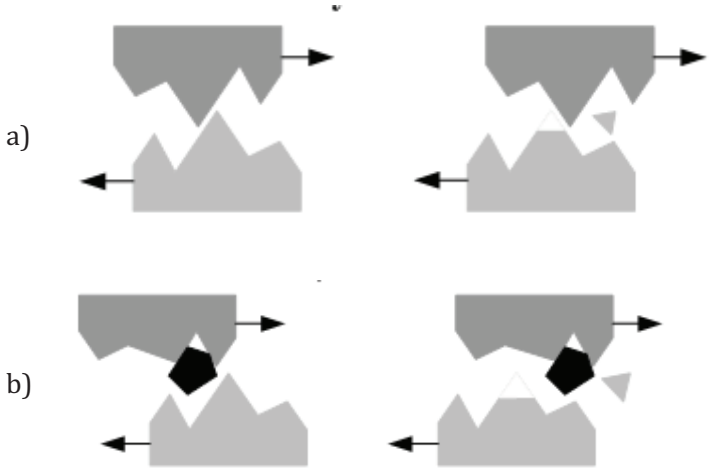

Figure 9. - Schematic representation for abrasive wear of two and three body process.

The abrasive wear equation (Eq. 2.5.4) is:

$$V = K_{abr} \frac{F_N}{H} \cdot d \quad \text{(Eq. 2.5.4)}$$

Where $K_{abr} = K \frac{a \cot \alpha}{\pi}$

And α=+1 to 2. Equation 2.5.4 is derived from the action of a single particle with an angle of attack (2α) and load (FN) causing wear on a work hardened surface of hardness H as in figure 10 The sequence to obtain the coefficient`s value is explained between the eq. 2.5.5 to 2.5.9. [1]

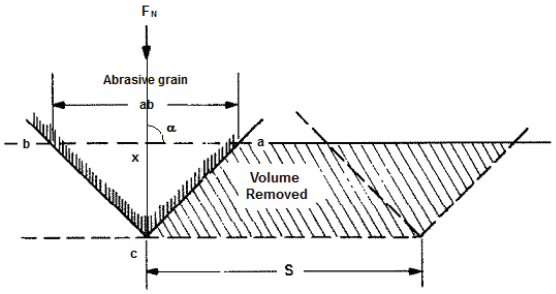

Figure 10. - Schematic abrasion model in which an ideal cone particle removes material from a surface.

$$2\tan\alpha = \frac{ab}{xc} \text{ (Eq. 2.5.5)}$$

were ab = wear length = 2xctanα. Now

$$H=\frac{F_N}{(ab)^2} \text{ or (Eq. 2.5.6)}$$

$$\frac{F_N}{H(ab)} = ab = 2(xc)\tan\alpha = \text{wear length} = \frac{V}{d} \text{ (Eq. 2.5.7)}$$

Or

$$\frac{V}{d} = \frac{F_N}{2H(xc)\tan\alpha} = \frac{F_N}{H} k_{abr} \text{ (Eq. 2.5.8)}$$

Or

$$k_{abr} = K\frac{a\cot\alpha}{\pi}\left(\frac{\pi}{a} = 2xc\right) \text{ (Eq. 2.5.9)}$$

2.5.3.3. - Corrosion

It takes place when a corrosive environment produces a reaction product on one or both of the rubbing surfaces and this reaction product is subsequently removed by the rubbing. For the most usually occurring environments such as air at room temperature containing humidity and other industrial vapors, corrosive wear is primarily important for surfaces. [30] Reactions with oxygen, carbon, nitrogen, sulfur, or flux result in the formation of an oxidized, carburized, nitride, sulfurized or slag layer on the surface. Temperature and time are two important factors controlling the rate and severity of corrosive attack.

The use of lubricants can protect the surfaces from the corroding environment, thus reducing or minimizing the corrosive wear that would otherwise result. But if the selection of lubricant is not appropriate it may react chemically with the surface, thus altering the type of compound and amount of wear that would otherwise occur. One form of wear corrosion is showed in the figure 11. The figure shows the severe case of wear for corrosion.

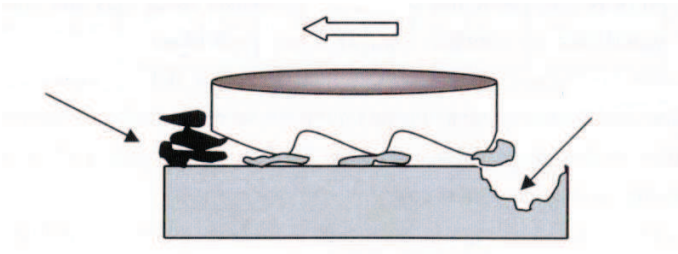

Figure 11. - Uncontrolled adhesive wear and rapid corrosion of the exposed surface.

2.5.3.4. - Surface Fatigue

The repetitive action of the counterbody, under a fluctuating load, causing wear of the main body, is more akin to fatigue process. Fatigue related wear not only results in material loss from the surface; it also can reduce the working life of the engineering component.

The continuing friction between parts in contact causes the accumulation of local palstic deformation on the surface of material, creating cracks after a certain number of cycles. Primary cracks are generated at the surface inwards of material; the primary cracks can create secondary cracks or coalesce between them and thus generate wear particles. As is showed in figure 12.

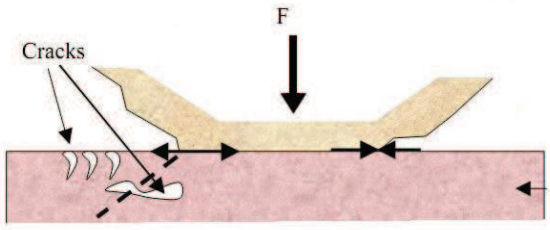

Figure 12. - Schematic representation for fatigue surface wear.

As mentioned at the beginning, two or more of the independent wear mechanisms may occur simultaneously and interact. A significant example of this is fretting; it occurs between two interacting mating surfaces, which are subjected to an oscillatory motion of small amplitude. When corrosion products form at the interface of two mating surfaces, the process is also known as fretting corrosion. Fretting wear occurs through a combination of fatigue, corrosion and adhesion processes.

The principal types of mechanical wear has been explained before, however, a number of minor types wear mechanism like erosion, impact chipping are considered for other authors.[30]

The wear mechanisms from its origins has been studied for metallic materials [30], but with the develop of new technologies and materials applications in the industry as ceramics and plastics that constitute two major groups of materials, which, apart from metals, are used extensively in applications requiring wear and corrosion resistance. The wear behavior depending of the kind of material and its properties. A brief description of the wear in ceramics is presented bellow.

2.5.4. - Wear of ceramics.

Factors affecting the wear of ceramics include plastic deformation and fracture toughness. The plastic deformation in ceramic materials is negligible. The wear in crystalline ceramics arises from crack formation during deformation and subsequent growth of those cracks.

Its well know that a fracture occurs when the stress intensity factor (K_I) reach the fracture toughness(K_c) value of the material and exceeds the fracture toughness (K_c) of the material [23]; according to this wear in ceramics materials is normally divided in three regimes depending of the factor of tension intensity.

If this factor is less than the toughness of worn material the regime is called mild wear, if the factor is greater than toughness the regime is called severe wear, and finally if the stress intensity factor is much higher than the toughness the wear regime is called ultra severe. The failure of brittle ceramic materials depends on the fracture toughness.

2.5.5. - Wear Transitions

A wear transition can be defined as a sudden change in the rate of wear. It can be produced by a minimal variation of the independent variables that affect the system, as time, load, velocity, temperature, and etcetera. And this transition occurs independently of the wear mechanism. It can be divided in three basic types of behavior; Type a) Here the transition is from a severe wear to a mild wear (usually

observed in metals). Type b) the wear behavior is constant without transition in the wear regimes. Type c) The transition occurred from a mild wear to a severe wear (typical behavior of ceramic materials). The regime transition is accompanied by an abrupt change in the friction coefficient, it increase or decrease depend of the transition type. The graphic in figure 13 shows the wear behavior as a function of transitions.

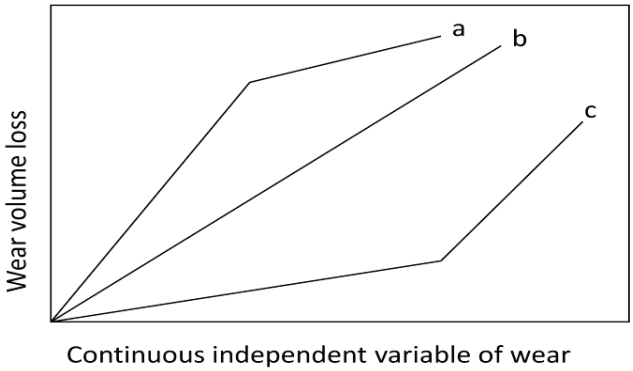

Figure 13.- Wear behavior as a function of transitions

2.6. - PROPERTIES OF COATINGS

2.6.1. - Al_2O_3-13TiO_2

The coatings realized with Al_2O_3-13TiO_2 and applied with APS process exhibit important characteristics: a dense surface with low porosity and very uniform lamellar structure. The porosity is caused by the reactions occurred during the APS process like de-oxidation and thus the generation of new compounds; porosity distribution is uniform and is not interconnected. The intersplat adhesion is favored by the alumina-titania glassy phase formed during the process. The use of bond coats improves the adhesion of the coating to the substrate. Definitely these are the ideal characteristics; but as will be described below, they depend of many factors like: parameters used in the APS process, powder characteristics as the size and morphology of the particle powders and its composition. However, there are some aspects that can be improved, as the residual stresses. These are product of the fast

cooling rates that the particles experiment with the impact on the surface. Another research topic can be the heterogeneity of the material, due the process there are zones that have higher concentrations than others; in some applications these can be weakly zones and produce a failure in the component.

One of the most interesting properties of Al_2O_3-13TiO_2 applied with APS, is the wear resistance. Its tribological behavior is a continuous research topic. Tests to evaluate their properties have been carried out in a wide range of conditions; dry and wet friction, abrasion, and tribo-corrosion, to name a few.

Usually the main factors that are correlated with the wear process are hardness, porosity and toughness; these parameters depend on the material composition, in particular the titanium content. The effect of TiO_2 content increases the toughness, improve wear resistance but causes hardness reduction [32]. Many models try to explain the behavior of evolution in the microstructure. Actually, is considered that the phase transformation occurs from α (stable) to γ (metastable) Al_2O_3-13TiO_2 and that TiO_2 is in solution in gamma phase, after APS process [33]. The transformations occurred during the process are difficult to understand Goberman et al. [9] shows the distribution of the grain size and microstructure, and presents a scheme about particle behavior. The concentration and evolution of each particle depend on the cooling rate and the parameters of the process. Beyond the phase transformation many factors influence the behavior of a coating. Like the parameters used in the torch depending of the process, after these the final mechanical and tribological properties must be tested to obtain the best quality.

The characteristics of a coating and the applications must consider all the aforementioned aspects. In some cases, materials that usually present less properties can be processed in a different way, and improve the structure [34-35].

The most studied process is APS because it presents better applicative features for this particular mixture of powders, the use of different application processes found more porous coating structures and in dry sliding wear process the results are not satisfactory [36].

In APS the usual wear effects under dry sliding contact are: a plastic deformation, crack propagation and delamination [32].

In the tribological study of coatings, recalling the aforementioned parameters, the application of specific factors, that can be calculated in order to get wear forecast can be useful; an example is clearly described and studied by Bolelli et al. [37] where introduce the use of KIC-L related to crack propagation resistance in a direction parallel to the substrate. And a combination between KIC-L and Vickers micro-hardness has been suggested to predict the dry particles abrasion resistance of plasma-sprayed ceramics.

In the case of composites that involve a large number of materials, a particular component can greatly affect the general properties of the material and in some cases also the application.

As the bond coat performs the adhesion between the coating and the substrate depending of both; in the case of the coating the titania effect has great influence in the wear behavior of the material. To a certain extent the addition of titania in APS Al_2O_3-TiO_2 coating has been demonstrated to increase the toughness and wear resistance [13].

Another particular field of interest in wear resistant coatings is the residual stress, due to the fact that the high temperatures, high cooling rates, and high particle impact velocity to which powders are subjected are the main factors to create it. The residual stress build-up process in thermally sprayed coatings involves several factors, the most relevant ones being connected to the quenching and cooling stages. Quenching stresses are due to the shrinkage of lamellae upon cooling from the solidification temperature to the overall system equilibrium temperature, whereas cooling stresses are due to the difference in thermal expansion coefficient between the coating and the substrate. Additional sources of residual stresses can be phase transitions in the deposited material [38].

New perspectives for the application of these materials arise day by day; one is in the Invar massive molds, the particular properties of these materials like low hardness, and poor wear behavior, make them ideal candidates to be coated with a wear resistant film, in the case of APS with Al2O3-13TiO2, the result shows a good wear resistance and an important hardness increase compared to that of the Invar mold in normal condition [39].

More than wear resistance, these materials must be resistant to corrosive environments due to the ceramic properties like low reacting materials. The University of Ferrara in the Corrosion center realize tests to evaluate the tribo-corrosion behavior of these coatings under severe environmental and load conditions, and the results show that depending on the material characteristics, the main application for these coatings is in wear resistance but with a moderate effect in corrosion resistance [40].

2.6.2. - WC- 12Co. APS

The APS process used to apply WC-12Co produces coatings where the presence of a porous surface is characteristic, due to the high temperatures and lower velocities than those produced by HVOF process.

In some cases the control of the porosity produced in the coatings is an important parameter when the service is under lubricating conditions.

Not many studies have been carried out with this particular kind of coating due to the structure characteristics. The main studies involve wear resistance in dry conditions and the chemical reactions that occur at high Plasma temperatures as decarburizing and dissolution of carbides.

As described by Nerz et al.

$2WC \rightarrow W_2C+C$

$W_2C \rightarrow 2W+C$

This reaction is kinetically driven, i.e., time and temperature dependent, with the degree of decarburization being related to the manufacturing method of the starting powder and to the deposition process flame temperature and flame velocity [41].

However, depending on the purpose, the WC-12Co applied with APS present advantages over other process like HVOF; plasma and HVOF processes are characterized differently in regard to two principal aspects. These are the thermal and kinetic engines of the sprayed particles. A comparison of atmospheric plasma spraying (APS) and high velocity oxy-fuel (HVOF) spraying shows that the plasma processes offer higher plasma temperature at relative low velocities whereas in the

HVOF process is the opposite. The temperature of the HVOF spray stream does have some dependence on the choice of fuel gas. In addition, it has to be taken into account that the HVOF spray distance exceeds the plasma spray distance and when HVOF is used at shorter spray distances it can lead to overheating of the substrate. Another issue is the porosity that can be an important factor that can be exploited in infiltration of solid lubricant or others materials to increase wear properties [21].

As to wear mechanism such as particle erosion, adhesion and abrasion, some results have been presented in a general way by Kim et al. whom states that "Atmospheric plasma-sprayed WC-12%Co coatings are composed of individual splats with different chemical compositions as well as unmelted particles, porosity, retained carbides, and many transverse and lateral cracks. Porosity, hardness, surface roughness, and retained carbide of the coatings are not the principal factors for wear performance. The cohesive strength of the thermal spray coating is the most important factor affecting the wear performance of the material. As the cohesive strength of the coating increases, the wear resistance to abrasive, adhesive, and particle erosion also increases" [11].

The importance of wear in coatings, offer more opportunities to study its tribological behavior. Varying parameters and composition to improve the cohesion, and discover new properties of these composites.

More tests have been carried out to evaluate the resistance of these kind of coatings and the use of diverse parameters like elastic modulus, residual stress, and the chemical reactions that occur when the powders transform during plasma process; the APS can be improved by changing some parameter in the process like the use of optimized Ar–He mixtures that reduced the influence of the spraying environment and the degree of decarburization, thus allowing the fabrication of cermets characterized by a higher content of retained WC; the amount of other brittle phases, crystalline and amorphous, can be minimized. by optimizing spraying parameters and, mainly, the plasma forming gas flow, APS can be approach to create WC–Co coatings characterized by high anti-wear performance, comparable to those produced by HVOF [42-43]

The developments in materials processing give the possibility to use nanometric powders, increasing the applications in many fields like those described above for Al2O3-13TiO2.

Nano-powders are also used in WC-12Co, where the tests results open its possible utilization in coating. In the high temperature spraying process application the presence of molten and unmolten areas depends largely on plasma intensity; at higher plasma intensity, the fully molten regions increase. For micrometric coatings, porosity changes drastically with plasma intensity but at low intensity plasma energy is not high enough to melt micrometric powder. In nanometric coatings, porosity is not significantly affected by plasma intensity; the porosity found is associated to that of the feedstock [44].

These results have a great influence on coating wear and erosion behavior.

2.6.3.- WC- 12Co. HVOF

The coatings produced with the HVOF technique present a surface where the porosity is caused by the gas produced during the process. The liberation of carbon through the decarburization reactions results in two possibilities: oxidation of the carbon according to $2C + O_2 \rightarrow 2CO$ (gas) or diffusion of carbon into the matrix material [41]

The sample preparation (polishing) to observe the coatings, allows the pulling out of the carbide particles, creating more than the real porosity inside the coatings. The porosity is not intercommunicated and the pulling out is moderate. The presence of the amorphous bending phase seems to have ductile properties. Decomposition of the carbides is the same reaction explained before for Nerz et al. [41]

Many studies have been carried out in coatings applied with these process; the topics include particle effect, the effect of the Co quantity, the effect of nano-powders, etc. And many related with tribological properties.

Some studies consider also the fuel gas selection and its effect on the microstructure and wear resistance; if the fuel gas power increases an overheating of the WC-Co powder, and the appearance of undesirable phases occurs, it will be enhanced by increasing the oxygen to fuel ratio [45].

Some particular models have been created to explain particles evolution during coating process and accurate studies have been carried out by Verdon et al. where the microstructural evolution, the decomposition and the amorphous phase have been consider. They proposed realistic phisico-chemical processes that take into account the microstructural changes in the material. In figure 14 a schematically representation of the microstructure, on a cross section of the coating. It is made up of elongated islands parallel to the substrate, which contains various amounts of WC phase according to the extent of WC dissolution in cobalt. This dissolution produces a nanocrystalline binder phase after cooling. Therefore the composition of the binder fluctuates through the microstructure and the tungsten concentration in the binder increases at the expense of the volume fraction of the remaining WC grains. These phenomena account for the appearance of sub-carbide W_2C, tungsten grains, and only small amount of metallic cobalt in a nano-crystalline matrix under cooling. The matrix contains cobalt, tungsten and carbon in proportions that fluctuate through the coating, in relation with the fluctuation of temperature and decarburization levels experienced by the impacting particles [46].

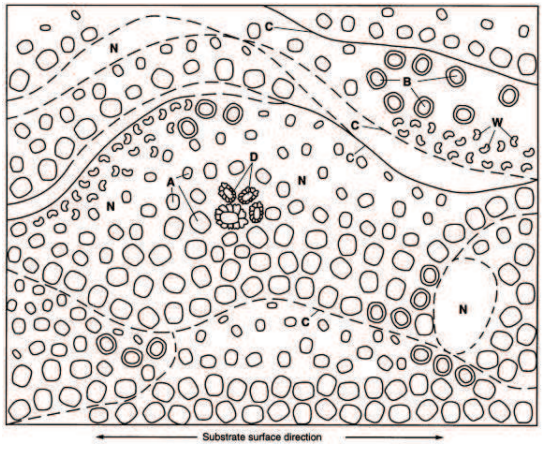

Figure 14. - Schematics of the coating microstructure perpendicular to the substrate. Each phase is represented by a different pictogram. (A) WC carbides. (N) Nano-crystalline matrix. (B) WC+W2C. W–W crystallites. (D) Co dendrites surrounding WC grains. (C) Splat boundaries. The different phases and crystallites are not drawn at the same scale for the sake of clarity. [46]

Considering the wear mechanism in abrasive tests, the performance of the coatings have been found to depend on the abrasive used to test the coatings, and the main mechanisms in these coatings resulting from micropolishing and gradual degradation of the lamellae include plastic deformation and interlamellae brittle fracture.

The main conclusion for wear resistance under abrasion condition is that the interlamellae cohesion is critical for the coating resistance [47].

Other tests have been carried out to see the influence of the particle size in the abrasive wear resistance of the coatings. The authors used different average sizes of the WC grains powders and the results indicate that the WC carbide size influence greatly the abrasive wear, establishing that the relative abrasive wear of WC-Co coatings is proportional to the square root of the relative carbide size. The effect of Co has also been studied and shown that increasing the Co content reduces the hardness of the coating because it causes a reduction of WC and W2C phase. But it is possible that, as in the Al2O3-13TiO2 coatings the toughness increases, also the wear resistance augments with a Co increase [14].

With the new process, many fields could take advantage of the nanoparticles that in many cases will improve the behavior of the same component processed just with a different size material.

In the case of WC-12Co the characteristics of the coatings using normal and nano powders, under a wide range of abrasive test conditions, shows that wear rates of an HVOF-sprayed WC–Co nanocomposite coating were between 1.4 and 3.1 times higher than those of a coating sprayed from conventional powders. The increase in wear rate was attributed to the greater degree of decomposition suffered by the nanocomposite powder particles during spraying, which leads to a reduction in the volume fraction of the wear-resistant primary WC phase. Then for those cases in wear process the use of conventional powders is better than that of nanocomposites[48-50].

The sequence of the process is very similar to that one proposed by Goberman just that in the WC-12Co case the cobalt particles are not fully melted. The two schemes presented in figure 15 have been proposed by Verdon et al. and Stwart et al. [46,48] respectively; their sequences are very similar; in both cases a fully melted structures

did not appear, just a partial melting matrix and a partial decomposition of carbides have been considered.

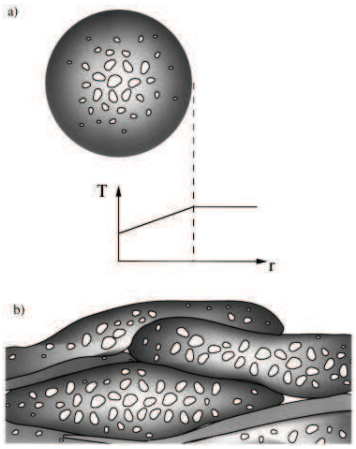

(a) A particle during flight. (b) Resulting islands in the coatings. The brighter color of the gray scale gradation corresponds to a lower W concentration in the liquid (a) and in the matrix (b), respectively [46].

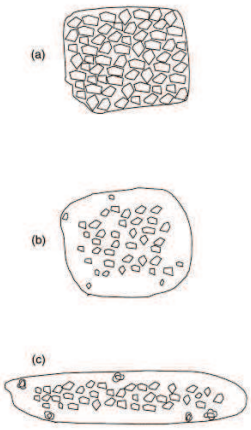

Processes involved in melting, WC dissolution and decarburization of a WC/Co powder particle. The expected changes during the HVOF process (a), (b) until the formation of a lenticular splat on impact with the substrate is illustrated in (c) [48].

Figure 15.- Schematic illustration of the microstructure formation during spraying process

2.6.4. - WC-12Co properties compared between APS and HVOF

Attempts to compare the characteristics of the same materials processed in different ways and that present very different structures after being processed have been carried out.

Some tests have been carried out on the wear phenomenon that occur in a surface during a friction process; the findings depend on the final properties of the material, but the principal fact is on the material cohesion, if the cohesion between the splats and particles increases the abrasion resistance of those kind of materials also increases. Liao et al. established that it is very important to increase the cohesion between the carbide particles and the cobalt matrix; this cohesion is related to the amorphous or nano-crystalline phase interaction in the coatings at the interface between the carbides and the matrix [51].

Some studies have been carried out in order to understand the effects of the application technique on microstructure, and tribological properties of different coatings; and the overall results indicate a porosity reduction for the coatings applied with HVOF process (which is significantly lower than, that of those applied with APS process), the interlamellar cohesion increase, and the grains in HVOF are smaller and more equiaxed; while, larger and mostly columnar morphology of the structures are characteristic of the APS process.

By the tribological side in abrasive test the HVOF sprayed coatings are superior to APS ones [52-53].

REFERENCES

1) J. R. Tavares Branco, R. Gansert, S. Sampath, C.C. Berndt, H. Herman, (2004), "Solid particle erosion of plasma sprayed ceramic coatings", Materials Research, Vol 7 pp 147-153
2) 2001, "Composites ASM Handbook Volume 21". ASM International Handbook Committee.
3) I. Levin, (1998), "Metastable alumina polymorphs: crystal structures and transition sequences", Journal of the American Ceramics Society, Vol. 81, No. 8, pp 1995-2012
4) P.Souza Santos, H. Souza Santos, S.P. Toledo, (2000) "Standar Transition Aluminas. Electron Microscopy Studies", Material Research, Vol. 3, No. 4, pp 104-114.
5) M. Uma Devi, (2004), "New phase formation in Al2O3-based thermal spray coatings", Ceramics International, Vol. 30, pp 555-565
6) R. Hengerer, B. Bolliger, M. Erbudak, M. Grätzel, (2000), "Structure and stability of the anatase TiO2 (101) and (001) surfaces", Surface Science, Vol. 400, pp 162-169

7) N. Berger-Keller, G. Bertand, C. Filiatre, C. Meunier, C.Coddet. (2003), "Microstructure of plasma-sprayed titania coatings deposited from spray dried powder". Surface and coatings technology, Vol. 168, pp 281-290
8) J-Y. Park, C. Lee, K-W. Jung, D. Jung, (2009), "Structure related photocatalytic properties of TiO2", Bull. Korean Chemical Society, Vol. 30, pp 402-404
9) D. Goberman, Y.H. Sohn, E. Jordan, M. Gell, (2002), "Microstructure development of Al2O3-13TiO2 plasma sprayed coatings derived from nanocrystalline powders", Acta Materalia Vol. 50, pp 1141-1152
10) M. Khechba, F. Hanini, R. Halimi, (2010), "Study of structural and mechanical properties of tungsten carbides coatings", Nature & Technology, No 5, pp 9-11
11) S. Kim, S-H Han, J-K Park, H-E Kim, (2003), "Variation of WC grain shape with carbon content in the WC-Co alloys during liquid-phase sintering", Scripta Materialia, Vol 48, pp 635-639.
12) Timm et al., (1990), "Unites States Patent", patent number 4,923,512.
13) R. Yilmaz, A.O. Kurt, A. Demir, Z. Tatli, (2007), "Effects of TiO2 on the mechanical properties of the Al2O3-13TiO2 plasma sprayed coating", Journal of the European Ceramic Society. Vol 27, pp 1319-1323
14) P. Chivavibul, M. Watanabe, S. Kuroda, K. Shinoda, (2007), "Effects of carbide size and Co contento n the microstructure and mechanical properties of HVOF-sprayed WC-Co coatings", Surface & Coatings Technology, Vol 202, pp 509-521
15) H. Saito, A. Iwabuchi, T. Shimizu, (2006), "Effect of Co content and Wc grain size on wear of WC cemented carbide", Wear, Vol 261, pp 126-132.
16) C-L. Li, A. Ohmori, K. Tani, (1999), "Effect of WC Particle Size on the Abrasive Wear of Thermally Sprayed WC-Co Coatings", Materials and Manufacturing Processes, Vol 14, pp 175-184
17) J. Musil, (1997), "Commentary", Journal of Thermal Spray Technology, Vol 6, pp 387
18) K. O. Legg, B. D. Sartwell, J-G. Legoux, M. Nestler,C. Dambra, D. Wang, J. Quets, P. Natishan, P. Bretz, J. Devereaux, (2006), "Investigation of Plasma Spray Coatings as an Alternative to Hard Chrome Plating on Internal Surfaces", SERDP Project WP-1151 Final Report, pp 1-181

19) (1994), “ASM Metals handbook Vol. 05 Surface Engineering”, Ed. ASM International.

20) S. Kuroda, M. Watanabe, K. Kim, H. Katanoda, (2011), “Current Status and Future Prospects of Warm Spray Technology”, Journal of Thermal Spray Technology, Vol 20, pp 653-676

21) G. Barbezat, (2005), “Advanced thermal spray technology and coating for lightweight engine blocks for the automotive industry”, Surface and Coatings Technology, Vol 200, pp 1990-1993.

22) R. Nieminen, P. Vuoristo, K. Niemi, T. Mantyla, G. Barbezat, (1997), “Rolling contact fatigue failure mechanisms in plasma and HVOF sprayed WC-Co coatings”, Wear, Vol 212, pp 66-77.

23) R. Chattopadhyay, Surface Wear analysis, treatment and prevention. ASM International. 2001

24) O. Borrero Lopez, Desgaste por deslizamiento lubricado en ceramicos de SiC sinterizados con fase líquida, Tesis Doctoral, Depto. Ciencias de los materiales e Ingenieria Metalurgica. Universidad de Extermadura. 2006

25) Y. Wang, S. Hsu, Wear and wear transition mechanisms of ceramics. Wear 195 (1996) pp 112-122

26) ASTM International, Standards word wide. G99, D4172, G40, G65, G76, G102, 2276

27) R. F. Bunshah, (1982), Selection and use of wear test for coatings: a symposium, ASTM Special Technical Publication 769, 1982, p. 3

28) K. Kato, (1992), “Micro-mechanisms of wear – wear modes”, Wear 153, pp 277-295.

29) D. Van Steenkiste, S. Plasschaert, P. De Baets, J. De Pauw, Y. Perez Delgado and J. Sukumara, (2011), “Abrasive wear of link chains”, Sustainable Construction and Design. Laboratory Soete, Belgium.

30) J. T. Burwell Jr. (1958), “Survey of possible wear mechanism”, Wear 1, pp 119-141.

31) L.C. Erickson, (2001), "Correlations between microstructural parameters, micromechanical properties and wear resistance of plasma sprayed ceramic coatings", Wear 250, pp 569-575.

32) V. Fervel, B. Normand. C. Coddet, (1999), "Tribological behavior of plasma sprayed Al2O3-based cermet coatings", Wear 230, pp 70-77.

33) B. H. Kear, Z. Kalman, R. K. Sadangi, G. Skandan, J. Colaizzi, W.E. Mayo., (2000)., "Plasma-Sprayed Nnostructured Al2O3/TiO2 Powdwes and Coatings", Journal of Thermal Spray Technology, Vol 9, No.4, pp 483-487

34) R.S. Lima, B.R. Marple, (2005) "Superior performance of HIGH-velocity OXIFUEL-SPRAYED NANOSTRUCTURED TiO2 IN Comparison to Air Plasma Sprayed Conventional Al2O3-13TiO2" , Journal of Thermal Spray Technology" Vol 14 , pp 397-404

35) R. Tomaszek, L. Pawlowski, J. Zdanowski, J. Grimbolt, J. Laureyns, (2004), "Microstructural transformations of TiO2, Al2O3+13TiO2 and Al2O3+40TiO2 at plasma spraying and laser engraving", Surface and Coatings Technology 185, pp 137-149

36) K.A.Habib, J.J. Saura, C. Ferrer. M.S. Damra, E. Gimenez, L. Cabedo., (2006)., "Comparison of flame sprayed Al2O3/TiO2 coatings: Their microstructure mechanical properties and tribology behaviour", Surface and coatings technology, Vol. 201, pp. 1436-1443.

37) G. Bolelli, V. Cannillo, L. Lusvarghi, T. Manfredini, (2006), "Wear behaviour of thermally sprayed ceramic oxide coatings", Wear 261, pp 1298-1315

38) G. Bolelli, L. Lusvarghi, T. Varis, E. Turunen, M leoni, P.Scardi, C. L. Azanza-Ricardo, M. Barletta, (2008), "Residual stress in HVOF-sprayed ceramic coatings", Surface and coatings Technology 202, pp 4810-4819

39) C. Giolli, M. Turbil, G.Rizzi, M. Rosso, A. Scrivani, (2009), "Wear resistance improvement of small dimension invar massive molds for CFRP components", Journal of Thermal Spray Technology, Vol 18, pp 652-664

40) C. Monticelli, A. Balbo, F. Zucchi, (2011), "Corrosion and tribocorrosion behaviour of thermally sprayed ceramic coatings on steel", Surface and coatings technology. Vol 205, pp 3683-3691

41) J. Nerz, B. Kushner, A. Rotolico, (1992), "Microstructural Evaluation of Tungsten Carbide-Cobalt Coatings", Journal of Thermal Spray Technology, Vol I (2), 147-152

42) A. Koutsomichalis, N.M. Vaxevanidis, G. Pertropolos, A. Mourlas, S.S. Antoniou, (2008), "Friction, Wear and Mechanical Behaviour of Plasma Sprayed WC-12%Co Coatings on Mild Steel" Procedings of the 7th International Conference The Coatings in Manufacturing Engineering, pp 259-268

43) G. Di Girolamo, (2009), "Tribological Characterization of WC-Co Plasma Sprayed Coatings", Journal of American Ceramic Society 92, pp 1118-1124.

44) V. Bonache, M. D. Salvador, J. C. García, E. Sánchez and E. Bannier, (2011), "Influence of Plasma Intensity on Wear and Erosion Resistance of Conventional and Nanometric WC-Co Coatings Deposited by APS", Journal of Thermal Spray Technology, Vol 20, 549-559

45) M.D.F. Harvey, A.J. Sturgeon, F.J. Blunt, S.B. Dunkerton, (1995), "Investigation into the relationships between fuel gas selection, wear performance and microstructure of HVOF sprayed WC-Co coatings", Thermal Spraying-Current Status and Future Trends. Vol 1, pp 471-476

46) C. Verdon, A. Karimi, J. L. Martin, (1998), "A study of high velocity oxy-fuel thermally sprayed tungsten carbide based coatings. Part 1: Microstructures", Materials Science & Engineering, A246, pp 11-24

47) A. C. Bozzi, J. D. Biasoli de Mello, (1999), "Wear resistance and wear mechanisms of WC-12%Co therma sprayed coatings in three-body abrasión", Wear 233-235, pp 575-587

48) D.A. Stewart, P.H. Shipway, D.G. Mc Cartney,(2000)," Microstructural evolution in thermally spayed WC-Co coatings: comparison between nanocomposite and conventional starting powders", Acta Materialia 48, pp 1593-1604

49) D.A. Stewart, P.H. Shipway, D.G. Mc Cartney, (1999), "Abrasive wear behaviour of conventional and nanocomposite HVOF-Sprayed WC-Co coatings", Wear 225-229, pp 789-798

50) P.H. Shipway, D.G. Mc Cartney, T. Sudaprasert, (2005), "Sliding wear behaviour of conventional and nanostructured HVOF sprayed WC-Co coatings", Wear 259, pp 820-827

51) H. Liao, B. Normand, C. Coddet, (2000), "Influence of coating microstructure on the abrasive wear resistance of Wc/Co cermet coatings", Surface and coatings Technology, Vol 124, pp 235-242

52) G. Bolleli, L. Lusvarghi, T. Manfredini, F. Pighetti Mantini, R. Polini, E. Turunen, T. Varis, S-P. Hannula, (2007), "Comparison between plasma- and HVOF-sprayed ceramic coatings. Part I: Microstructural and mechanical properties", Int. J. Surface Science and Engineering, Vol 1, pp 38-61

53) G. Bolleli, L. Lusvarghi, T. Manfredini, F. Pighetti Mantini, E. Turunen, T. Varis, S-P. Hannula, (2007), "Comparison between plasma- and HVOF-sprayed ceramic coatings. Part II: tribological behavior", Int. J. Surface Science and Engineering, Vol 1, pp 62-79

III

EXPERIMENTAL PROCEDURE

In this chapter the equipment, materials and experimental conditions are presented. The materials have been characterized and tested to understand and document wear behavior.

3.1. - COATINGS ON STEEL SUBSTRATE.

The coatings have been realized by ZOCA industry on steel disks with the composition shown in the table I. Disk diameter is 75 mm with a thickness of 5 mm ±0.5 mm (depending of the kind of coating), the geometry is according with the tribometer equipment requirements with a design given by the equipment supplier. The coating thickness depends of process and materials used, the specific values are reported in table II. The studied coatings and its application technique and size particle as reported in the Materials chapter. The different disk surfaces are shown in figure 1; the color varies depending on the application technique and kind of material used.

Three commercial coatings were prepared, two of WC-12Co coating applied one by air plasma spray technique (APS) and the other by high velocity oxi-fuel (HVOF) and one of Al_2O_3-13TiO_2 applied by APS; in this case in order to improve the material adhesion onto the steel substrate the coating has been deposited onto a Ni-20Cr bond coat (also obtained by APS).

The deposition parameters are confidential.

Table I. - Chemical composition (wt.%) of disk´s steel.

C	Mn	Ni	Cr	Si	Cu	Mo	S	Fe
0.22	0.88	0.87	0.84	0.30	0.20	0.06	0.03	Balance

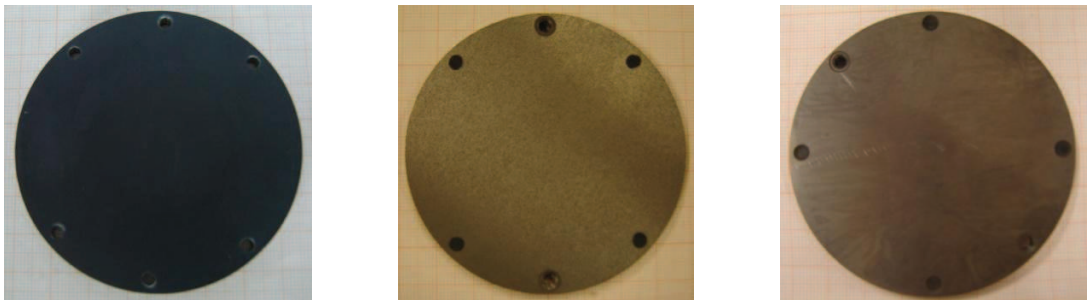

Al_2O_3-13TiO_2 WC-Co (APS) WC-Co (HVOF)

Figure 1. - Disk appearance in as received condition

Table II. - Chemical composition (wt.%) of the feedstock powders.

	Al_2O_3-13TiO_2	WC-12Co (APS)	WC-12Co (HVOF)
Type	FST C-335.23 by Flame Spray Technologies	Amperit 515.2 by H.C. Stack	WOKA 3102 by Sulzer
Composition	13.12%TiO2, 0.22%ZrO2, 0.15Nb2O5, 0.1%SiO2, 0.09%MgO, 0.07%CaO, 0.24% other oxides, balance Al2O3.	4.2%C, 11.2%Co, 0.8%Fe, balance W	5.38% C, 11.99%Co, 0.04%Fe, balance W
Particle dimension	-45+15	-88+44	-45+15
Thickness*	200 ±25 µm	150 ±50 µm	150 ±25 µm

* It can be vary because is also affected by the polishing process.

3.2. - COATINGS CHARACTERIZATION.

3.2.1. - Optical Microscope (OM)

The first observations and measurement of surface and cross sections of the coatings were carried out in an optical microscope LEICA MEF4M equipped with image analysis software Archive4Images v.3.20b. The surface porosity has been calculated with the same software in a polished surface at 500X with a media value between the calculi of 20 images of the surface.

3.2.2. - Scaning Electron Micrpscope (SEM)

The microstructure of the samples was observed in SEM, both on the surface and transversal section, in as received and polished conditions; the sample has been polished with abrasive paper from 800 to 1200 grid, and again with a polishing cloth with diamond solution from 9μm to 1 μm.

The samples for SEM observation have been prepared metalizing the ceramic surface in order to make the sample conductive. The images have been obtained with secondary and retro-dispersed electron. The SEM equipped by Energy Dispersion Spectroscopy (EDS) was used to investigate the chemical composition of microstructures.

3.2.3. - X-Ray Diffraction (XRD)

The Diffraction analysis has been realized in Saltillo Coahuila, Mexico in Instituto Tecnológico de Saltillo, in Badajoz, Spain in Universidad de Extremadura. The XRD analysis realized in Mexico has been carried out in a PHILIPS* X`Pert X-ray diffractometer (XRD) using Cu Kα radiation (λ= 1.54Å), with an intensity scanner vs. diffraction angle between 15° and 120° (step size of 0.06°), a voltage of 40 kV and 30 mA filament current.

The used equipment in UNEX is a high-resolution diffractometer D8 ADVANCE Bruker using a Cu Kα radiation (λ= 1.50562Å), with an intensity scanner vs. diffraction angle between 20° and 80° (step size of 0.02°), time count 3 s/step.

Another XRD Analyses has been carried out in the University of Ferrara UNIFE. These analysis has been performed in a high resolution X-Ray diffractometer X'Pert Pro MRD XL PANalytical, with the next parameters: Cu Kα radiation (λ= 1.540598 Å), with an intensity scanner vs. diffraction angle between 15° and 80° (step size of 0.0001°), time count 3 s/step. Voltage 40 kV, Current 40mA.

3.2.4. – Instrumented Indentation Test (IIT) and Hardness

To evaluate the hardness and elastic modulus of coatings an instrumented indentation testing (IIT) has been carried out. The mechanics of IIT is like a hardness test, an

indenter with a well-defined geometry is forced into the surface of a sample using a known test force as shown in figure 1. Unlike a hardness test, where only the indent size or depth is measured after the total force has been removed, IIT utilizes high-resolution instrumentation to continuously monitor and control the displacement of the indenter as it penetrates into and is withdrawn from the sample. The data points generated during the indentation process are stored together in the memory of a computer. A visual load/unload curve as presented in figure 2 is normally generated from the data. All of these data are then analyzed by any number of specifically developed algorithms to determine the desired material property of the sample [1].

The test has been carried out in a Nanotest, Micro Materials Ltd., Wrexham, UK, with a Berkovich diamond indenter. The equipment has a dual head accessory; one to apply nanometric loads (from 0.1 to 500 mN) and the other in the micrometric range (from 0.1 to 20 N) from the slope of the unload section of the penetration depth curve vs. the applied load, the equipment provides the effective modulus of elasticity, Ee, (equation 3.1) defined as:

$$\frac{1}{E_e} = \frac{1-\upsilon^2}{E} + \frac{1-\upsilon_i^2}{E_i} \qquad \text{Eq. (3.1)}$$

Where ν is the Poisson`s coefficient, E the Young´s modulus (from the sample), νi Poisson´s coefficient (0.07), E the Young´s modulus (1141 GPa) (from the indentor).

From Eq. 3.2 is possible to obtain the reduced Young`s modulus $\left(\frac{E}{1-\nu^2}\right)$ for the studied material as:

$$\frac{E}{1-\nu^2} = \frac{1}{\frac{1}{E_e} - \frac{1-\nu_i^2}{E_i}} \qquad \text{Eq. (3.2)}$$

The equipment also gives the material hardness H, defined as:

$$H = \frac{P}{A} \qquad \text{Eq. (3.3)}$$

Where P is the maximum applied load and A is the contact area projected on the tested surface.

49 indentations in a matrix array of 7 x 7 have been performed on all materials; the indentations had a distance of 395 μm between them on the surface of each sample, the velocity of the applied load was 350 mN/s, the load was calculated by the machine

in order to obtain a depth impression not greater than 10 μm to avoid the substrate hardness influence; the maximum load permanence on the surface was 10s.

For the AL_2O_3-13TiO_2 the load was 8640±404 mN, for WC-12Co APS coating the applied load was 6214±1218 mN and for WC-12Co HVOF coating the applied load was 9637±852mN.

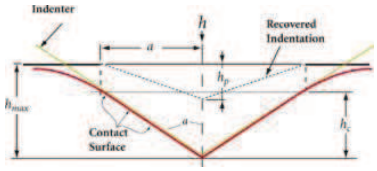

Figure 1. - Mechanics of IIT.

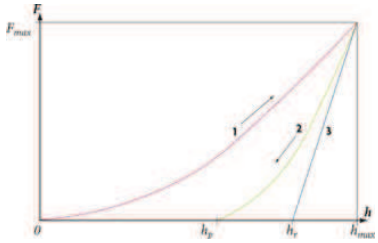

Figure 2. - Load/unload example curves.

Another hardness test has been carried out with a micro-hardness Tester FM Future-Tech and with a load of 300 gr.

3.2.5. - Wear.

The wear test has been carried out in a multispecimen tester TR-750 DUCOM, with a pin on disc configuration according to ASTM G99 [2].

REFERENCES

1) ASTM, (2003), Instrumented Indentation Testing. ASTM Committee E28 on Mechanical Testing.
2) ASTM, (2005), Standard Test Method for Wear Testing with a Pin-on-Disk Apparatus. G99-05".

PAPERS

Article A

EFFECT OF RELATIVE HUMIDITY AND APPLIED LOADS ON THE TRIBOLOGICAL BEHAVIOUR OF A STEEL/Cr_2O_3-CERAMIC COUPLING

Mattia Merlin, Chiara Soffritti, Reyna Vazquez

Department of Engineering - ENDIF
University of Ferrara
I-44122 Ferrara
Italy

Preprint 2012

ABSTRACT

The friction and wear behaviour of a carbon steel in sliding contact with a plasma-sprayed ceramic coating (Cr_2O_3) is investigated under different conditions of normal load and relative humidity, through a pin-on-disk equipment. The samples are analysed by means of Optical Emission Spectroscopy (OES), Optical Microscope (OM), Scanning Electron Microscope (SEM) with Energy Dispersive Spectroscopy (EDS), X-ray Diffraction (XRD), surface roughness, fracture toughness and microhardness. During tests, friction was continuously monitored while the wear rate of coatings was evaluated by measurements of wear scar profiles after the tests. The wear rate of the pins was determined by weighting them before and after the wear tests. For all the normal loads applied in dry conditions, the metallic film transfer onto ceramic surface was observed. In wet conditions, metal transfer was greatly depending on the normal load applied. On Cr_2O_3 wear scars microcracks along splat and columnar grains boundaries were distinguished. The observations of the worn surfaces of the pins indicate a mild-oxidational wear mechanism with the appearance of ploughing and plastic deformation

KEYWORDS: Diesel engine; Steel; Plasma-spray coating; Friction; Wear; Metal transfer.

1. INTRODUCTION

In the last decade many efforts are made to improve the performance of diesel engine in terms of fuel efficiency and low emissions. These include the possibility to operate on engine subsystems like the engine block with its pistons and cylinders, the transmission, fuel system, the valve train and the exhaust system. Many studies concern the use of multi-component alloys in valves and valve seats [1-3]. Such alloys are resistant to high temperatures and in corrosive environment of combustion gases but are very expensive. For example, Stott et al. investigated the effect of high-temperature oxidation on the sliding wear of superalloys [4-6]. They dealt with the ability of so-called 'glaze' layers to protect the surfaces during sliding wear at high temperatures and under relatively low loads and sliding speeds.

It is well-known that heat, either frictional or externally applied, has a great influence on the wear processes of metallic components. High temperatures can facilitate oxidation of the contacting surface, causing considerable decrease in wear rate and giving a transition from severe to mild wear. This change is usually associated with the generation of oxide and partially-oxidized metal debris on the mating surfaces. At higher temperatures a glaze, a top layer of compacted particles, can form on the surface reducing friction and wear rates. However, when the sliding speed at room temperature is very high, the removal of the oxide glaze can occur, leading to severe-oxidational wear [7-10]. The capability of this oxide to give protection against the wear damage by acting as a barrier is due to the rate of diffusion of the reactants across the barrier layer. On exposure to air at temperatures upward of 500°C iron and mild steel form protective glazes (tribo-layers) of Fe_3O_4. These are effective barriers to diffusion, but the phase FeO becomes stable at higher temperatures. It develops at the metal/ Fe_3O_4 scale interface and is a poor barrier to diffusion of reactants [11, 12].

The effects of oxygen in reducing wear of metallic components have been investigated for many years. However, in practical applications also the humidity greatly affects the wear rates of metals. Some authors proposed that increasing humidity inhibits the delamination and adhesion wear of steels. They suggested it is due to the reduction of

the oxidation rate on the steel worn surface and to the formation of iron hydroxide and ferri-oxide-hydrate. These oxides and the water adsorption act as protective layers preventing metal/metal interaction [13, 14]. Goto and Buckley found the opposite, which is a direct correlation between wear and humidity: the lack of oxygen adsorption in the presence of water vapour can reduce the rate of oxidation and thus increase the wear [15]. On the other hand, Bregliozzi et al. found both the wear and friction coefficient for un-lubricated sliding of stainless steel significantly dropped, though the oxidation rate reduces with increasing humidity [15, 16]. Finally, other authors demonstrated that the sliding speed significantly influences the effect of humidity in sliding wear of steels: at high sliding speed, the wear increases with humidity, while a converse of this situation is observed at low sliding speed [17].

An interesting alternative to the use of ferrous alloys or superalloys in engine subsystems is the employment of ceramic coatings thermally sprayed on cheaper and shock resistant materials, such as carbon steels. Some ceramics have already found engineering applications as tribological components like cutting tool inserts, rolling bearings, braking devices, water pumps, ash scrapers, cylinder head fire decks, piston crowns, exhaust valve faces and so on [18]. Moreover, thermal-sprayed coatings are resistant to many corrosive environments, they possess chemical stability and very high hardness and they can stand high temperatures. However, the choice of suitable coatings is difficult. In literature many studies investigated the friction of hard materials, such as ceramics against steels [19-23]. They examined the existence of many cracks at the metal surface or the formation of grooves and wear debris with subsequent metal removal. The metal particles were transferred onto the ceramic by adhesion. Only scratches due to plastic deformation were seen on the ceramic surface. It was also shown that the transfer between metal and ceramic depended on the load (more precisely on the Hertzian pressure) and on the temperature at the interface. It also depended on the specific properties of the ceramic, like its hardness, its roughness, its affinity with the metal, the cohesion among grains and the tensile strength of the antagonist. Fernandez et al. evaluated the wear behaviour of plasma-sprayed Cr_2O_3 coatings against steel in a wide range of loads and sliding speeds. The results demonstrated the wear of the coatings increased with increasing load.

Moreover, in dry sliding of the Cr_2O_3 coating there existed a minimum-wear sliding speed (about 0.5 m/s) and a maximum-wear sliding speed (about 3 m/s) [24].

The aim of this work is to evaluate the tribological behaviour of the plasma-sprayed Cr_2O_3 coating against a carbon steel under different sliding wear conditions, through pin-on-disk testing. Compared to the loads that occur in diesel engine applications, relatively low normal loads are used because of the limitations of the test equipment. However, this can provide useful indications of the potential of the coating for use in sliding wear services. All tests are carried out at room temperature and at 15% and 95% of relative humidity. The effect of both the environmental conditions and the applied load on the wear mechanisms is discussed.

2. MATERIALS AND EXPERIMENTAL DETAILS

A plasma-sprayed Cr_2O_3 ceramic coating with a thickness of 150 µm (powder: Amperit®, -45 +22.5 µm, fused and crushed) on an about 20 µm-thick Ni-20%Cr bond coat (powder: Metco 43CNS, -106 +45 µm) to improve the ceramic material adhesion, are deposited onto circular steel plates (80 mm in diameter and 6 mm in thickness). The spray parameters are confidential. The chemical composition of the steel plates was determined by Optical Emission Spectroscopy (OES), whereas the composition of the feedstock powder was directly provided by the manufacturer. Details of the steel plates and feedstock powders chemical composition are reported in Table I.

Table I - Steels and feedstock powders used to produce top and bond coatings.

	Composition
Cr_2O_3	0.06% SiO_2; 0.03% Fe_2O_3; <0.02% TiO_2; balance Cr_2O_3
Ni-20%Cr	19.07% Cr; 1.1% Si; 0.4% Fe; 0.02% C; balance Ni
Disk	0.22% C; 0.88% Mn; 0.87% Ni; 0.84% Cr; 0.30% Si; 0.20% Cu; 0.06% Mo; 0.03% S; 0.02% V; 0.02% P; balance Fe
Pin	0.23% C; 0.86% Mn; 0.95% Ni; 0.91% Cr; 0.26% Si; 0.10% Cu; 0.06% Mo; 0.02% S; 0.02% V; 0.01% P; balance Fe

The coating microstructure was investigated by a Philips X'PERT PW3050 diffractometer, using Cu Kα radiation (λ=1.54 Å), with an intensity scanner vs. diffraction angle between 15° and 120° (step size of 0.06°, scanner velocity of 2 s/step and 1.5 grid), a voltage of 40 kV and a 30 mA filament current. The LEICA MEF4M Optical Microscope on properly polished cross-sections was also employed. The micrographs were elaborated by means of Image-Pro Plus v6.0 image analysis software to evaluate coating porosity. Roughness parameters (R_a and R_z) were calculated by the portable Handysurf E35_A ZEISS-TSK rugosimeter. Before each measurement all the coating surfaces were cleaned by ultrasonic bath. Microhardness (3 N load and 15 s loading time) and fracture toughness (10 N load) measurements were performed on polished cross-sections of the coating by means of a Future-Tech FM-model Vickers microindenter. A mean of 15 indentations were carried out for each microhardness and toughness measurement. In particular, fracture toughness was evaluated by measures of the indentation diagonals and crack lengths from optical micrographs, employing the Evans-Wilshaw equation:

$$K_{IC} = 0.079(P/a^{3/2})\log(4.5a/c) \quad (1)$$

where a is the half diagonal of the indentation (μm), c is the crack length (μm) and P is the load (mN). This formula is developed for "half-penny-shaped" cracks, but in literature is reported it is valid also for Palmqvist cracks. Unique limitation is that the ratio between the crack and the half diagonal length must be between 0.6 and 4.5 [25, 26].

Pin-on-disk dry sliding tests were performed with a Multispecimen Tester tribometer produced by DUCOM Instruments, in accordance with ASTM G99-05 "Standard test method for wear testing with a pin-on-disk apparatus", using cylindrical steel pins of 6 mm in diameter and 22 mm in height as counterpart material. The chemical composition of the pin is listed in Table 1. All the surfaces of the pin were cemented for about 500 μm in thickness. The Vickers microhardness of the pins was determined (1 N load and 15 s loading time) on cleaned cross-sections, at a distance of 100 μm

from the coupling surface. Four different sets of tribological parameters were employed, varying the normal load and relative humidity (RU). In particular, normal loads were fixed at 450 N and 650 N respectively, whereas the values of 15% and 95% of the relative humidity were selected. For each test, the sliding speed of 1 m/s and the sliding distance of 7500 m were maintained constant. All tests were carried out at room temperature. Equipment directly calculated the friction coefficient. The wear rates of pins were evaluated by weighting the specimens before and after the tests. Weight loss was converted to volume loss by dividing it by the density of the material. Wear rate of disks were evaluated by measuring the area of the wear track cross-section by a Hommelwerk T2000 profilometer. Each area, obtained as an average value of four measurements along the wear circumference, was used to calculate the wear volume. In order to understand the main wear mechanisms, the coating worn surfaces were investigated by means of X-ray Diffraction (XRD), Scanning Electron Microscope (SEM) and Energy Dispersive Spectroscopy (EDS) microprobe. The pin worn cross-sections were characterised by OM and SEM analyses and Vickers microhardness measurements.

3. RESULTS AND DISCUSSION

3.1 Microstructure and mechanical properties

In Figures 1a and 1b are reported two optical micrographs of the investigated Cr_2O_3 coating showing the typical lamellar microstructures of a plasma-sprayed ceramic coating. It is characterised by a homogeneous microstructure with a prevalence of inter-lamellar cracks and uniformly distributed pores. Inter-lamellar cracks, caused by thermal residual stresses, are the main reason for the low intersplat cohesion exhibited by the coating. The Ni-20%Cr bond coat is markedly irregular in order to facilitate the adhesion of the coating to the substrate (Figure 1a). At higher magnification the optical micrograph of the steel/bond coat interface shows the evidence of pores and sandblast residues (Figure 1b). The coating porosity determined by image analysis is about 9%, due to splat stacking faults and gas entrapment [27]. The XRD analysis of the coating cross-section, depicted in Figure 2,

reveals it is fully consisted in eskolaite phase (Cr_2O_3). Hardness, roughness parameters and fracture toughness of the coating are listed in Table 2. After the Vickers indentations for the measurement of fracture toughness, micrographs of the coating cross-sections showed that crack preferentially propagate along splat boundaries, parallel to the substrate interface. It is a further evidence of the low intersplat cohesion.

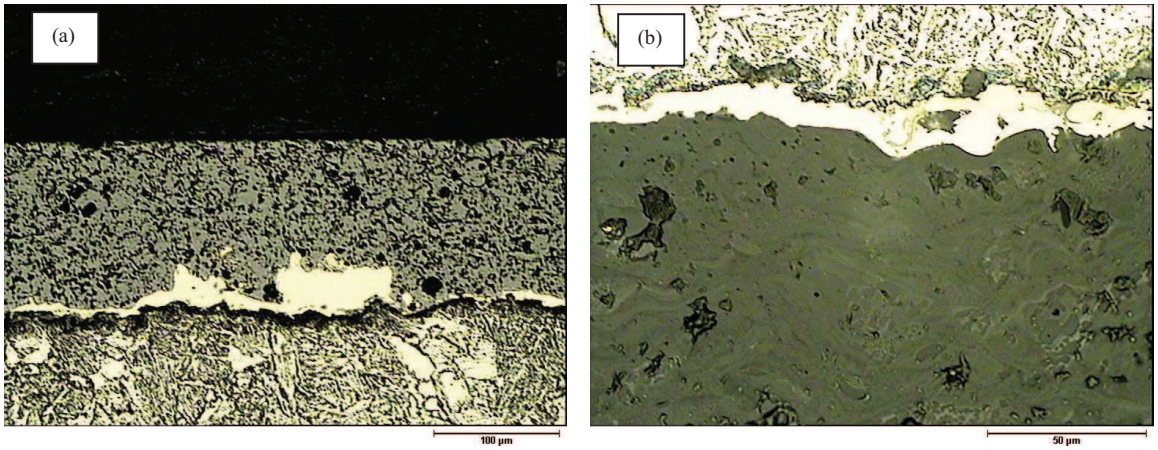

Figure 1. - Optical micrographs showing cross-sections of Cr_2O_3 coating and Ni-20%Cr bond coat.

Micrographs collected in Figures 3a and 3b describe the microstructure of a steel pin near the coupling surface. Figure 3a allows to evaluate a thickness of the hardened layer of about 500 µm. At higher magnification the cemented layer exhibits a martensitic microstructure with a little amount of carbides (Figure 3b), whereas the unaffected material possesses a homogeneous lower bainitic microstructure. Vickers microhardness of the martensitic + carbide microstructure, near the coupling surface, is listed in Table II.

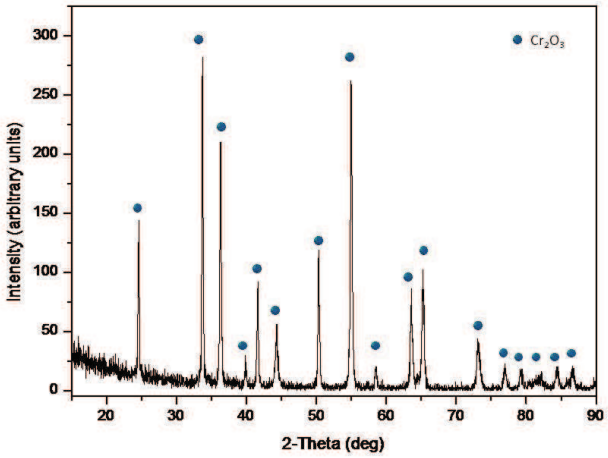

Figure 2. - XRD pattern of Cr_2O_3 coating.

Table II– Mechanical properties and roughness of the ceramic coating and of the steel pins.

	HV_{1N} [GPa]	HV_{3N} [GPa]	R_a [μm]	R_z [μm]	K_{IC} [MPa·m$^{1/2}$]
Cr_2O_3	-----	11.88 ± 0.45	0.15 ± 0.02	1.78 ± 0.19	3.07 ± 0.71
Pins*	6.70 ± 0.05	-----	-----	-----	-----

* Vickers microhardness is evaluated on the pin cross-section, at a distance of 100 μm from the coupling surface.

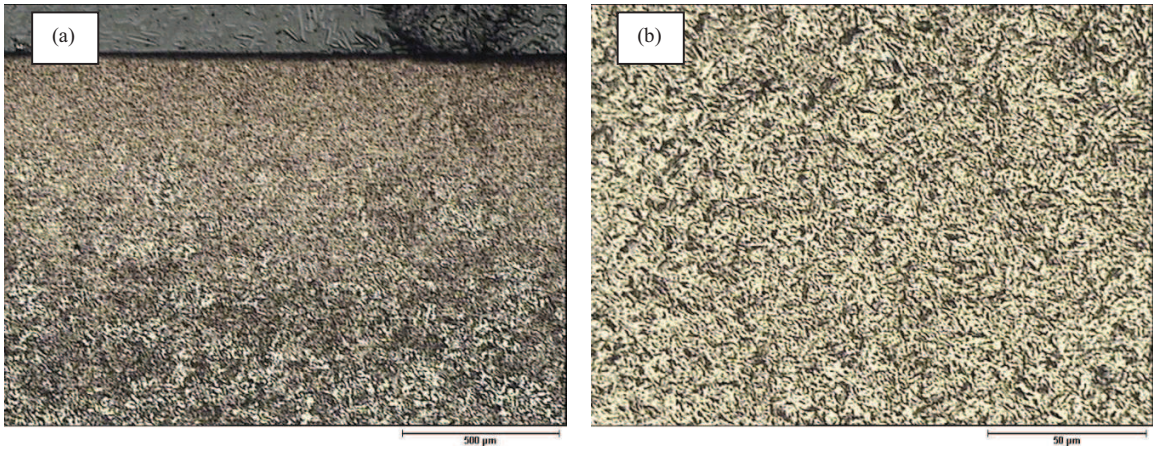

Figure 3. - Optical micrographs showing cross-sections of the steel pins in the cemented zone: (a) 50x, (b) 500x.

3.2 Pin-on-disk wear tests

Figures 4a and 4b depict the friction coefficient calculated by the equipment during the tests. When a 650 N normal load is applied in dry and wet conditions (Figure 4a), the friction coefficient shows many fluctuations around the average value. These fluctuations are associated with high frequency squeaky noise developed concurrently with the rise of friction coefficient and the metallic film deposition on the ceramic surfaces. Both curves follow the same pattern. At the beginning of each test the friction coefficients are quite low ($\mu \cong 0.1 \div 0.2$) and then progressively increase as the test proceeds. After about 2000 m, values reach a quasi steady-state ($\mu \cong 0.3 \div 0.4$). These values remain constant until the end of the tests. When a 450 N normal load is applied in dry condition (Figure 4b) the friction coefficient rises rapidly during the first few minutes and reach the quasi steady-state at only 500 m. The increasing of friction coefficient is due to the continuous generation of wear debris in the form of hard particles entrapped between the worn surfaces. Plastic deformation process during friction also increases hardness of these particles, so they scrape the surrounding material. When a 450 N normal load is applied in wet condition the tribological behaviour is very different. The friction coefficient remains constant at very low value ($\mu \cong 0.1$) until the sliding distance of 3000 m. Then rises slowly until it reaches the value of about $\mu \cong 0.2$ at the end of the test.

Figure 5a shows total wear when a 650 N normal load is applied, in dry and wet conditions. Also in this case, both curves follow the same pattern. Wear is negative up to a sliding distance of about 3500 m in dry conditions, and then progressively increases as the test proceeds. At the end of the tests wear is positive and equal to 0.45 mm. In wet conditions wear reverses its trend for a sliding distance of about 2500 m and reaches at the end of the test approximately the same value as the previous case. When a 450 N normal load is applied in dry conditions (Figure 5b) the wear rises rapidly after about 2500 m up to the positive value of 0.29 mm. As for the friction coefficient, when a 450 N normal load is applied in wet conditions the tribological behaviour is very different. The total wear remains negative and gradually

decreasing. Negative wear in Figure 5a for both wet and dry conditions and negative wear in Figure 5b only for a relative humidity of 15% indicate material build-up on the coating surface; this is caused by the formation of a thick oxide layer under condition of high surface temperatures (e.g. due to high load and sliding speed) and subsequent wear debris transfer from pin onto the disk. The oxide developed on the surface may be partially removed or retained as freely-moving particles between the contacting materials, acting as three-body abradents. If the oxide layer is well-adherent to the metal substrate, it can continue to thicken and can reduce metal/ceramic contact, providing protection against wear damage [11]. The positive wear during the second part of the tests is due to fragmentation of tribolayer and to abrasion damage of coating surface. When a 650 N normal load is applied at the humidity of 95% wear reverses its trend for a sliding distance less than in dry conditions. The increasing of relative humidity reduces surface temperatures by water adsorption on ceramic coatings. In wet conditions the tribolayer is thinner than in dry condition, providing a less effective wear protection. As the test proceeds, the water desorption on Cr_2O_3 coating and the partially removal of oxide layer determine the progressive increase of total wear. When a 450 N normal load is applied in wet conditions (Figure 5b) the water adsorption on ceramic coating and the lower contact pressure prevent the increase of surface temperature. It is well-known that oxide surfaces adsorb water either dissociatively or molecularly. If water is dissociatively adsorbed many strongly bound surface hydroxyl groups are formed to the surface. The water desorption on Cr_2O_3 occurs above 500°C and leads to a surface structure, which cannot be recovered by rehydroxylation of the surface [28, 29]. In this case the surface temperature is widely lower than 500°C and the total wear remains negative for the duration of the test. Some authors also suggest that the reduction of the oxidation rate is due to the formation of iron hydroxide and ferri-oxide-hydrate [13, 14]. These oxides can act as protective layers preventing metal/ceramic interaction.

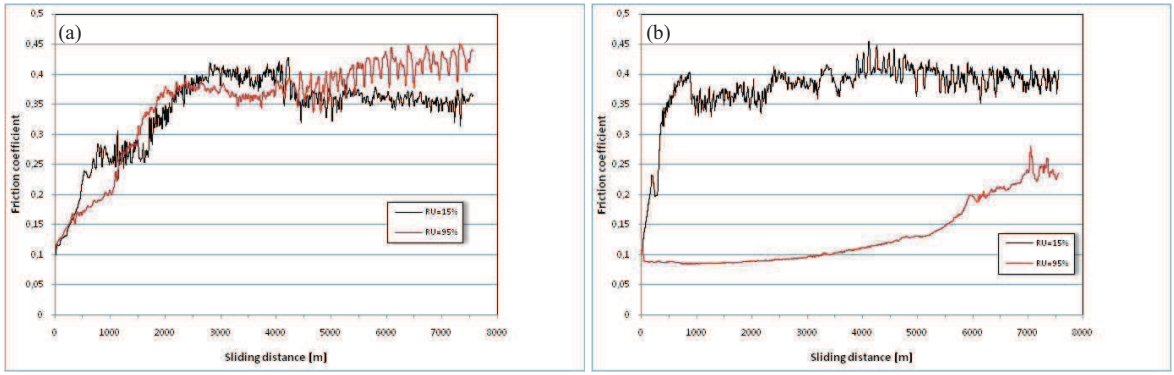

Figure 4. - Friction coefficient variation in different conditions for (a) 650 N and (b) 450 N normal loads.

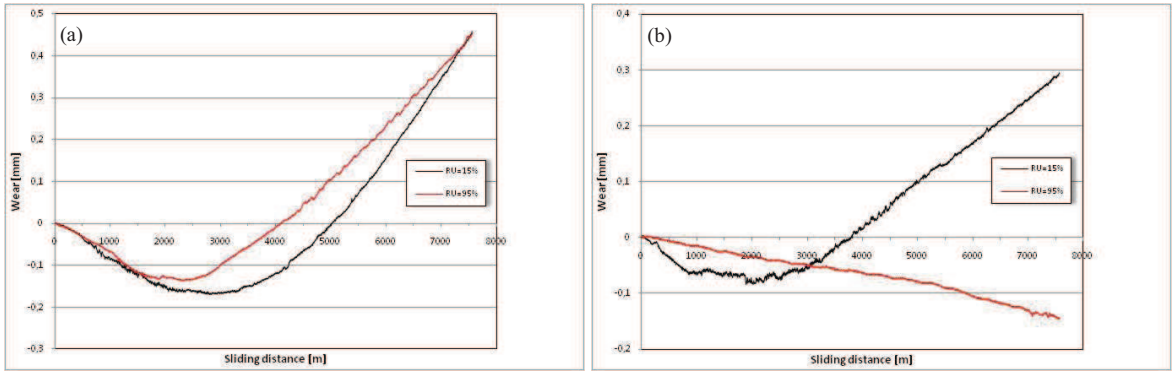

Figure 5. - The amount of wear in different conditions for (a) 650 N and (b) 450 N normal loads.

Figure 6a shows the wear scar profiles of the disks under different normal load and relative humidity conditions. It can be seen that the depth of wear track increases in the following order 450N_RU95% < 450N_RU15% < 650N_RU95% < 650N_RU15%. When a normal load of 450 N is applied in wet conditions, no wear damage is found and the wear scar profile (blue line in Figure 6a) is comparable with the roughness of the ceramic coating. In contrast, when the same load is applied in dry conditions, metallic film transfer occurs on the Cr_2O_3 coating due to localised melting of oxide interlayers. Correspondingly, isolated peaks are observed inside the wear track (green line in Figure 6a). When a 650 N normal load is applied in dry and wet conditions, a greater quantity of peaks inside the wear tracks is observed (red and black lines in Figure 6a). Moreover, some others peaks can be seen at the edges of the wear tracks.

The sliding motion between metal and ceramic is accompanied by the formation of wear debris. Some of these particles are thrown out from the contact area and accumulated along the sides of the sliding tracks.

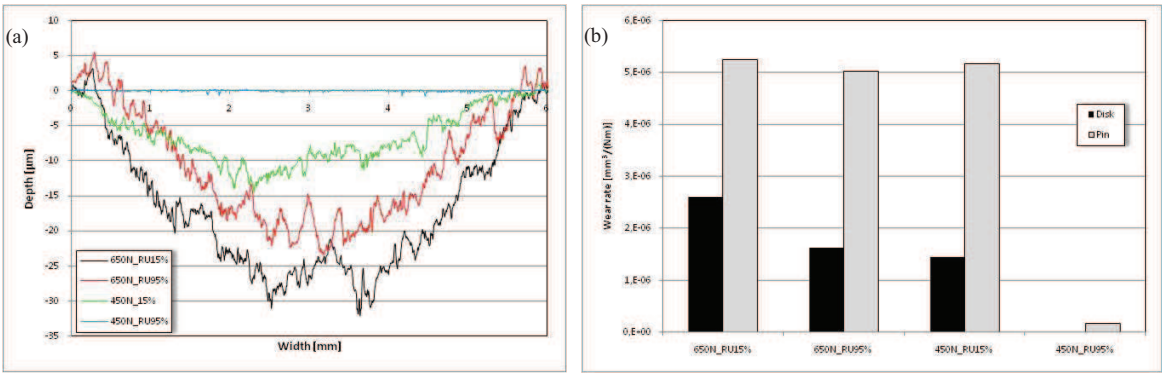

Figure 6. - (a) Wear scar profiles of the disks under different normal load and relative humidity conditions. (b) Wear rate of pins and disks under the same different conditions.

Figure 6b depicts the wear rate of pins and disks under the same different normal load and relative humidity conditions. In any case, the pin undergoes a significant loss of material. Except for a 450 N normal load applied in wet conditions, the wear rate is approximately 5 x 10^{-6} mm^3/(Nm). When a 450 N load is applied in wet conditions, the wear rate is one order of magnitude lower than those for the other pins. Many studies concerning the tribological behaviour of high carbon steels in dry sliding suggested that if the wear rate is greater than 1 x 10^{-8} mm^3/(Nm), the wear can be considered as severe wear. Moreover, they found the greater wear rate corresponds to the higher friction temperature [30-33]. The wear rate of the disks decreases in the following order 650N_RU15% > 650N_RU95% > 450N_RU15%. However, when a 450 N normal load is applied in dry conditions, the wear rate is comparable with the value obtained when a 650 N normal load is applied in dry conditions. No wear rate is indicated for the disk when a 450 N normal load is applied in wet conditions, because the wear damage is three orders of magnitude lower than all the others.

The SEM micrographs of the coating worn surface, for a 650 N normal load applied in dry conditions, are shown in Figures 7a, 7b and 7c. It can be seen the material transfer from metallic pin onto the ceramic surface (Figure 7a). In particular, the wear scar

with metallic film deposition could be divided into two zones. The first one is covered by a smooth iron oxide layer (Figure 7b). It is in good agreement with previous studies, which show that, if the thermal conductivity of a material is not sufficiently high, the surface temperature can exceed melting temperature. Consequently, the melting of local areas on the worn surfaces and in the subsurface layers can be observed. Some works indicate localised melting occurs not only at higher normal loads and sliding speeds, but even at sliding speeds as modest as 1 m/s [20, 33, 34]. Metallic film is firmly attached to the Cr_2O_3 coating, because of the strong adhesion between the sliding surfaces: it is plastically deformed and oriented in the direction of the sliding motion. Scratches and local plastic deformations are indicated in Figure 7b. This adhesive metal transfer justifies the peculiar pattern of the ceramic wear scar profile observed in Figure 6a. In the second zone, many pits are uniformly distributed over the wear track (Figure 7c): wear debris in the form of flakes is also generated. During sliding in dry conditions, microcracks and dislocation networks can produce fine wear debris as observed in the worn surface. Some wear particles are entrapped in the contact interface and subjected to continued fracture, deformation or chemical reaction, producing microsized powders. It can be demonstrated that at higher loads, wear debris can not be taken away and the amount of wear particles deposited on the worn surface increases with normal load applied. Moreover, smooth oxide layers are bigger and scratches are deeper in higher loading conditions [23, 35].

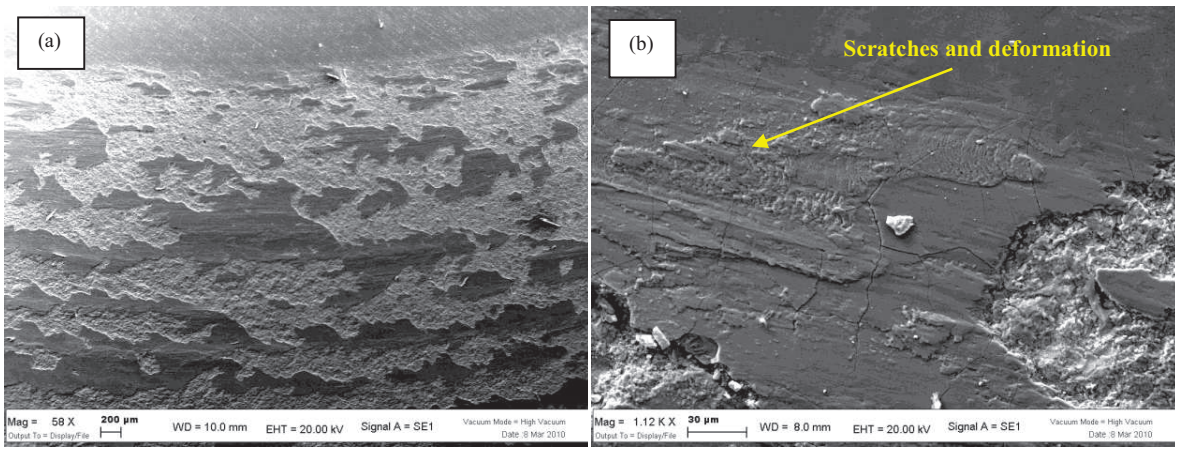

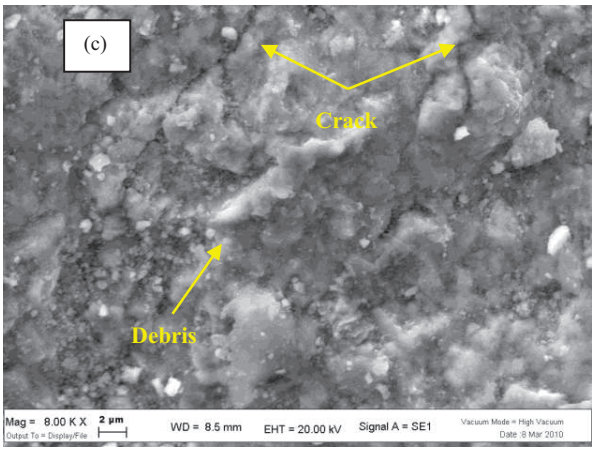

Figure 7 - SEM micrographs of the Cr_2O_3 worn surface for a 650 N normal load applied in dry condition: (a) overview of the wear scar, (b) detail of the metallic film transfer, (c) details of cracks and wear debris.

Figure 8 shows the SEM micrograph of the worn coating surface and corresponding EDS analyses results, when a 650 N normal load is applied in dry conditions. EDS analysis on the metallic film indicates the presence of a great amount of iron and traces of other alloying elements such as chromium and nickel, transferred onto the ceramic coating. In contrast, EDS analysis of the original ceramic surface indicates the presence of a great amount of chromium and traces of iron as wear particles. A subsequent X-ray diffractometry examination enabled the type of film to be distinguished (Figure 9). It is a Fe_2O_3 compound, which generally forms when the contact temperature rises over about 200 °C. A comparison between Figure 9 and Figure 2 shows that Cr_2O_3 coating does not change its chemical composition after the wear test.

When a 650 N normal load is applied in wet conditions and for a 450 N normal load applied in dry conditions (Figure 10), the morphology of the coating worn surfaces and the wear mechanisms are similar to the previous case. The SEM micrograph in Figure 10a depicts an overview of the wear scar. The amount of smooth oxide layers can be compared to metal transfer observed in Figure 7a, but scratches are shallow. Figure 10b shows the details of fracture on the original ceramic surface. In agreement with the microstructure of the coating, it can be seen that microfractures develop along the columnar grains in perpendicular direction to the surface and along splat

boundaries since their strength usually is not high enough. At higher magnification, pits are also visible (Figure 10c).

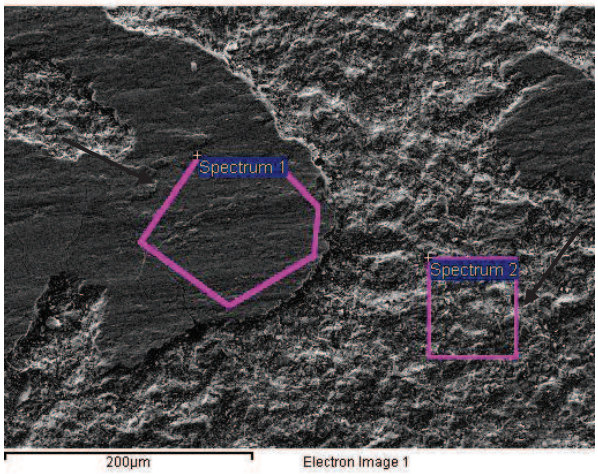

Figure 8. - SEM micrograph and EDS analyses' results of Cr_2O_3 worn surface, when a 650 N normal load is applied in dry conditions.

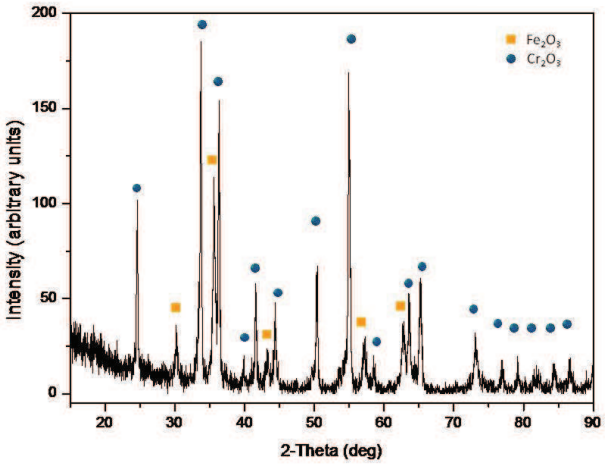

Figure 9. - XRD pattern of Cr_2O_3 worn surface for a 650 N normal load applied in dry condition.

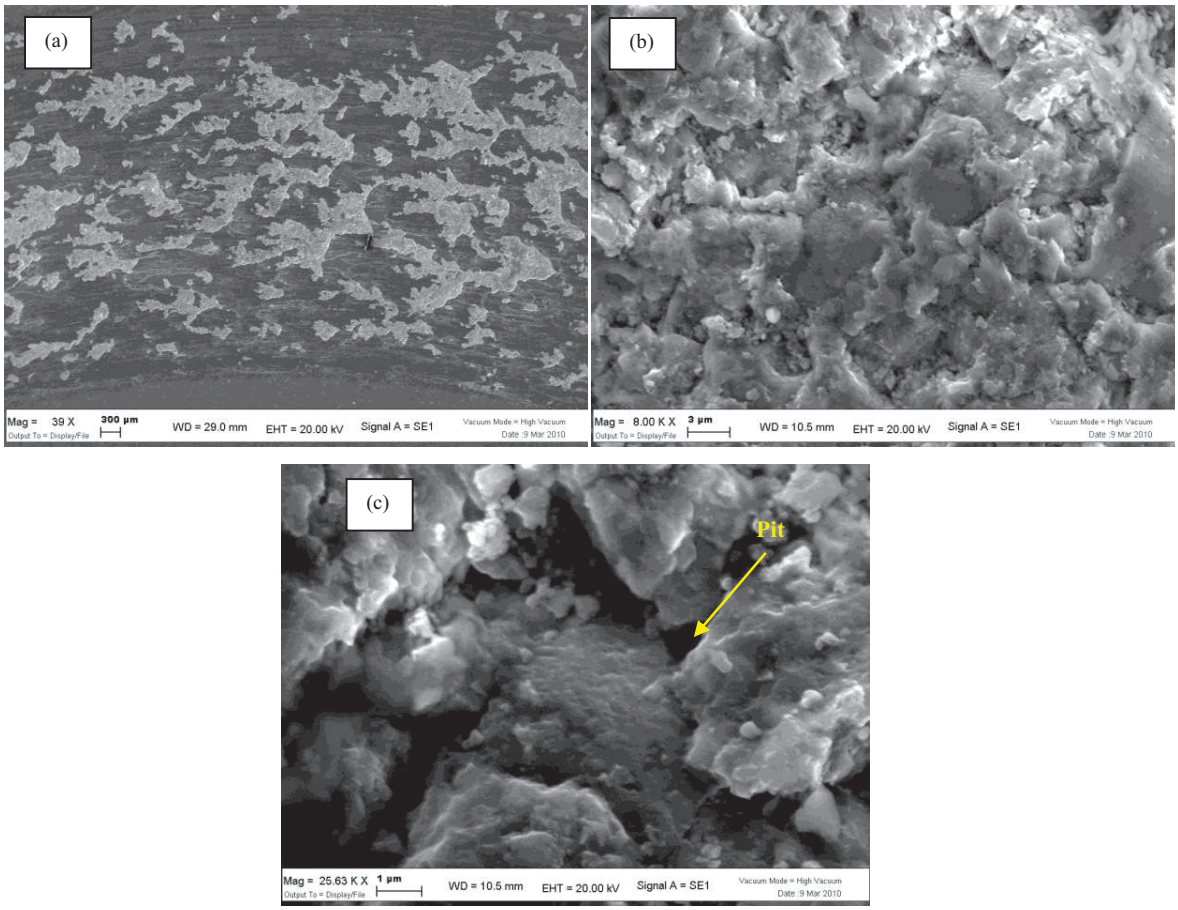

Figure 10 - SEM micrographs of Cr_2O_3 worn surface, when a 450 N normal load applied in dry condition: (a) overview of the wear scar, (b) detail of cracks and wear debris, (c) detail of a pit.

When a 450 N normal load is applied in wet conditions, no wear damage is observed on the ceramic coating (Figure 11a). The surface appears smoother without evidence of significant wear and pores remain open in the flattened surface (Figure 11b).

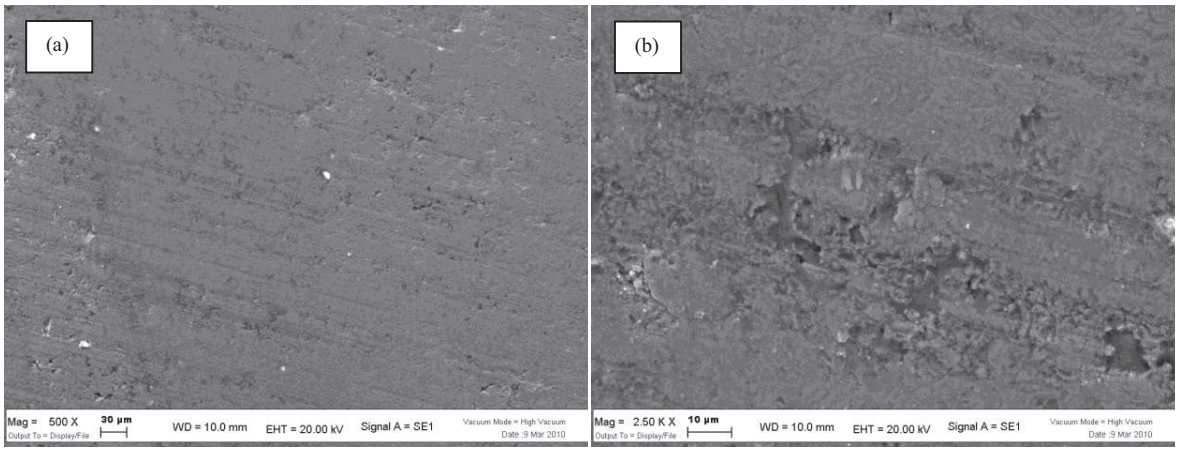

Figure 11 - SEM micrographs of Cr_2O_3 worn surface for a 450 N normal load applied in wet condition: (a) overview of the wear scar, (b) detail of open porosity.

The SEM micrographs of a pin worn surface for a 650 N normal load applied in dry conditions and when a 450 N normal load is applied in wet conditions are shown in Figure 12a and 12b, respectively. In the first case (Figure 12a), the surface is very rough and plastically deformed with the ploughing appearance typical of adhesive wear. A thick film of iron oxide covers the worn surface with a mainly dark grey colour as revealed by optical microscopic observations (Figure 13). The metallic film is discontinuous, indicating the wear mechanism involves both the removal and re-formation of the oxide film and wear of free metallic surface. Many studies suggest that, in the mild-oxidational wear regime, oxidation is caused by frictional heat. The oxide film grows until it reaches a critical thickness (about 10 µm for steel), then it spalls off as wear debris. For high normal loads and sliding speeds a transition to severe-oxidational wear can occurs. This is associated with the localised melting of the oxide layer to a viscous liquid that can flow under the sliding action. At this time, the melt-dominated wear replaces adhesion and delamination-dominated mechanisms [10, 11, 31-33]. When a 650 N normal load is applied in wet conditions and for a 450 N normal load applied in dry conditions, the morphology of the pin worn surfaces and the wear mechanisms are similar to the previous case. When a 450 N normal load is applied in wet conditions, no significant wear damage is observed (Figure 12b). Only a

little amount of metallic oxide appears on the pin worn surface. Moreover, the working marks are still visible.

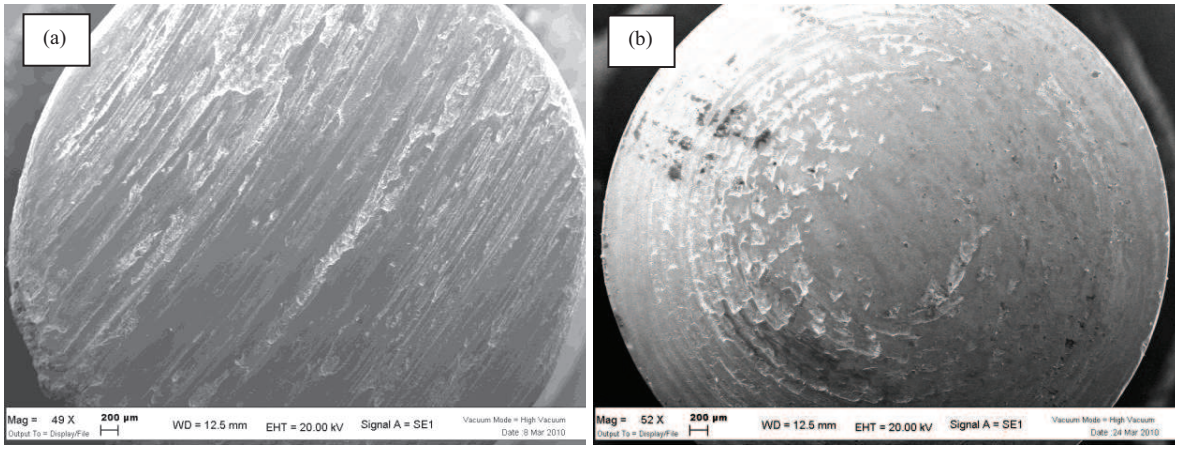

Figure 12 - SEM micrographs of pins worn surface: (a) for a 650 N normal load applied in dry conditions, (b) when a 450 N normal load is applied in wet conditions.

For a 650 N normal load applied in dry conditions, optical microscope observations of the pin cross-sections can provide information about the dynamic changes in worn surface layers (Figure 13). The sliding wear between metal and ceramic surfaces results in a laminated structure. In particular, it consists of an about 10 µm-thick iron oxide layer (A); a layer of a very fine structure without a defined position and orientation (B); a fine structure with a clearly defined position and orientation (C); a plastically deformed layer (D) and the unaffected structure (E). It is well-known that, for a given material, the characteristic structural layers appear depending upon test conditions. In general, the thickness of the plastically deformed layer is related to the properties of material itself. Structures with low plasticity and low thermal conductivity (e.g. martensite) are difficult to deform. It results in a higher surface temperature and a thinner plastically deformed layer. In contrast, structures with good plasticity and high thermal conductivity (e.g. pearlite) are easier to deform and less heat accumulates at surface. Accordingly, a thicker plastically deformed layer can form. The morphology of the material build-up, accumulated at the edge of the pin worn surface, is observed in Figure 14a. It is plastically deformed due to the sliding

motion and the highest surface temperature. It also consists of a very fine sorbitic microstructure with a great amount of carbides uniformly distributed (Figure 14b). Optical microscope examinations of the pins' cross-sections, for a 450 N normal load applied in wet conditions, show the same microstructure found before the wear test (Figure 15). No evidence of a laminated structure and of the material build-up, accumulated at the edge of the pin worn surface, are observed.

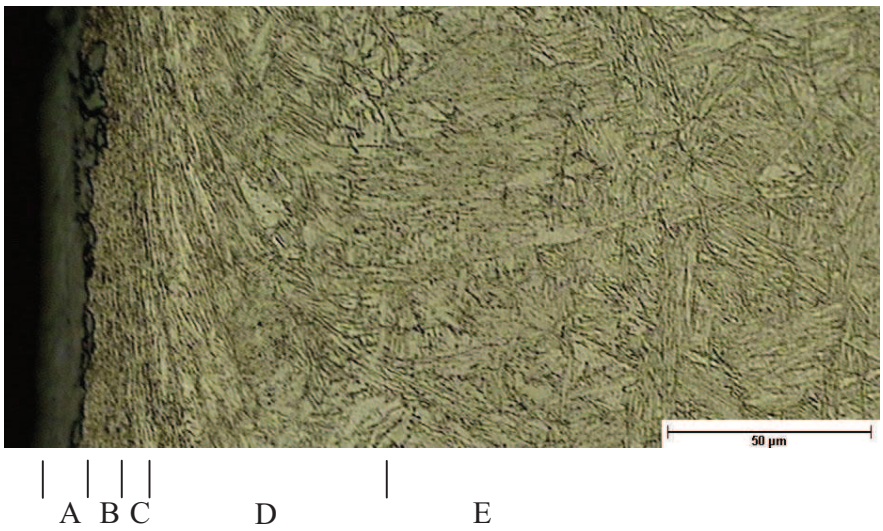

Figure 13 - Optical micrographs of a pin worn surface, when a 650 N normal load is applied in dry conditions.

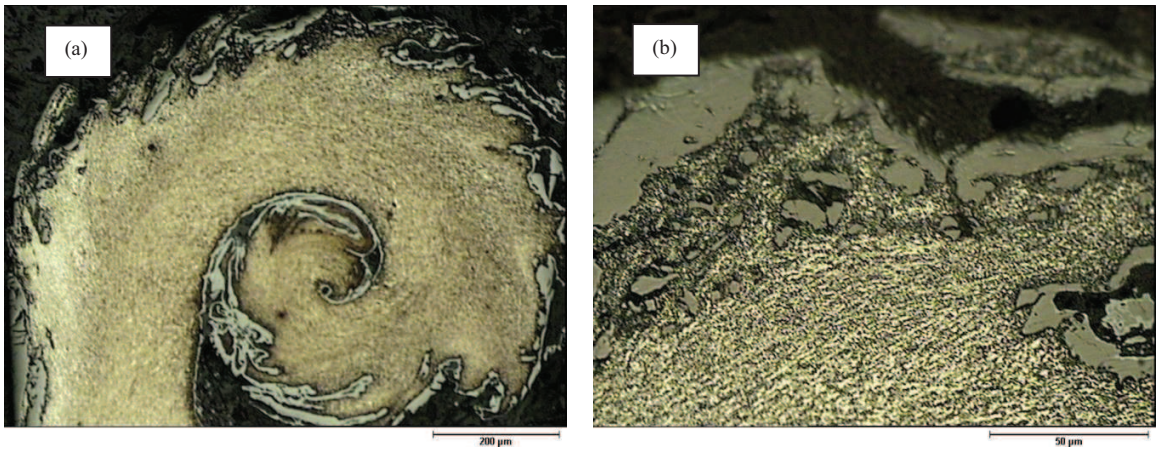

Figure 14 - Optical micrographs of a pin worn surface, when a 650 N normal load is applied in dry conditions: (a) detail and (b) microstructure of the material build-up at the edge of the sliding surface.

Figure 15 - Optical micrographs of a pin worn surface, when a 450 N normal load is applied in wet conditions.

Figure 16a shows the microhardness profiles of the pin worn surfaces, when a 650 N normal load is applied in different conditions. It can be seen there is a very narrow region just below the worn surface with high microhardness. Both curves rapidly decrease and reach values comparable to the microhardness of the base un-cemented material. During sliding wear, friction energy is used to produce plastic deformation and heat. Strain gradient and temperature gradient in worn surface layers affect the hardness distribution. Many internal factors affect the hardness of worn surface layers of a steel, such as strain hardening, recovery and recrystallization, precipitation hardening, thermal martensitic transformation tempering and so on. Therefore, the hardness profiles measured after wear tests reflect the competition between the factors that cause hardening and those that cause softening. It can be also demonstrated that a originally softer microstructure, which has a higher value of the work hardening coefficient (e.g. pearlite), is likely to show hardening. An originally harder microstructure, which has a lower value of the work hardening coefficient (e.g. martensite), is likely to show softening. This is in accordance with drop of the microhardness profile observed in Figure 16a. The wear volume is also related to the hardening and softening behaviour resulting from dynamic changes in worn surface layers. Generally, a smaller softening response corresponds to a better wear resistance [31-33]. When a 450 N normal load is applied in dry conditions the

softening trend of surface layers is the same as the previous cases (Figure 16b). For a 450 N normal load applied in wet conditions, the microhardness profile is typical of a steel subjected to an hardening surface treatment. There is no evidence of strain hardening or softening due to the sliding wear.

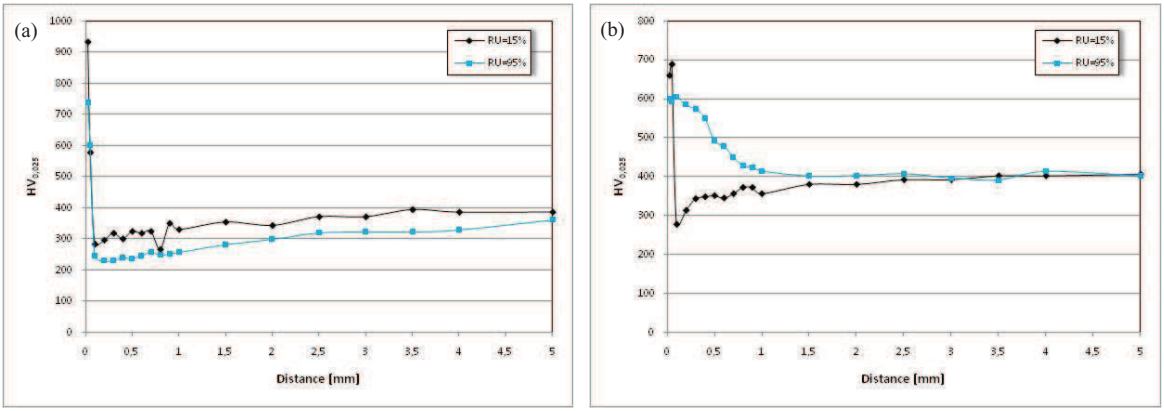

Figure 16. - Microhardness profiles of the pins' worn surfaces when: (a) a 650 N and (b) a 450 N normal load are applied in different humidity conditions.

4. CONCLUSIONS

Based on the results obtained regarding friction and wear behaviour of a carbon steel in sliding contact with a Cr_2O_3 plasma-sprayed ceramic coating, the following conclusions can be drawn:

- In dry and wet conditions, wear rates of the ceramic coating decrease with normal load. In dry conditions, wear rates of pins are independent of the normal loads applied. For a lower normal load applied in wet conditions, the wear rate of pins is reduced of about six orders of magnitude.
- For all the normal loads applied in dry conditions, metal/ceramic sliding contact produces a metallic film transfer onto the ceramic surface. Metallic film consists of a Fe_2O_3 compound usually formed at temperatures over about 200 °C. The presence of this oxide suggests a progressive increase in the contact

temperatures as wear tests proceed. The observations of pins' worn surfaces indicate that the principal involved wear mechanism is the mild-oxidational wear, with ploughing and a plastic deformation appearance. The dynamic changes in the surface layers of the material also result in a laminated structure. The subsequent transition to severe-oxidational wear is associated with the localised melting of the oxide layer and its spreading on the ceramic surface. As concern the ceramic coating, the observations of Cr_2O_3 worn surfaces indicate it undergoes microfractures along splat and columnar grains boundaries.

- In wet conditions, the normal load applied influences the tribological behaviour of metal/ceramic sliding couplings. For the highest normal load the wear mechanisms are the same involved in dry conditions. For the lower normal load the reduction of the surface temperatures, and consequently of the oxidation rate, is due to the water adsorption on the worn surfaces. The moisture adsorbed can act as a protective layer preventing metal/ceramic interaction.

ACKNOWLEDGEMENTS

The authors would like to thank Zocca Officine Meccaniche (Funo, BO) for the thermally sprayed coating manufacturing, and Ing. Marco Vitali for the contribution to the experimental activity.

REFERENCES

[1] H.A. Bolton, J.M. Larson, Valvetrain system design and materials, ASM International, Materials Park, OH, (2002).

[2] C.T. Sims, N.S. Stolloff, W.C. Hagel, Superalloys II: high temperature materials for aerospace and industrial power, Wiley- Interscience, New York, (1987).

[3] M.J. Donachie, S.J. Donachie, Superalloys - a technical guide, 2nd edn., ASM International, Materials Park, OH, (2002).

[4] F.H. Stott, D.S. Lin, G.C. Wood, 'Glazes' produced on nickel-based alloys during high temperature wear, Nature 242 (1973) 75-77.

[5] F.H. Stott, D.S. Lin, G.C. Wood, Structure and mechanism of formation of the 'glaze' oxide layers produced on Ni-based alloys during wear at high temperatures, Corrosion Science 13 (66) (1973) 449-469.

[6] P.J. Blau, T.M. Brummett, B.A. Pint, Effects of prior damage on high-temperature oxidation of Fe-, Ni-, and Co-based alloys, Wear 267 (2009) 380-386.

[7] F.H. Stott, G.C. Wood, The influence of oxides on the friction and wear of alloys, Tribology International 11 (4) (1978) 211-218.

[8] T.F.J. Quinn, Review of oxidational wear Part I: The origins of oxidational wear, Tribology International 16 (5) (1983) 257-271.

[9] S.C. Lim, M.F. Ashby, Overview no. 55 Wear-mechanism maps, Acta Metallurgica 35 (1) (1987) 1-24.

[10] F.H. Stott, High-temperature sliding wear of metals, Tribology International 35 (2002) 489-495.

[11] F.H. Stott, The role of oxidation in the wear of alloys, Tribology International 31 (1-3) (1998) 61-71.

[12] P.J. Blau, Elevated-temperature tribology of metallic materials, Tribology International 43 (2010) 1203-1208.

[13] W.Y.H. Liew, Effect of relative humidity on the unlubricated wear of metals, Wear 260 (2006) 720-727.

[14] P. De Baets, G. Kalacska, K. Strijckmans, F. Van De Velde, A.P. Van Peteghem, Experimental study by means of thins layer activation of humidity influence on the fretting wear of steel surface, Wear 216 (1998) 131-137.

[15] H. Goto, D.H. Buckley, The influence of water vapour in air on the friction behaviour of pure metals during fretting, Tribology International 18 (4) (1985) 237-245.

[16] G. Bregliozzi, S.I.-U. Ahmed, A. Di Schino, J.M. Kenny, H. Haefke, Friction and wear behaviour of austenite stainless steel: influence of atmospheric humidity, load range and grain size, Tribology Letters 17 (2004) 697-704.

[17] E. Tsuji, A. Ando, Effects of air and temperature on speed dependency of sliding wear of steel, JSLE ASLE International Lubrication Conference, Tokyo (1975) 101-109.

[18] S. Asanabe, Applications of ceramics for tribological components, Tribology International 20 (1987) 355-364.

[19] V. Aronov, T. Mesyef, Wear in ceramic/ceramic and ceramic/metal reciprocating sliding contact. Part1, ASME/ASLE Joint Tribology Conference, Atlanta (1985) 16-21.

[20] G.W. Stachowiak, G.B. Stachowiak, A.W. Batchelor, Metallic film transfer during metal-ceramic unlubricated sliding, Wear 132 (1989) 361-381.

[21] B. Wang, Z.R. Shui, A.V. Levy, Sliding wear of thermal-sprayed chromia coatings, Wear 138 (1990) 93-110.

[22] A. Tronche, P. Fauchais, Frictional behaviour against steel of aluminium substrates plasma-sprayed with hard coatings, Materials Science and Engineering: A 102 (1988) 1-12

[23] H. Cetinel, E. Celik, M.I. Kusoglu, Tribological behaviour of Cr_2O_3 coatings as bearing materials, Journal of Materials Processing Technology 196 (2008) 259-265.

[24] J.E. Fernandez, Y. Wang, R. Tucho, M.A. Martin-Luengo, R. Gancedo, A. Rincón, Friction and wear behaviour of plasma-sprayed Cr_2O_3 coatings against steel in a wide range of sliding velocities and normal loads, Tribology International 29 (4) (1996) 333-343.

[25] C.B. Ponton, R.D. Rawlings, Vickers indentation fracture toughness test. Part 1: Review of literature and formulation of standardised indentation toughness equations, Materials Science and Technology 5 (1989) 865-872.

[26] C.B. Ponton, R.D. Rawlings, Vickers indentation fracture toughness test. Part 2: Application and critical evaluation of standardised indentation toughness equations, Materials Science and Technology 5 (1989) 961-976.

[27] G. Bolelli, V. Cannillo, L. Lusvarghi, T. Manfredini, Wear behaviour of thermally sprayed ceramic oxide coatings, Wear 261 (2006) 1298-1315.

[28] S. Kittaka, K. Morishige, J. Nishiyama, T. Morimoto, The effect of surface hydroxyls of Cr_2O_3 on the adsorption of N_2, Ar, Kr, and H_2O in connection with the two-dimensional condensation, Journal of Colloid and Interface Science 91 (1) (1983) 117-124.

[29] M. Harju, T. Mäntylä, K. Vähä-Heikkilä, V. Lehto, Water adsorption on plasma sprayed transition metal oxides, Applied Surface Science 249 (2005) 115-126.

[30] E. Takeuchi, Friction and wear of machine parts - Surface heat treatments for increase wear resistance, Machine Tools 23 (5) (1979) 68-74.

[31] Y. Wang, T. Lei, J. Liu, Tribo-metallographic behaviour high carbon steels in dry sliding I. Wear mechanisms and their transition, Wear 231 (1999) 1-11.

[32] Y. Wang, T. Lei, J. Liu, Tribo-metallographic behaviour high carbon steels in dry sliding II. Microstructure and wear, Wear 231 (1999) 12-19.

[33] Y. Wang, T. Lei, J. Liu, Tribo-metallographic behaviour high carbon steels in dry sliding III. Dynamic microstructural changes and wear, Wear 231 (1999) 20-37.

[34] X.D. Li, Y. Wang, J.J. Liu, A study on dry friction of eutectoid steel, Wear 150 (1991) 59-65.

[35] H.S. Ahn, O.K. Kwon, Tribological behaviour of plasma-sprayed chromium oxide coating, Wear 225-229 (1999) 814-824.

Article B

FRICTION AND WEAR BEHAVIOR OF APS AND HVOF ADVANCED CERAMIC COATINGS

Mattia Merlin, Chiara Soffritti, Reyna Vazquez, Gian Luca Garagnani

Department of Engineering - ENDIF
University of Ferrara
I-44122 Ferrara
Italy

M. MERLIN, C. SOFFRITTI, R. VAZQUEZ, G. L. GARAGNANI, "Comportamento tribologico di rivestimenti ceramici avanzati applicati mediante tecniche APS e HVOF"/ "Friction and wear behavior of APS and HVOF advanced ceramic coatings", La Metallurgia Italiana, Consedit, Grado (GO), 11 (2011), p. 17-23, (ISSN 0026-0843).

ABSTRACT

Ceramic and cermet coatings are widely used in many industrial applications due to their friction and wear resistance, high hardness, chemical stability, oxidation-resistance at high temperatures and thermal barrier properties. In particular, it is a generally accepted practise to coat high temperature components in civil and military aero, marine and industrial gas turbines. The coatings can be deposited on the high temperature components such as liner, nozzles, first stage turbine blades and vanes in order to increase the firing temperature and subsequently the efficiency of the turbine. A variety of coatings and coating processes are available for protecting components in gas turbine engines operating in a variety of conditions. With reference to coated turbine blades and vanes the philosophy is that the base component material is developed to possess optimised mechanical properties whilst the coating is selected to achieve maximum protection from the service environment. Accordingly, the properties required by a surface coating system for blade and vane applications are high corrosion, oxidation and erosion resistance, good interfacial adhesion to the metallic substrate, as well as high mechanical and aerodynamic properties.

In this paper is reported a research activity carried out in order to evaluate the tribological behaviour of four types of advanced ceramic coatings, Al_2O_3-13TiO_2, Cr_2O_3, WC-12Co and Cr_3C_2-37WC-18Me, deposited onto cemented steel plates. The ceramic coatings are applied by plasma-spraying (APS), while the cermet coatings are deposited by HVOF-spraying technique. Pin-on-disk wear tests are performed by means of a DUCOM tribometer in accordance with ASTM G99-05 standard, using alumina pins as counterpart material. The tests are carried out under different conditions of relative humidity (20% and 70%); other test parameters, such as normal load, test duration, sliding speed and temperature, are maintained constant. Optical Microscope (OM) and Scanning Electron Microscope (SEM) observations of the worn surfaces show the interaction of different wear mechanisms, confirming the importance of relative humidity in relation to the nature of the coatings employed. In particular, the ceramic coatings (Al_2O_3-13TiO_2 and Cr_2O_3) are more sensitive to moisture than the cermet coatings (WC-12Co and Cr_3C_2-37WC-18Me), as highlighted

by both the friction coefficient and wear rate results. Moreover, comparing the behaviour of the investigated coatings, the cermets present the best wear resistance. The SEM observations of the Al_2O_3-13TiO_2 worn surface show a non-protective tribolayer and the generation of surface microcracks with the consequent removal of wear debris in the form of flakes. The Cr_2O_3 worn surface appears smoother without evidence of significant wear and the pores remain open in the flattened surface. Many cracks are also propagated in the same direction as the applied normal load. WC-12Co coating is less sensitive to moisture due to the formation of oxide layers acting as a solid lubricant. Finally, the morphology of Cr_3C_2-37WC-18Me does not clarify the influence of relative humidity on the tribological behaviour of this coating. In this case, further analyses by X-ray diffraction (XRD) could provide others information about the involved wear mechanisms.

Keywords: Sliding wear, Thermal spraying, Advanced ceramic coatings, Relative humidity

1. - INTRODUCTION

The ceramic and cermet materials are widely used in industrial applications that require high resistance to friction and wear, thanks to their high hardness, good chemical inertness, resistance to oxidation at high temperatures and their properties of thermal barrier [1]. However, the high cost of production and the fragility limit the application of bulk ceramics, which is why these types of materials are most frequently used in form of coatings that are applied onto less expensive materials, including steels. These types of coatings such have been used as an example, in the production of dies for hot extrusion, drying cylinders for paper mills, bearings and valves [2-7].

Compared to traditional coating techniques, thermal spraying is often considered a valid alternative for the realization of wear resistant surfaces. In fact, many materials, including ceramics and cermets, can be deposited on various substrates in order to obtain coatings characterized by high hardness, without altering thermally the coated material; the advantage is significant in cases where you need to respect stringent design tolerances and coating thin components or materials susceptible to thermal alteration (like Al and Mg). In general, the formation of the coating has been using powder particles of varying sizes, including nanometric size, which are melted in a torch, ejected and projected at temperature and velocity variables in form of droplets on the substrate to be coated. Compared with bulk materials, the presence of porosity, oxide inclusions and any other phases or partially molten particles that may form during the deposition, may reduce the tribological performance of the coating. In addition, the low adhesion coating-substrate that characterizes the obtained coatings by thermal spraying, severely limits technological applications. For these reasons in recent years intensive research has been aimed at assessing the influence of such typical defects on the performance and quality of these types of coatings.

The most commonly techniques used in thermal spraying are the APS (Air Plasma Spray) and HVOF (High Velocity Oxygen Fuel), as they allow obtaining high-quality anti-wear coatings. The HVOF was developed to overcome the limitations of plasma

spraying. And is well known that this technology, when is used for the production of cermet coatings, is more powerful than APS, because the higher speed deposition and lower spray flame temperature allows to create coatings with low porosity, limited oxidation of fused particles and low decomposition particle and / or carbides dissolution [8-11]. However, the HVOF has some limitations mainly related to the cost and difficulty of preparation of the starting powders and the lack of commercial availability of torches used for the deposition on the substrate. The APS is still the most widely used technique for the production of ceramic such as Al_2O_3 and Cr_2O_3;

APS coatings are more porous and fragile than HVOF sprayed cermet, due mainly the lower speed of impact of particles [12 -15]. Nevertheless, the APS coatings have very high hardness and low susceptibility to corrosion in many environments and can resist high temperatures.

A precise evaluation of the wear mechanisms that occur in APS and / or HVOF coatings can enable their correct use in many applications, even when the environmental conditions of humidity are critical to the proper functioning of the tribological system [2, 3]. In particular, ceramic or cermet are currently used as thermal protection as coating components of gas turbines for civil, military, marine and industrial; they are deposited on the "hot" parts as the turbine liners, nozzles and vanes of the first stage, allowing to raise the operation temperature and, consequently, the efficiency of the machine. The required properties of these coatings are highly resistant to corrosion, oxidation and erosion, good stability, and interfacial adhesion to the metal substrate, as well as high mechanical and aerodynamic [16].

The performance of gas turbine machines degrade with increasing temperature of the air flowing from the external. At higher temperatures, the efficiency of the gas turbine is closely related to the use of specific methods of cooling air inlet; for example, by the controlled injection of droplets of water in the form of fog, through the inlet air (a process known as wet compression). The amount of water injected into the inlet of the compressor, at close range from the admission of the outlet, can reach up to about 2% of the mass flow of air processed by the compressor. This is a superior amount of the sufficient saturation state that takes place at external environmental conditions. The rapid evaporation of the droplets of water helps to reduce the inlet temperature to the

compressor and the engine inlet air humidity increases... The temperature reduction results to the increase of power and efficiency, while the humidity increase results to a power increase but to an efficiency decrease. The temperature effect is greater than the humidity effect resulting to the improvement of the engine performance with inlet air cooling. [17]. This technology is therefore one of the most effective method to recover efficiency because it allows to obtain, rapidly, a significant proportion of additional power (15-20% of nominal power). In general, the benefits of the use of wet compression, mainly the increase in power output of the turbine, the improvement of the specific heat consumption of the plant and the reduction of NOx produced by the combustion system. Although these factors make it very attractive from the technological point of view, several authors have shown that the introduction of water in the early stages of the compressor is the main cause of the intense wear of the blades against erosion [18-20]. It was shown that the damage is closely related to the size, and velocity dispersion of droplets injected [21]. The use of wet compression also results in a range of issues related to the effect of excessive humidity within the lines of draining the compressor and the use of deminerelized water into the inlet. In relation with this application and the deposition of ceramic and cermet coatings on the vanes of the first stage of the compressor, in the research presented in this paper have been investigated four types of coatings, applied on a case-hardened steel substrate, in particular , were taken into consideration the coatings Al_2O_3-13TiO_2 and Cr_2O_3, applied with APS technique, and WC-12Co and Cr_3C_2-37WC-18Me, applied with HVOF technique. The main objective of the study is to assess their resistance to wear under a load of 50 N and two different values of relative humidity (20% and 70%). It 'has been observed that this parameter can significantly influence the tribological behavior of the system.

2. - MATERIALS AND METHODS

Four types of coating, namely Al_2O_3-13TiO_2 (powder: FST C-335.23, -45 +15 μm), Cr_2O_3 (powder: AMPERIT® 707.001, -45 +22.5 μm), WC-12Co (powder: WOKA 3102, -45 +15 μm) and Cr_3C_2-37WC-18Me (powder: WOKA 7505, -38 +10 μm), were deposited onto cemented steel plates (75 mm in diameter and 6 mm in thickness).

Chemical composition of the steel substrate was evaluated by Optical Emission Spectroscopy (OES) and the main results are collected in Table I. A bond coat Ni-20%Cr was applied between the steel substrate and the first two ceramic coatings, in order to improve adhesion. All ceramic and cermet coatings were made by a company specialized in industrial applications of coating of metal surfaces; the spraying parameters are therefore confidential.

Table I. - Chemical composition (wt.%) of the steel substrate.

C	S	Mn	P	Si	Cr	Ni	Mo	Cu	V	Fe
0.22	0.033	0.88	0.021	0.30	0.84	0.87	0.06	0.202	0.022	bal.

The coatings were characterized by Vickers microhardness measurements (300 *gf* load and 15s loading time) carried out by means of a Microhardness Tester FM Future-Tech. Roughness parameters (Ra and Rz) were calculated by the portable Handysurf E35_A ZEISS-TSK rugosimeter. Before each measurement all the coating surfaces are cleaned by ultrasonic bath. The LEICA MEF4M optical microscope, equipped with Archive4Images v.3.20b software for image analysis, was also employed on properly polished cross-sections to analyse the coatings microstructure. Image-Pro Plus v6.0 software was used in order to quantify coating porosity. Pin-on-disk dry sliding tests were carried out with a Multispecimen Tester tribometer produced by DUCOM Instruments, in accordance with ASTM G99-05 “Standard test method for wear testing with a pin-on-disk apparatus”, using cylindrical alumina pins of 6 mm in diameter and 22 mm in height as counterpart material. Normal load (5÷1000 N), sliding speed (20÷1400 rpm), temperature (≤ 200°C), relative humidity (0÷100%), test duration and total wear were continuously monitored during the tests. For each test, an applied normal load of 50 N, a sliding speed of 100 rpm and test duration of 1 h were maintained constant, whereas
the values of 20% and 70% of relative humidity were selected. Moreover, a mean of 10 tests for each coating were performed to verify the results. Wear rate of disks was evaluated by measuring the area of the wear track cross-section by an Optacom VC-10

profilometer. Each area, obtained as an average value of four measurements along the wear circumference, was used to calculate the wear volume. In order to understand wear mechanisms the coating worn surfaces were investigated by means of Optical Microscope (OM), and Scanning Electron Microscope (SEM).

3. - RESULTS AND DISCUSSIONS

3.1 Microstructure and mechanical properties

Optical micrographs in Figure 1 show the microstructure of the four examined coatings. The Al_2O_3-13TiO_2 possesses a lamellar microstructure characterized by the presence of titania lamellae well-melted and partially mixed with alumina (Figure 1a). Moreover, pores and coarse particles can be seen at the steel/bond coat interfaces; these residues are probably resulting from the sandblasting process, normally performed before thermal spraying in order to improve the coating/substrate adhesion. As concern the Cr_2O_3 coating, also the optical micrograph in Figure 1b depicts a lamellar microstructure typical of coatings produced by plasma spray technique. Microstructure of both WC-12Co and Cr_3C_2-37WC-18Me coatings (Figure 1c and Figure 1d, respectively), consists of carbide particles embedded into a metallic matrix; at higher magnifications the carbides appear non-uniformly distributed and variable in size, generally in the range of 1÷10 μm. Moreover, for WC-12Co coating, micro-cracks developed in parallel direction to the coating surface generate interconnecting porosity.

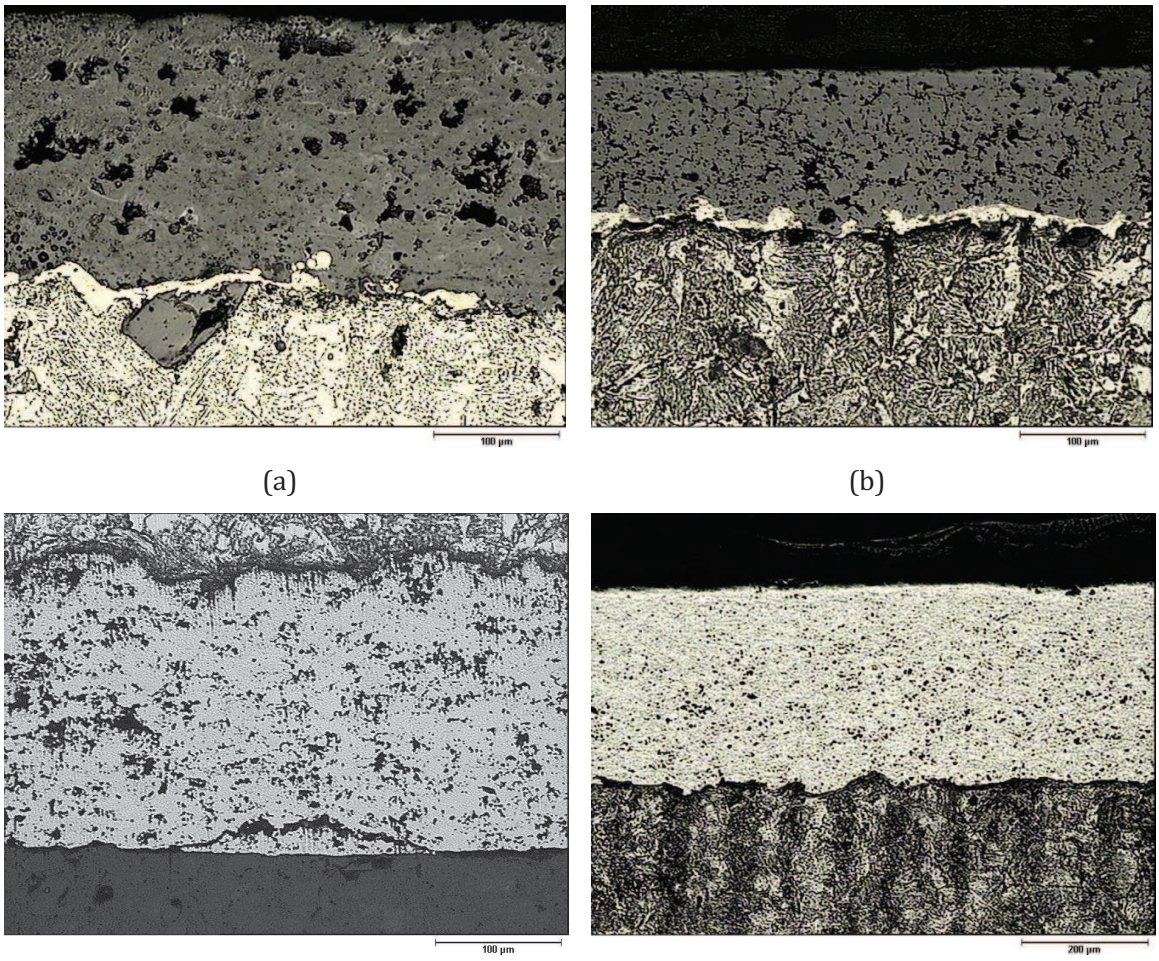

(a) (b)

(c) (d)

Figure 1 .- Optical micrographs of the examined coatings: (a) Al_2O_3-13TiO_2, (b) Cr_2O_3, (c) WC-12Co, (d) Cr_3C_2-37WC-18Me.

The mechanical properties of each coating are investigated by Vickers microhardness and roughness measurements; in addition, the porosity is evaluated by image analysis performed by Image-Pro Plus v6.0 software. The main results are collected in Table II.

Table II. – Mechanical properties, roughness and porosity of the coatings.

	Thickness [µm]	Hardness $HV_{0.3}$	R_a [µm]	R_z [µm]	Porosity [%]
Al_2O_3-13TiO_2	200	778 ± 53	0.25 ± 0.01	2.66 ± 0.23	13.7
Cr_2O_3	110	1188 ± 45	0.15 ± 0.02	1.78 ± 0.19	10.8
WC-12Co	150	1076 ± 186	0.35 ± 0.04	2.65 ± 0.27	14.7
Cr_3C_2-37WC-18Me	300	1181 ± 260	0.41 ± 0.03	2.93 ± 0.21	9.2
Pin in Al_2O_3	-----	1500÷1650	-----	-----	-----

3.2 Tribological behaviour

The wear tests highlight the influence of relative humidity on the tribological behaviour of the examined advanced ceramic coatings. In Figure 2 are reported the mean values of the friction coefficient calculated at the end of the wear tests. For Cr_2O_3 and Cr_3C_2-37WC-18Me coatings the friction coefficient decreases as the relative humidity increases. In both cases, this behaviour can be attributed to the boundary lubrication due to water adsorption on coating surfaces; the "lubricant" is interposed between the coupling surfaces, reducing friction and wear [22]. The wear tests also suggest that the Cr_2O_3 is more sensitive to water adsorption, it improves the tribological behaviour. The coating Cr_3C_2-37WC-18Me shows that the relative humidity seems to lead to a slight decrease in the coefficient of friction.

Friction coefficients obtained for the WC-Co coating are comparable for both values of the relative humidity. It is caused by two opposing phenomena: at low relative humidity the generation of a protective tribolayer, acting as solid lubricant, greatly reduces the friction coefficient. At high relative humidity the tribolayer is less

adherent to the substrate; consequently, the predominant mechanism is the water adsorption [8, 23].

The tribological behaviour of Al_2O_3-13TiO_2 coating is very different: the friction coefficient increases as the relative humidity increases. The lower microhardness (see Table II) and the presence of an alumina-titania glassy phase weaken the ceramic material. Moreover, this coating does not form an adequately compact tribolayer and therefore shows unfavourable properties in terms of friction coefficient and wear rate (see Figure 4) [7].

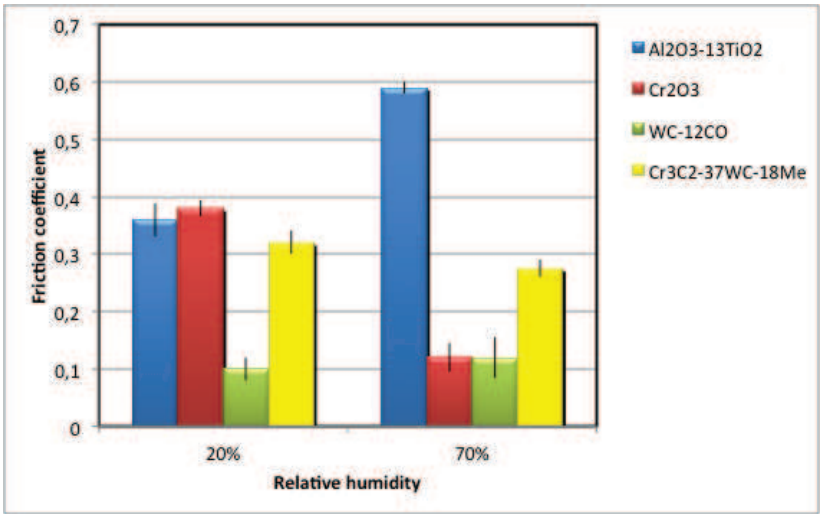

Figure 2. - Mean values of friction coefficient.

Figure 3 shows an example of a wear scar profile of the Al_2O_3-13TiO_2 coating. The profiles are used to measure the area of the wear track cross-section; each area, obtained as an average value of four measurements along the wear circumference, is then employed to calculate the wear volume.

Wear rate is obtained dividing loss volume [mm3] by the product of normal load applied [N] and sliding distance [m]. Mean values of the wear rate calculated at the end of the wear tests are reported in Figure 4.

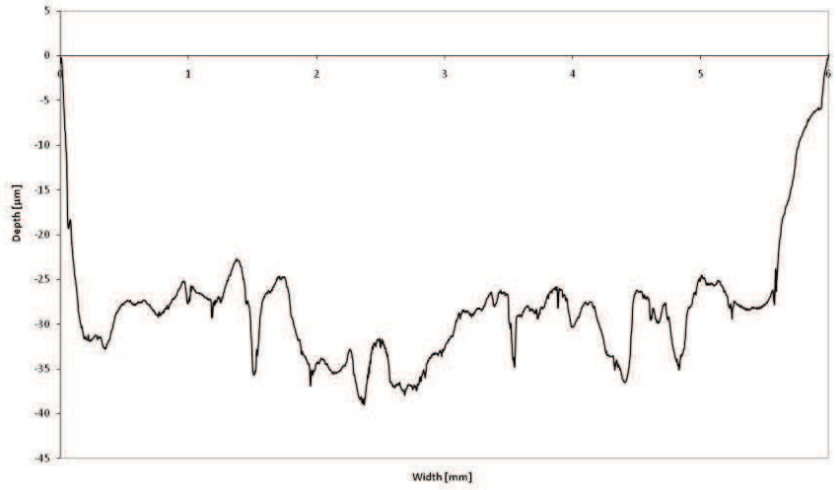

Figure 3. – Wear scar profile of the Al_2O_3-13TiO_2 coating after a wear test carried out under an applied normal load of 50 N and relative humidity of 70%

As can be seen, cermet coatings possess the highest wear resistance, typical of carbide-based coatings, with a wear rate in the range of 10^{-6} mm3/Nm. The wear rates of plasma-spraying coatings at the two different humidity conditions are the highest, with the maximum values corresponding to the Al_2O_3-13TiO_2 coating.

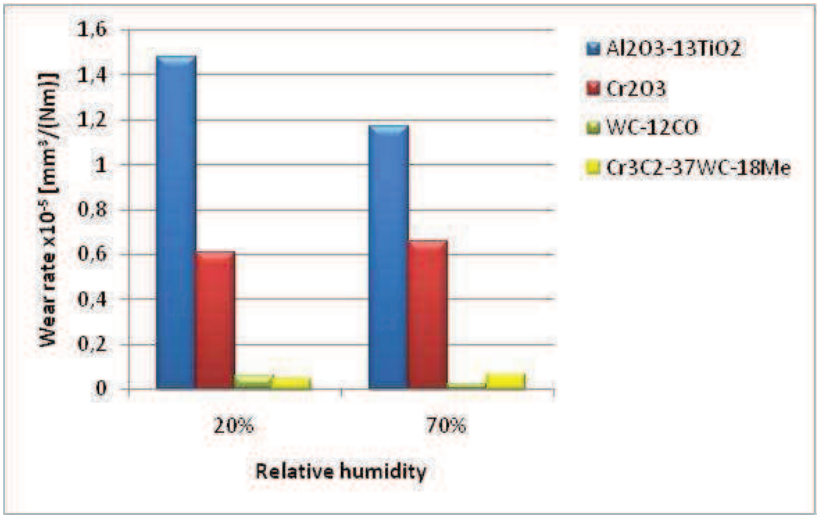

Figure 4. – Mean values of wear rate.

3.3 Analysis of worn surfaces

SEM micrographs in Figure 5 depict the Al_2O_3-13TiO_2 worn surfaces when the wear tests are performed under 20% and 70% relative humidity conditions. As can be noted, the worn surfaces are composed of smooth regions and rough regions. On the rough areas (Figure 5a) many microcracks and the removal of micro-sized sheet debris can be observed. It is also confirmed that the surface microfractures take place along the columnar grains and splat boundaries, since their strength is usually not high enough. The smooth areas (Figure 5b) are characterised, particularly in wet conditions, by the presence of small debris due to the removal of a thin aluminium hydroxide film, produced by tribochemical reactions between water vapour and the coating surface. The tribolayer is softer than the coating and is therefore able to reduce the wear damage, limiting the generation of surface microcracks [24-26].

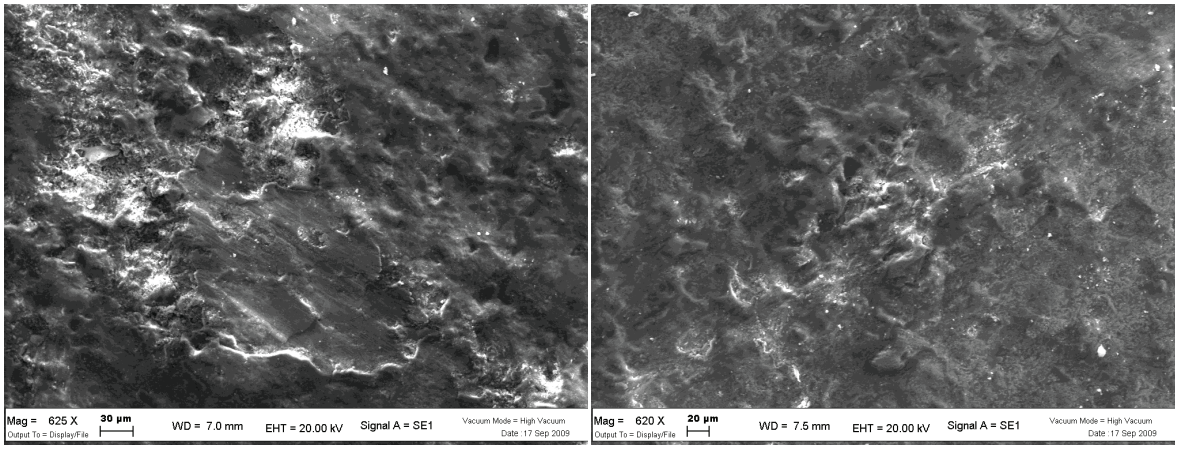

(a) (b)

Figure 5. - SEM micrographs of Al_2O_3-13TiO_2 worn surfaces, after the wear test (a) under a relative humidity of 20%, (b) under a relative humidity of 70%.

SEM micrographs of Cr_2O_3 worn surfaces are shown in Figure 6. In both dry and wet conditions open pores and wear particles are visible; many cracks are also developed from the open porosity in perpendicular direction to the coating surface, generating interconnecting porosity (Figure 7).

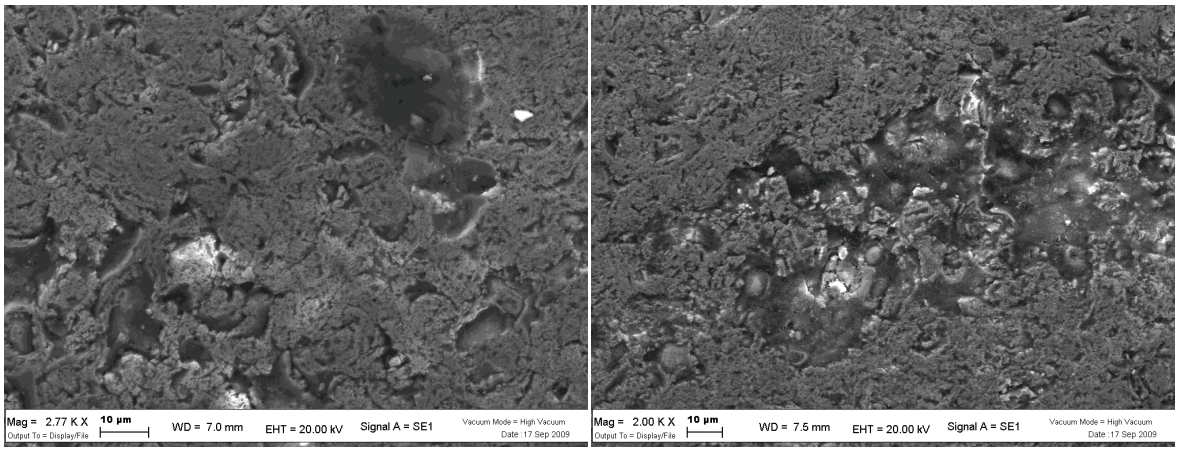

(a) (b)

Figure 6. - SEM micrographs of Cr_2O_3 worn surfaces, after the wear test: (a) under a relative humidity of 20%, (b) under a relative humidity of 70%.

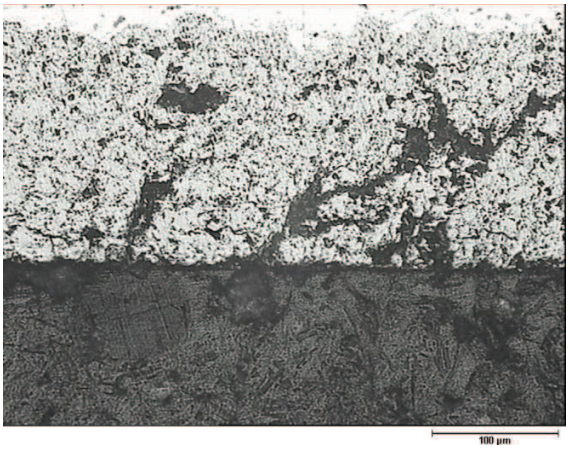

Figure 7. – Optical micrograph of Cr_2O_3 coatings ´cross-section after a wear test carried out under a relative humidity of 70%.

In Figure 8 are reported the SEM micrographs of WC-12Co worn surfaces. For this coating, the wear mechanism that can explain the low friction coefficient and the low wear rate is the formation of lubricant oxides, such as CoO and WO3. At the beginning of the test the material loss mainly comes from the Co matrix removal. The removal of the metallic binder is followed by a decrease of the adhesion of WC particles, which are pull off giving as a result the formation of wear debris. The wear particles are subsequently flaked and oxidized, promoting the generation of lubricant oxides which

are retained between the coupling surfaces [27, 28]. As the wear test proceeds the tribolayer is cracked and progressively removed (Figure 8a). In particular, for the highest value of relative humidity the tribolayers appears more discontinuous, confirming that the presence of water particles reduces the adhesion of the oxide film (Figure 8b).

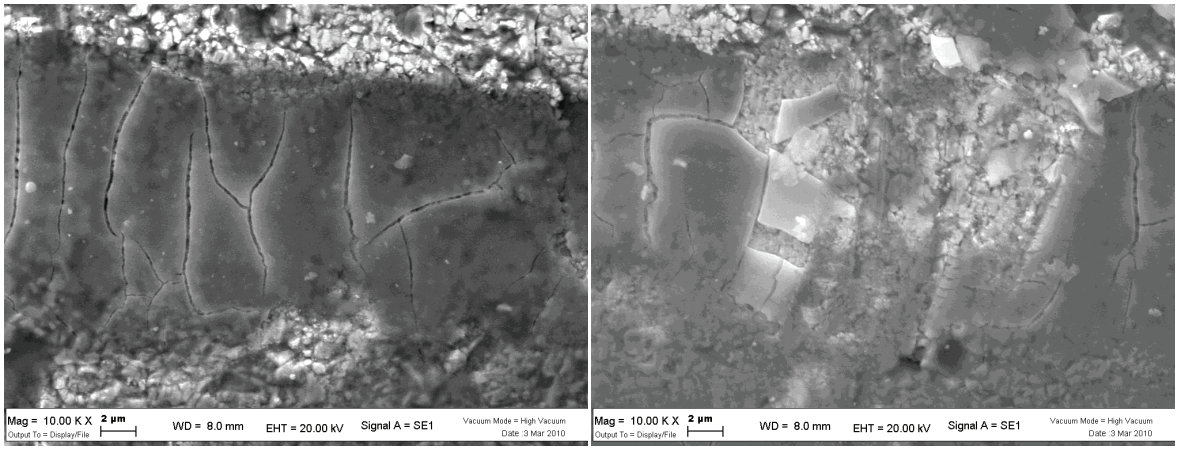

(a) (b)

Figure 8. - SEM micrographs of WC-12Co worn surfaces, after the wear test: (a) under a relative humidity of 20%, (b) under a relative humidity of 70%.

Figure 9 shows a SEM micrograph of the Cr_3C_2-37WC-18Me worn surface, after a wear test carried out under a relative humidity of 70%. In any case, no wear damage is observed on this cermet coating. The Scanning Electron Microscope (SEM) observation is not clarifying of the wear mechanism that seems compatible with both the formation of a protective tribolayer and the plastic deformation of the asperities due to the high surface roughness that characterizes this coating (see Table II). Further analyses by X-ray diffraction (XRD) could provide others information about the involved wear mechanisms.

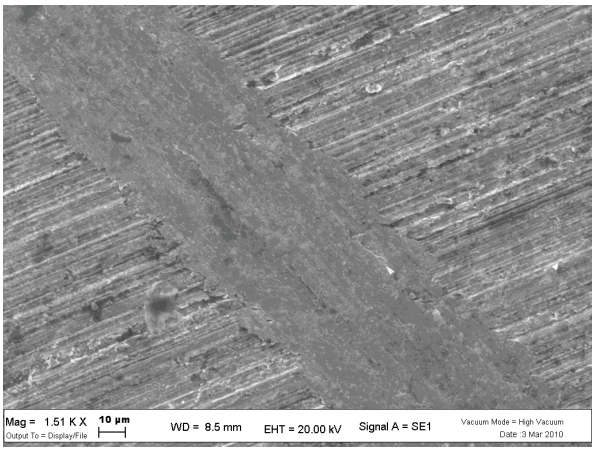

Figure 9. - SEM micrograph of Cr_3C_2-37WC-18Me coating after a wear test carried out under a relative humidity of 70%.

4. - CONCLUSIONS

The analyses performed in this research activity demonstrate the importance of relative humidity on the tribological behaviour of ceramic and cermet coatings realised by means of plasma-spraying and HVOF-spraying techniques. In particular, the ceramic coatings (Al_2O_3-13TiO_2 and Cr_2O_3) are more sensitive to moisture than the cermet coatings (WC-12Co and Cr_3C_2-37WC-18Me), as highlighted by both the friction coefficient and wear rate results.

Moreover, comparing the behaviour of the investigated coatings, the cermets ones present the best wear resistance. The SEM observations of the Al_2O_3-13TiO_2 worn surface show a non-protective tribolayer and the generation of surface microcracks with the consequent removal of wear debris in the form of flakes. The Cr_2O_3 worn surface appears smoother without evidence of significant wear and the pores remain open in the flattened surface. Many cracks are also propagated in the same direction as the normal load applied. WC-12Co coating is less sensitive to moisture due to the formation of oxide layers acting as a solid lubricant. Finally, the morphology of Cr_3C_2-37WC-18Me does not clarify the influence of relative humidity on the tribological behaviour of this coating.

ACKNOWLEDGEMENTS

The authors would like to thank Zocca Officine Meccaniche (Funo, BO) for the manufacturing of thermal-sprayed coating.

REFERENCES

1) J.E. FERNANDEZ et al., Friction and wear behaviour of plasma-sprayed Cr_2O_3 coatings against steel in a wide range of sliding velocities and normal loads, Tribology International 29-4, (1996), p. 333-343
2) M. HARJU et al., Influence of long-term aqueous exposure on surface properties of plasma sprayed oxides Al_2O_3, TiO_2 and their mixture Al_2O_3-$13TiO_2$, Applied Surface Science 254, (2008), p. 7272-7279
3) M. HARJU et al., Influence of aqueous aging on surface properties of plasma sprayed oxide coatings, Journal of Colloid and Interface Science 313, (2007), p. 194-201
4) D.A. STEWART, P.H. SHIPWAY, D.G. McCARTNEY, Microstructural evolution in thermally spayed WC-Co coatings: comparison between nanocomposite and conventional starting powders, Acta Materialia 48, (2000), p.1593-1604
5) H.S. AHN, O.K. KWON, Tribological behaviour of plasma-sprayed chromium oxide coating, Wear 225-229, (1999), p. 814-824
6) V. ARONOV, T. MESYEF, Wear in ceramic/ceramic and ceramic/metal reciprocating sliding contact: Part 1, Journal of Tribology 108, (1986), p. 16-21
7) G. BOLELLI et al., Wear behaviour of thermally sprayed ceramic oxide coatings, Wear 261, (2006), p. 1298-1315
8) J.M. GUILEMANY et al., Role of three-body abrasion wear in the sliding wear behaviour of WC-Co coatings obtained by thermal spraying, Surface and Coatings Technology 140, (2001), p. 141-146
9) A. SCRIVANI et al., A contribution to the surface analysis and characterization of HVOF coatings for petrochemical application, Wear 250, (2001), p. 107-113
10) P.H. SHIPWAY, L. HOWELL, Microscale abrasion-corrosion behaviour of WC-Co hardmetals and HVOF sprayed coatings, Wear 258, (2005), p. 303-312

11) J. VINCENZI et al., HVOF-coatings against high-temperature erosion (≈300°C) by cold fly ash in thermoelectric power plant, Materials & Design 27, (2006), p. 236-242

12) H. HERMAN, S. SAMPATH, R. McCUNE, Thermal spray: current status and future trends, in: S. SAMPATH, R. McCUNE (Eds), Thermal Spray Processing of Materials, MRS Bulletin, (2000), p. 17-25

13) Y. LIU, T.E. FISHER, A. DENT, Comparison of HVOF and plasma-sprayed alumina/titania coatings-microstructure, mechanical properties and abrasion behaviour, Surface and Coatings Technology 167, (2003), p. 68-76

14) R.S. LIMA, B.R. MARPLE, Optimized HVOF titania coatings, Journal of Thermal Spray Technology 12, (2003), p. 360-369

15) L. BIANCHI et al., Microstructural investigation of plasma-sprayed ceramic splats, Thin Solid Films 299, (1997), p. 125-135

16) T.N. RHYS-JONES, Coatings for blade and vane applications in gas turbines, Corrosion Science 29-6, (1989), p. 623-646

17) I. ROUMELIOTIS, K. MATHIOUDAKIS, Evaluation of water injection effect on compressor and engine performance and operability, Applied Energy 87, (2010), p. 1207-1216

18) P.E. SANJEEV JOLLY, Wet compression - a powerful means of enhancing combustion turbine capacity, Presented at the Power - Gen International, Orlando, Florida, December 10-12, (2002), p. 1-11

19) P.E. SANJEEV JOLLY, Performance enhancement of GT 24 with wet compression, Presented at the Power - Gen International, Las Vegas, NV, December 9-11, (2003), p. 1-12

20) M. CHAKER, C.B. MEHER-HOMJI, Inlet fogging of gas turbine engines: climatic analysis of gas turbine evaporative cooling potential of international locations, Proceedings of ASME Turbo Expo, Amsterdam, Netherlands, June 3-6, (2002), p. 1-16

21) H. GAJJAR et al., Inlet fogging for a 655 MW combined cycle power plant - design, implementation and operating experience, Proceedings of ASME Turbo Expo, Power for Land, Sea and Air, Atlanta, Georgia USA, June 16-19, (2003), p. 1-9

22) J.K. LANCASTER, A review of the influence of environmental humidity and water on friction, lubrication and wear, Tribology International 23-6, (1990), p. 371-389

23) R.J.K. WOOD, Tribology of thermal sprayed WC-Co coatings, International Journal of Refractory Metals & Hard Materials 28, (2010), p. 82-94

24) X. DONG et al., Tribological characteristics of α-alumina at elevated temperatures, Journal of the American Ceramic Society 74, (1991), p. 1036-1044

25) W. TIAN et al., Sliding wear and electrochemical corrosion behaviour of plasma sprayed nanocomposite Al_2O_3-13TiO_2 coatings, Materials Chemistry and Physics 118, (2009), p. 37-45

26) B. NORMAND et al., Tribological properties of plasma sprayed alumina-titania coatings: role and control of the microstructure, Surface and Coatings Technology 123, (2000), p. 278-287

27) M. MAGNANI et al., Influence of HVOF parameters on the corrosion and wear resistance of WC-Co coatings sprayed on AA7050 T7, Surface & Coatings Technology 202, (2008), p. 4746-4757

28) P.H. SHIPWAY et al., Sliding wear behaviour of conventional and nanostructured HVOF sprayed WC-Co coatings, Wear 259, (2005), p. 820-827

Article C

AMORPHOUS PHASE CONSIDERATIONS IN WEAR RESISTANT COATINGS

Reyna Vazquez, Chiara Soffritti, Mattia Merlin, Gian Luca Garagnani.

Engineering Department
University of Ferrara, Via Saragat 1,
44122 Ferrara
Italy

Preprint 2012

ABSTRACT

A wear study using air plasma sprayed technique (APS) on Al_2O_3-13TiO_2 coating against carbon steel in a pin-on-disk configuration using two different loads was carried out, in order to evaluate the effect of the amorphous-glassy TiO_2 phase. Surface analyses were carried out by Optical Microscope (OM), Scanning Electron Microscope (SEM) with Energy Dispersive Spectroscopy (EDS), X-ray Diffraction (XRD); surface roughness, and Instrumented Indentation Testing (IIT) have been used to evaluate hardness and elasticity modulus. The surface structure presents a not full transformation of $\alpha \rightarrow \gamma$ Al_2O_3 and an amorphous phase of TiO_2. The wear process results in an adhesive mechanism from the steel pin to the ceramic surface. The EDS present different Ti concentration depending on the damage to the surface. The hardness considered for this material was lower than the one reported by other authors; in our case, considering that the instrumented indentation testing (IIT) and the elastic modulus were lower than in a ceramic material, nearer to that of glass, the amorphous glassy phase of the matrix is confirmed. Also through micro-XRD was possible to identify non crystalline zones.

Metal transfer and wear, were greatly dependant on the load applied. The observations of the worn surfaces of the pins indicate a mild-oxidation wear mechanism with the appearance of ploughing and plastic deformation.

Keywords: crystal, amorphous phase, powder transformation.

1. - INTRODUCTION

Ceramic coatings are widely used to protect softer and reactive materials from wear and corrosion even at elevated temperatures; due to their resistant and inert properties the main industries that apply this technology are chemical, naval and oil industries [1,2].

Ceramics are the principal materials applied with the APS technique because their final structure; the ceramic powders can be even mixtures of several ceramics. The Al_2O_3-$13TiO_2$ is widely used by the industries mentioned above and in biocompatible applications it is used also in pharmaceutical and food industries due to the absence of heavy metal contamination [3].

The wear process in ceramic coatings has been extensively studied. But the effect of the amorphous glassy phase has not been studied in detail. The large contact area of the substrate associated with the lamellae facilitates rapid heat transfer which may be sufficient to form the amorphous phase. Rapid solidification, arising from the high cooling rates in APS produces amorphous phases from ceramics such as Alumina [4].

APS coating application technique affects the initial composition of the powders as in the case of Al_2O_3 which transforms from $\alpha \rightarrow \gamma$ Al_2O_3 where the hardness of each phase is different; the γ phase is softer than α, and the distribution of the crystal phase affects the wear properties of the coating. TiO_2 is also dissolved into α phase and transformed into an amorphous matrix that contains the remainder crystalline phase [5]. The final phases in coating depend of the parameters in the APS. Understanding the amorphous phase formation can help to produce coatings with less variability.

2. - MATERIALS AND METHODS

The materials used in this study are composites; In this case a mix of powders and bond material are combined to create a coating to protect a steel surface.

The coated geometry is a cemented steel plate (75 mm in diameter and 6 mm in thicknesses) the composition of the disk is showed in the Table I. The pin is a carbo-cemented steel cylinder with a length of 22mm, diameter of 6mm and weight 4.78 ±0

.01 gr The studied coating is Al_2O_3-13TiO_2 applied with APS technique with the powder described in Table II. The powders for coatings are mixed, fused and crushed to dimensions around -45+15µm. The bond coat is a Ni-20Cr to improve the ceramic material adhesion onto the steel substrate (also obtained by APS). Deposition parameters are confidential.

Table I. - Chemical composition (wt. %) of the steel substrate and pin.

	C	Mn	Ni	Cr	Si	Cu	Mo	S	Fe
Coated plate steel	0.22	0.88	0.87	0.84	0.30	0.20	0.06	0.03	Balance
Pin steel	0.23	0.86	0.95	0.91	0.26	0.10	0.06	0.02	Balance

Table II. - Chemical composition of the feedstock powders.

	Al_2O_3-13TiO_2
Type	FST C-335.23 by Flame Spray Technologies
Composition	13.12%TiO_2, 0.22%ZrO_2, 0.15Nb_2O_5, 0.1%SiO_2, 0.09%MgO, 0.07%CaO, 0.24% other oxides, balance Al_2O_3.
Particle dimension	-45+15

The microstructural characterization of the coatings has been carried out in an optical microscope LEICA MEF4M equipped with image analysis software Archive4Images v.3.20b. The microstructure of the samples were, also observed in Scanning Electron Microscope (SEM) the samples were observed in as received and polished conditions. For the last condition the samples were prepared using abrasive paper from 800 to 1200 grid and after the samples have been polished with a cloth and diamond solution from 9µm to 1µm, the samples were observed in surface and transversal sections. The SEM equipped with Energy Dispersion Spectroscopy (EDS) has been used to analyze

the chemical composition. Diffraction analysis has been realized in Saltillo Coahuila, Mexico at Instituto Tecnológico de Saltillo in a PHILIPS* X`Pert X-ray diffractometer (XRD) using Cu Kα radiation (λ= 1.54Å), with an intensity scanner vs. diffraction angle between 15° and 120° (step size of 0.06°), a voltage of 40 kV and 30 mA filament current. and in Badajoz, Spain at Universidad de Extremadura in a high-resolution diffractometer D8 ADVANCE Bruker using a Cu Kα radiation (λ= 1.54183Å), with an intensity scanner vs. diffraction angle between 20° and 80° (step size of 0.02°), time count 3 s/step. To evaluate the hardness and elastic modulus of coatings an instrumented indentation testing (IIT) has been performed. The test has been carried out in a Nanotest, Micro Materials Ltd., Wrexham, UK, with a Berkovich diamond indenter; 49 indentations in a matrix array of 7 x 7; with a distance of 395 μm between them, on the surface of each sample, the velocity of the applied load was 350 mN/s, the load was calculated by the machine in order to obtain a depth impression not greater than 10 μm to avoid the substrate hardness influence; the maximum load permanence onto the surface was 10 s. For the AL_2O_3-13TiO_2 the load was 8640±404 mN. Another hardness test has been carried out with a micro-hardness Tester FM Future-Tech and with a load of 300 gr. The wear test has been carried out in a multispecimen tester TR-750 DUCOM, in a pin on disc configuration according to ASTM G99 [6]. The applied loads were of 450 and 650N with a sliding velocity of 160 RPM in absence of humidity (relative humidity 15%). The sliding distance was 7500m.

3. - RESULTS AND DISCUSSION

3.1 Microstructural Characterization

The microstructure of the as-received condition is shown in the figure 1. The SEM micrograph a) shows the surface where is possible to appreciate the removal of material due to the surface finishing process; this image is obtained with the back scattered electrons and shows a good distribution of the elements in the surface. Micrograph b) shows with more detail the surface where is possible to observe a not fully molten particle and the pores produced by the gas during the APS process, weakly attached small crystals and a dense matrix are also visible.

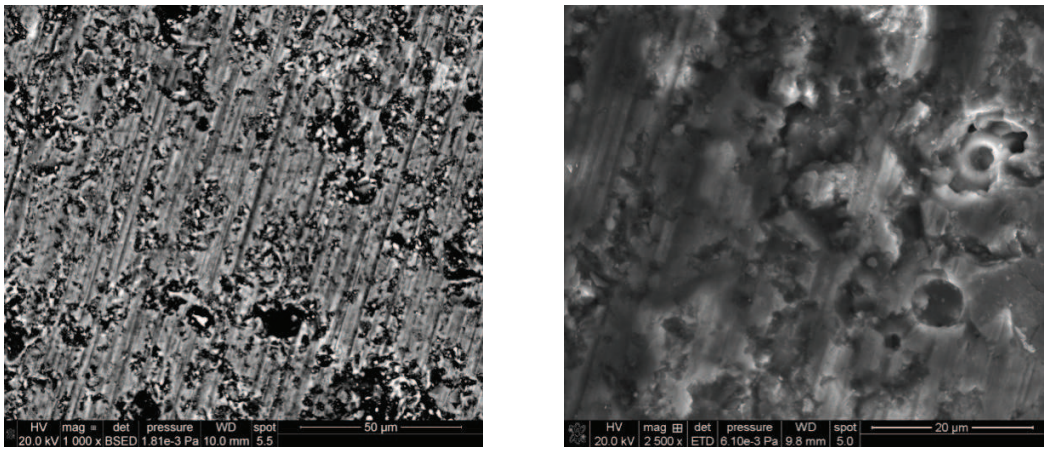

(a) (b)

Figure 1. - Coating In as received condition, SEM image at 1000X (a) and 2500X (b). Detail of the finishing process, porosity and chipping.

The microstructure of the surface and transversal section after polishing is shown in figure 2; in the optical micrograph (a) is possible to observe zones where chipping has been produced by polishing; this effect is more evident in the light grey areas where a considerable crystal concentration is possible. The matrix around these crystal concentrations is pour and the binder effect is not so effective. The more stable zones appear to be those where the surface shows uniform color that indicates a full solution of the crystalline phase into the amorphous binder phase; it is also evident that the crystal richer zones are the prone areas where the pulling out start.

The transversal section; figure 2 b) shows the lamellar structure, the presence of partially melted particles and a less porous surface are observable; the presence of crystals in the TiO_2 rich matrix is evident. In transversal section the visible porosity is produced by deoxidation during the process. Image 2c) shows zones in which the microstructure was 1) a fully melted structure composed by melted TiO_2 and the gamma alumina phase, 2) a partially melted structure with bright white particulates embedded in a splat melted structure with a morphology that can vary from round to splat.

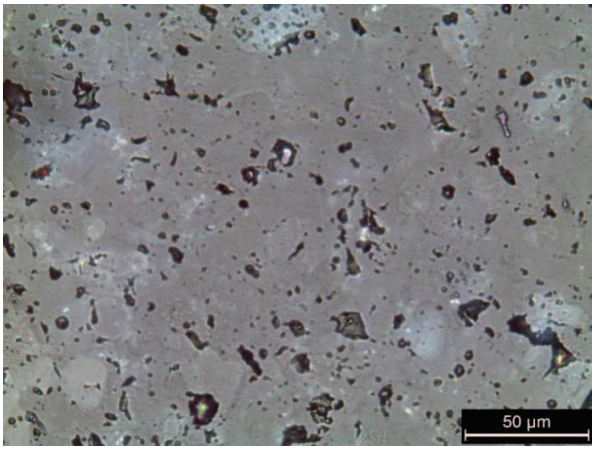

(a)

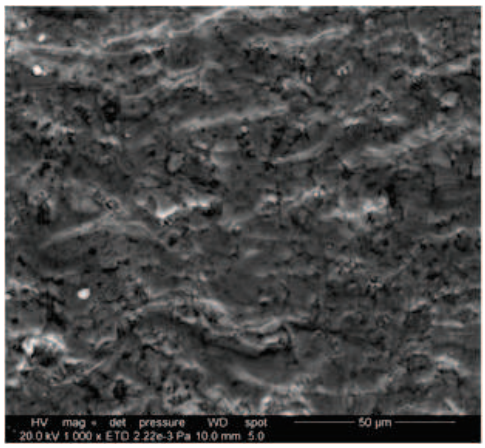

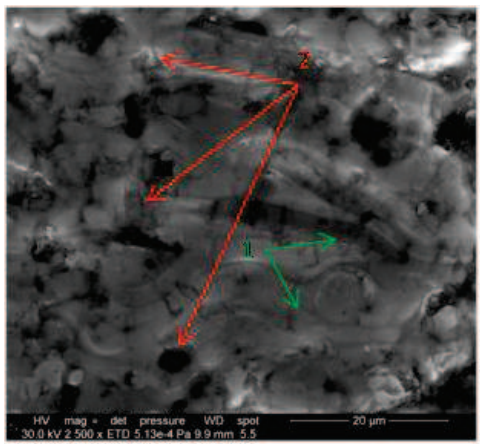

(b) (c)

Figure 2.- Optical and SEM micrograph of polished surface (a) and transversal section (b and c)

The EDS analysis confirms that the morphology changes as the concentration of Ti is reduced, as shown in figure 3, where in the flat zones (point number 3) the Ti concentration is higher than in the zones with crystals; the second Ti concentration is the less damaged zone (point number 2); and in the more damaged zone the Ti concentration is considerably lower (point number 1). This can be explained as the amorphous phase is a glassy phase basically formed by melted TiO_2 with solution of γ Al_2O_3 crystals, the best surface properties have been considered in the Ti rich zones; a

good distribution of the crystals into the amorphous phase increase the wear resistance of the material as is evident in the polished surface picture of the optical microscope where the susceptible zones are those where the Al_2O_3 crystals are concentrated; this is also evident in the pictures of the transversal section. It is because the harder phase (γ Al_2O_3) is well anchored to the matrix that the wear resistance increases in those zones.

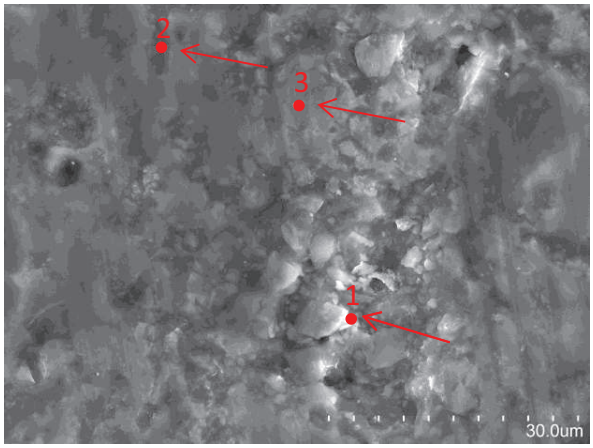

EDS Analysis point	% Ti
1	4.11
2	11.52
3	18.08

Figure 3.- SEM micrograph of the particular points analyzed via EDS.

The powder with original α phase after being subjected to high temperatures undergoes a transformation of α → γ (and others) depending on the time and temperature at which the powders are exposed. [3,5].

3.2 X-Ray Diffraction analysis

Figure 4 present the diffraction patterns obtained by XRD analyses and shows a partial transformation of the α- Al_2O_3 to γ- Al_2O_3 phase due to the APS process. The powders used for this process usually have an α phase but the alumina is a polymorphic material, and high temperatures favor phase transformation; high temperature into the flame provides the energy to carry out this transformation. It is possible that, depending on these conditions, other phases may appear [5].

The transformation from α→γ Al_2O_3 is due that the nucleation energy of γ-Al_2O_3 is lower than that of α-Al_2O_3, the gamma phase is a meta-stable form of Al_2O_3 and can exist due the melting and fast quenching.

As hardness of α- Al_2O_3 is higher than that of γ- Al_2O_3 it is possible that, by a partial transformation of this phase, wear resistance can increase when compared with coatings that present a full transformation.

The most representative peaks shown by this coatings through a general diffraction pattern (UNEX and ITS) are the peaks of γ-Al_2O_3 phase; the morphology of these peaks shows a high intensity and they are wider than the others; this is associated with a small crystal size. The peaks corresponding to the α-Al_2O_3 phase are narrower, indicating that the crystal dimension is bigger, this is due to the powders used to create the coatings; it is also possible that this powders grow when are subjected to high temperatures is in the sintered materials that shows a wide variation in carbide grain size with no apparent porosity. The larger carbide grains are due to coarsening that occurred during liquid phase sintering. [7, 17]. Other authors indicate that the size of the γ- Al2O3phase is smaller than α-Al_2O_3; according to this, it is also possible that the α-Al_2O_3 phase remains without transformation into a partially melted matrix of TiO_2 as the melting point of TiO_2 is lower than that for α- Al_2O_3 (1854 ºC y 2040 ºC respectively) [8]. TiO_2 does not appear in crystalline form after been applied as a coating with the APS technique; but the small peaks of $AlTiO_2$ and Al_2TiO_5 have been analyzed before by other authors. [3,8-9].

The contact areas between both powder oxides (Al_2O_3 y TiO_2) are important to be considered (it depends of the size particles); due to this a reaction between the components during the APS process, and the result of that reaction is AL_2TiO_5 .That is according with the phase diagram for Al_2O_3–TiO_2 but the creation of that phase has a negative effect in the hardness and toughness. [3,9-10].

According with the melting point of each phase and amount, usually TiO_2 melts first and due to the high cooling rate of the process is transformed in the amorphous phase that contains the crystalline particles of Al_2O_3.

The small quantity of TiO_2 indicates that it dissolves into Al_2O_3, contributing to the glassy phase with a lower melting point that results in the good inter-splat cohesion. [11].

A graphics presents the punctual analysis of the results of the amorphous and crystal concentration in the coating; an example of the diffraction patterns obtained in this study is shown in figure 4, where the micro-domains of crystal and amorphous phase can be appreciated.

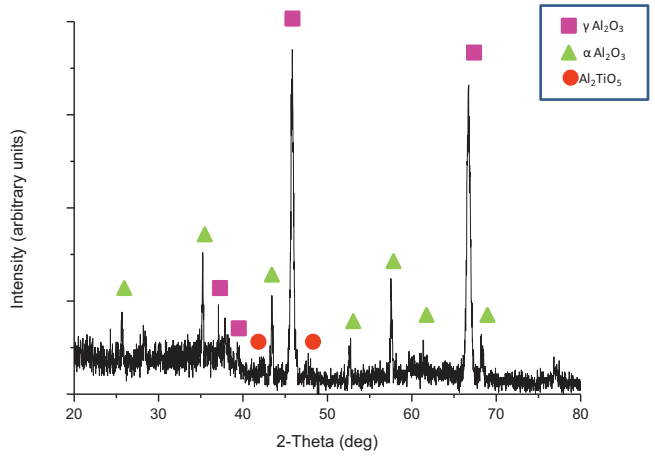

(a)

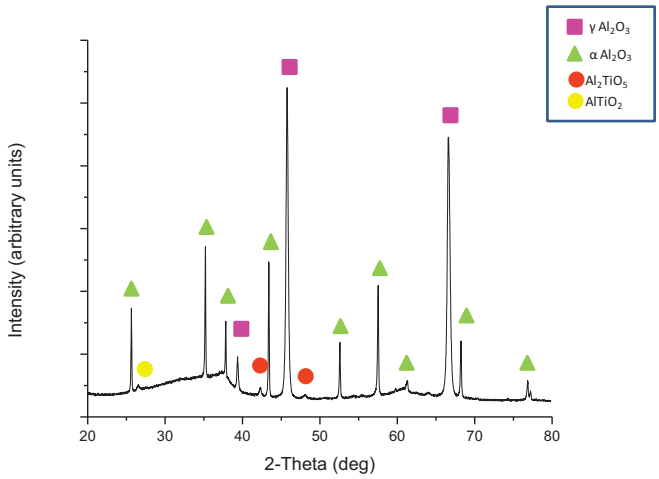

(b)

Figure 4. - XRD patterns realized with PHILIPS* X`Pert (a) and D8 ADVANCE Bruker (b).

3.3 Instrumented Indentation Test IIT

3.3.1 Hardness

The hardness values reported by other authors [2-3,8-9,11-12] present diverse grades, in a range from 10.78 GPa to 7.84 GPa (1100Kg/mm^2 -800Kg/mm^2). The most common value for these coatings is between 7.84 GPa - 8.82 GPa (800-900 Kg/mm^2), the reported hardness is usually performed with a Vickers indenter, where the geometry of the mark must satisfy some characteristics according with the ASTM C1327-03 [13]. The results found with IIT are reported in Table III, showing the used load, indentation depth, hardness and elastic modulus. This technique allows to avoid the substrate effect and gives a general idea of the material hardness. Since the standard deviation is within the tolerance these values must be considered for these kinds of coatings.

Table III.- Load conditions and results of IIT.

Depth of indentation mark (nm)	**Applied Load (mN)**	**Hardness (GPa)**	**Elastic Modulus (GPa)**
8697 ±155	8640 ±404	6.5 ±0.7	120 ±3

The results shows a lower hardness than that one reported by other authors which is coherent because the material is not a full sintered material and the presence of porosity and splat adhesion influence the real hardness of the material. Kear [9] reports a value around 8.33 GPa (850 Kgf/mm2) for α Al_2O_3 phase; considering the partial transformation from α → γ Al_2O_3 after APS process, where the γ Al_2O_3 phase is softer than α phase. The TiO_2 percent mixed in these coatings (Al_2O_3-13TiO_2) caused a decrease in hardness [8]; so the value may be appropriated.

The hardness value with IIT is lower than the one found by the classic microhardness Vickers technique (according to the ASTM C1327-03 standard), the found value after 25 indentations is 7.96 GPa (812 Kgf/mm^2).

3.3.2 Elastic modulus

With the IIT the elastic modulus has been calculated considering the general surface; the resulting 120 GPa is not so different from those reported earlier: 141 GPa and 100 GPa [1,11]. Then, considering the general surface the elastic modulus is close to the elastic modulus of glasses as is shown in table IV [14, 15]; this is another important remark as Young's modulus for ceramics is higher than that for glasses, therefore confirming the existence of a glassy (Amorphous) phase.

Table IV. - Room-Temperature Elastic Moduli, for Various Materials [14]

Material	Modulus of Elasticity (GPa)
	Metal Alloys
Tungsten	407
Steel	207
Nickel	207
Titanium	107
	Ceramic Materials
Aluminium oxide (Al_2O_3)	393
Spinel ($MgAl_2O_4$)	205
Mullite ($3Al_2O_3$-$2SiO_2$)	145
Glass-ceramic (Pyroceram)	120

4. - WEAR TEST

In the case of study at 650 N , the surface analysis at low magnifications, shows an apparently homogeneous surface. In a specific area where the surface presents a particular adhesion a semi-quantitative analysis has been carried out with the EDS (point 1), where the presence of iron on the surface confirms the adhesion of the pin to the coating.

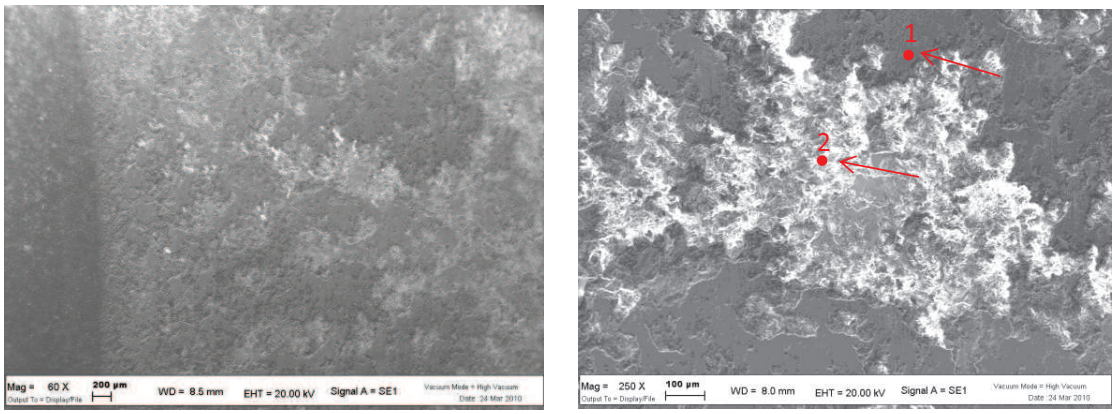

(a) (b)

Figure 5.- SEM micrograph of the damaged surface after the wear test.

Table V. - EDS Punctual Analysis of the wear surface.

EDS Analysis point	% O	%Al	%Ti	%Cr	%Fe
1	27.33	5.46	1.03	0.74	65.44
2	51.34	39.74	6.88	0.01	2.02

Another punctual analysis has been realized in a zone where the coating has been detached (point 2), and the results are reported in table V; the microanalysis confirms that the Al content is low, therefore, alumina crystals have been removed, and the Ti content is slightly lower than the nominal content, indicating that after crystal removal can exist zones where the surface has a good distribution of alumina and titania phases.

The presence of debris of a weak tribofilm [11] has been found in the surface, an image is presented in figure 6 where the main composition of this debris is Al. This shows evidence that the Al_2O_3 crystals are removed trying to create a tribofilm and that the possibility to interact with the Ti matrix and create a strong bond is not possible under sliding conditions.

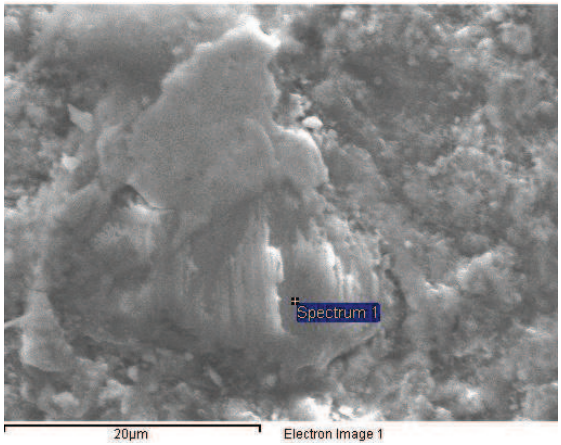

EDS Analysis	
O	49.84 (% Wt.)
Al	45.62 (% Wt.)
Ti	0.48 (% Wt.)
Fe	4.06(% Wt.)

Figure 6.- SEM micrograph of a wear debris analyzed via EDS.

In order to understand the effect of the load, the wear scar profiles on the disks have been analyzed and are presented in figure 7. The difference between the two tests is easy to appreciate in the figure where the load at 650N shows a deeper profile than 450 N. The peaks in the profiles manifest the presence of material derived from the steel pin adhered onto the surface; previously analyzed with SEM.

The evidence of the loose material from the pin is presented in the table VI where the differences of length (Δl) and weight, before and after wear test were measured.

To calculate the wear rate the used relation appears in eq (1):

$$\text{Wear rate} = \frac{V\ \text{loss}}{Fn\ d} \qquad (1)$$

That is the ratio between the volume of material removed by wear (Vloss) and the product of the normal load applied on the specimen (Fn) and the sliding distance (d) [16].

Table VI. - Mean values of losing material of the pin and wear rate

Test	Δl (mm)	Lose weight (g)	Wear rate (mm^{-3}/Nm)
650N	1.36	0.29	7.835E-6
450	0.48	0.1	3.994E-6

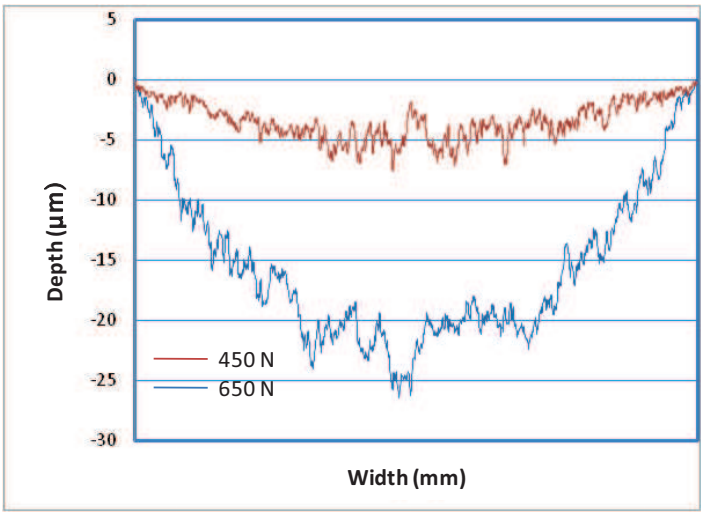

Figure 7. - Wear scar profiles of the disks under different normal load conditions.

5. - CONCLUSIONS

The material analysis shows that a good distribution of the crystalline phase into an amorphous matrix presents a homogeneous surface that looks more resistant than the crystal rich zones; the zones where the amorphous matrix is pour are the zones prone to start the pull out of a coating. The differences in intensity and peaks between diffraction patterns, show the presence of zones where it is possible to find different concentration phases, and these differences in structure and composition affect the wear behavior of the coating, demonstrating the existence of weaker areas.

The wear behavior of Al_2O_3-13TiO_2 under dry conditions, depend on the applied load. The main process is an adhesive wear from the pin to the surface. At high loads the coating undergoes abrasive wear trying to create a weak tribo-film.

ACKNOWLEDGEMENTS

The authors would like to thank Zocca Officine Meccaniche (Funo, BO) for the thermally sprayed coating manufacturing. And to Prof. Fernando Guiberteau and the GEMA group of University of Extremadura for the opportunity of the stage. And Prof.

Carmela Vaccaro and her geology group for their interest, help and advices. And thanks to Prof Florentino Sanchez for his patient and invaluable help.

REFERENCES

1) V. Fervel, B. Normand, C. Coddet, (1999), "Tribological behavior of plasma sprayed Al_2O_3-based cermet coatings", Wear, Vol 230, pp70-77
2) R.S. Lima, B.R. Marple, (2004), "Superior performance of high-velocity oxyfuel.sprayed nanostructured TiO_2 in comparison to air plasma sprayed conventional Al_2O_3-13TiO_2", Journal of Thermal Spray Technology, Vol 14, pp 397-404
3) C. Monticell, A. Balbo, F. Zucchi, (2011), "Corrosion and tribocorrosion behaviour of thermally sprayed ceramic coatings on steel", Surface and coatings technology. Vol 205, pp 3683-3691
4) K. A. Gross, C. C. Brendt, H. Herman, (1997), "Amorphous phase formation in plasma-sprayed hydroxyapatite coatings", Journal of biomedical materials research, Vol 39, No3, pp 407-414
5) M. Uma Devi, (2004), "New phase formation in Al_2O_3-based thermal spray coatings", Ceramics International, Vol. 30, pp 555-565
6) ASTM, (2005), Standard Test Method for Wear Testing with a Pin-on-Disk Apparatus. G99-05".
7) D. Louër, (2000) "Use of pattern decomposition to study microstructure: practical aspects and applications", Defect and microstructure analysis by diffraction; International Union of Crystallography, Oxford science publications, pp 673-697
8) R. Yilmaz, A.O. Kurt, A. Demir, Z. Tatli, (2007), "Effects of TiO_2 on the mechanical properties of the Al_2O_3-13TiO_2 plasma sprayed coating", Journal of the European Ceramic Society. Vol 27, pp 1319-1323
9) B. H. Kear, Z. Kalman, R. K. Sadangi, G. Skandan, J. Colaizzi, W.E. Mayo., (2000)., "Plasma-Sprayed Nnostructured Al_2O_3/TiO_2 Powdwes and Coatings", Journal of Thermal Spray Technology, Vol 9, No.4, pp 483-487

10) K.A.Habib, J.J. Saura, C. Ferrer. M.S. Damra, E. Gimenez, L. Cabedo., (2006)., "Comparison of flame sprayed Al_2O_3/TiO_2 coatings: Their microstructure mechanical properties and tribology behaviour", Surface and coatings technology, Vol. 201, pp. 1436-1443.

11) G. Bolelli, V. Cannillo, L. Lusvarghi, T. Manfredini., (2006), "Wear behaviour of thermally sprayed ceramic oxide coatings", Wear, Vol 261, pp 1298-1315.

12) C. Giolli, M. Turbil, G.Rizzi, M. Rosso, A. Scrivani, (2009), "Wear resistance improvement of small dimension invar massive molds for CFRP components", Journal of Thermal Spray Technology, Vol 18, pp 652-664

13) ASTM, (2003), Instrumented Indentation Testing. ASTM Committee E28 on Mechanical Testing

14) W. D. Callister Jr. (2000), "Fundamentals of material science and engineering / an interactive e-text", Wiley, pp 154.

15) A. Leyland, A. Matthews, (2004), "Design criteria for wear-resistant nanostructured and glassy-metal coatings", Surface and Coatings Technology, Vol 177-178, pp 317-324

16) M. Merlin, C. Soffritti, R. Vazquez, V. Mazzanti, G. L. Garagnani, (2011) "Analytical treatment of uncertainties for a macroscopic tribology instrumentation" proc. of the 8th International workshop on CETAS, OC57 pp. 383-390

17) S.F. Wayne, S.Sampath, (1992), "Structure/Property Relationships in Sintered and Thermally Sprayed WC-Co", Journal of Thermal Spray Technology, Vol 14, pp 307-315

Article D

MICROSTRUCTURAL HOMOGENEITY BETWEEN APS AND HVOF WC-12Co COATINGS

Reyna Vazquez

Engineering Department
University of , Via Saragat 1,
44122 Ferrara
Italy

Preprint 2012

ABSTRACT

WC-12Co coatings applied by APS and HVOF have been studied in order to understand the heterogeneity in its microstructure. Two coatings has been applied on steel plates, using APS and HVOF technique, the size particle of the feedstock powders vary depending of application technique, between -88+44μm to -45+15μm respectively. The used techniques for characterize the coatings were: Optical microscopy (OM), Scaning Electronic Microscopy (SEM), X- Ray Diffraction (XRD). The analysis shows that the coatings present zones with different crystal concentration. The importance of this studio can help to establish levels of efficiency and quality of the coatings.

Keywords: crystal, amorphous phase, powder transformation.

1.- INTRODUCTION

The industrial coatings used for a wide range of applications that includes the aerospace and other industrial markets serves several purposes; like wear, thermal and corrosion protection [1]. They also permit to lighten the materials in order to improve quality and extend the operative life. In particular WC-12Co coatings have been used extensively in many applications as a wear resistant surface. One of the main uses is on die casting molds. Many studies have been carried out studying the coating properties depending on particle size, parameters of application, and application technique. The results indicate that depending on the final use of coatings the microstructure is the responsible for the service conditions. [2]These kinds of coatings due to the characteristics of the feedstock powders, application and process present many imperfections like: porosity, internal stress, thickness control, etc. that can affect the failure of the part. This study can help to select the best coating option according to characteristics dependent on the application. In friction processes it has been found that the WC-12Co applied with HVOF process presents the best results due to the uniform distribution of the coating onto the applied surfaces [3], even when in these cases the microstructure is not perfectly uniform.

2. - MATERIALS AND METHODS

The materials used in this study are composites; In this case mixtures of powders are combined to create a coating to protect a steel surface. The coated geometry is a cemented steel plate (75 mm in diameter and 6 mm in thicknesses) the composition of the disk is shown in Table I. The studied coatings are WC-12Co applied with APS and HVOF techniques. The feedstock powder characteristics are given in Table II.

Table I. - Chemical composition (wt. %) of the steel substrate and pin.

	C	Mn	Ni	Cr	Si	Cu	Mo	S	Fe
Coated plate steel	0.22	0.88	0.87	0.84	0.30	0.20	0.06	0.03	Balance
Pin steel	0.23	0.86	0.95	0.91	0.26	0.10	0.06	0.02	Balance

Table II. - Chemical composition and characteristics of the feedstock powders.

	WC-12Co APS	WC-12Co HVOF
Type	Amperit 515.2 by H.C. Stark	WOKA 3102 by Sulzer Meteco
Forming Process	Sintered	Agglomerated and sintered
Composition	4.2 %C, 11.2 %Co, 0.8 %Fe, balance W	5.38 %C, 11.99 %Co, 0.4 %Fe, balance W
Particle dimension (µm)	-88+44	-45+15

The microstructural characterization of the coatings has been carried out in an optical microscope. The microstructure of the samples were also observed by Scanning Electron Microscope (SEM), samples were observed in as received and polished conditions, for the last condition the samples were prepared using abrasive paper from 800 to 1200 grid and after the samples had been polished with a cloth and diamond solution from 9µm to 1µm, the samples were observed in surface and transversal section. The SEM equipped with Energy Dispersion Spectroscopy (EDS) has been used to analyze the chemical composition. The Diffraction analysis has been realized in Badajoz, Spain in Universidad de Extremadura in a high-resolution diffractometer D8 ADVANCE Bruker using a Cu Kα radiation (λ= 1.54183Å), with an intensity scanner vs. diffraction angle between 20° and 80° (step size of 0.02°), time count 3 s/step. A micro XRD analysis has been carried out in Ferrara Italia in a high resolution X-Ray diffractometer X'Pert Pro MRD XL PANalytical, with the next parameters: Cu Kα radiation (λ= 1.540598 Å), with an intensity scanner vs. diffraction angle between 15° and 80° (step size of 0.0001°), time count 3 s/step. Voltage 40 kV, Current 40mA. This analysis has been carried out on the entire surface creating a matrix array of 49 points (7x7).

To evaluate the hardness and elastic modulus of coatings an instrumented indentation testing (IIT) has been performed. The test has been carried out in a Nanotest, Micro Materials Ltd., Wrexham, UK, with a Berkovich diamond indenter; 49 indentations in a

matrix array of 7 x 7; with a distance between them of 395 μm were made on the surface for each sample, the velocity of the applied load was 350 mN/s, the load was calculated by the machine in order to obtain a depth impression not greater than 10 μm to avoid the substrate hardness influence; the maximum load permanence onto the surface was 10 s. Another hardness test has been carried out with a micro-hardness Tester FM Future-Tech and a load of 300 gr.

3. - RESULTS AND DISCUSSION

3.1 Microstructural Characterization

The microstructure of these two coatings applied with APS and HVOF process at glance present very different structures as shows in the images (a) and (b) of figure 1 respectively. The microstructure belongs to the surface of the coatings in as received condition.

The microstructure of thermally sprayed WC-Co is strongly dependent on powder characteristics and processing conditions [4]. Due this the coatings present a great differences in the surface since the presence of an important porosity and low dens surface in the APS case; while in the HVOF process the surface present a very dense surface with a minimum porosity almost not visible in image b.

At higher magnifications the discontinuities in the surface for APS case are more evident also the presence of fractures and the presence of molten and unmolten areas that depend of the plasma intensity [5]. While in the HVOF case, also, at the same magnifications, the surface present a uniform and dense microstructure with a low porosity and where the finishing signs are still evident as in the image b.

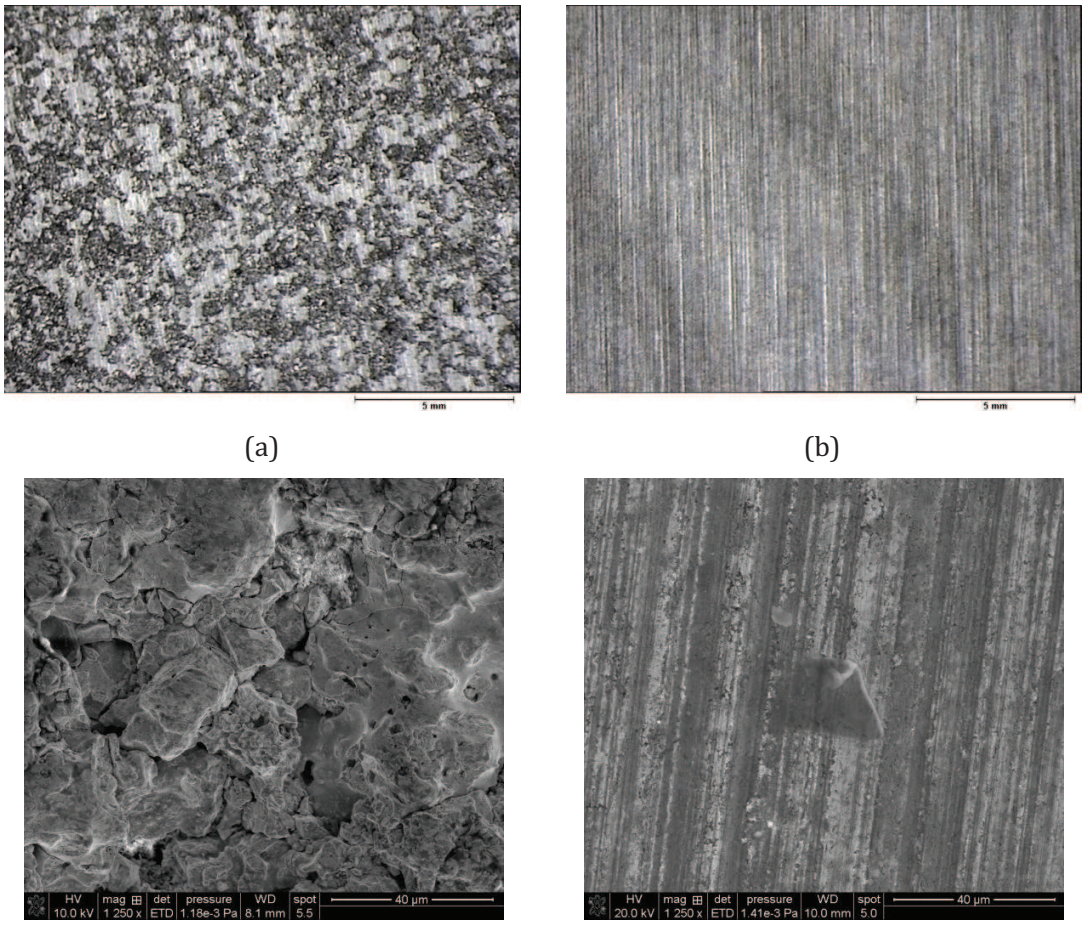

(a) (b)

(c) (d)

Figure 1. - Coating In as received condition, OM image (a and b) and SEM images (c and d). Detail of the finishing process, porosity and chipping in the surface of coatings, for APS (a and c) and HVOF (b and d) process.

The transversal section after polishing showed in figure 2 (a and c) for APS and (b and d) for HVOF respectively present in both cases an excellent adhesion with the steel surfaces. Some impurities due the previous process of the surface preparations are visible in the boundary between the metal and the coating.

The coatings present the same characteristics as in the surface for APS; and an important interconnects porosity and discontinuities in thickness of transversal section. In the HVOF in image (d) the porosity is visible but in less quantity than in APS process; some of the voids are due the sample preparation, presenting the chipping phenomena.

In the image (d) is possible to observe the typical microstructure, of lamellar splats for WC-12Co coatings applied with HVOF process.

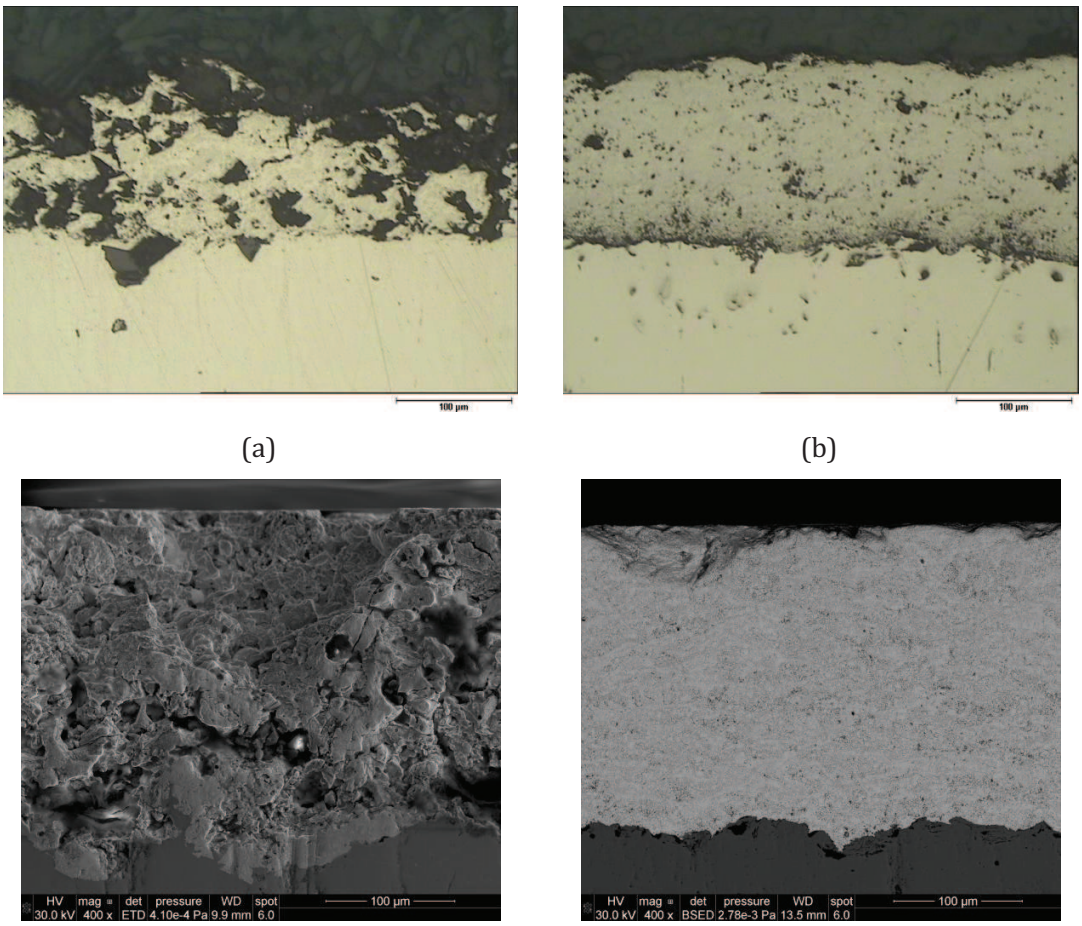

(a) (b)

(c) (d)

Figure 1. - Coating In as received condition, OM image (a and b) and SEM images (c and d). Detail of the transversal section, porosity and chipping, for APS (a and c) and HVOF (b and d) process.

At higher magnifications in the transversal section it is possible to observe that the microstructure is constituted by WC grains embedded into the Co-rich binder phase. The grains in the WC-Co material exhibit various shapes of WC, from truncated trigonal prism to triangular prisms, which are growth morphologies kinetically determined depending on the C content. The dependence of WC grain shape on the C content is attributed to an asymmetric occupation of carbon atoms in the crystal

structure of WC [6]. In figure 2, images (c) and (d), is easy to appreciate the differences in morphology of the carbides, between the round carbides in APS, and angular ones in HVOF. According to that is possible to hypothesize that the degree of decarburization is lower in the second process.

The APS process shows round pores due to the gas produced during the application process [7]. The limits between the not fully melted particles are also visible and the carbide morphology present a columnar and deformed morphology, in figure (c) the partial dissolved carbide morphology varies in size and shape.

The HVOF process shows large surfaces with densely packed fine carbide particles in the binder phase, smaller areas present an imperfection of a low concentration of the amorphous phase that can be produced for a lack of fusion during the spraying process.

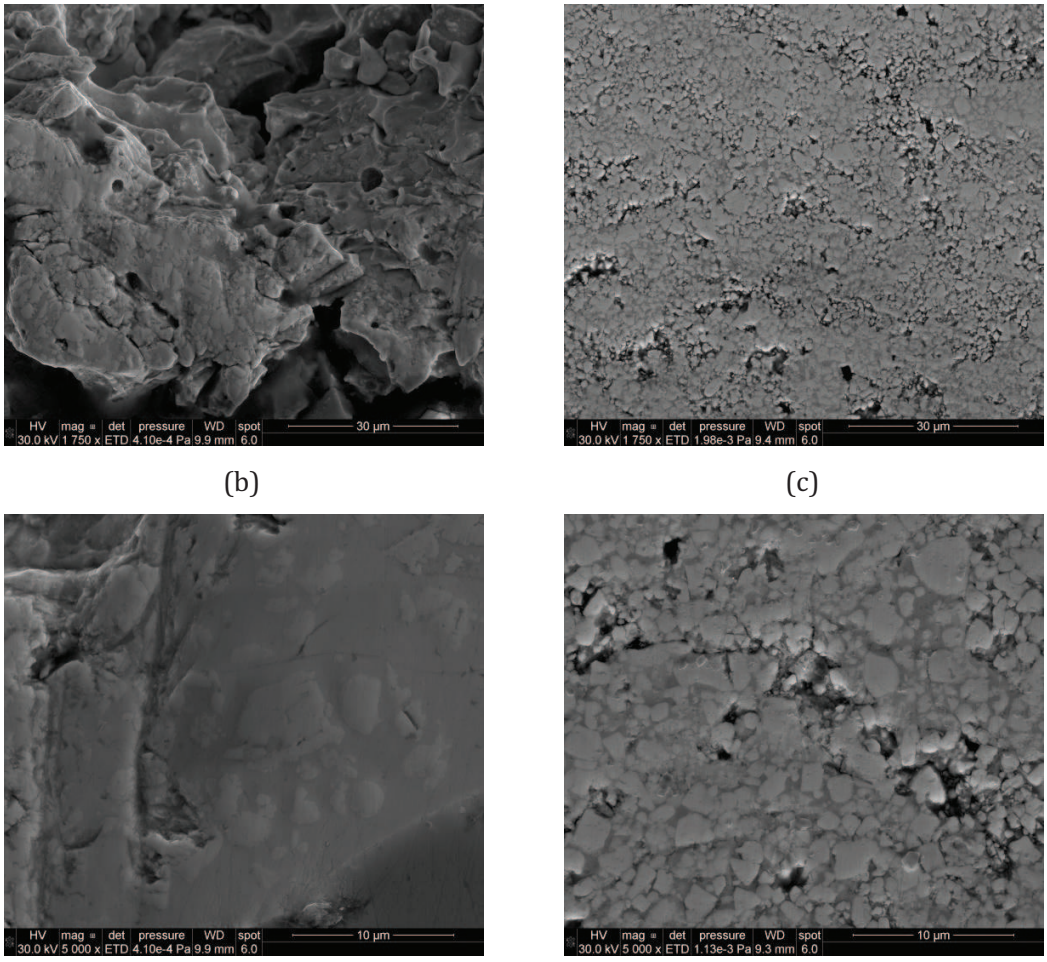

Figure 2.- SEM micrograph of polished surface of the transversal section for APS (a) and HVOF (b) process

An EDS analysis for APS coating has been performed, the results has been presented in the table III and it shows that in the point 1 the crystal composition is almost fully WC. The low Co content can be the background influence. The general analysis in the point 2 shows that the microstructural composition is rich in the Co content and the WC is lower than the nominal, it can be due that the selected area has not a uniform distribution of crystals and the Co concentration is higher than in other zones.

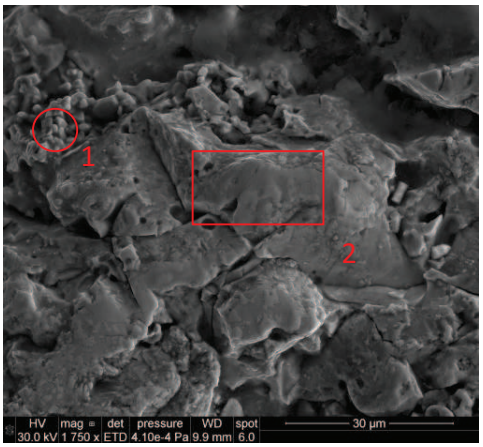

Figure 3.- SEM micrograph for WC-12Co APS process for the particular points analyzed via EDS.

Table III. - EDS analysis for APS coating.

EDS Analysis point	% C	%O	%Co	%W
1	13.39	3.16	2.58	80.87
2	3.56	0.47	15.43	80.54

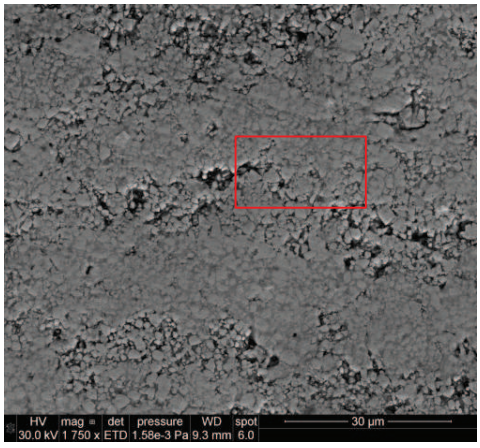

Figure 4. - SEM micrograph for WC-12Co APS process for the particular points analyzed via EDS.

Table IV. - EDS analysis for HVOF coating.

EDS Analysis	% C	%O	%Co	%W
	3.90	0.96	12.20	82.94

The results of the analyses carried out for the HVOF process show a more homogeneous composition, closer to the nominal one. The results are reported in Table IV and the selected area for the analysis is pictured in figure 4.

3.2.- X-Ray Diffraction analysis

The XRD analyses presents the general diffraction patterns in figure 5 that shows decomposition due decarburization of the WC-12Co. WC contains 6.13% C and has a microhardness of about 24 GPa, while W_2C contains 3.16% C and has a microhardness of about 30 GPa, but is more brittle than WC [8]. The importance in the decarburizing control is clearly related to the foregoing.

The decarburization increases, in a significantly way, in the APS coating, due to the higher temperature used in the process.

According to Verdon et al. an index of crystallinity *I* can be defined, connected with the fraction of the crystalline phases. I= 100% in the powder grains and it is smaller in the coatings in which a nanocrystalline binder has appeared during spraying The higher the amount of transformation, the lower the index of crystallinity.

The intensity in peaks is lower for APS than for HVOF process. The relative intensity of the diffraction peaks is determined from the structure factor of the unit cell. A reduction in the intensity of the peaks of WC denotes a reduction in the volume fraction of the primary carbide. Thus, a higher decomposition of WC, in the APS process. The W_2C/WC ratio increases as decarburization increases [9]. And a diminution in the intensity of the peaks and the increase of peaks quantity for W_2C in the APS process compared with HVOF; just with the analysis of diffraction patterns, confirms a greater decarburization for APS process.

The type and amount of structural disorder can greatly affect the relative intensity of the diffraction peaks. Doing a comparison between the differences in intensity is possible to do an estimation of proportions of different phases [10]. Thus the higher

intensity in HVOF shows more order in the distribution of phases in the coating and according with the identified peaks less transformation and higher crystal content. The mix of the Co amorphous phase with a mix of decomposed carbides weakens the binder phase. In rolling contact fatigue (RCF), an increase in Co content applied by HVOF process present good surface characteristics and results in the best coatings for applications involving RCF [11].

The absence of the Co peaks is related to almost all the metallic cobalt transformed into amorphous / nanocrystaline binder phase, diffraction haloes in 2θ values of approximately 34° and 50° indicate its presence. [3,7,12-16].

As has been explained above, the final characteristics of those materials depend on many parameters, like APS and HVOF spraying conditions, powder characteristics, size particle characteristics, etc.

In order to analyze the characteristics of the material with a non destructive technique is possible to analyze the samples creating a mapping of the surface in order to observe the surface homogeneity. With the XRD patherns reported in appendix ii for APS and iii for HVOF it is possible to observe the microstructural situation and establish the grade of microstructural uniformity.

The XRD patterns for APS show a lower intensity in all cases, as expected. In other cases, the presence of W_2C and the differences in microstructure are considerable, while for HVOF the analysis shows less dispersion in intensity and broadening.

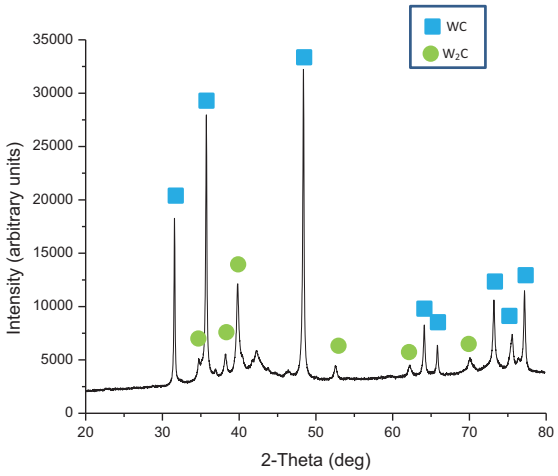

(a)

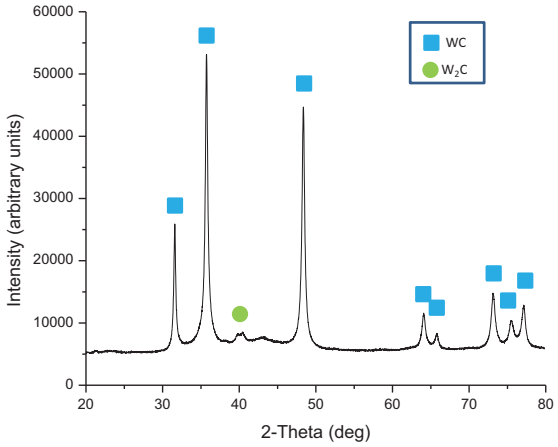

(b)

Figure 4. - XRD patterns realized with D8 ADVANCE Bruker. For APS (a) and HVOF (b) process.

3.3 Instrumented Indentation Test IIT

3.3.1 Hardness

The hardness values reported for other authors [5-7, 11,17] for the APS process and [11-14, 16, 18,] for HVOF process varies from 6.17-9.86 GPa (630-1000 Kg/mm^2), and 10.75-14.70 GPa (1097-1500 Kg/mm^2) respectively; the reported hardness is usually performed with a Vickers indenter, where the geometry of the mark must satisfy some characteristics according with the ASTM C1327-03 [19]. For both processes is

possible to follow the standard but in the case of APS process the porosity influence greatly the hardness behavior. Following the ASTM standard the hardness found for APS was around 1076.3 and for HVOF 1047.6.

For measurements were APS process was employed, to find proper zones for measurements is complicate due do to the surface characteristics; an image of the Vickers test in APS is showed in the figure 5. In the image it is possible to appreciate the influence of porosity, cracks and the amorphous bonding phase that shows a ductile behavior by not developing cracks after indentation test. The results found with IIT are reported in Table III, which shows the load used, the indentation depth, the hardness and elastic modulus. This technique allows avoiding substrate effect and gives a general idea of the material hardness. The standard deviation is considerable for the APS process but it is clearly influenced by the morphology of the very porous surface

Table III. - Load conditions and results of IIT.

Process	Depth of indentation mark (nm)	Applied Load (mN)	Hardness (GPa)	Elastic Modulus (GPa)
APS	9770 ±513	6214 ±1218	3 ±1	101 ±18
HVOF	8280 ±343	9637 ±852	8 ±2	171 ±11

The results for APS process shows an important lower hardness than that one reported for other authors but is coherent because the material is inhomogeneous with an important porosity, and splat adhesion that influence the real hardness of the material. For HVOF process the Hardness is lower but the differences with those reported for other authors the difference can be attributed to the parameter's process The hardness value with IIT is lower than that one find it using the classic microhardness Vickers technique (according to the ASTM C1327-03 standard), the found value after 25 indentations for APS is 10.55 GPa (1076.3 Kgf/mm^2) and for HVOF is 10.27 GPa (1047.6 Kgf/mm^2).

The hardness of coatings is related to decarburization, were WC transforms to W_2C.

On melting, the Co would wet the WC grains thus preventing direct contact with the gas phase. As a WC-Co powder particle enters the hot gas its temperature increases and the Co phase will begin to melt (pure Co melts at 1768 K) after a relatively short time. Once the Co is molten WC will begin to rapidly dissolve in it and the 1773 K isothermal section of the Co- W-C phase diagram calculated by Guillermet [20] indicates that at this temperature approximately 30 wt% W and 2.5 wt% C can dissolve. Furthermore, as a particle's temperature continues to increase more WC will dissolve. The liquidus surface projection calculated by Guillermet is shown in figure 6, and the estimated isotherms shown suggest that at 2273 K molten Co in equilibrium with WC could contain 50±60 wt% W and 3±3.5 wt% C. [stewart microstructural evolution]

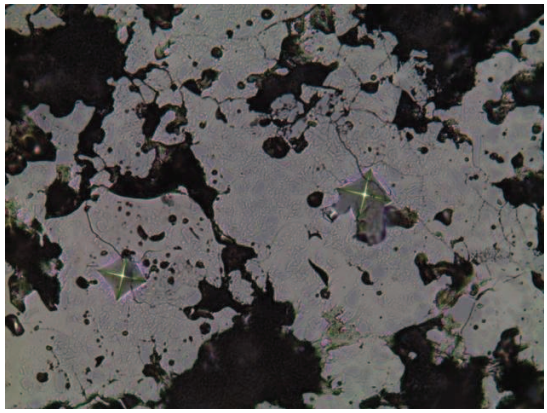

Figure 5. – Micrograph of hardness indentation after the hardness Vickers test for APS (500X).

Stewart et al. discus about that, the oxidation of carbon to CO is the most favorable reaction at temperatures when the Co phase is molten (i.e. > 1768 K). Therefore, the decarburization of a powder particle will be expected to proceed as follows: the cobalt will melt and WC will dissolve into the liquid as the temperature rises. Carbon will be removed from the melt either by reaction with oxygen at the melt/gas interface or through oxygen diffusion into the rim of the molten particle, leading to CO formation. However, removal of carbon, locally, from the melt will drive further dissolution of WC grains in this shell region as the system attempts to re-establish local equilibrium

at the WC-melt interface. The overall result will be WC grains which are considerably less angular in the outer shell regions (due to dissolution), a reduced WC volume fraction compared with the central regions of the particles, and a W:C atomic ratio in the melt greater than the unity.

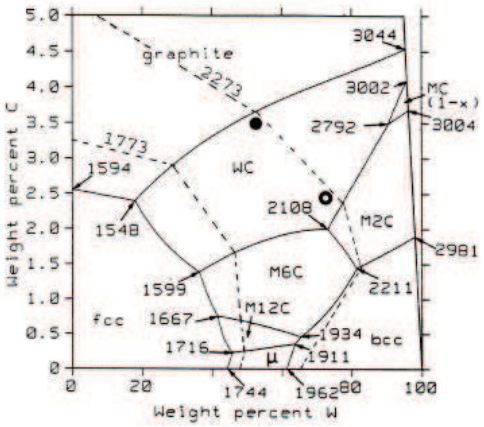

Figure 6.- The projection of the liquidus surface of the Co-W-C system.

3.3.2 Elastic modulus

With the IIT the elastic modulus has been calculated considering the general surface; the result is 101 GPa for the APS process and 171 GPa for the HVOF process, in both cases lower than that for ceramics. Then, considering that the elastic modulus for the general surface is closer to the elastic modulus of glasses and metals like aluminum [21-22]; is another important remark because of the Young's modulus for ceramics is higher than for glasses, thus confirming the existence of a glassy (Amorphous) phase.

The images for the IIT for both processes are shown in figure 7. The differences in the hardness marks show in a clear way the differences in the homogeneity of the two surfaces and the influence of the porosity in order to find specific areas as was done with the Vickers hardness test.

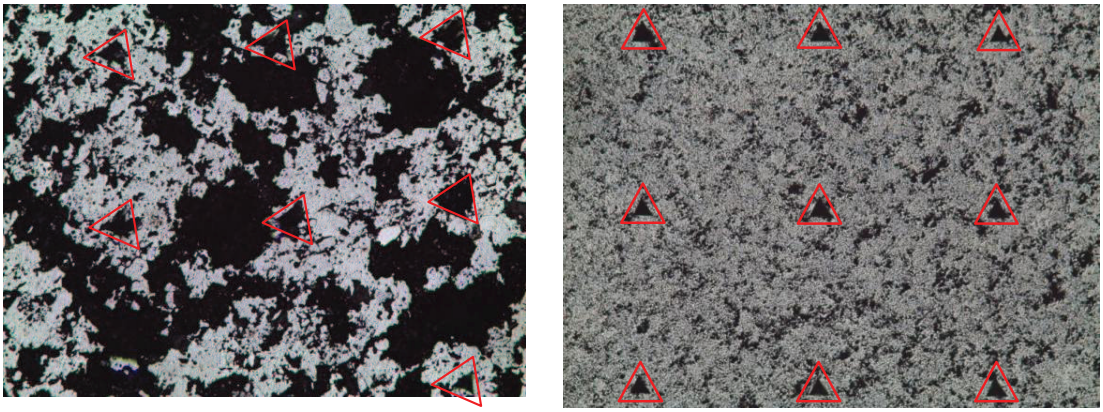

(a) (b)

Figure 7.- Micrograph of part of the matrix array for IIT for APS (a) and HVOF (b) process (100X)

4. - WEAR TEST

A wear test using a pin in Al_2O_3-13TiO_2 has been carried out just on the HVOF coating. The wear mechanism found, according to the morphology of the wear scars, was fully abrasive due the pin of agglomerated structure. A particular analysis of the worn surface with XRD shows the micro-domains in the coating. A specific analysis using particular points before and after the wear test can give more information in the structure deformation after a wear process.

5. - CONCLUSIONS

The material analysis shows that a good distribution of the crystalline phase into an amorphous matrix presents a homogeneous surface that looks more resistant than the rich crystal zones.

The differences between diffraction patterns, in intensity and peaks, show the presence of zones where micro-domains with higher transformation exist, particularly in the APS process and those zones depend on the application parameters used.

For these kinds of coatings, is important to control the transformation of the primary WC crystals as it improves the wetting and grip effect for the crystals into the binder amorphous phase. Also, the presence of W_2C contributes to create a fragile coating.

When less pure Co is used as a binder matrix, the properties of the coating decrease.

With the improved Micro-XRD technique an analysis of a wear surface can be useful to see the effect of wear mechanisms.

ACKNOWLEDGEMENTS

I would like to thank Prof. Fernando Guiberteau and the GEMA group of University of Extremadura for the opportunity of the stage. And Prof. Carmela Vaccaro and her geology group for their interest, help and advices. And thanks to Prof Florentino Sanchez for his patient and invaluable help.

REFERENCES

1) J. Nerz, B. Kushner, A. Rotolico, (1992), "Microstructural Evaluation of Tungsten Carbide-Cobalt Coatings", Journal of Thermal Spray Technology, Vol 1, pp 155-160
2) V. Chawla, B. Singh Sidhu, D. Puri, S. Prakash, (2008) "State of the art: plasma sprayed nanostructured coatings: a review", Materials Forum, Vol 32, pp 137-143.
3) H. Liao, B. Normand, C. Coddet, (2000), "Influence of coating microstructure on the abrasive wear resistance of Wc/Co cermet coatings", Surface and coatings Technology, Vol 124, pp 235-242
4) S.F. Wayne, S.Sampath, (1992), "Structure/Property Relationships in Sintered and Thermally Sprayed WC-Co", Journal of Thermal Spray Technology, Vol 14, pp 307-315
5) V. Bonache, M. D. Salvador, J. C. García, E. Sánchez and E. Bannier, (2011), "Influence of Plasma Intensity on Wear and Erosion Resistance of Conventional and Nanometric WC-Co Coatings Deposited by APS", Journal of Thermal Spray Technology, Vol 20, 549-559
6) S. Kim, S-H Han, J-K Park, H-E Kim, (2003), "Variation of WC grain shape with carbon content in the WC-Co alloys during liquid-phase sintering", Scripta Materialia, Vol 48, pp 635-639.
7) G. Di Girolamo, (2009), "Tribological Characterization of WC-Co Plasma Sprayed Coatings", Journal of American Ceramic Society 92, pp 1118-1124.

8) P.Ctibor, M. Kašparová, J. Bellin, E. Le Guen, F. Zahálka, (2009), "Plasma Spraying and Characterization of Tungsten Carbide-Cobalt Coatings by the Water-Stabilized System WSP", Advances in Materials Science and Engineering, Vol 2009, pp 1-11

9) J.M. Guilemany, S.Dosta, J. R Miguel, (2006), "The enhancement of the properties of WC-Co HVOF coatings through the use of nanostructured and microstructured feedstock powders", Advances in Surface &Coatings Technology 201, pp 1180-1190

10) E. E. Fullerton, I.K. Schuller, (1992), "Structural refinement of superlattices from x-ray diffraction", Physical Review B , Vol 45, pp 9292-9310

11) R. Nieminen, P. Vuoristo, K. Niemi, T. Mantyla, G. Barbezat, (1997), "Rolling contact fatigue failure mechanisms in plasma and HVOF sprayed WC-Co coatings", Wear, Vol 212, pp 66-77.

12) D.A. Stewart, P.H. Shipway, D.G. Mc Cartney,(2000)," Microstructural evolution in thermally spayed WC-Co coatings: comparison between nanocomposite and conventional starting powders", Acta Materialia 48, pp 1593-1604

13) D.A. Stewart, P.H. Shipway, D.G. Mc Cartney, (1999), "Abrasive wear behaviour of conventional and nanocomposite HVOF-Sprayed WC-Co coatings", Wear 225-229, pp 789-798

14) A. C. Bozzi, J. D. Biasoli de Mello, (1999), "Wear resistance and wear mechanisms of WC-12%Co thermal sprayed coatings in three-body abrasion", Wear 233-235, pp 575-587

15) C. Verdon, A. Karimi, J. L. Martin, (1998), "A study of high velocity oxy-fuel thermally sprayed tungsten carbide based coatings. Part 1: Microstructures", Materials Science & Engineering, A246, pp 11-24

16) P.H. Shipway, D.G. Mc Cartney, T. Sudaprasert, (2005), "Sliding wear behaviour of conventional and nanostructured HVOF sprayed WC-Co coatings", Wear 259, pp 820-827

17) A. Koutsomichalis, N.M. Vaxevanidis, G. Pertropolos, A. Mourlas, S.S. Antoniou, (2008), "Friction, Wear and Mechanical Behaviour of Plasma Sprayed WC-

12%Co Coatings on Mild Steel" Proceedings of the 7th International Conference The Coatings in Manufacturing Engineering, pp 259-268

18) P. Chivavibul, M. Watanabe, S. Kuroda, K. Shinoda, (2007), "Effects of carbide size and Co content on the microstructure and mechanical properties of HVOF-sprayed WC-Co coatings", Surface & Coatings Technology, Vol 202, pp 509-521

19) ASTM, (2003), Instrumented Indentation Testing. ASTM Committee E28 on Mechanical Testing

20) A.F.Guillerment, (1989), "Thermodynamic Properties of the Co-W-C System", Metallurgical Transactions, 20A, pp 935-956

21) W. D. Callister Jr. (2000), "Fundamentals of material science and engineering / an interactive e-text", Wiley, pp 154.

22) A. Leyland, A. Matthews, (2004), "Design criteria for wear-resistant nanostructured and glassy-metal coatings", Surface and Coatings Technology, Vol 177-178, pp 317-324

APPENDIXES

XRD Patterns for Al_2O_3-13TiO_2

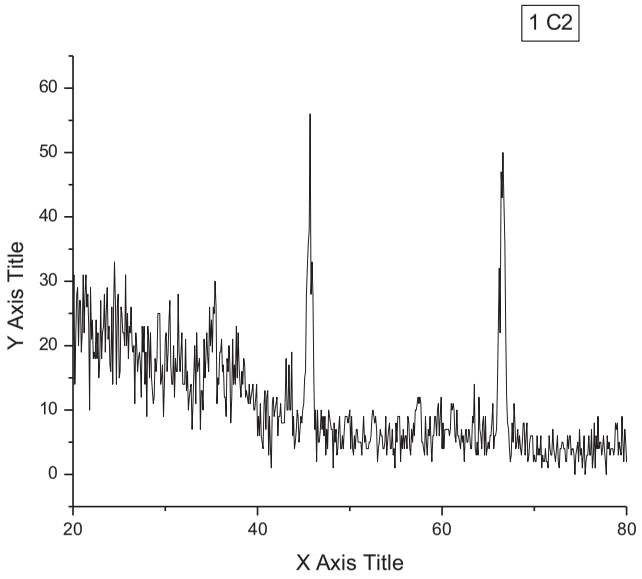
1 C2
Y Axis Title
X Axis Title
0
10
20
30
40
50
60
20
40
60
80

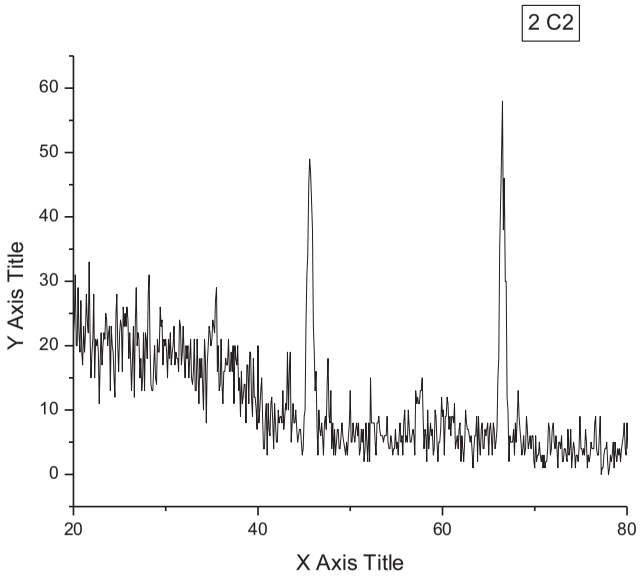
2 C2
Y Axis Title
X Axis Title
0
10
20
30
40
50
60
20
40
60
80

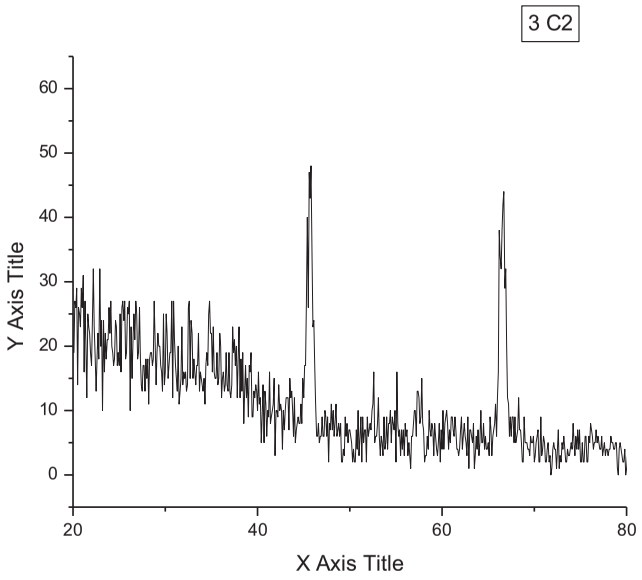
3 C2
Y Axis Title
X Axis Title
0
10
20
30
40
50
60
20
40
60
80

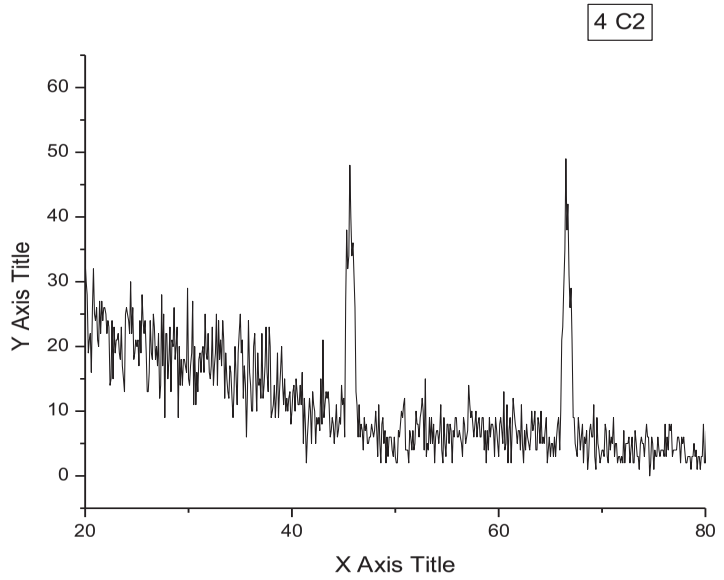
4 C2
Y Axis Title
X Axis Title
0
10
20
30
40
50
60
20
40
60
80

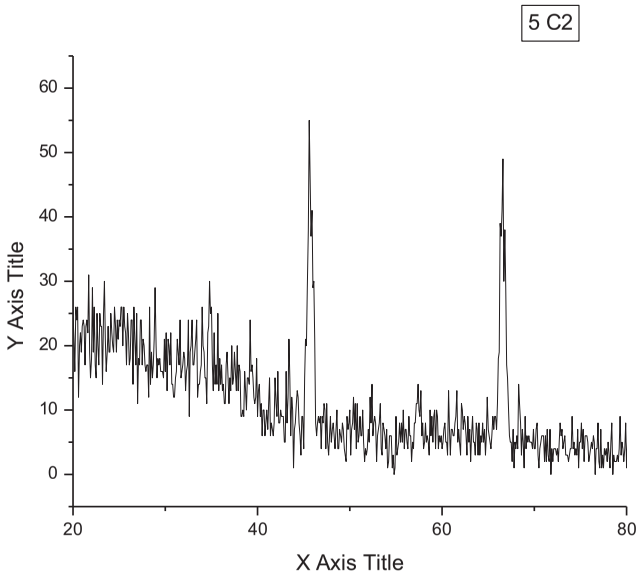
5 C2
Y Axis Title
X Axis Title
0
10
20
30
40
50
60
20
40
60
80

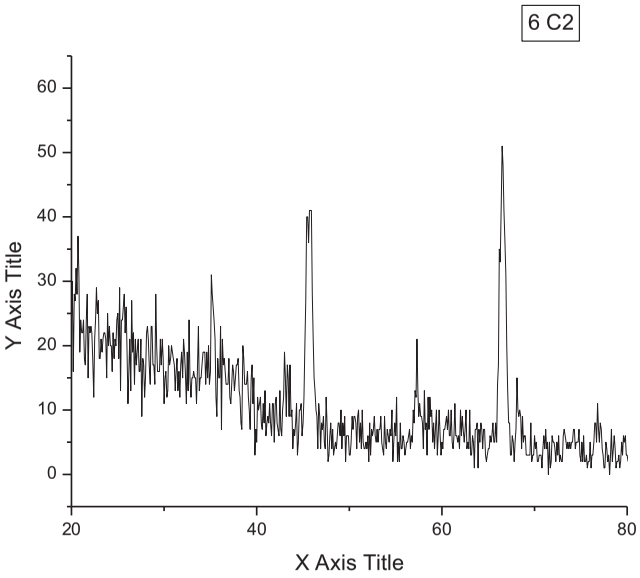
6 C2
Y Axis Title
X Axis Title
0
10
20
30
40
50
60
20
40
60
80

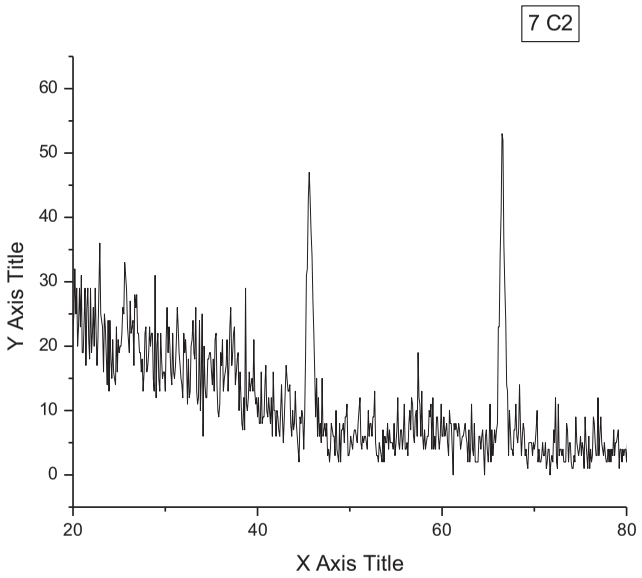
7 C2
Y Axis Title
X Axis Title
0
10
20
30
40
50
60
20
40
60
80

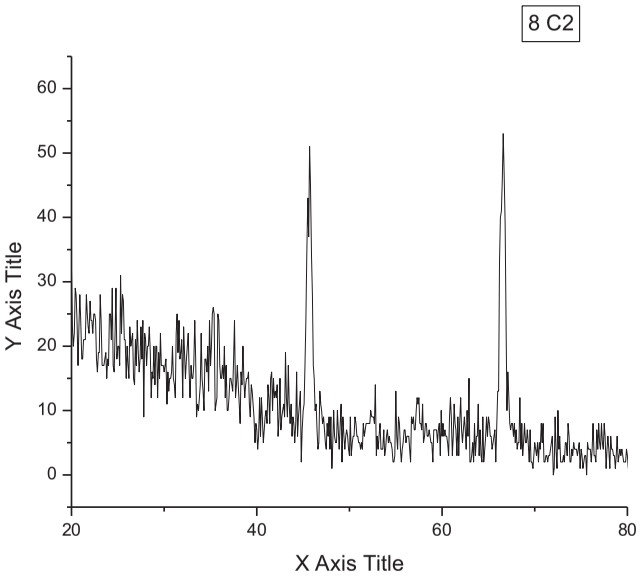
8 C2
Y Axis Title
X Axis Title
0
10
20
30
40
50
60
20
40
60
80

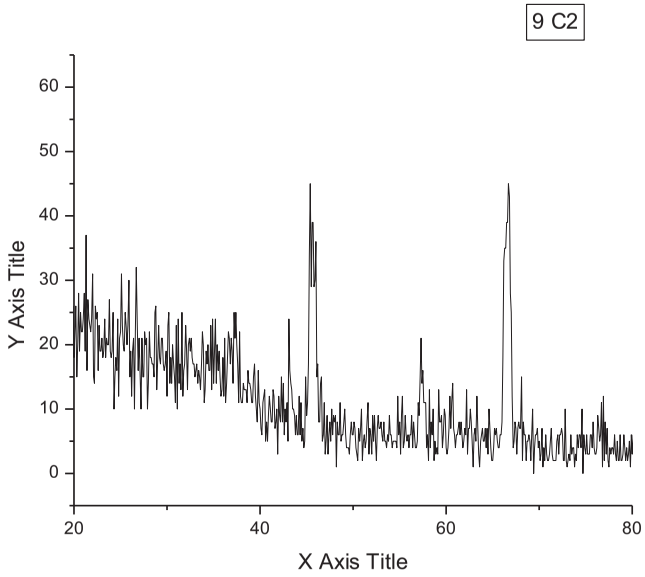
9 C2
Y Axis Title
X Axis Title
0
10
20
30
40
50
60
20
40
60
80

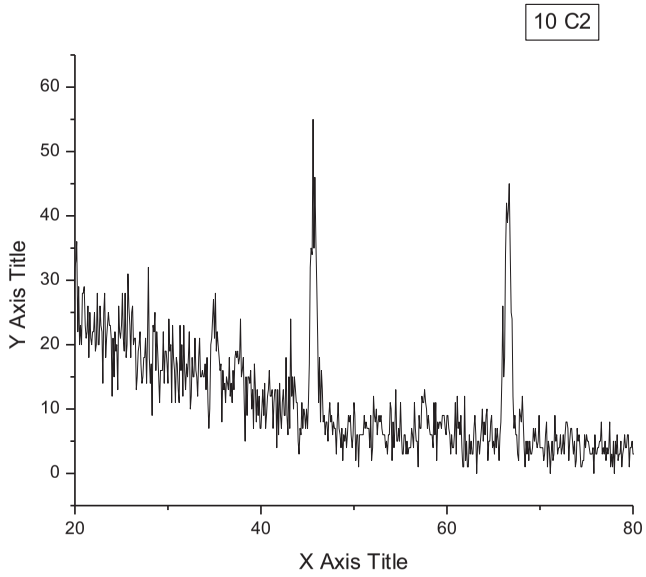
10 C2
Y Axis Title
X Axis Title
0
10
20
30
40
50
60
20
40
60
80

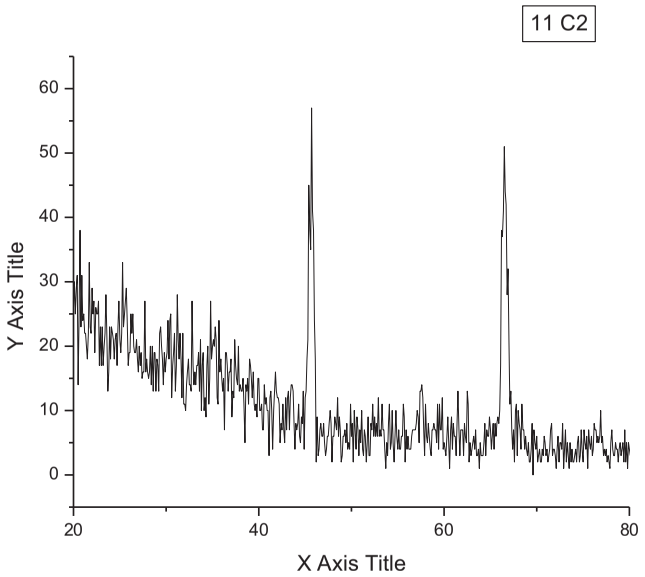
11 C2
Y Axis Title
X Axis Title
0
10
20
30
40
50
60
20
40
60
80

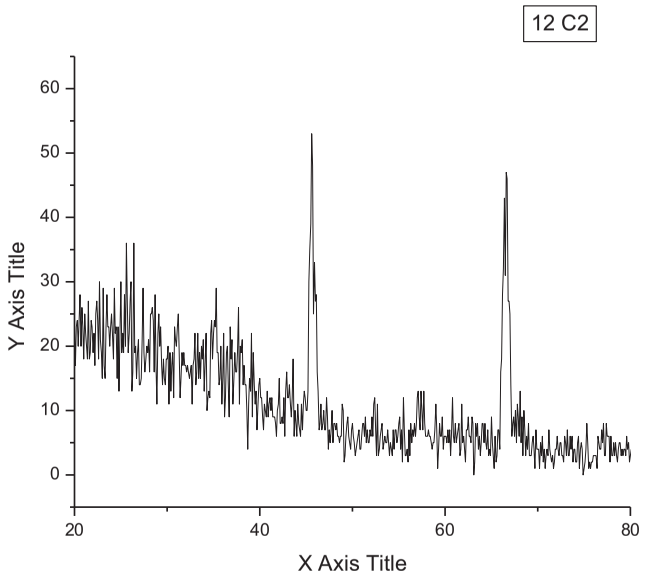
12 C2
Y Axis Title
X Axis Title
0
10
20
30
40
50
60
20
40
60
80

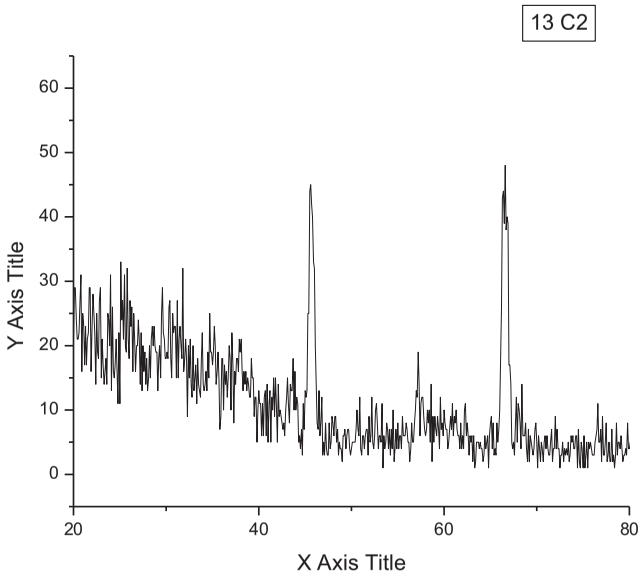
13 C2
Y Axis Title
X Axis Title
0
10
20
30
40
50
60
20
40
60
80

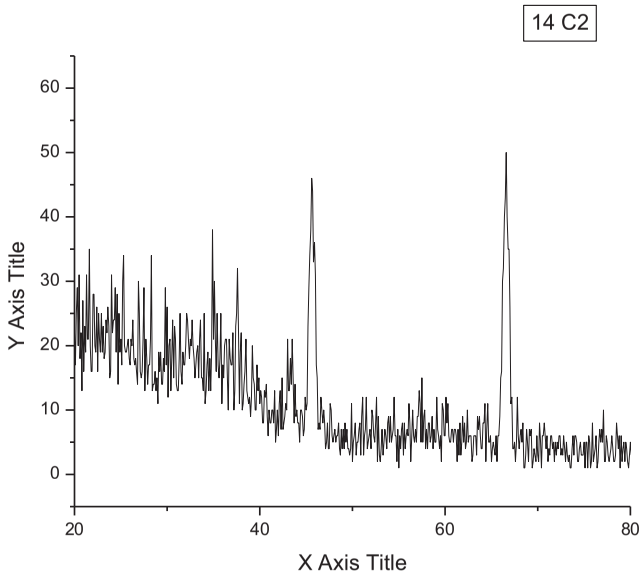
14 C2
Y Axis Title
X Axis Title
0
10
20
30
40
50
60
20
40
60
80

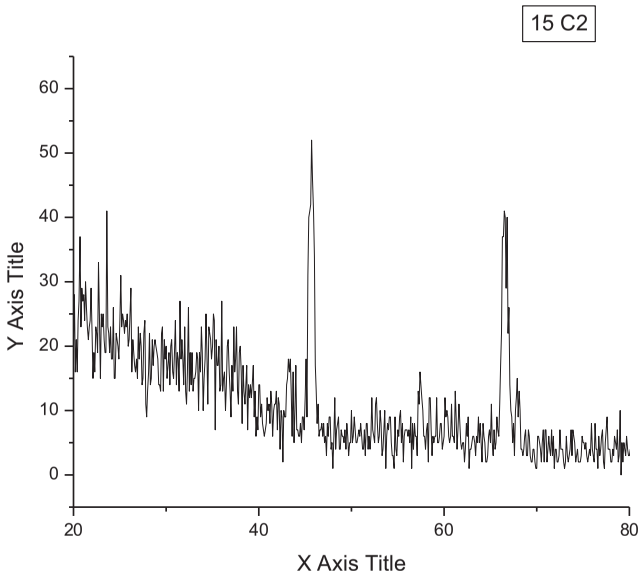
15 C2
Y Axis Title
X Axis Title
0
10
20
30
40
50
60
20
40
60
80

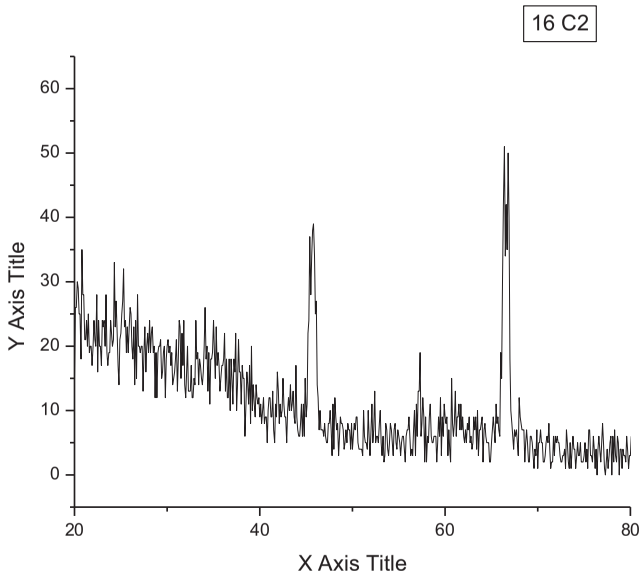
16 C2
Y Axis Title
X Axis Title
0
10
20
30
40
50
60
20
40
60
80

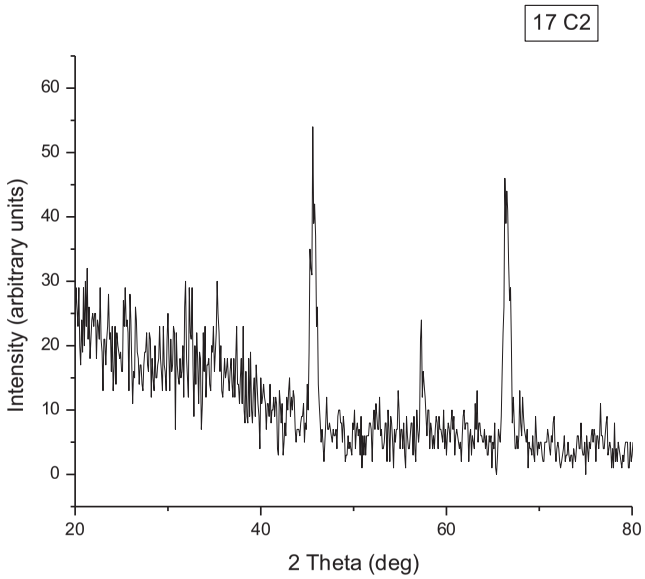
17 C2
Intensity (arbitrary units)
2 Theta (deg)
0
10
20
30
40
50
60
20
40
60
80

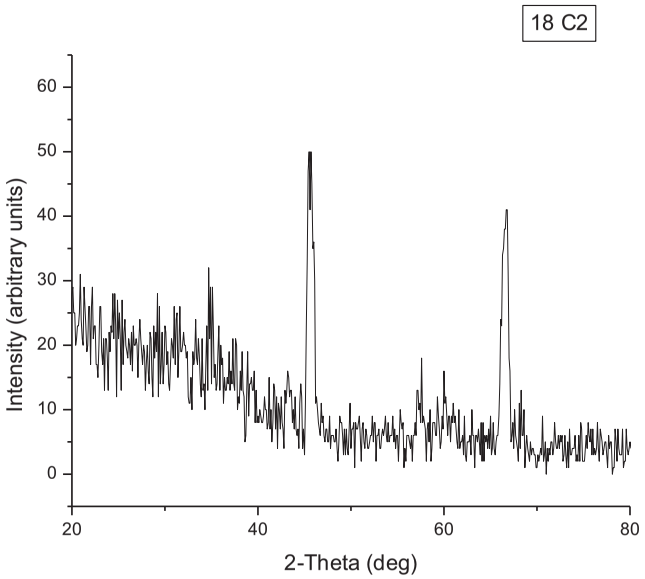
18 C2
Intensity (arbitrary units)
2-Theta (deg)
0
10
20
30
40
50
60
20
40
60
80

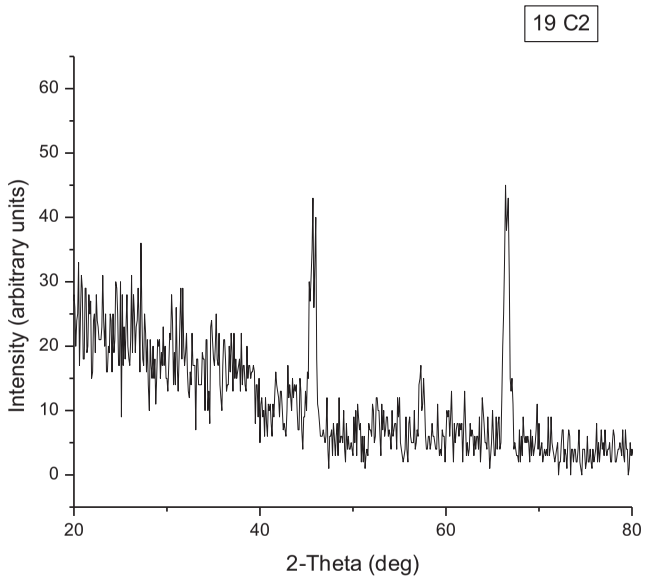
19 C2
Intensity (arbitrary units)
2-Theta (deg)
0
10
20
30
40
50
60
20
40
60
80

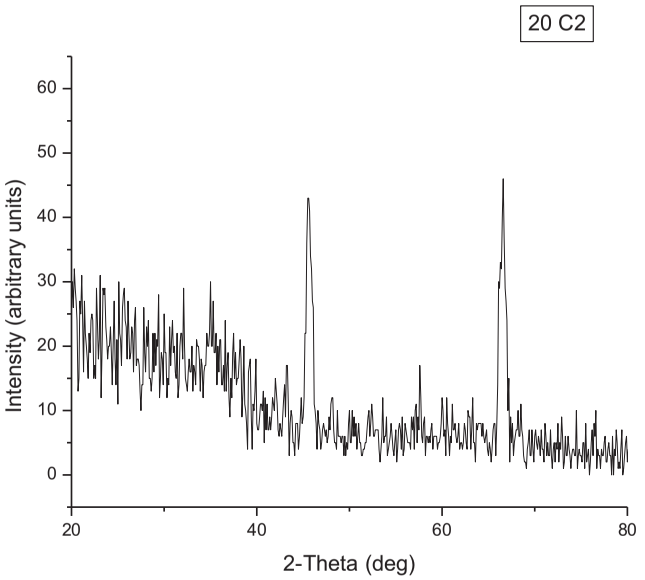
20 C2
Intensity (arbitrary units)
2-Theta (deg)
0
10
20
30
40
50
60
20
40
60
80

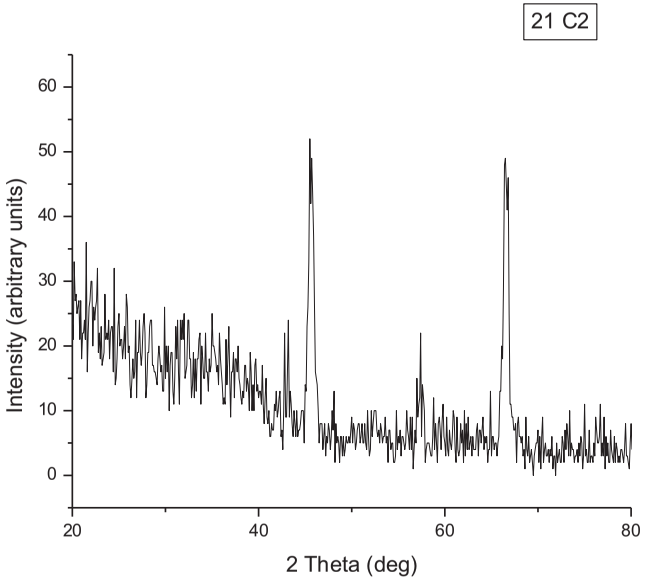
21 C2
Intensity (arbitrary units)
2 Theta (deg)
0
10
20
30
40
50
60
20
40
60
80

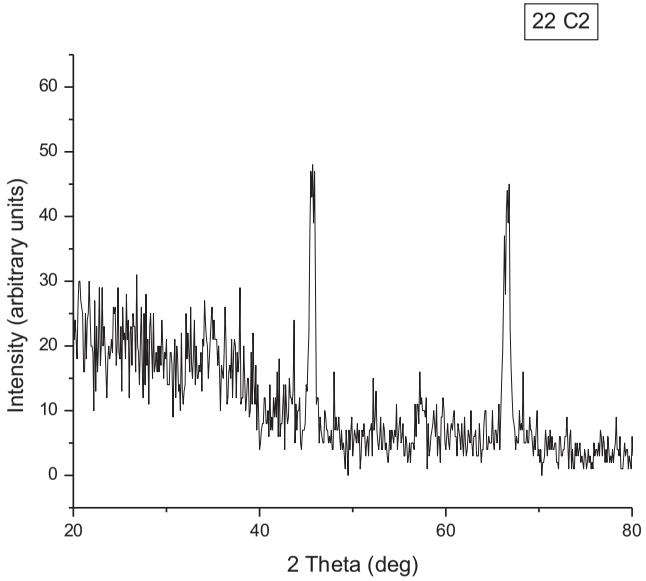
22 C2
Intensity (arbitrary units)
2 Theta (deg)
0
10
20
30
40
50
60
20
40
60
80

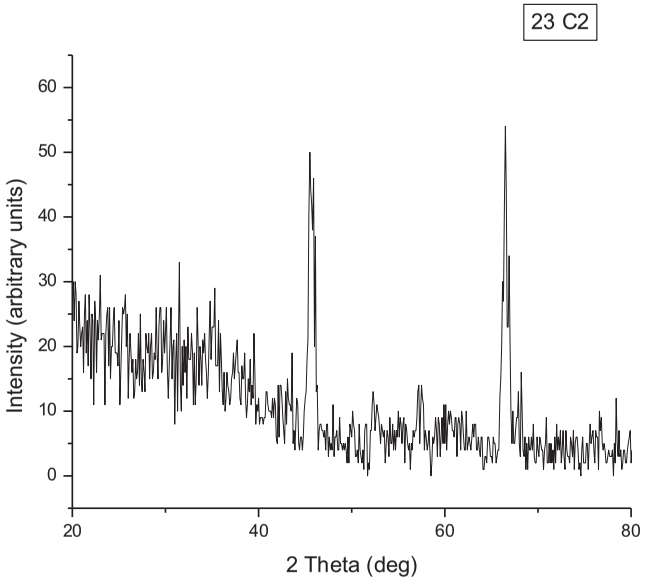
23 C2
Intensity (arbitrary units)
2 Theta (deg)
0
10
20
30
40
50
60
20
40
60
80

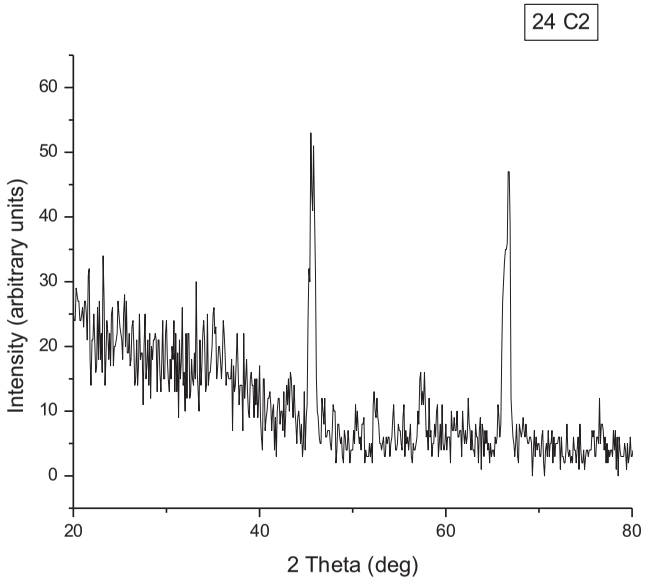
24 C2
Intensity (arbitrary units)
2 Theta (deg)
0
10
20
30
40
50
60
20
40
60
80

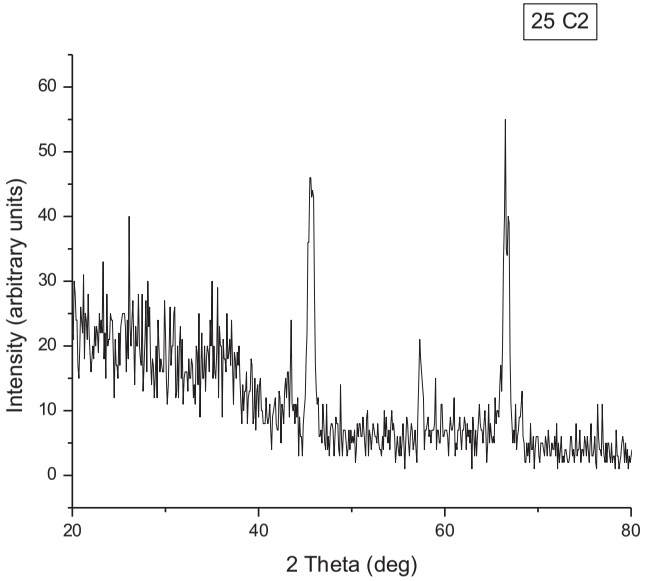
25 C2
Intensity (arbitrary units)
2 Theta (deg)
0
10
20
30
40
50
60
20
40
60
80

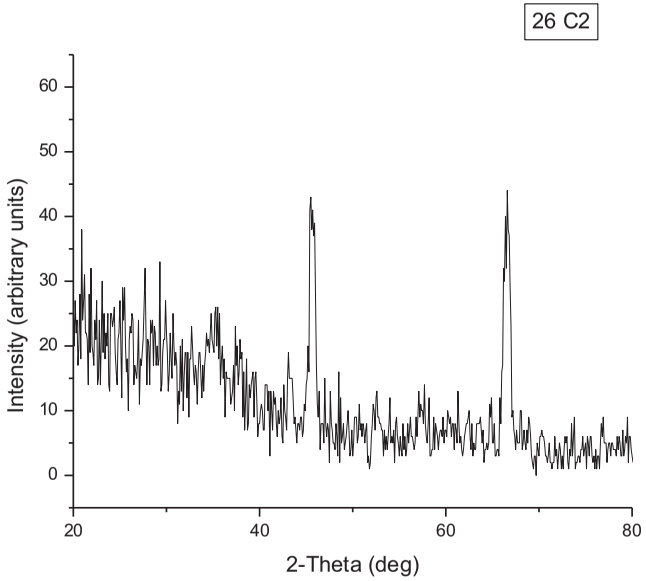
26 C2
Intensity (arbitrary units)
2-Theta (deg)
0
10
20
30
40
50
60
20
40
60
80

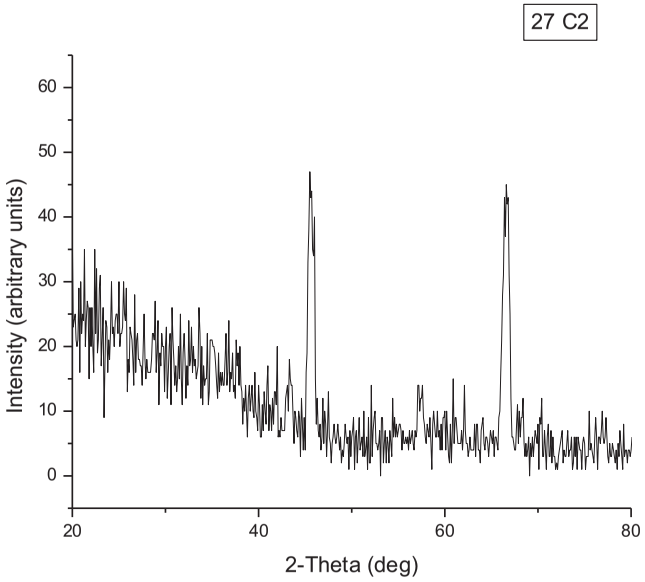
27 C2
Intensity (arbitrary units)
2-Theta (deg)
0
10
20
30
40
50
60
20
40
60
80

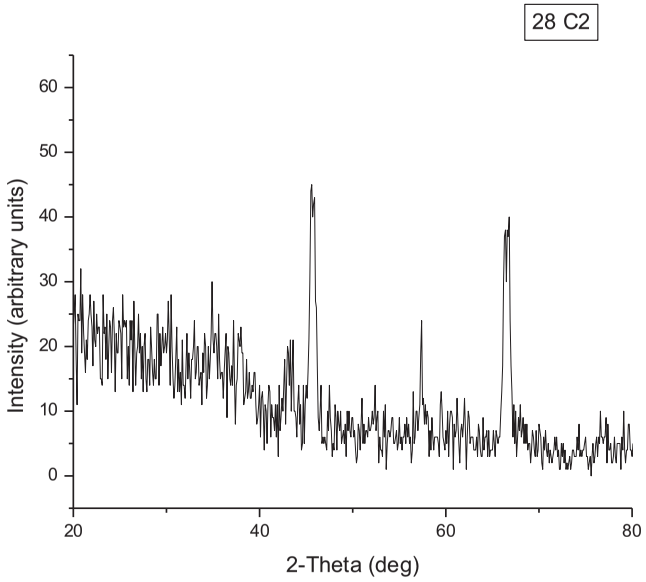
28 C2
Intensity (arbitrary units)
2-Theta (deg)
0
10
20
30
40
50
60
20
40
60
80

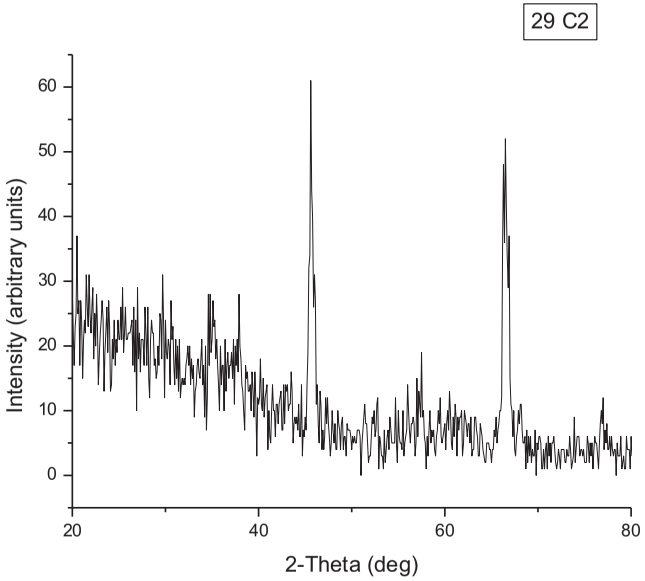
29 C2
Intensity (arbitrary units)
2-Theta (deg)
0
10
20
30
40
50
60
20
40
60
80

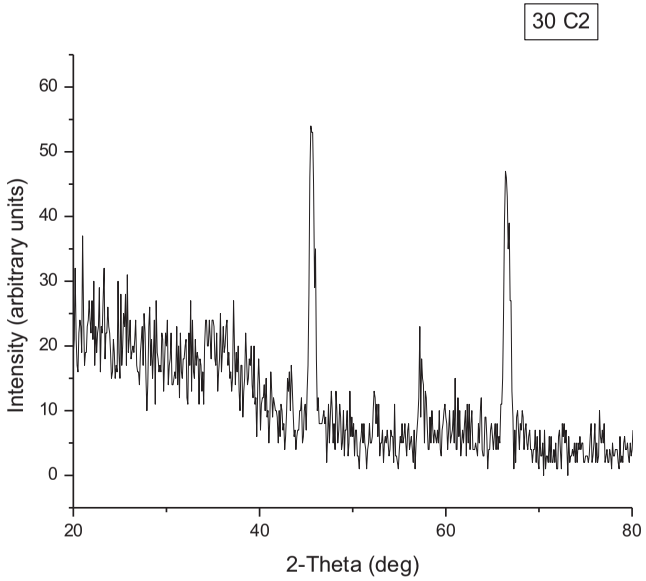
30 C2
Intensity (arbitrary units)
2-Theta (deg)
0
10
20
30
40
50
60
20
40
60
80

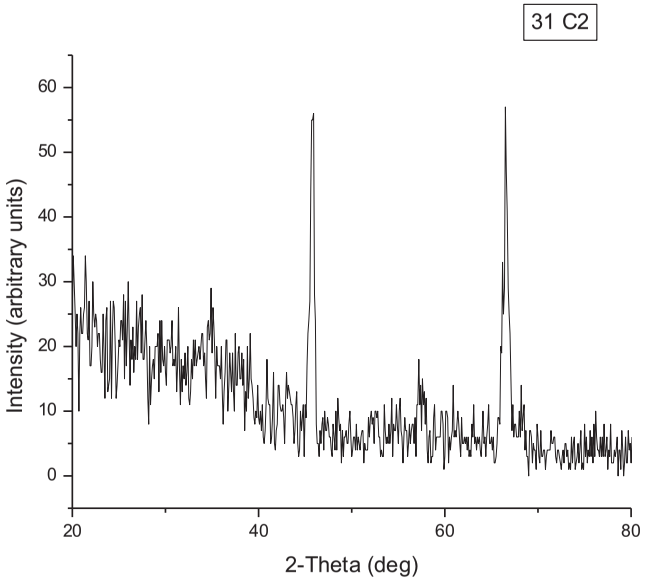
31 C2
Intensity (arbitrary units)
2-Theta (deg)
0
10
20
30
40
50
60
20
40
60
80

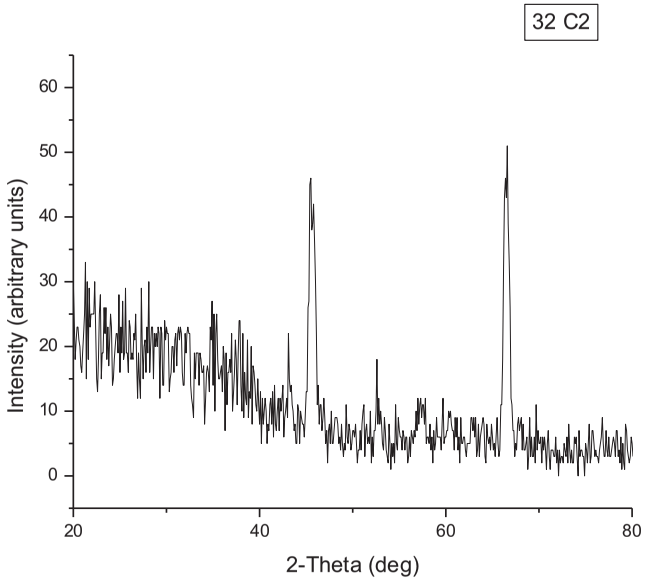
32 C2
Intensity (arbitrary units)
2-Theta (deg)
0
10
20
30
40
50
60
20
40
60
80

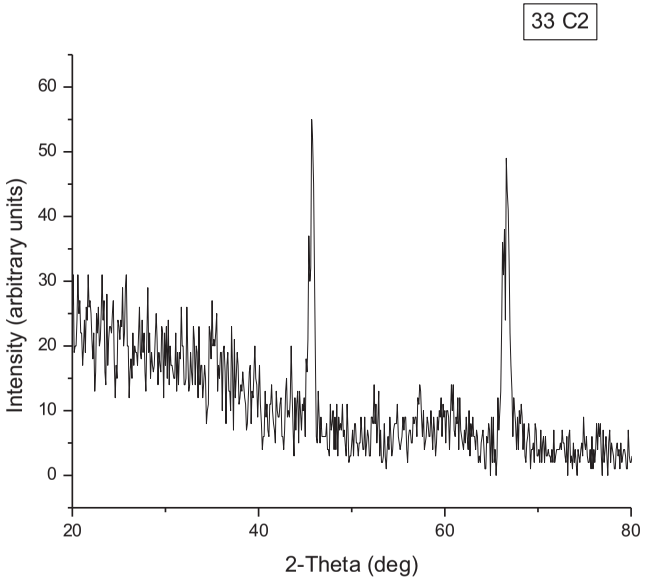
33 C2
Intensity (arbitrary units)
2-Theta (deg)
0
10
20
30
40
50
60
20
40
60
80

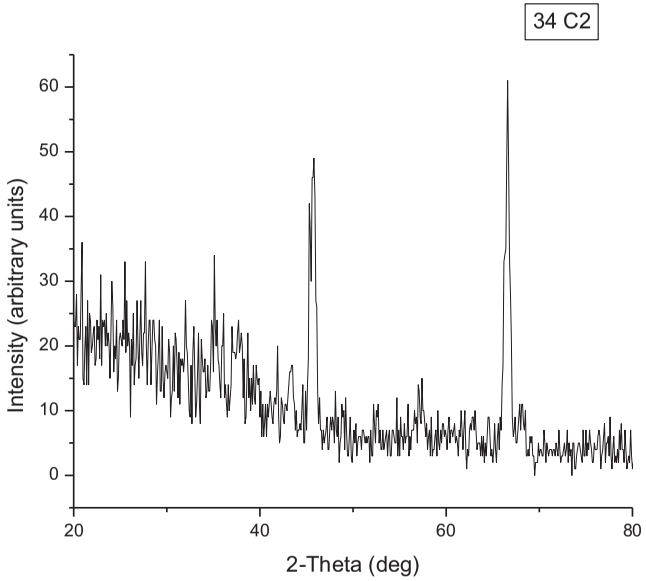
34 C2
Intensity (arbitrary units)
2-Theta (deg)
0
10
20
30
40
50
60
20
40
60
80

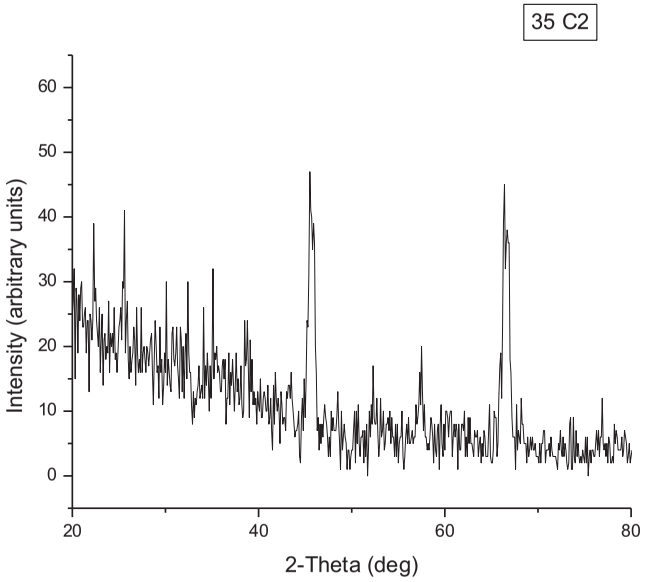
35 C2
Intensity (arbitrary units)
2-Theta (deg)
0
10
20
30
40
50
60
20
40
60
80

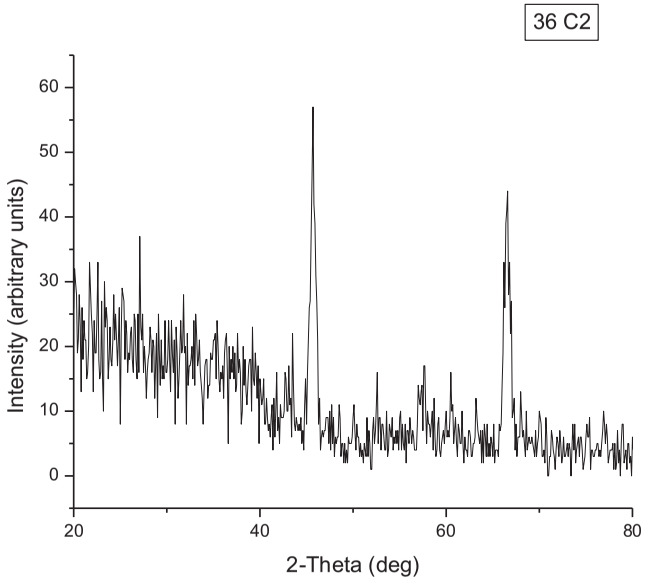
36 C2
Intensity (arbitrary units)
2-Theta (deg)
0
10
20
30
40
50
60
20
40
60
80

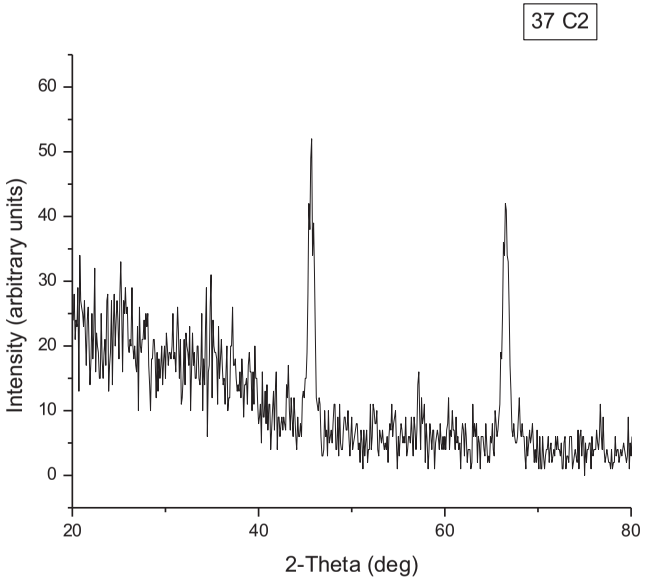
37 C2
Intensity (arbitrary units)
2-Theta (deg)
0
10
20
30
40
50
60
20
40
60
80

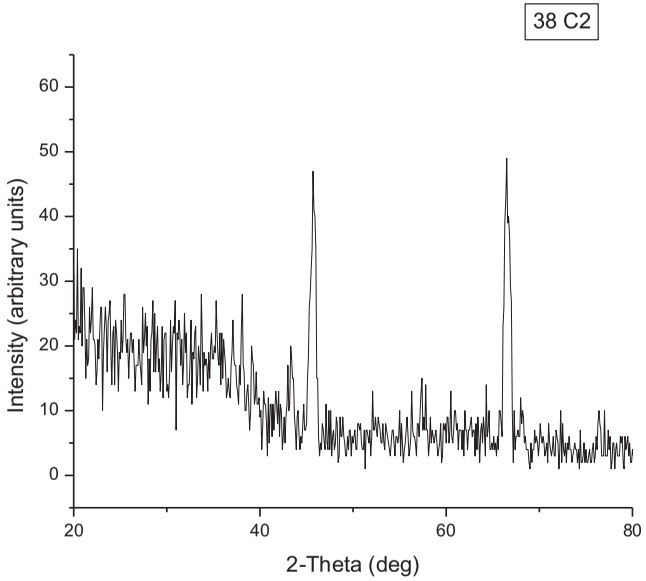
38 C2
Intensity (arbitrary units)
2-Theta (deg)
0
10
20
30
40
50
60
20
40
60
80

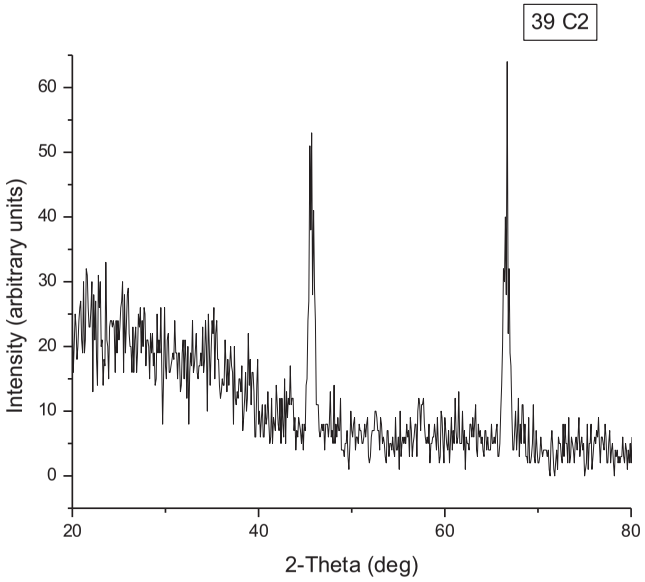
39 C2
Intensity (arbitrary units)
2-Theta (deg)
0
10
20
30
40
50
60
20
40
60
80

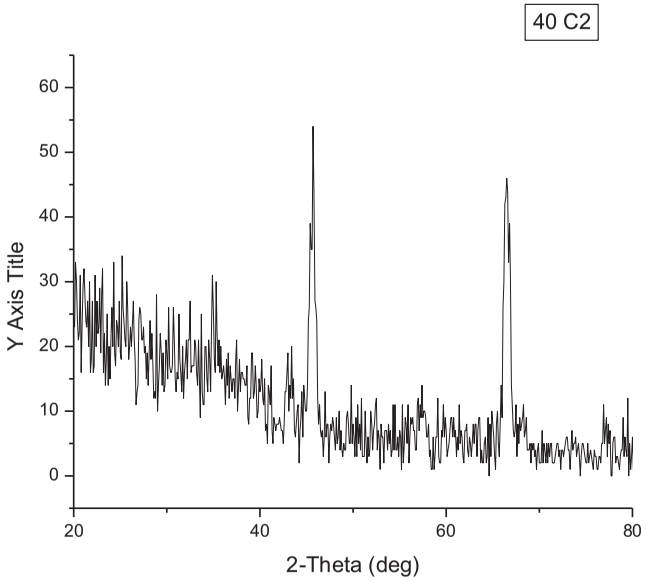
40 C2
Y Axis Title
2-Theta (deg)
0
10
20
30
40
50
60
20
40
60
80

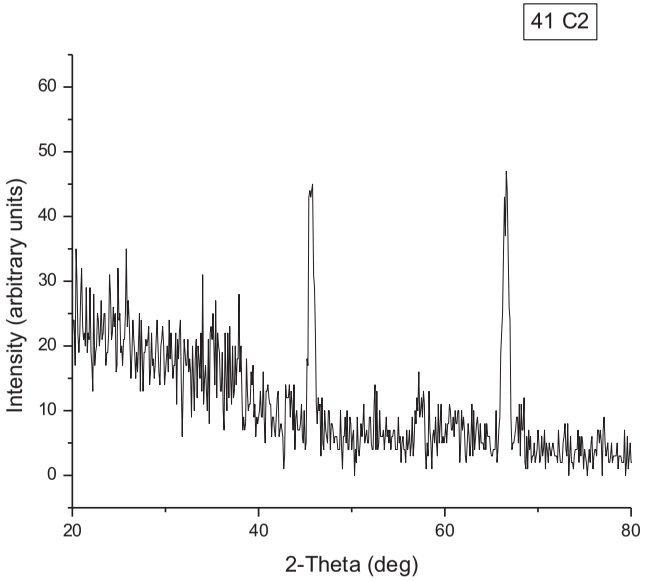
41 C2
Intensity (arbitrary units)
2-Theta (deg)
0
10
20
30
40
50
60
20
40
60
80

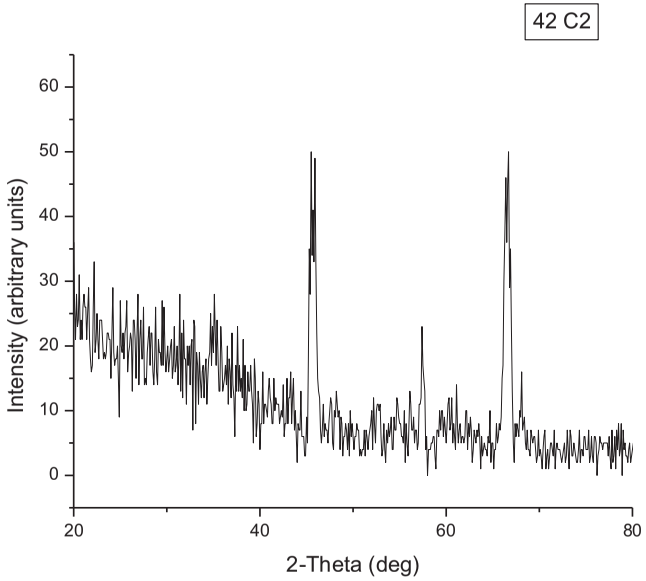
42 C2
Intensity (arbitrary units)
2-Theta (deg)
0
10
20
30
40
50
60
20
40
60
80

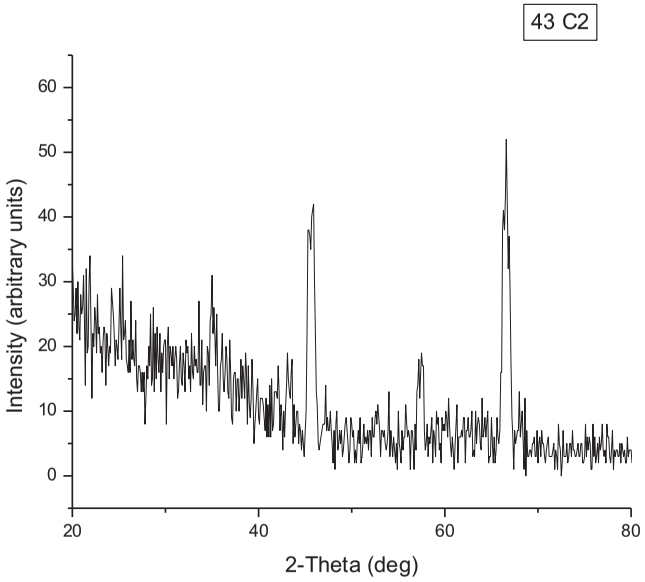
43 C2
Intensity (arbitrary units)
2-Theta (deg)
0
10
20
30
40
50
60
20
40
60
80

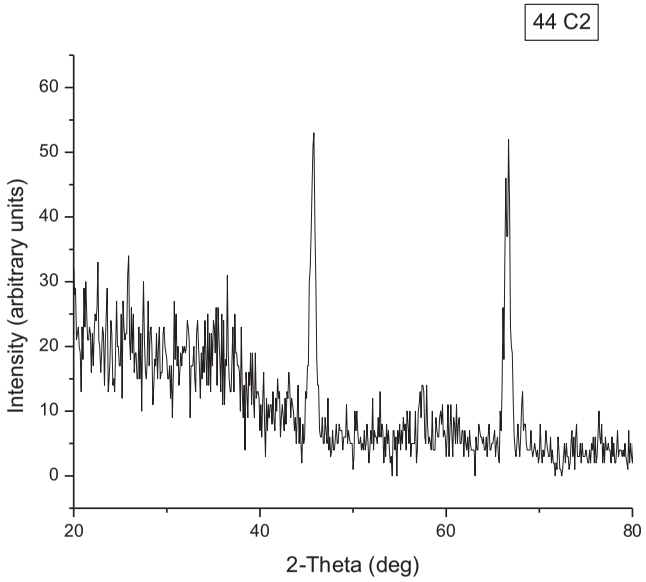
44 C2
Intensity (arbitrary units)
2-Theta (deg)
0
10
20
30
40
50
60
20
40
60
80

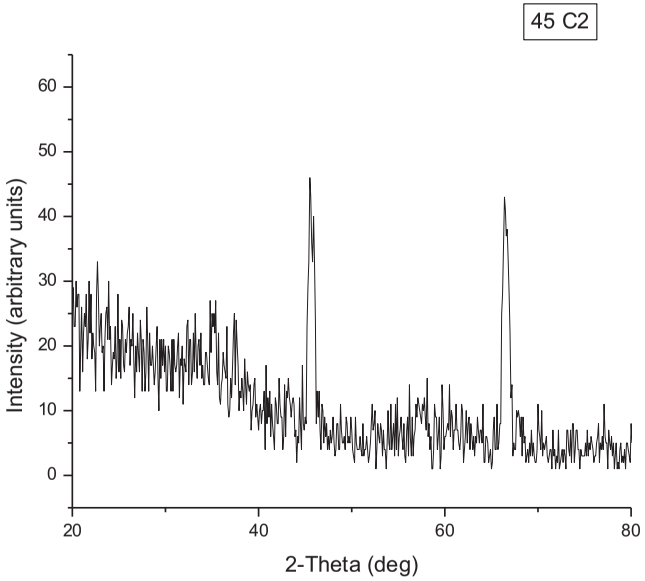
45 C2
Intensity (arbitrary units)
2-Theta (deg)
0
10
20
30
40
50
60
20
40
60
80

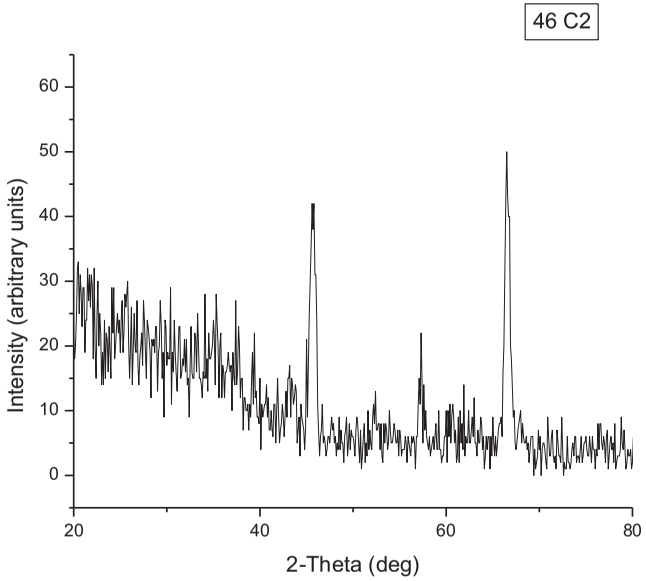
46 C2
Intensity (arbitrary units)
2-Theta (deg)
0
10
20
30
40
50
60
20
40
60
80

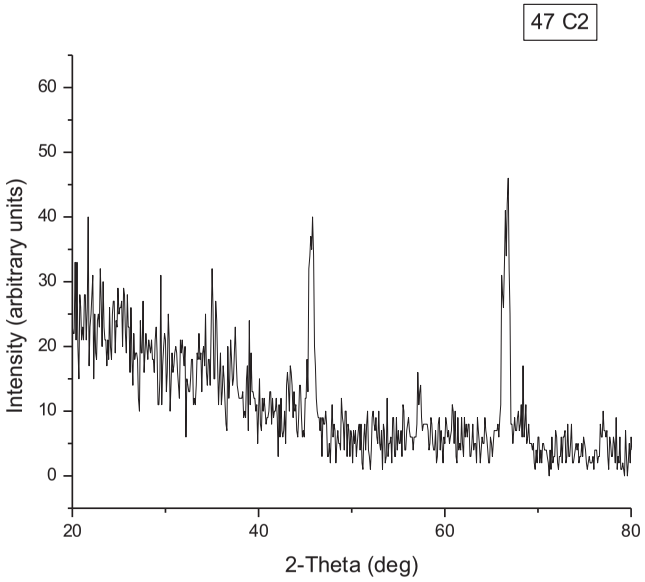
47 C2
Intensity (arbitrary units)
2-Theta (deg)
0
10
20
30
40
50
60
20
40
60
80

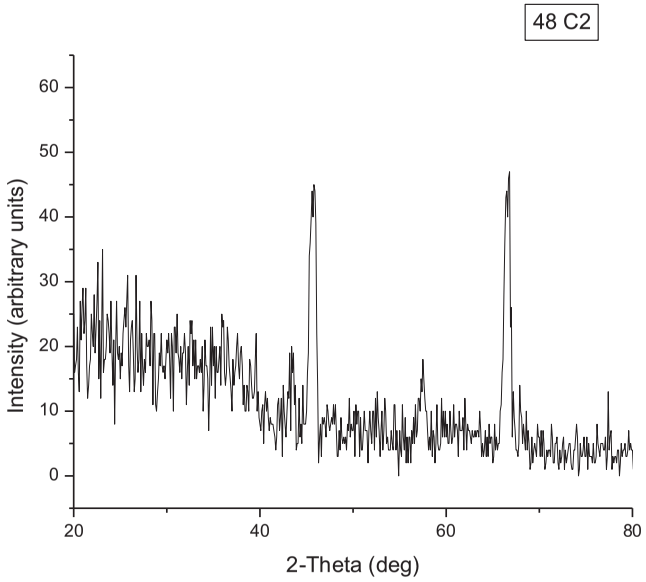
48 C2
Intensity (arbitrary units)
2-Theta (deg)
0
10
20
30
40
50
60
20
40
60
80

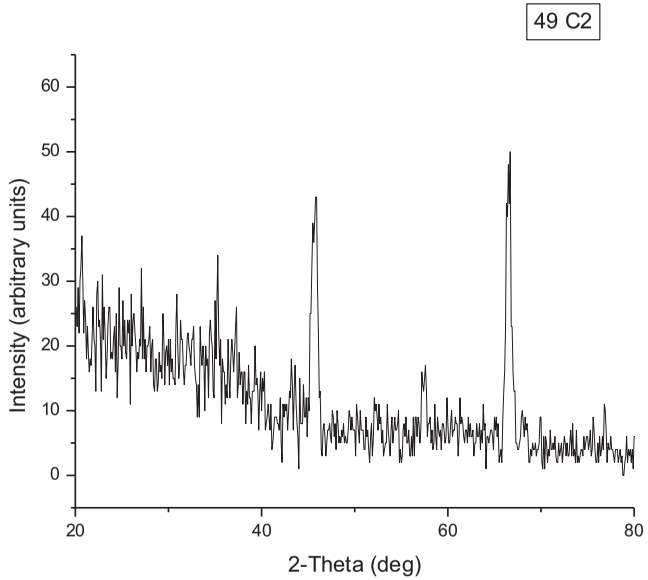
49 C2
Intensity (arbitrary units)
2-Theta (deg)
0
10
20
30
40
50
60
20
40
60
80

XRD Patterns for WC-12Co APS

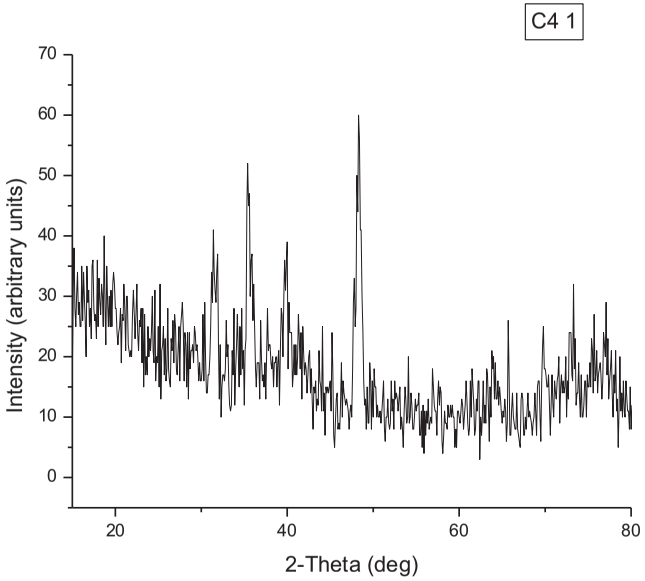
C4 1
Intensity (arbitrary units)
2-Theta (deg)
0
10
20
30
40
50
60
70
20
40
60
80

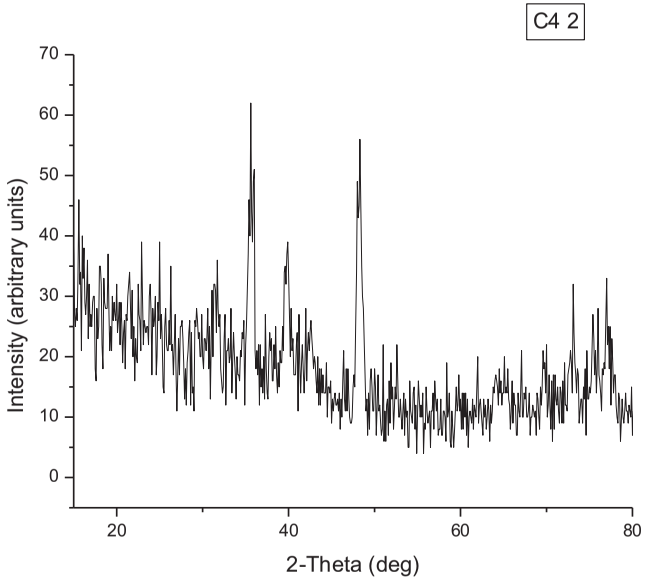
C4 2
Intensity (arbitrary units)
2-Theta (deg)
0
10
20
30
40
50
60
70
20
40
60
80

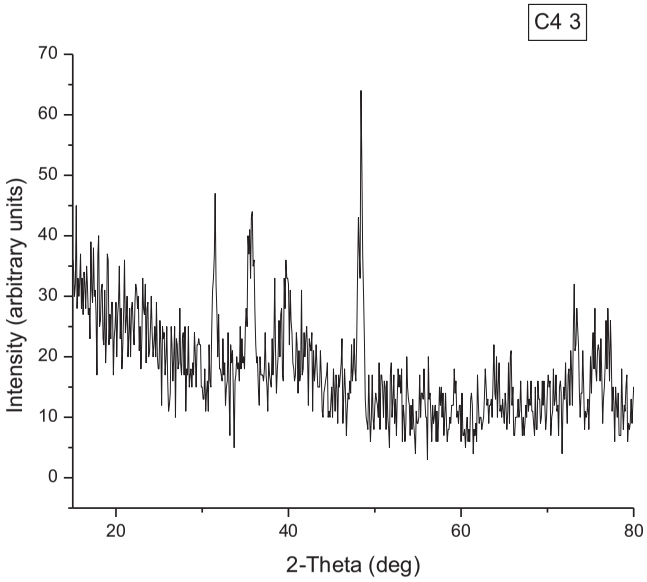
C4 3
Intensity (arbitrary units)
2-Theta (deg)
0
10
20
30
40
50
60
70
20
40
60
80

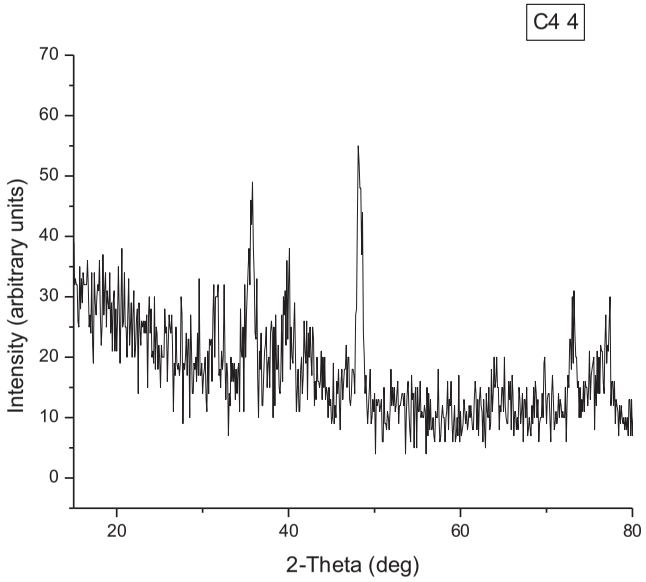
C4 4
Intensity (arbitrary units)
2-Theta (deg)
0
10
20
30
40
50
60
70
20
40
60
80

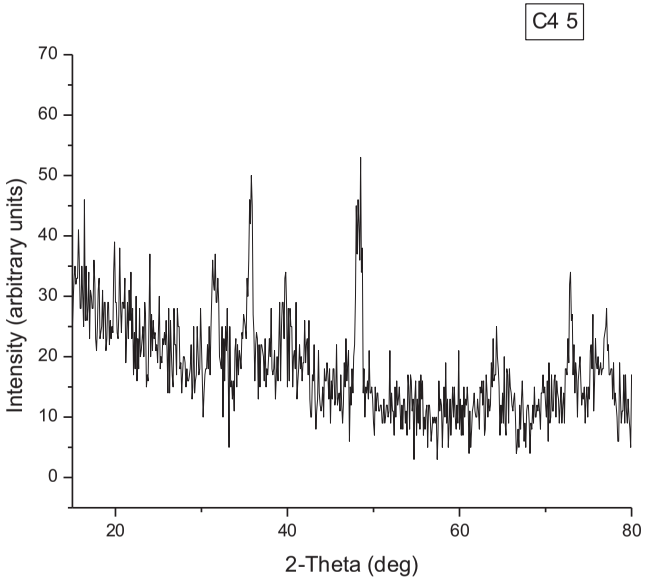
C4 5
Intensity (arbitrary units)
2-Theta (deg)
0
10
20
30
40
50
60
70
20
40
60
80

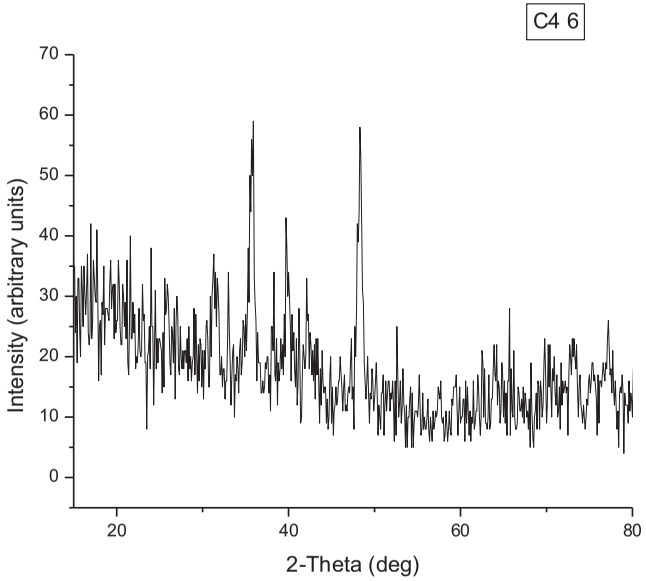
C4 6
Intensity (arbitrary units)
2-Theta (deg)
0
10
20
30
40
50
60
70
20
40
60
80

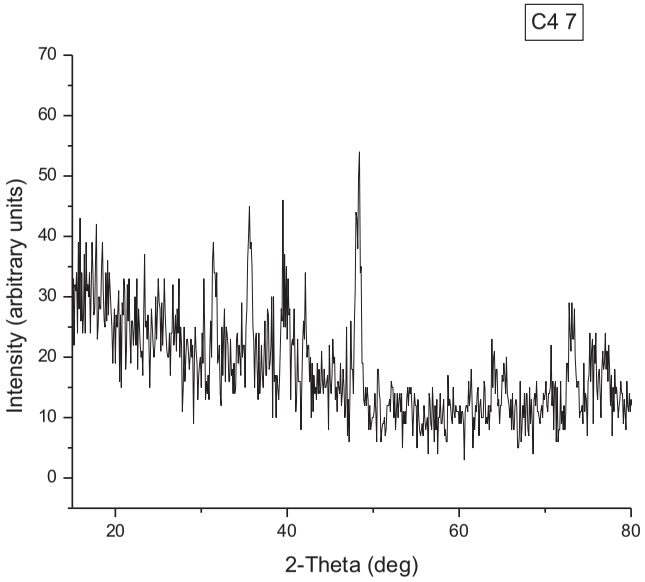
C4 7
Intensity (arbitrary units)
2-Theta (deg)
0
10
20
30
40
50
60
70
20
40
60
80

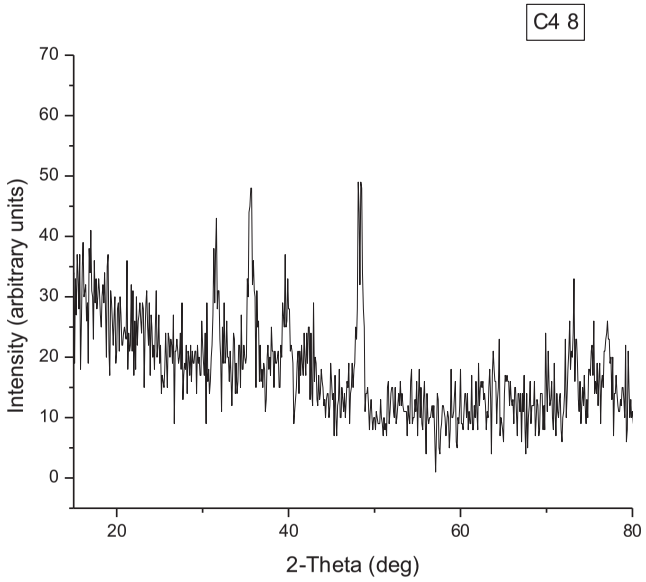
C4 8
Intensity (arbitrary units)
2-Theta (deg)
0
10
20
30
40
50
60
70
20
40
60
80

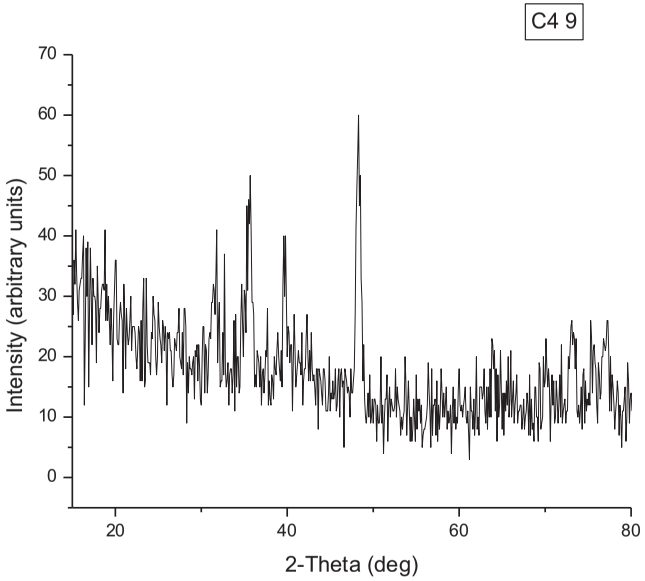
C4 9
Intensity (arbitrary units)
2-Theta (deg)
0
10
20
30
40
50
60
70
20
40
60
80

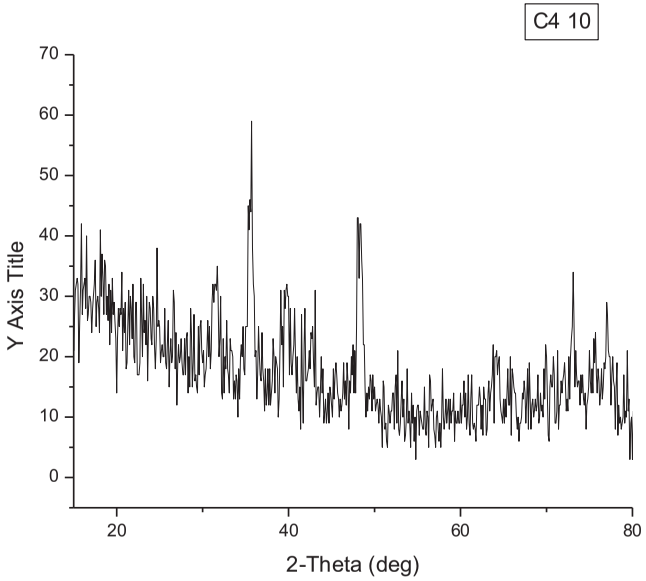
C4 10
Y Axis Title
2-Theta (deg)
0
10
20
30
40
50
60
70
20
40
60
80

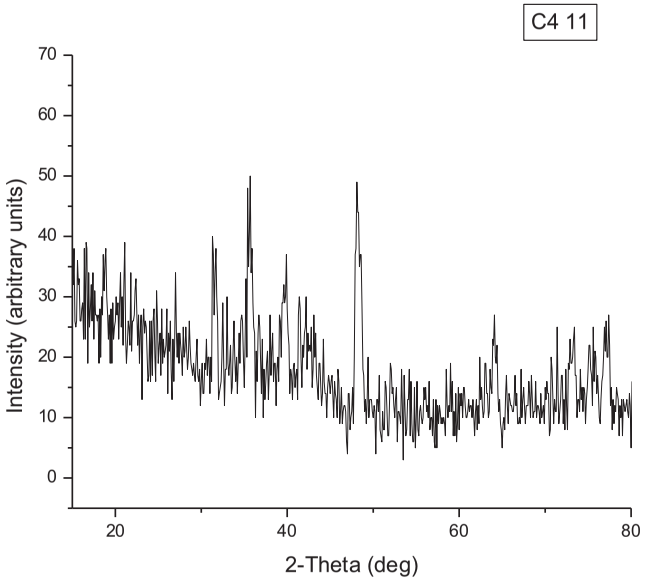
C4 11
Intensity (arbitrary units)
2-Theta (deg)
0
10
20
30
40
50
60
70
20
40
60
80

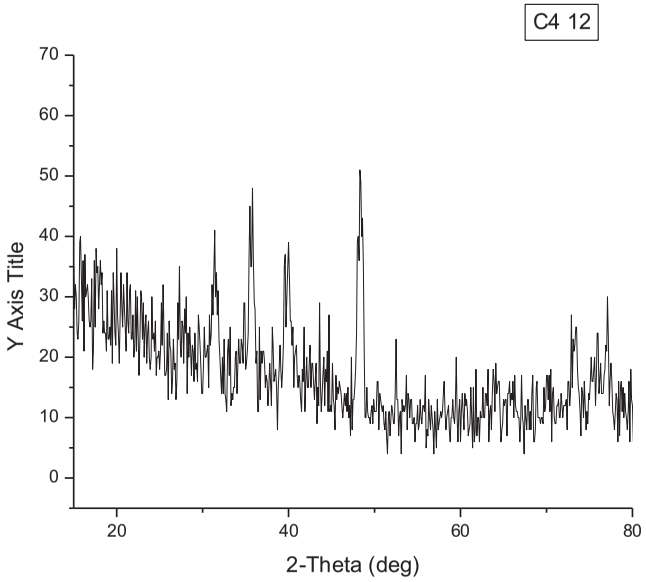
C4 12
Y Axis Title
2-Theta (deg)
0
10
20
30
40
50
60
70
20
40
60
80

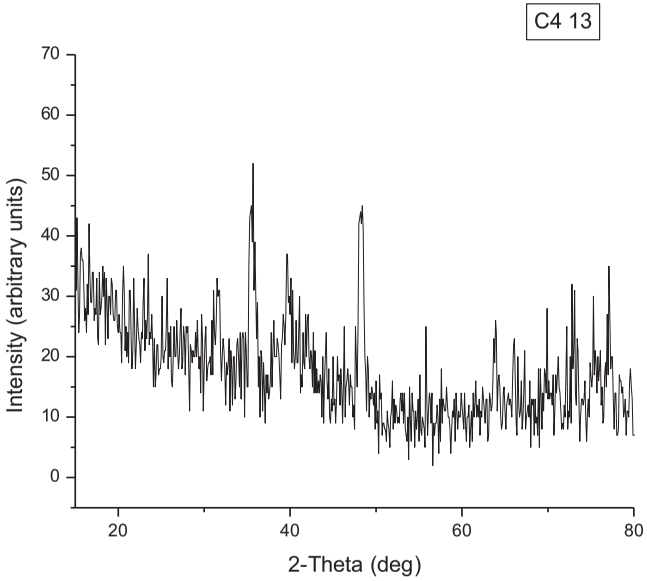
C4 13
Intensity (arbitrary units)
2-Theta (deg)
0
10
20
30
40
50
60
70
20
40
60
80

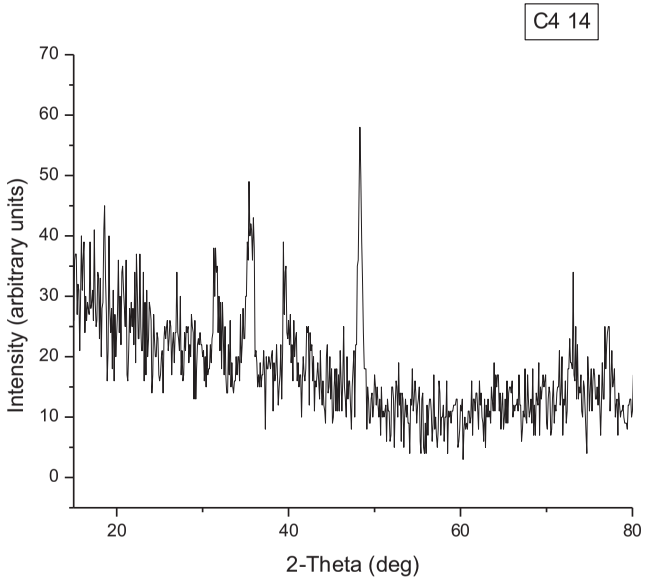
C4 14
Intensity (arbitrary units)
2-Theta (deg)
0
10
20
30
40
50
60
70
20
40
60
80

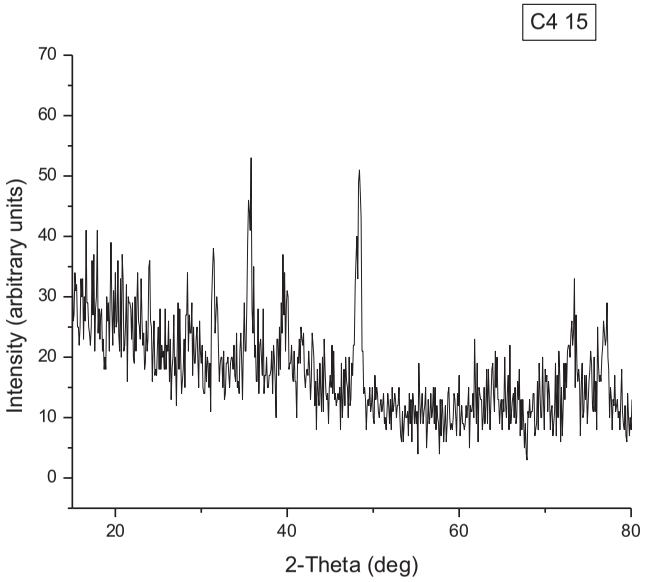
C4 15
Intensity (arbitrary units)
2-Theta (deg)
0
10
20
30
40
50
60
70
20
40
60
80

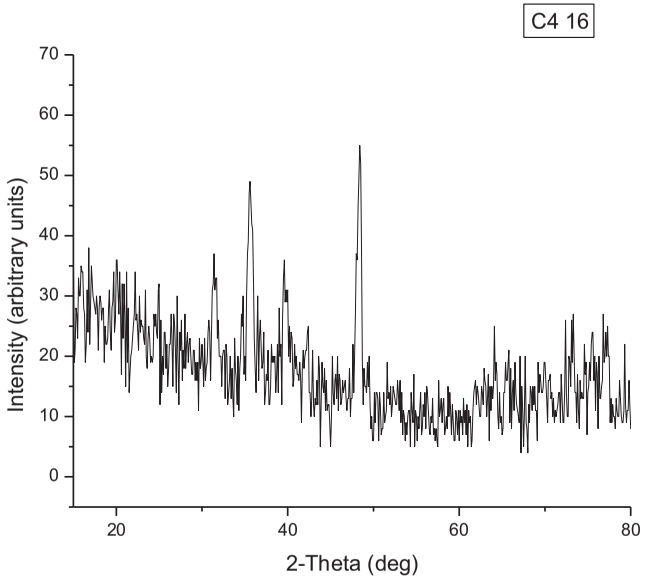
C4 16
Intensity (arbitrary units)
2-Theta (deg)
0
10
20
30
40
50
60
70
20
40
60
80

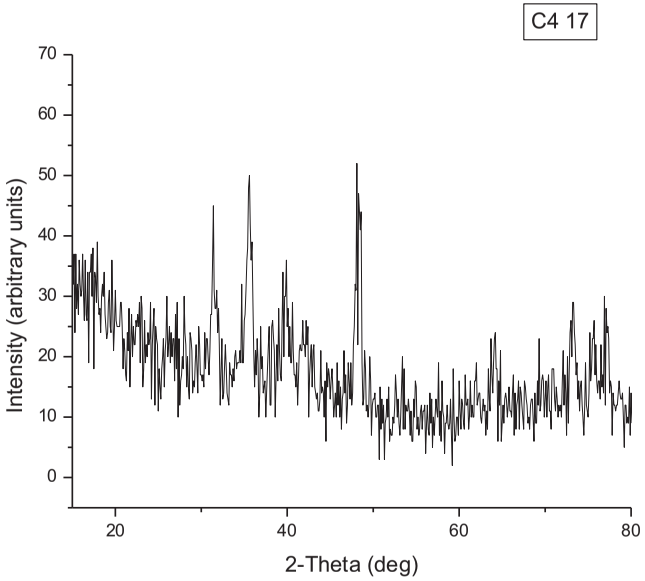
C4 17
Intensity (arbitrary units)
2-Theta (deg)
0
10
20
30
40
50
60
70
20
40
60
80

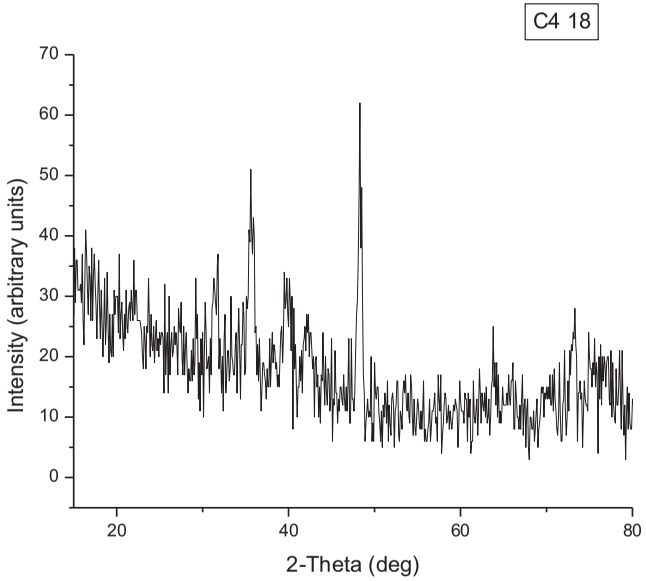
C4 18
Intensity (arbitrary units)
2-Theta (deg)
0
10
20
30
40
50
60
70
20
40
60
80

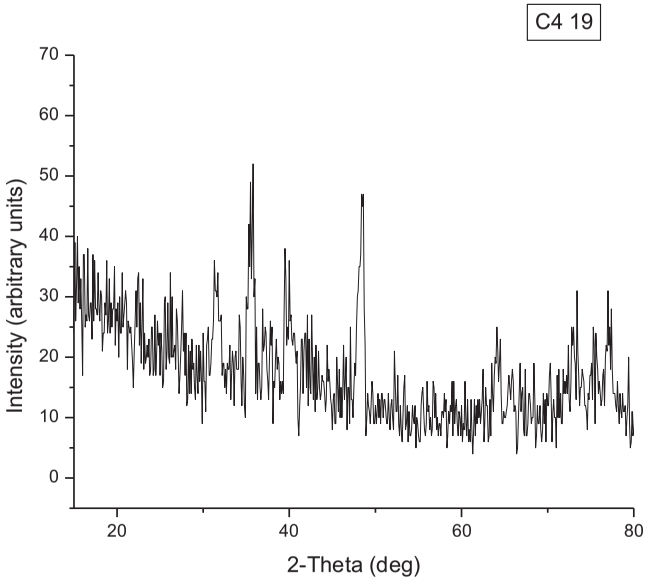
C4 19
Intensity (arbitrary units)
2-Theta (deg)
0
10
20
30
40
50
60
70
20
40
60
80

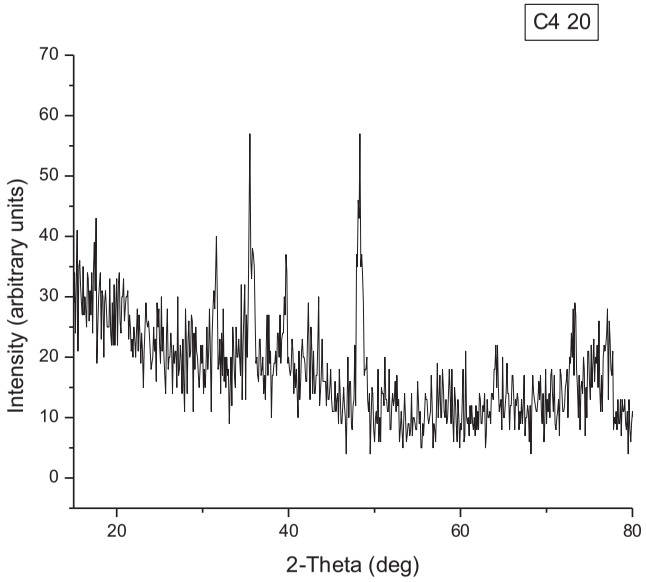
C4 20
Intensity (arbitrary units)
2-Theta (deg)
0
10
20
30
40
50
60
70
20
40
60
80

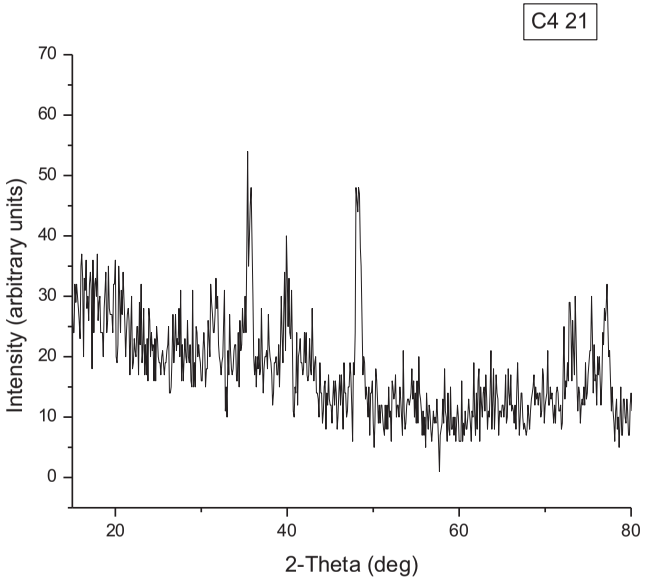
C4 21
Intensity (arbitrary units)
2-Theta (deg)
0
10
20
30
40
50
60
70
20
40
60
80

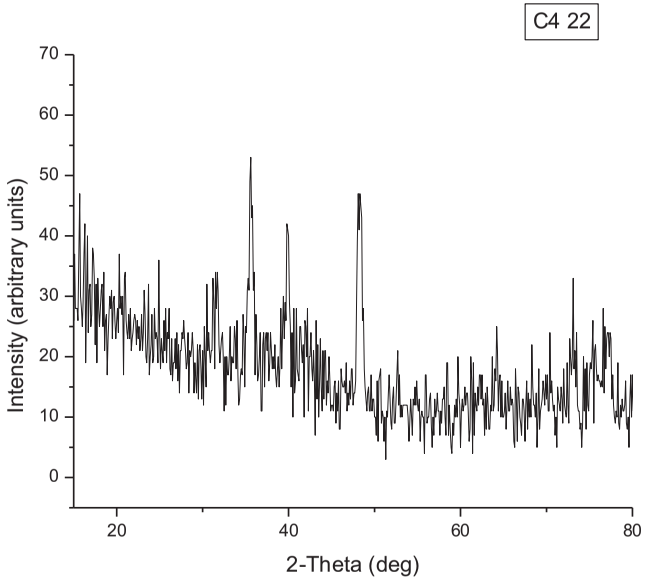
C4 22
Intensity (arbitrary units)
2-Theta (deg)
0
10
20
30
40
50
60
70
20
40
60
80

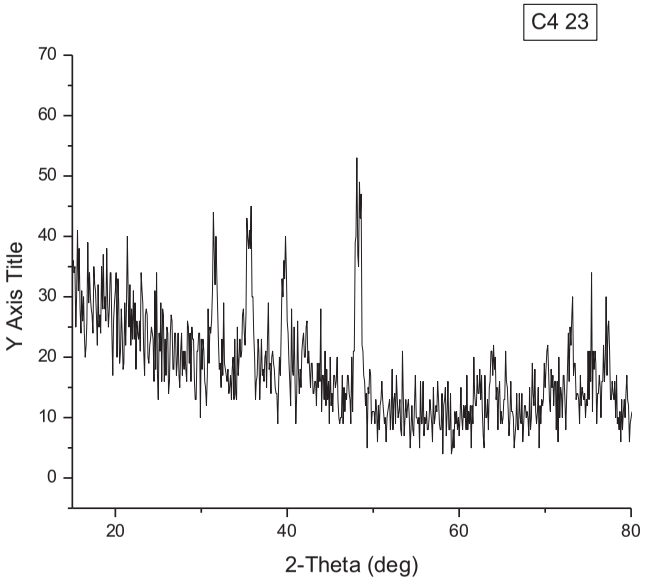
C4 23
Y Axis Title
2-Theta (deg)
0
10
20
30
40
50
60
70
20
40
60
80

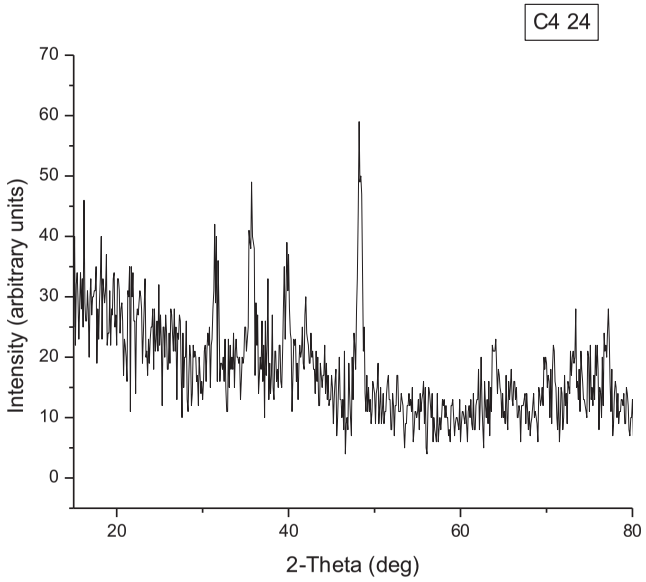
C4 24
Intensity (arbitrary units)
2-Theta (deg)
0
10
20
30
40
50
60
70
20
40
60
80

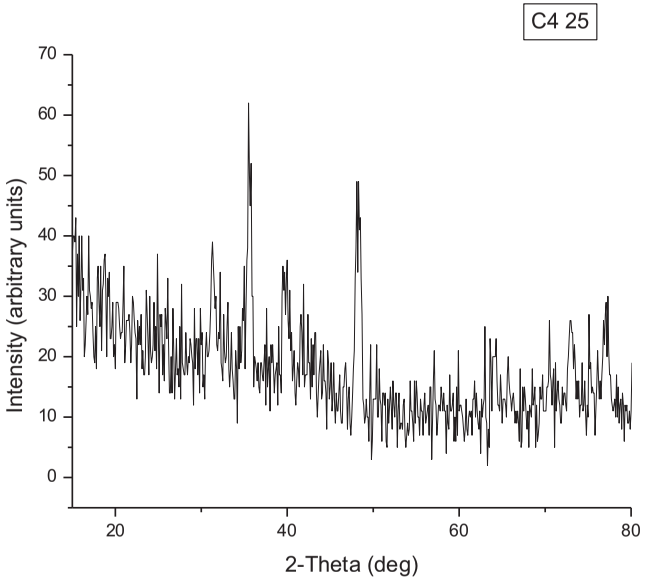
C4 25
Intensity (arbitrary units)
2-Theta (deg)
0
10
20
30
40
50
60
70
20
40
60
80

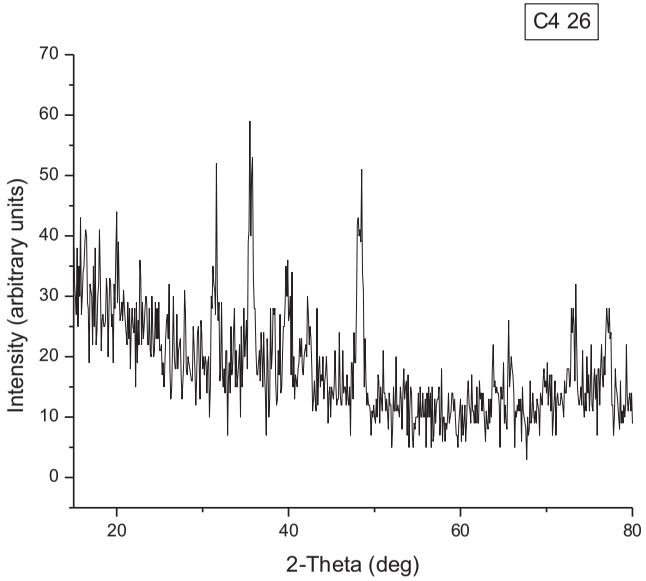
C4 26
Intensity (arbitrary units)
2-Theta (deg)
0
10
20
30
40
50
60
70
20
40
60
80

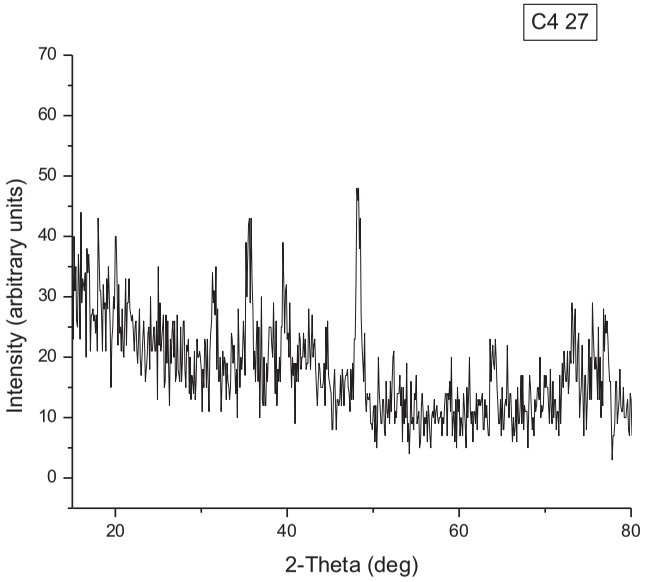
C4 27
Intensity (arbitrary units)
2-Theta (deg)
0
10
20
30
40
50
60
70
20
40
60
80

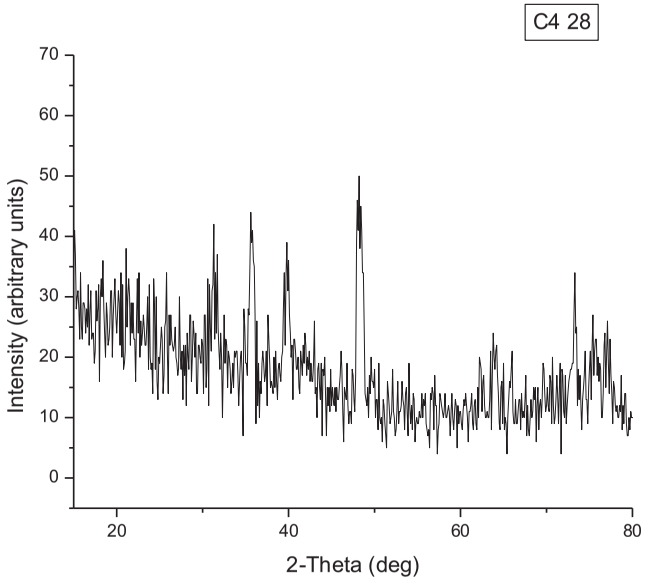
C4 28
Intensity (arbitrary units)
2-Theta (deg)
0
10
20
30
40
50
60
70
20
40
60
80

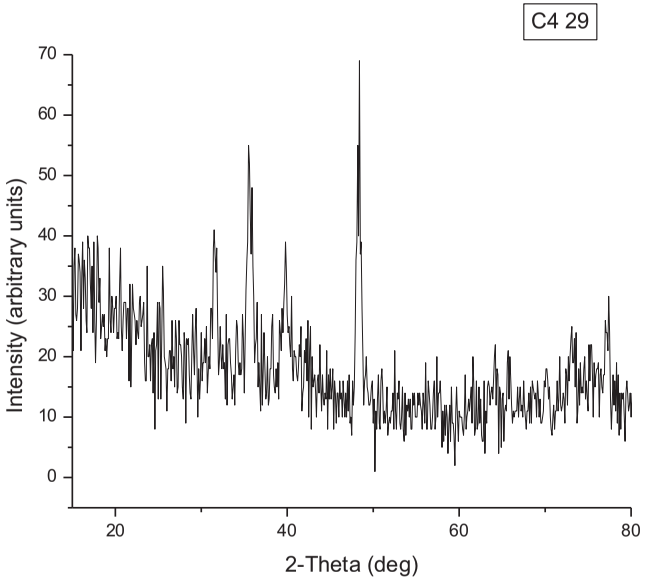
C4 29
Intensity (arbitrary units)
2-Theta (deg)
0
10
20
30
40
50
60
70
20
40
60
80

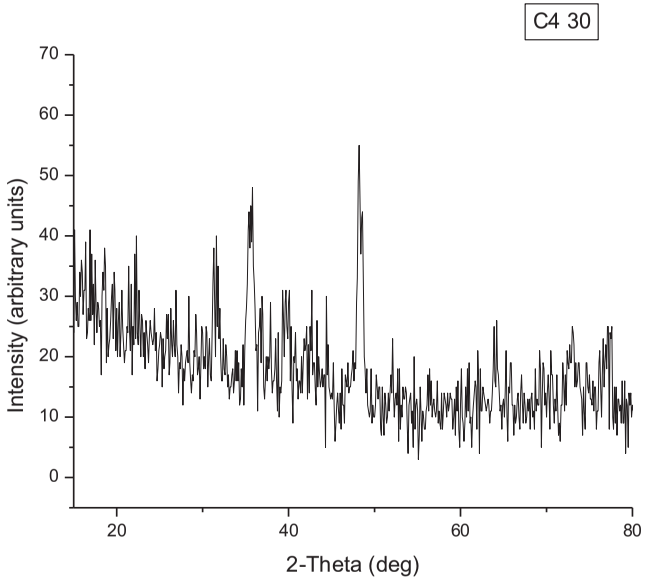
C4 30
Intensity (arbitrary units)
2-Theta (deg)
0
10
20
30
40
50
60
70
20
40
60
80

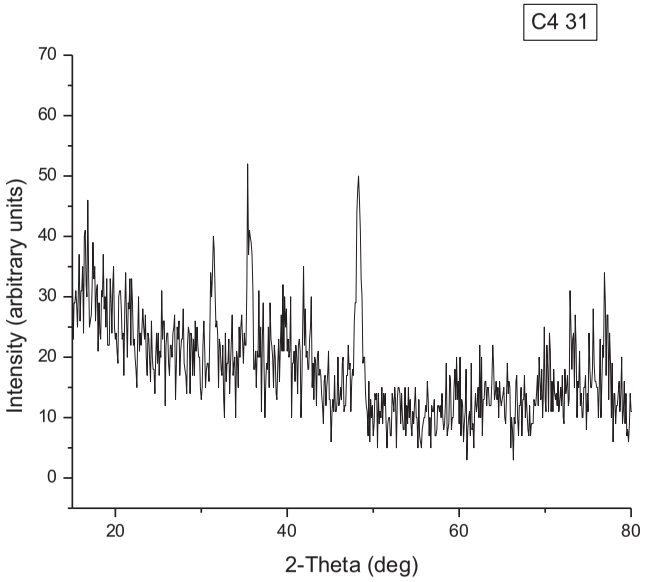
C4 31
Intensity (arbitrary units)
2-Theta (deg)
0
10
20
30
40
50
60
70
20
40
60
80

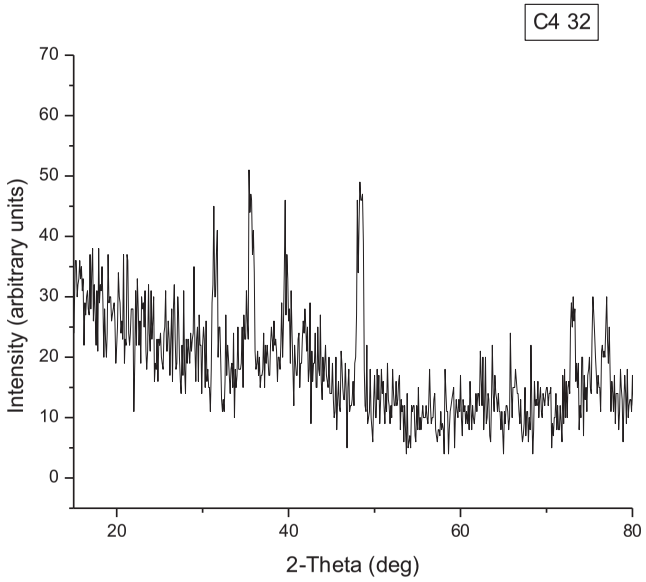
C4 32
Intensity (arbitrary units)
2-Theta (deg)
0
10
20
30
40
50
60
70
20
40
60
80

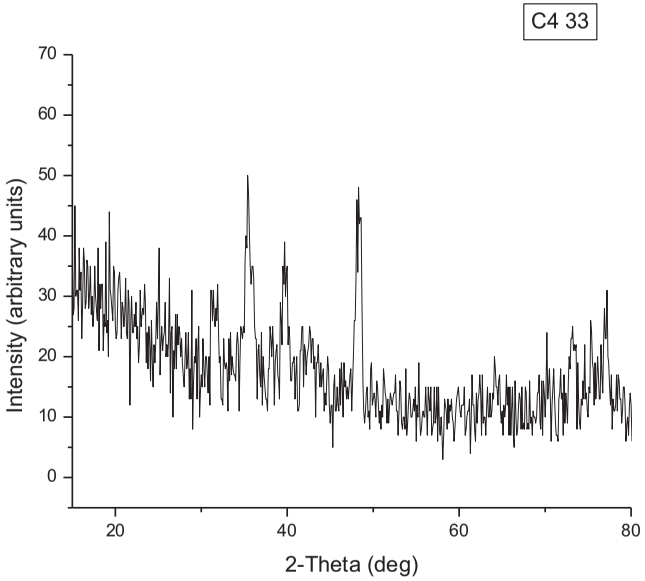
C4 33
Intensity (arbitrary units)
2-Theta (deg)
0
10
20
30
40
50
60
70
20
40
60
80

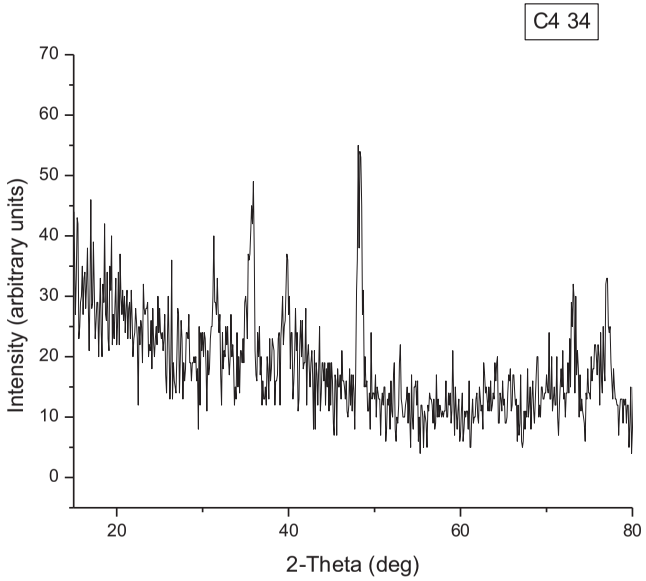
C4 34
Intensity (arbitrary units)
2-Theta (deg)
0
10
20
30
40
50
60
70
20
40
60
80

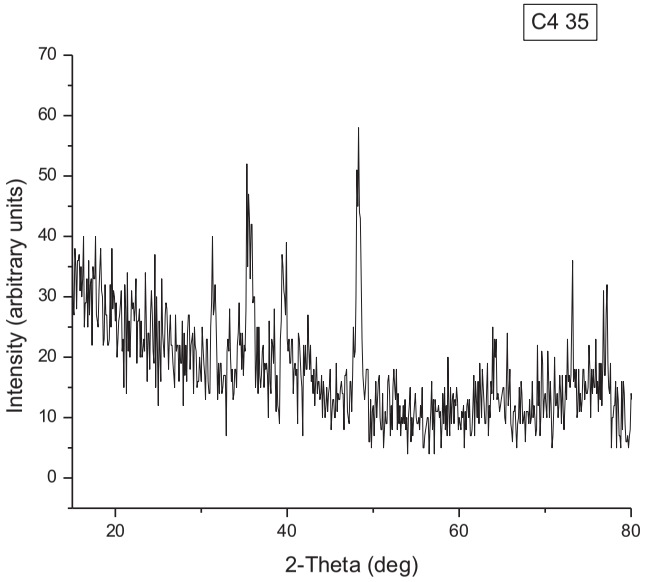
C4 35
Intensity (arbitrary units)
2-Theta (deg)
0
10
20
30
40
50
60
70
20
40
60
80

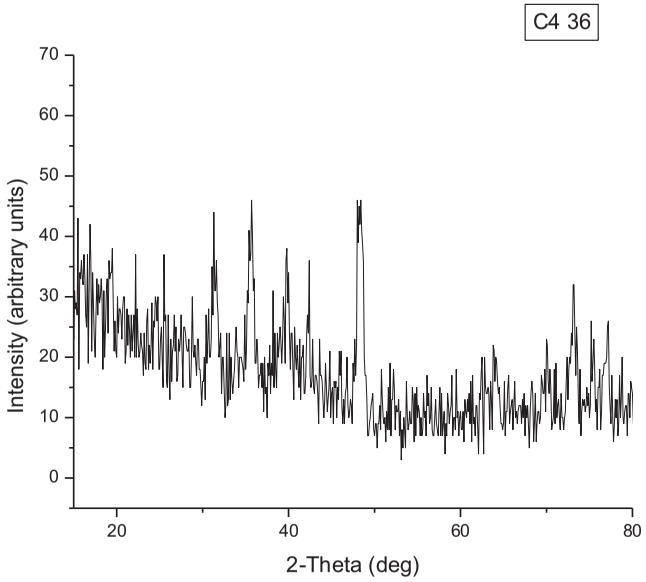
C4 36
Intensity (arbitrary units)
2-Theta (deg)
0
10
20
30
40
50
60
70
20
40
60
80

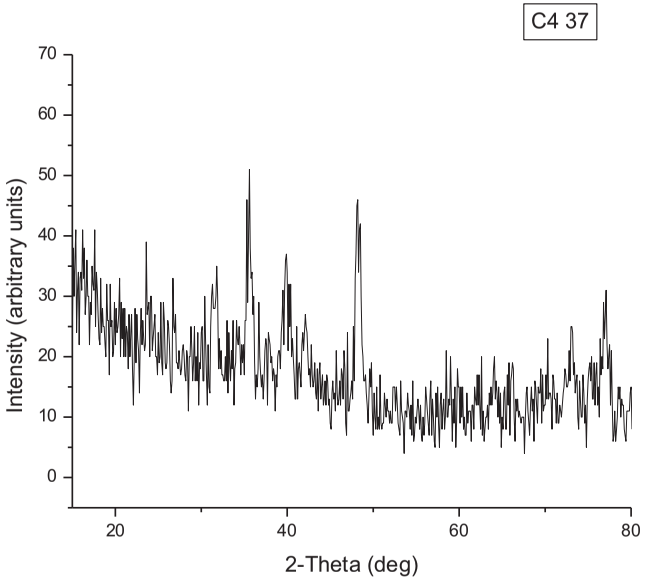
C4 37
Intensity (arbitrary units)
2-Theta (deg)
0
10
20
30
40
50
60
70
20
40
60
80

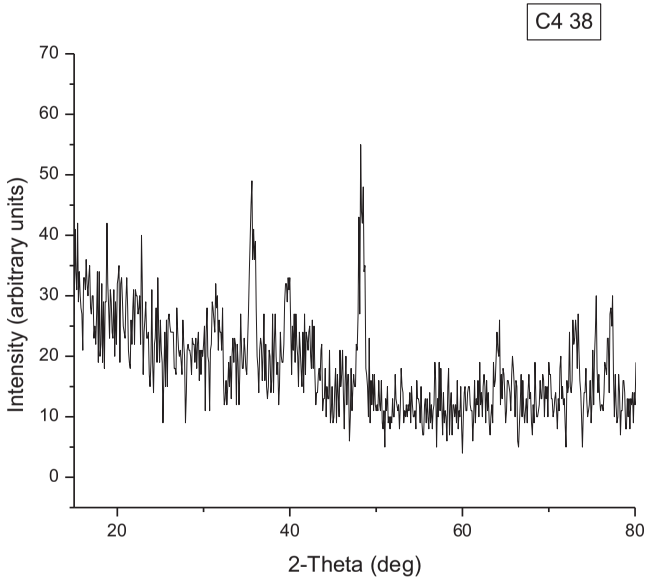
C4 38
Intensity (arbitrary units)
2-Theta (deg)
0
10
20
30
40
50
60
70
20
40
60
80

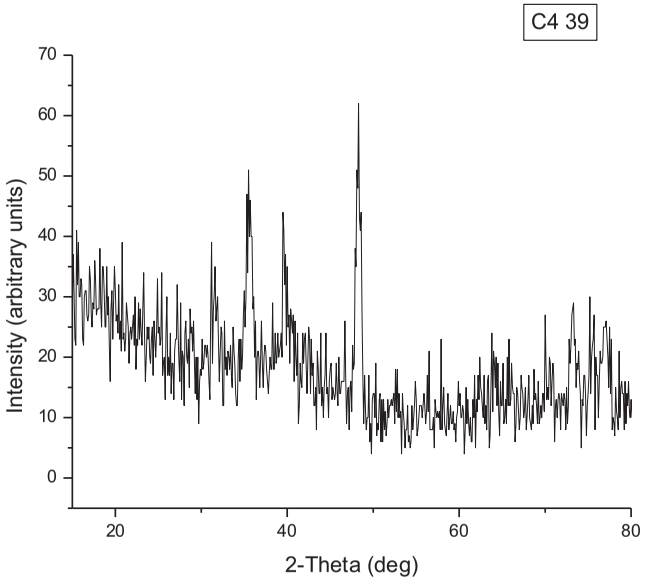
C4 39
Intensity (arbitrary units)
2-Theta (deg)
0
10
20
30
40
50
60
70
20
40
60
80

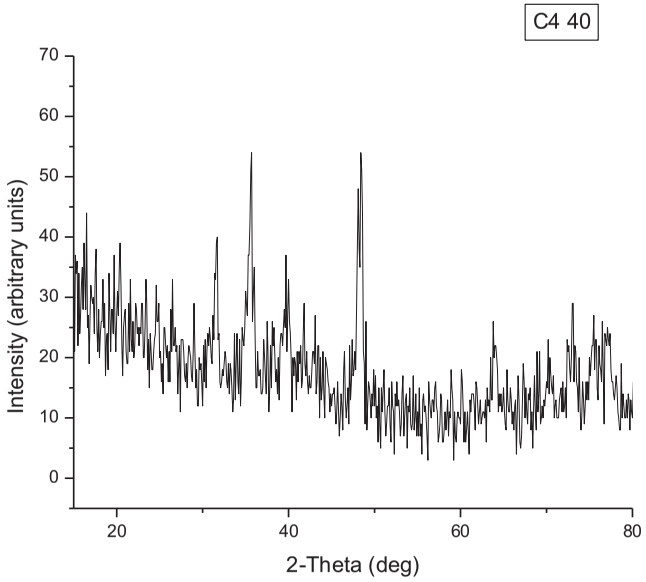
C4 40
Intensity (arbitrary units)
2-Theta (deg)
0
10
20
30
40
50
60
70
20
40
60
80

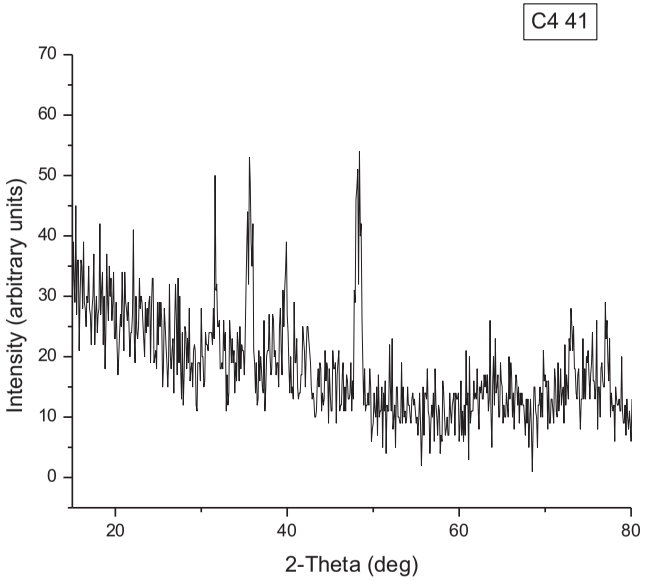
C4 41
Intensity (arbitrary units)
2-Theta (deg)
0
10
20
30
40
50
60
70
20
40
60
80

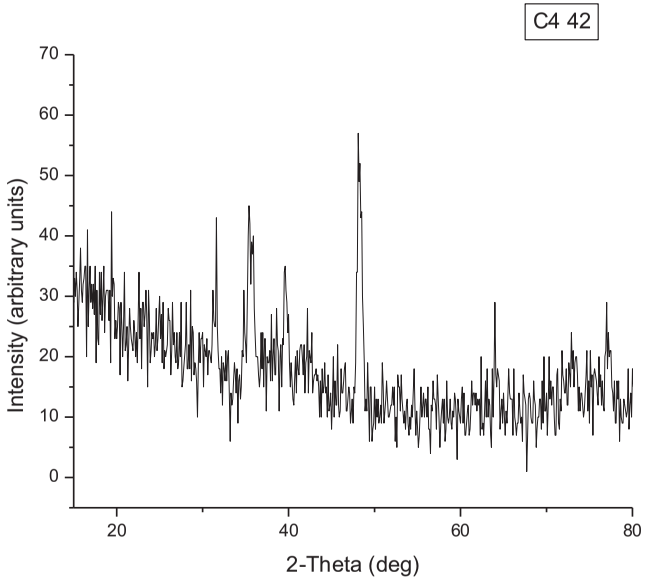
C4 42
Intensity (arbitrary units)
2-Theta (deg)
0
10
20
30
40
50
60
70
20
40
60
80

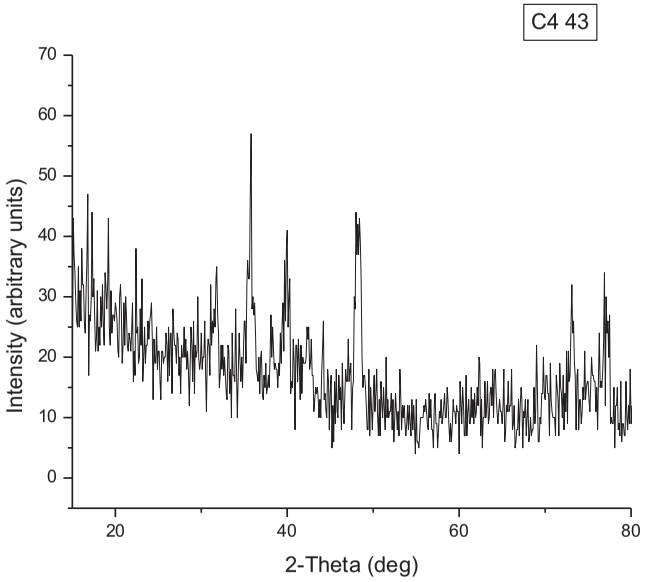
C4 43
Intensity (arbitrary units)
2-Theta (deg)
0
10
20
30
40
50
60
70
20
40
60
80

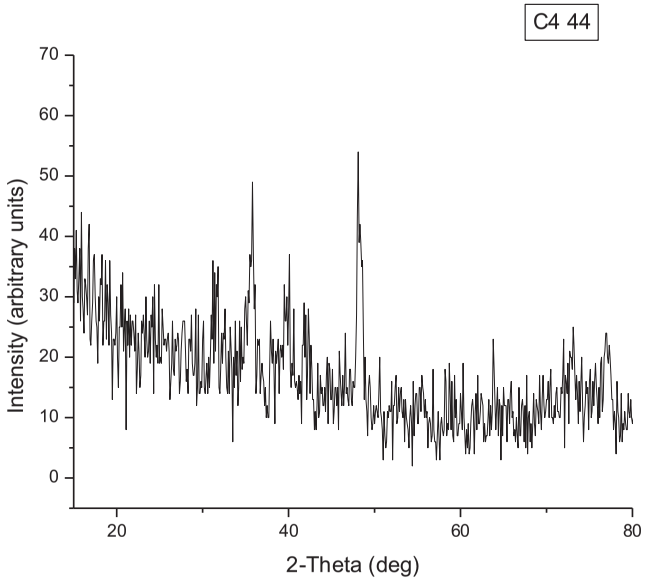
C4 44
Intensity (arbitrary units)
2-Theta (deg)
0
10
20
30
40
50
60
70
20
40
60
80

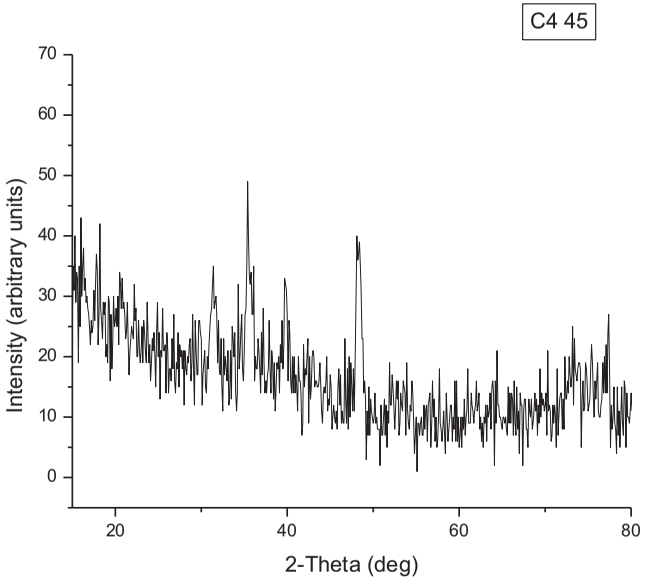
C4 45
Intensity (arbitrary units)
2-Theta (deg)
0
10
20
30
40
50
60
70
20
40
60
80

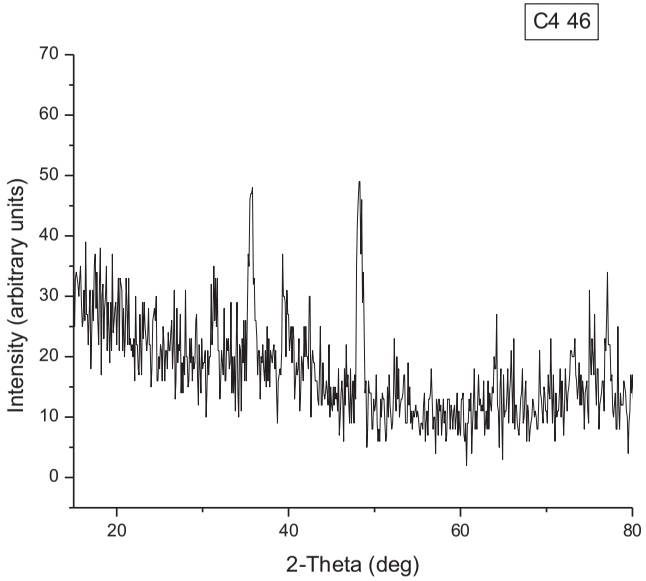
C4 46
Intensity (arbitrary units)
2-Theta (deg)
0
10
20
30
40
50
60
70
20
40
60
80

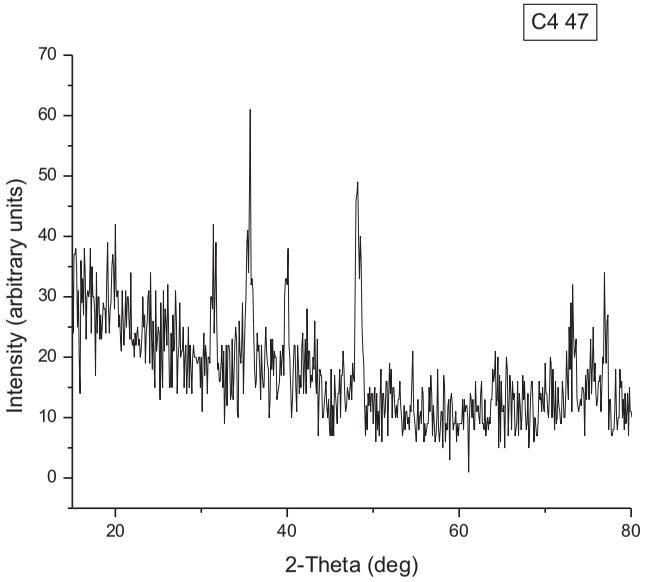
C4 47
Intensity (arbitrary units)
2-Theta (deg)
0
10
20
30
40
50
60
70
20
40
60
80

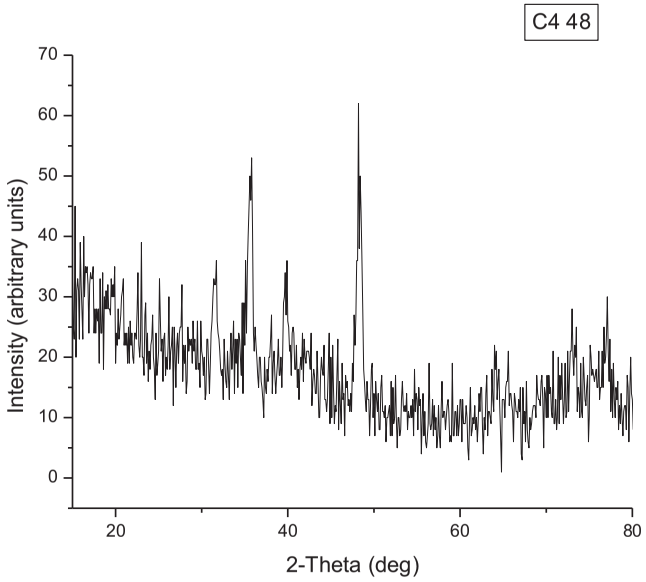
C4 48
Intensity (arbitrary units)
2-Theta (deg)
0
10
20
30
40
50
60
70
20
40
60
80

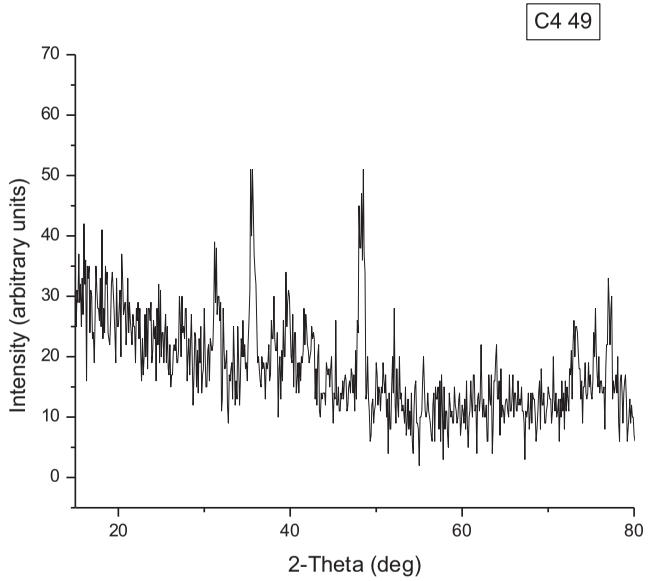
C4 49
Intensity (arbitrary units)
2-Theta (deg)
0
10
20
30
40
50
60
70
20
40
60
80

153

XRD Patterns for WC-12Co HVOF

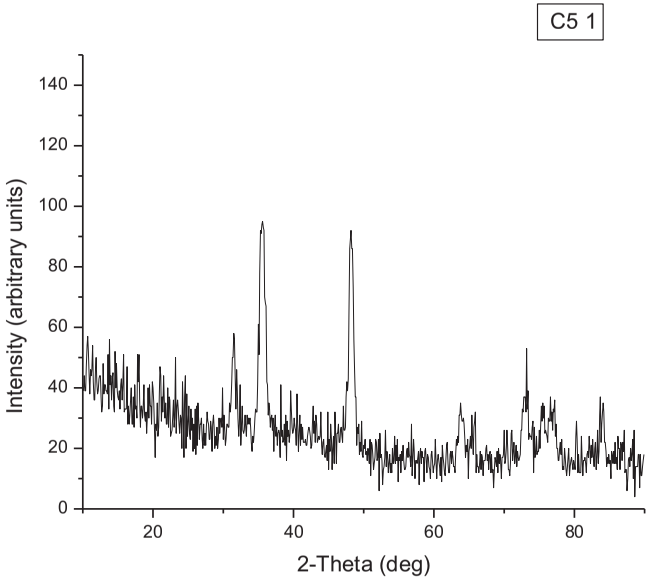
C5 1
Intensity (arbitrary units)
2-Theta (deg)
0
20
40
60
80
100
120
140

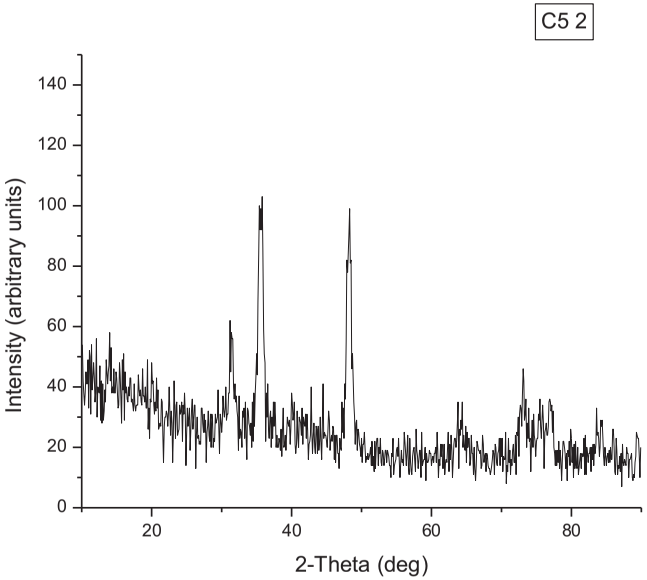
C5 2
Intensity (arbitrary units)
2-Theta (deg)
0
20
40
60
80
100
120
140

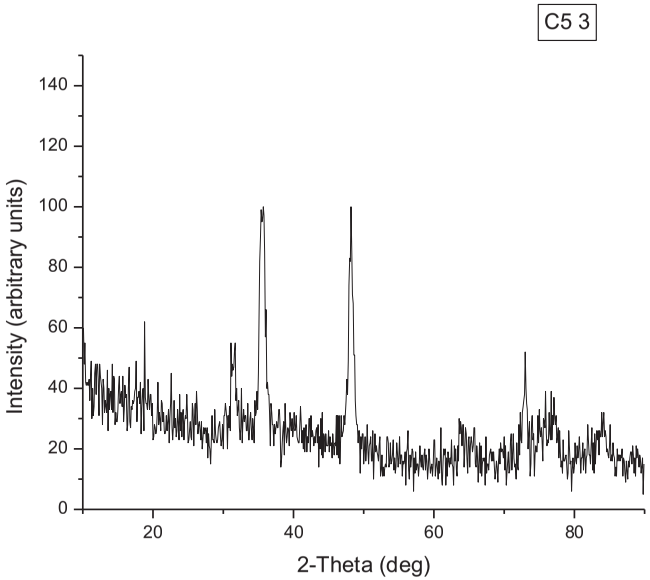
C5 3
Intensity (arbitrary units)
2-Theta (deg)
0
20
40
60
80
100
120
140

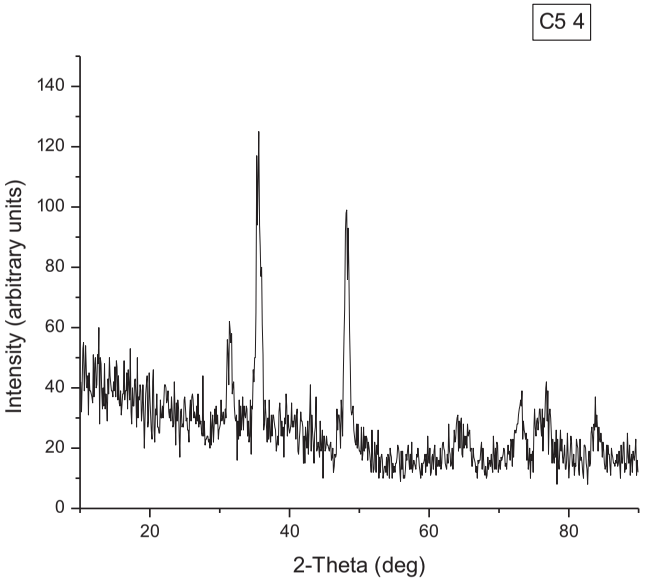
C5 4
Intensity (arbitrary units)
2-Theta (deg)
0
20
40
60
80
100
120
140

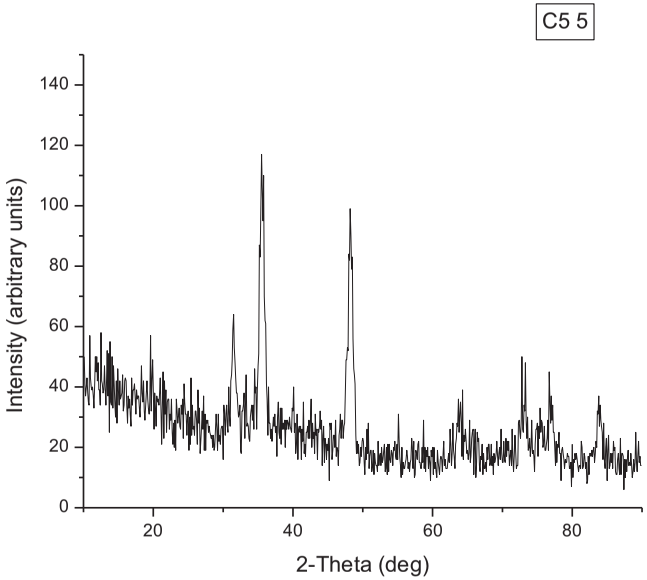
C5 5
Intensity (arbitrary units)
2-Theta (deg)
0
20
40
60
80
100
120
140
20
40
60
80

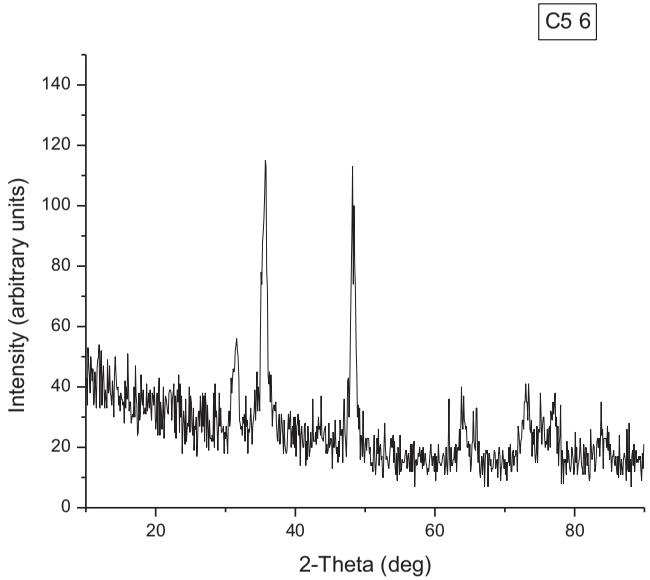
C5 6
Intensity (arbitrary units)
2-Theta (deg)
0
20
40
60
80
100
120
140
20
40
60
80

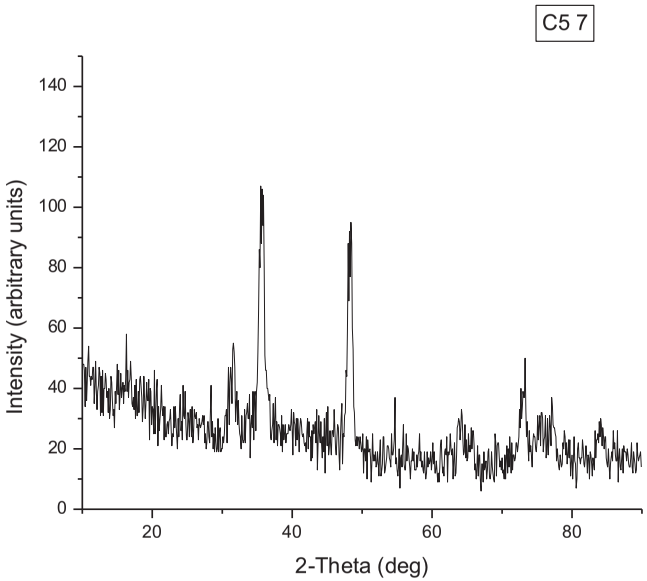
C5 7
Intensity (arbitrary units)
2-Theta (deg)
0
20
40
60
80
100
120
140
20
40
60
80

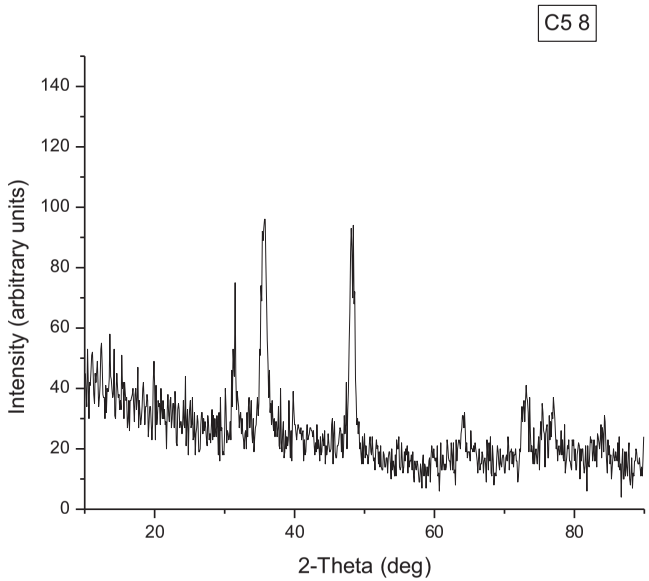
C5 8
Intensity (arbitrary units)
2-Theta (deg)
0
20
40
60
80
100
120
140
20
40
60
80

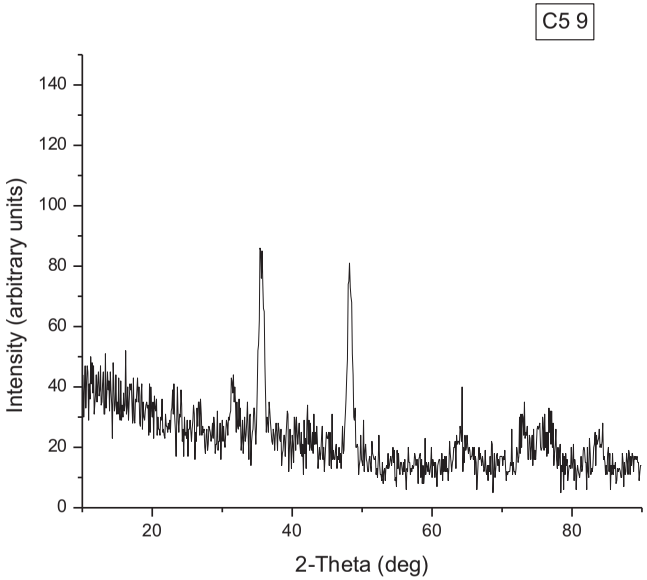
C5 9
Intensity (arbitrary units)
2-Theta (deg)
0
20
40
60
80
100
120
140
20
40
60
80

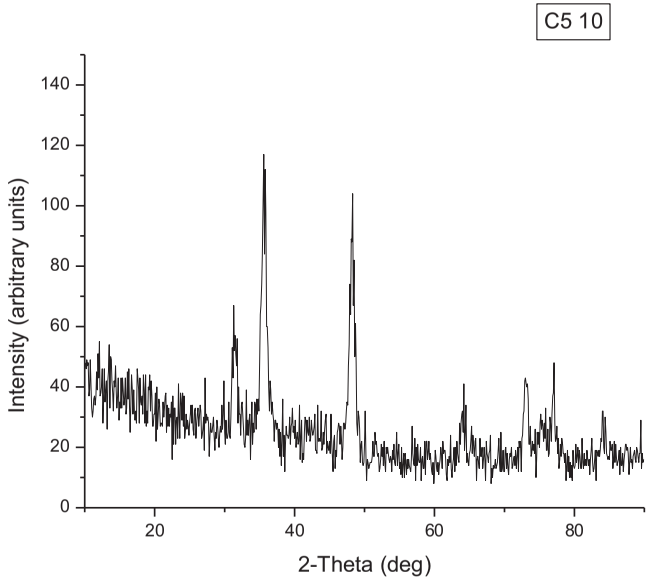
C5 10
Intensity (arbitrary units)
2-Theta (deg)
0
20
40
60
80
100
120
140
20
40
60
80

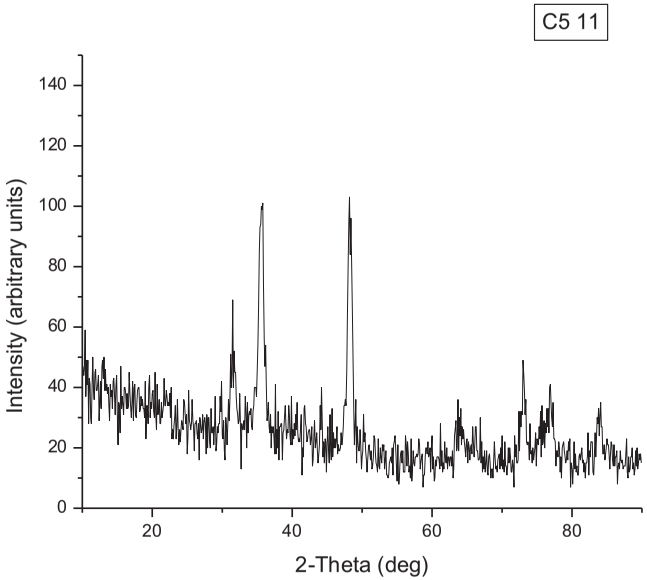
C5 11
Intensity (arbitrary units)
2-Theta (deg)
0
20
40
60
80
100
120
140
20
40
60
80

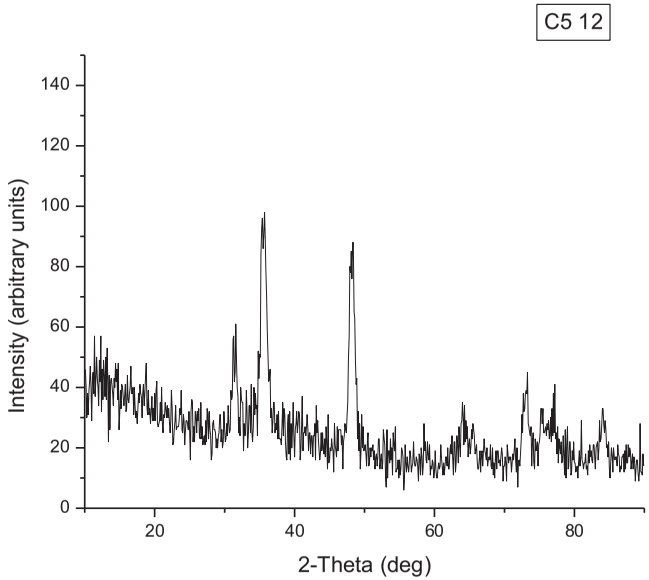
C5 12
Intensity (arbitrary units)
2-Theta (deg)
0
20
40
60
80
100
120
140
20
40
60
80

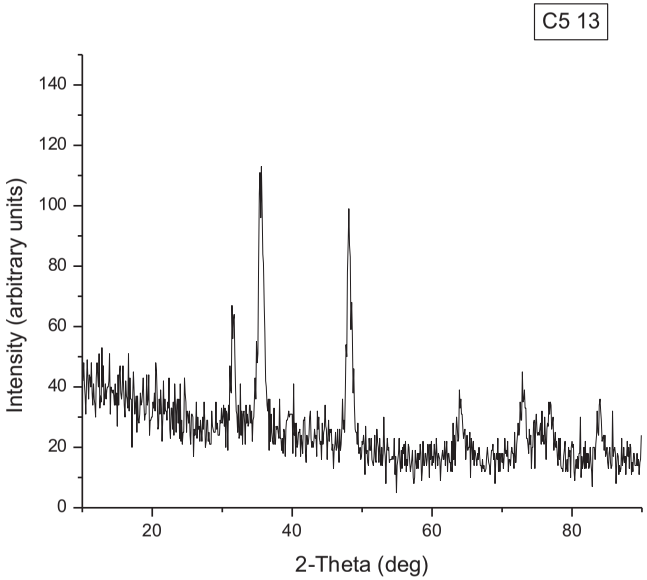
C5 13
Intensity (arbitrary units)
2-Theta (deg)
0
20
40
60
80
100
120
140

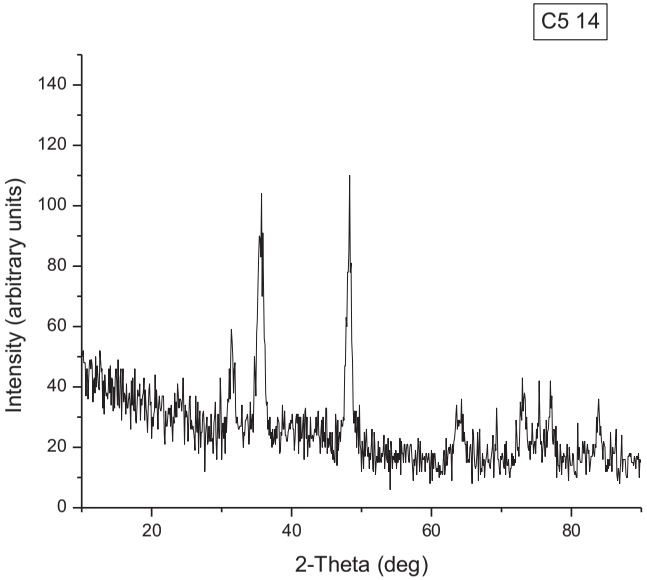
C5 14
Intensity (arbitrary units)
2-Theta (deg)
0
20
40
60
80
100
120
140

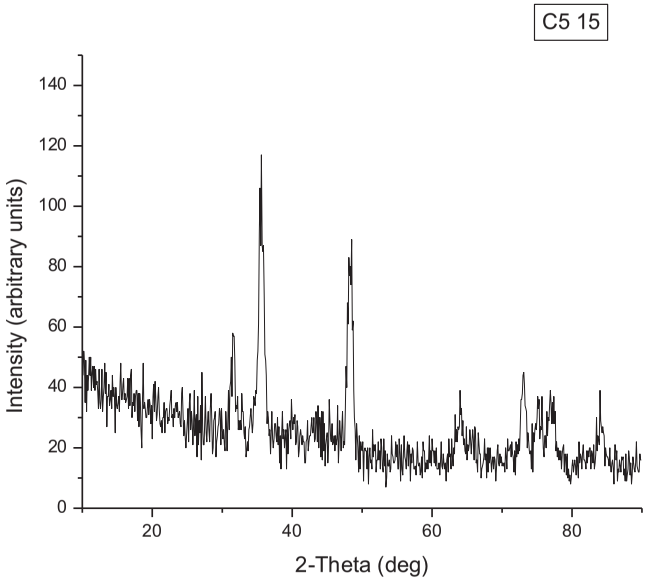
C5 15
Intensity (arbitrary units)
2-Theta (deg)
0
20
40
60
80
100
120
140

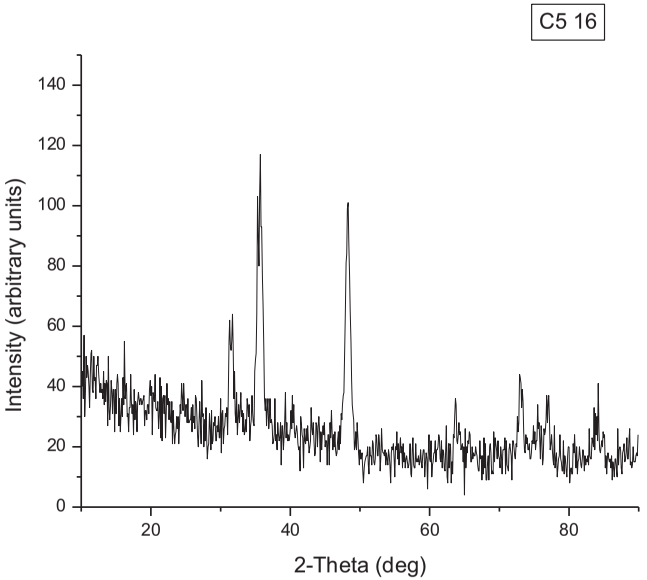
C5 16
Intensity (arbitrary units)
2-Theta (deg)
0
20
40
60
80
100
120
140

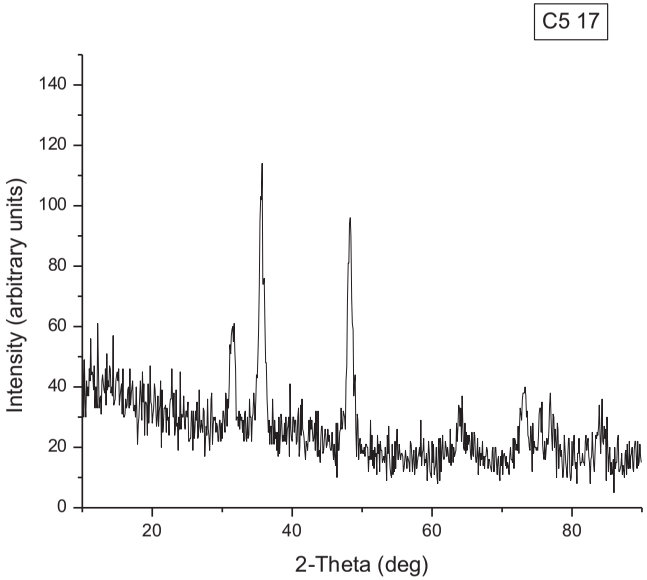
C5 17
Intensity (arbitrary units)
2-Theta (deg)
0
20
40
60
80
100
120
140
20
40
60
80

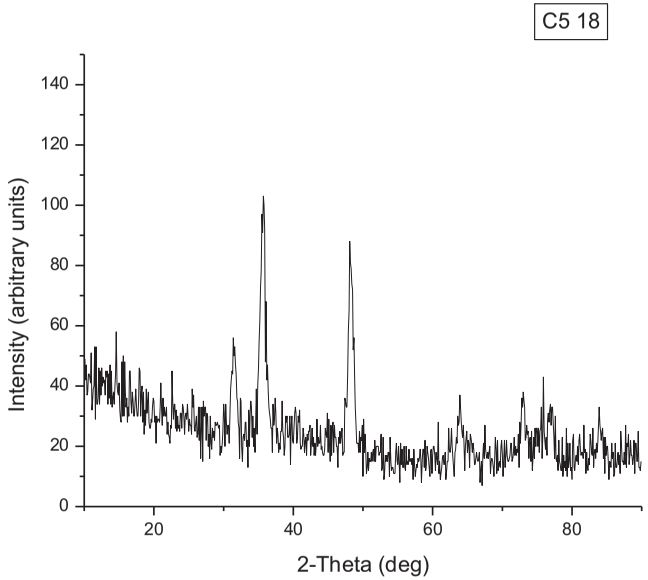
C5 18
Intensity (arbitrary units)
2-Theta (deg)
0
20
40
60
80
100
120
140
20
40
60
80

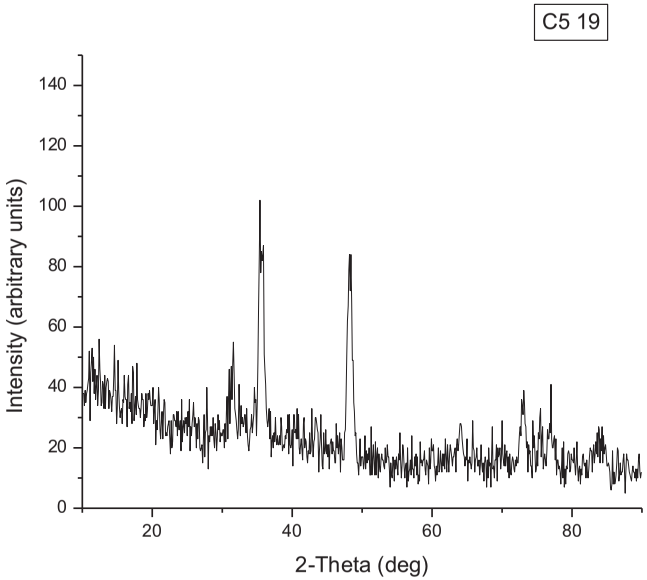
C5 19
Intensity (arbitrary units)
2-Theta (deg)
0
20
40
60
80
100
120
140
20
40
60
80

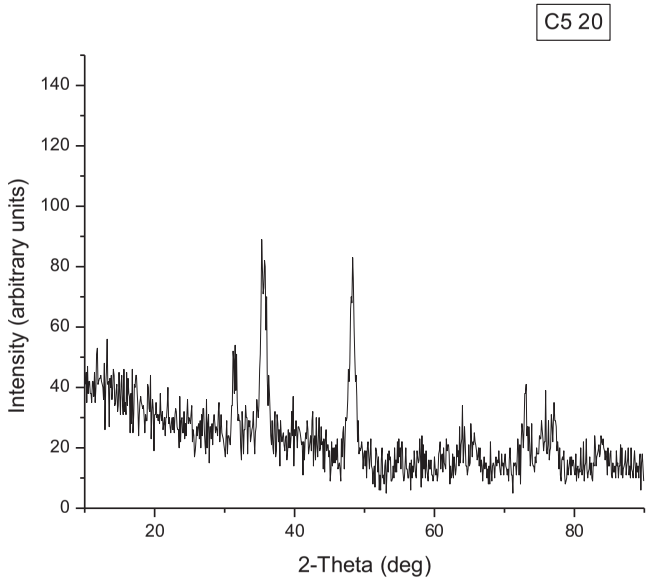
C5 20
Intensity (arbitrary units)
2-Theta (deg)
0
20
40
60
80
100
120
140
20
40
60
80

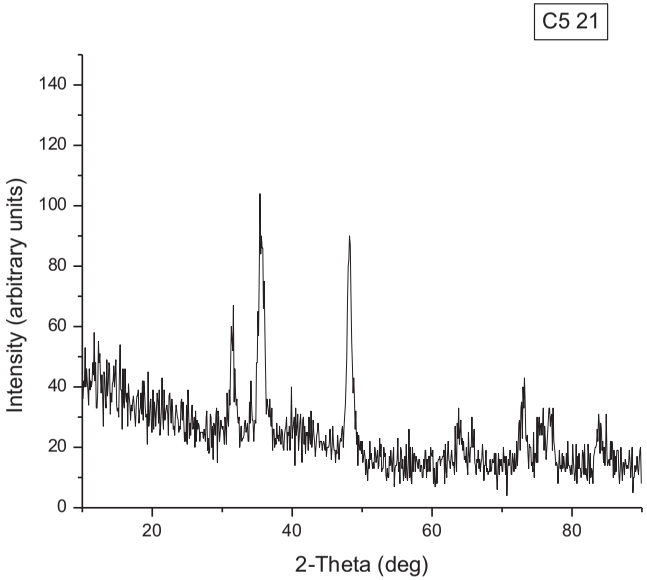
C5 21
Intensity (arbitrary units)
2-Theta (deg)
0
20
40
60
80
100
120
140

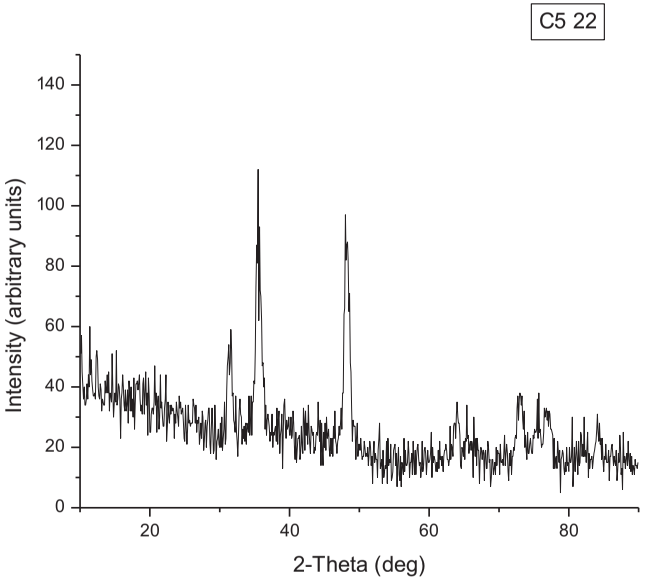
C5 22
Intensity (arbitrary units)
2-Theta (deg)
0
20
40
60
80
100
120
140

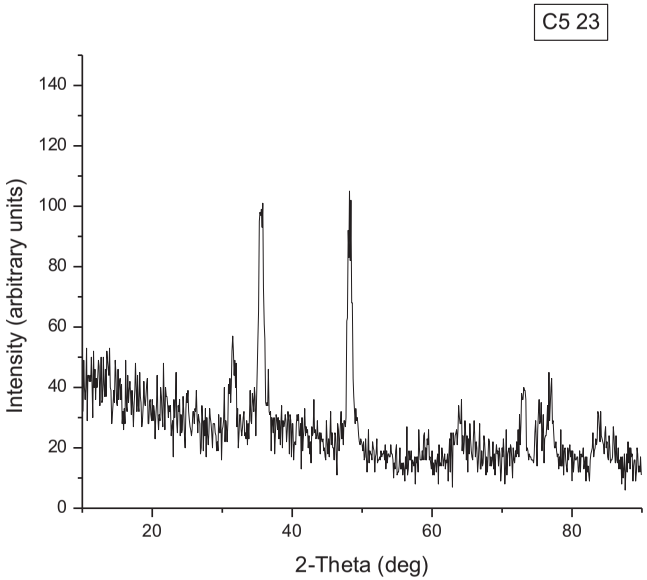
C5 23
Intensity (arbitrary units)
2-Theta (deg)
0
20
40
60
80
100
120
140

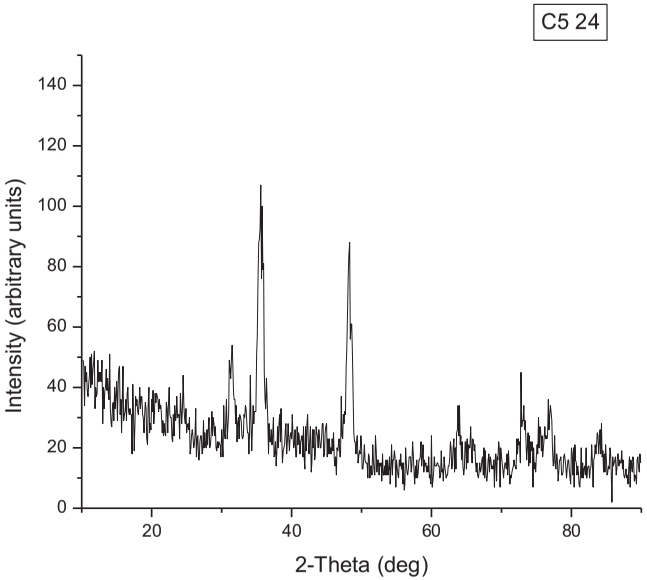
C5 24
Intensity (arbitrary units)
2-Theta (deg)
0
20
40
60
80
100
120
140

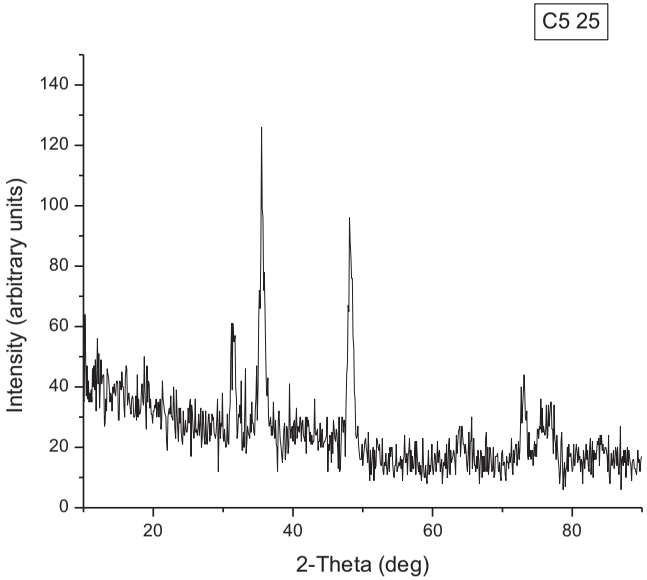
C5 25
Intensity (arbitrary units)
2-Theta (deg)
0
20
40
60
80
100
120
140
20
40
60
80

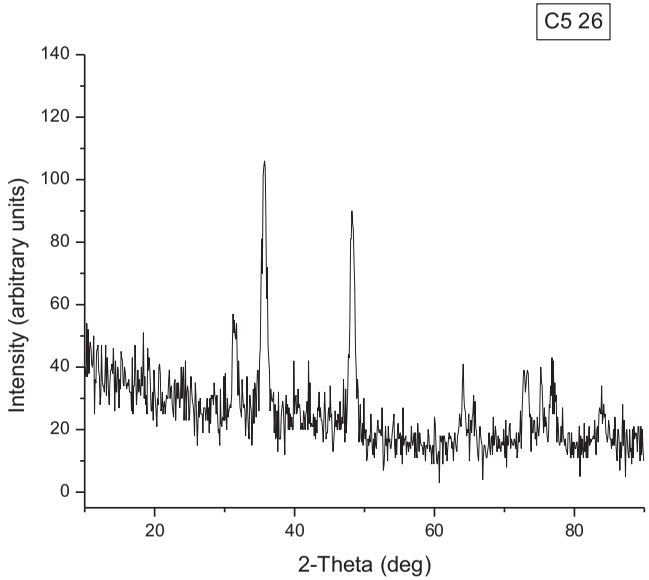
C5 26
Intensity (arbitrary units)
2-Theta (deg)
0
20
40
60
80
100
120
140
20
40
60
80

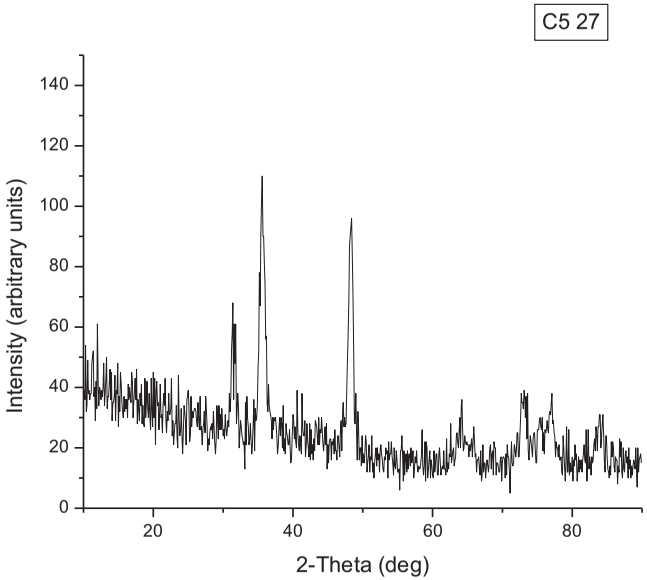
C5 27
Intensity (arbitrary units)
2-Theta (deg)
0
20
40
60
80
100
120
140
20
40
60
80

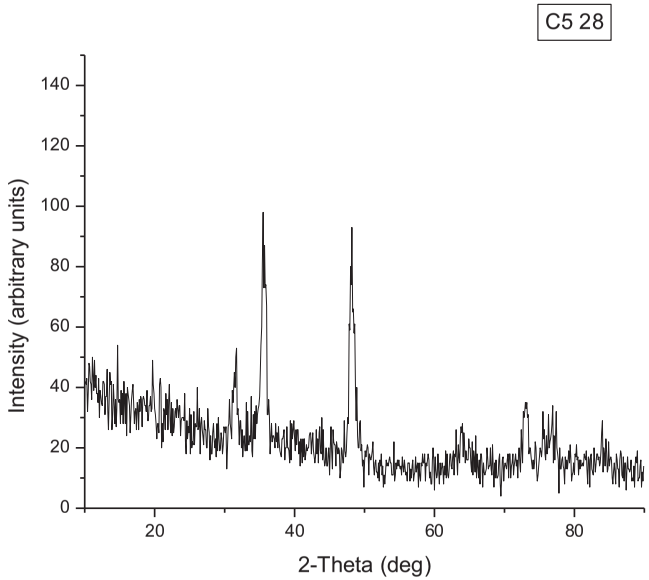
C5 28
Intensity (arbitrary units)
2-Theta (deg)
0
20
40
60
80
100
120
140
20
40
60
80

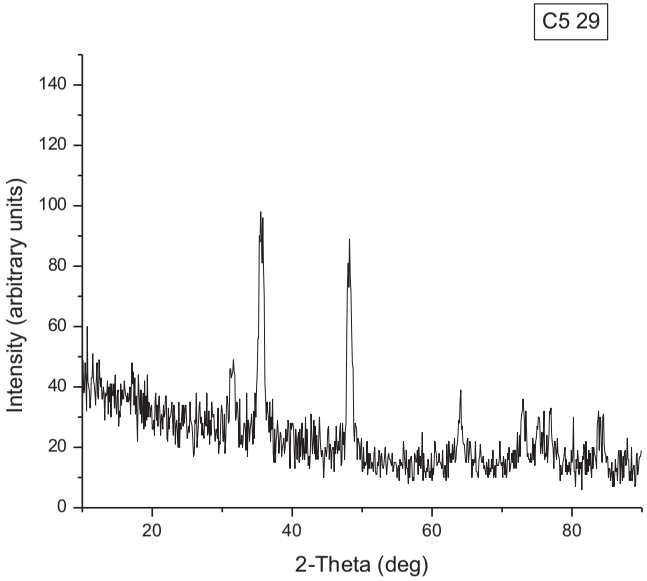
C5 29
Intensity (arbitrary units)
2-Theta (deg)
0
20
40
60
80
100
120
140
20
40
60
80

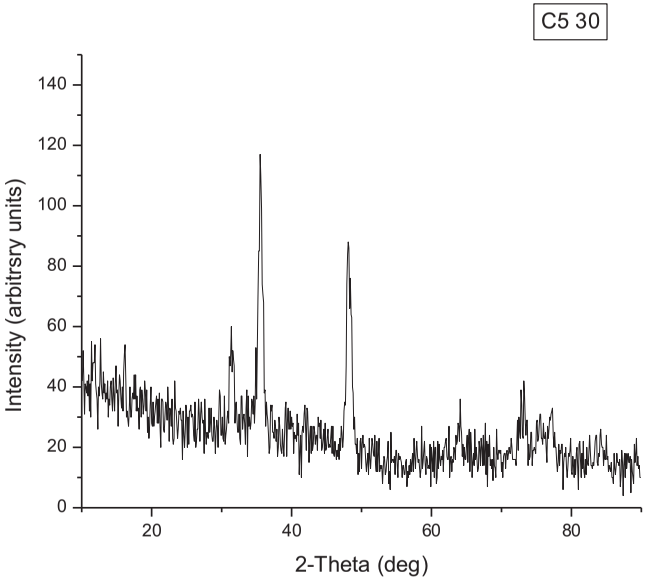
C5 30
Intensity (arbitrsry units)
2-Theta (deg)
0
20
40
60
80
100
120
140
20
40
60
80

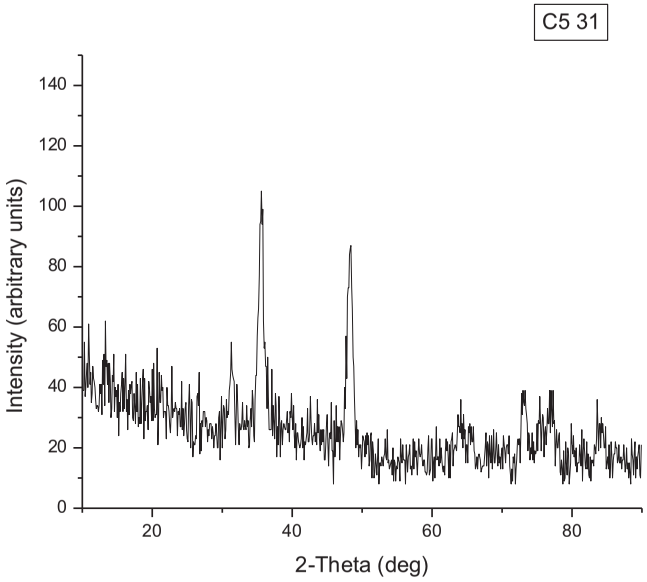
C5 31
Intensity (arbitrary units)
2-Theta (deg)
0
20
40
60
80
100
120
140
20
40
60
80

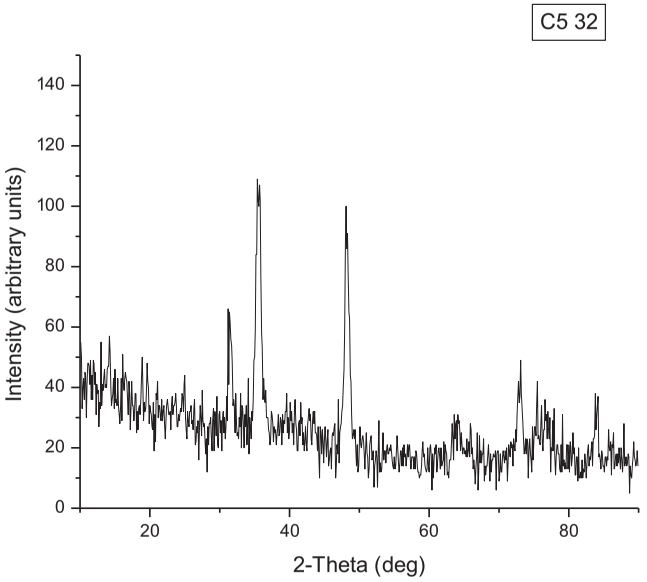
C5 32
Intensity (arbitrary units)
2-Theta (deg)
0
20
40
60
80
100
120
140
20
40
60
80

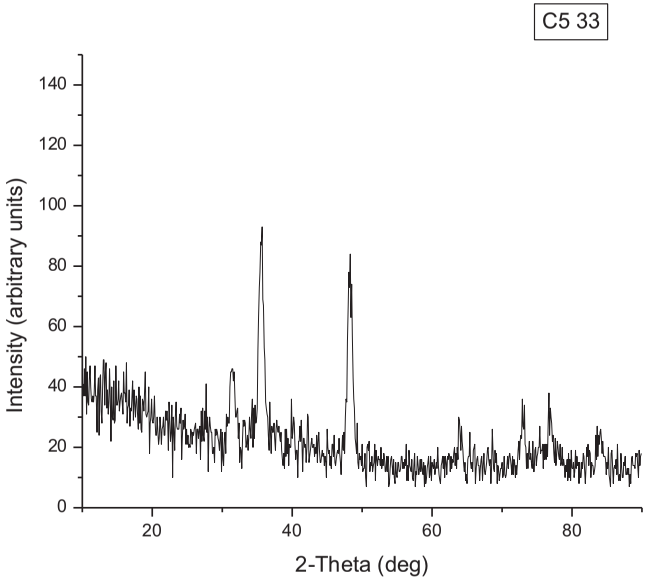
C5 33
Intensity (arbitrary units)
2-Theta (deg)
0
20
40
60
80
100
120
140
20
40
60
80

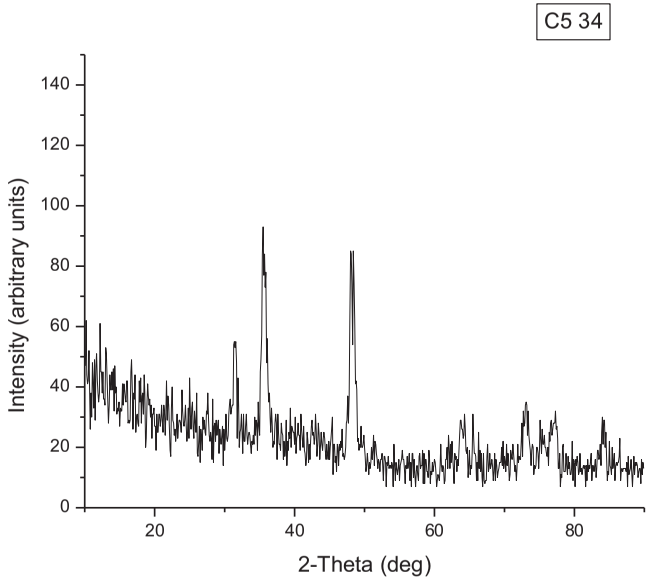
C5 34
Intensity (arbitrary units)
2-Theta (deg)
0
20
40
60
80
100
120
140
20
40
60
80

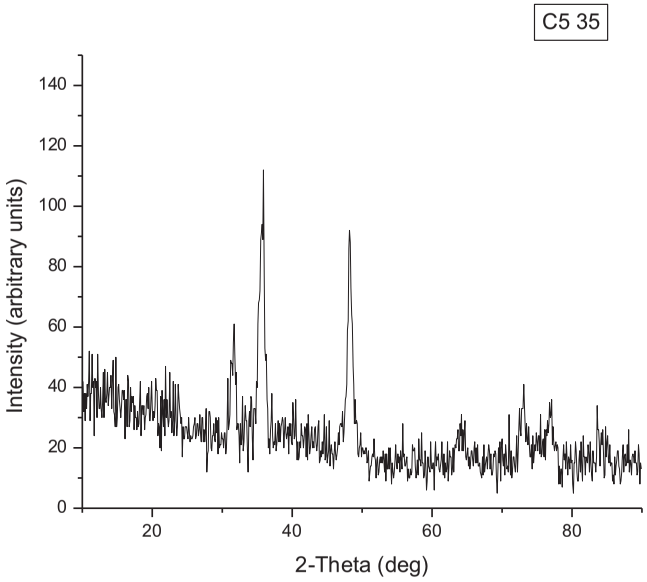
C5 35
Intensity (arbitrary units)
2-Theta (deg)
0
20
40
60
80
100
120
140
20
40
60
80

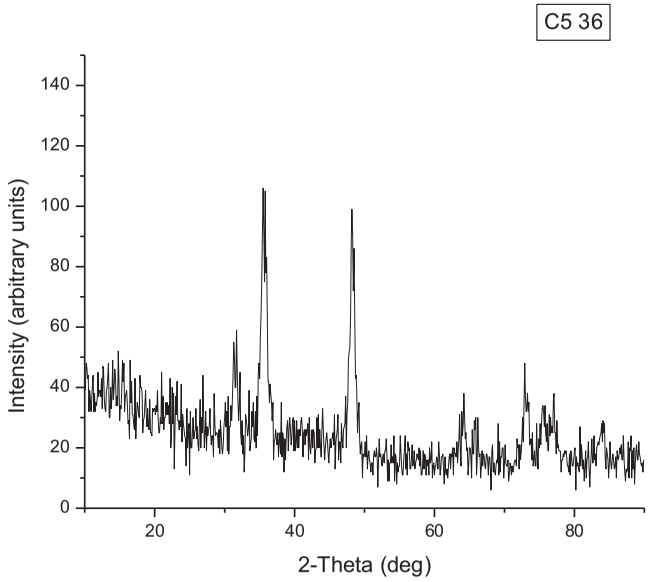
C5 36
Intensity (arbitrary units)
2-Theta (deg)
0
20
40
60
80
100
120
140
20
40
60
80

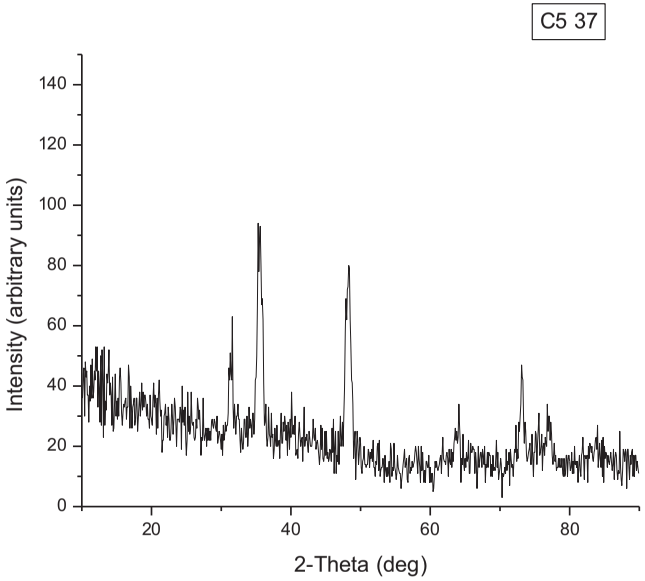
C5 37
Intensity (arbitrary units)
2-Theta (deg)
0
20
40
60
80
100
120
140
20
40
60
80

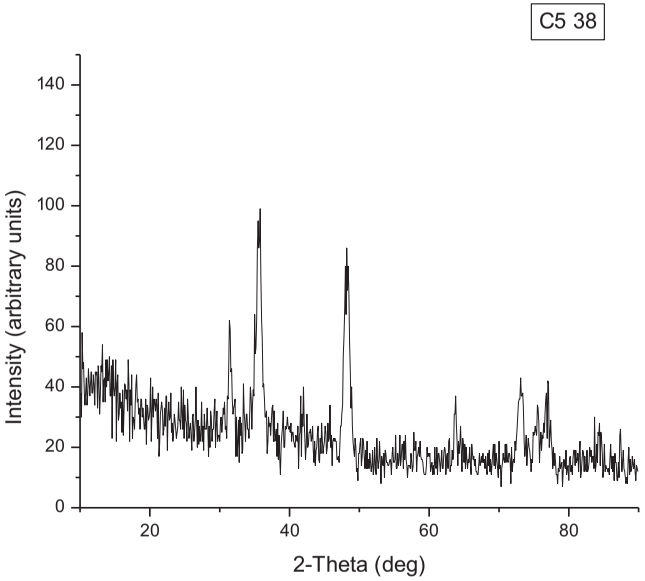
C5 38
Intensity (arbitrary units)
2-Theta (deg)
0
20
40
60
80
100
120
140
20
40
60
80

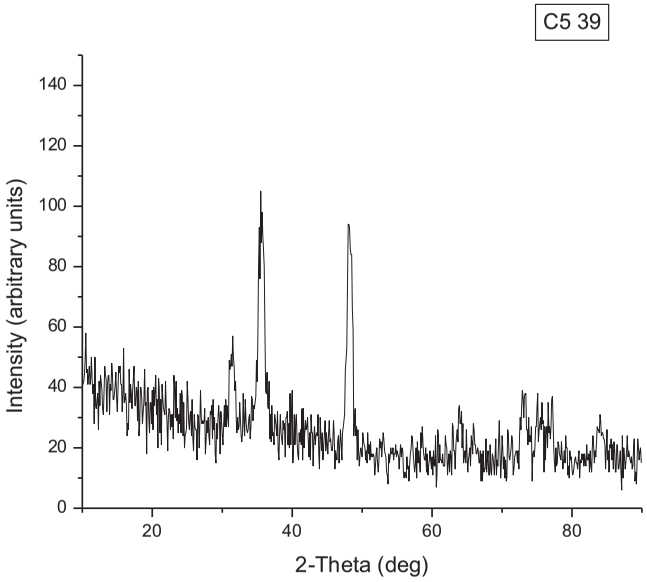
C5 39
Intensity (arbitrary units)
2-Theta (deg)
0
20
40
60
80
100
120
140
20
40
60
80

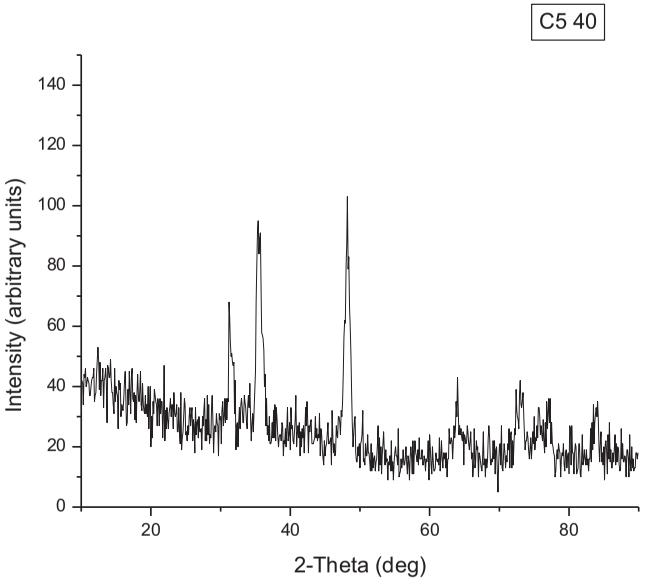
C5 40
Intensity (arbitrary units)
2-Theta (deg)
0
20
40
60
80
100
120
140
20
40
60
80

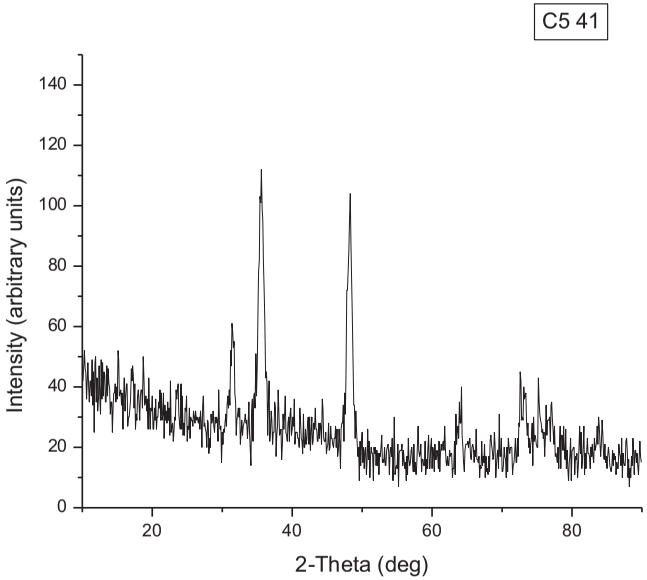
C5 41
Intensity (arbitrary units)
2-Theta (deg)
0
20
40
60
80
100
120
140
20
40
60
80

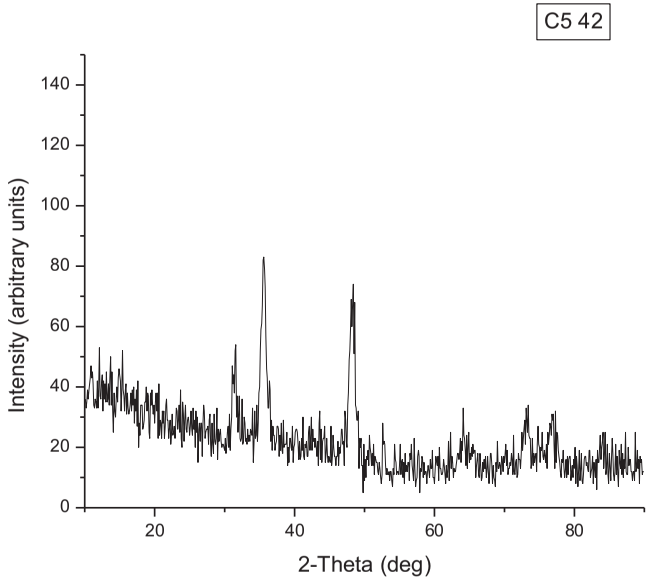
C5 42
Intensity (arbitrary units)
2-Theta (deg)
0
20
40
60
80
100
120
140
20
40
60
80

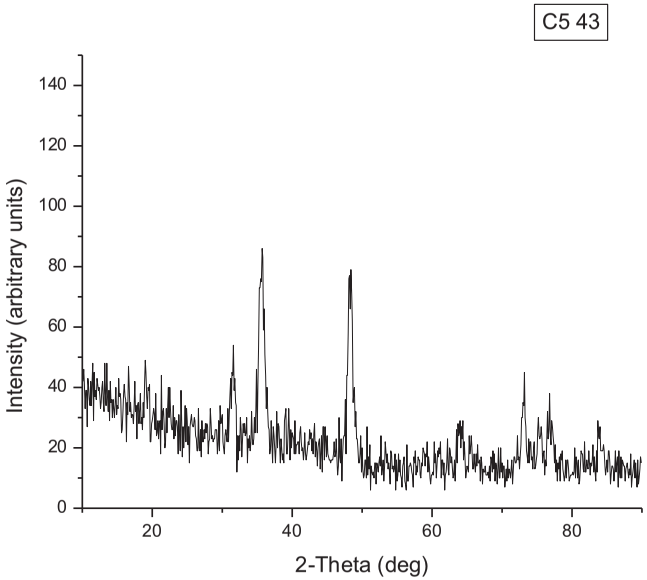
C5 43
Intensity (arbitrary units)
2-Theta (deg)
0
20
40
60
80
100
120
140
20
40
60
80

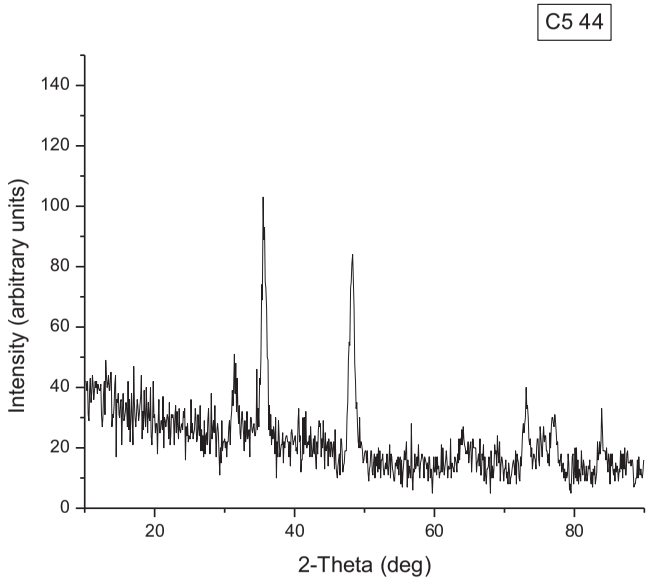
C5 44
Intensity (arbitrary units)
2-Theta (deg)
0
20
40
60
80
100
120
140
20
40
60
80

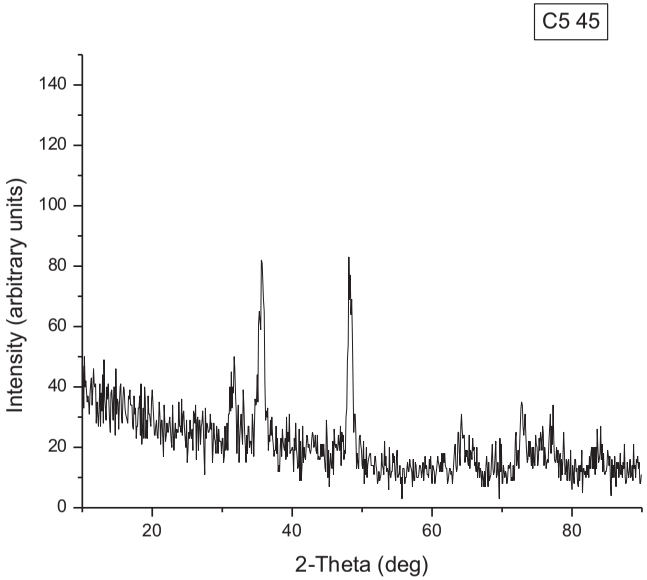
C5 45
Intensity (arbitrary units)
2-Theta (deg)
0
20
40
60
80
100
120
140
20
40
60
80

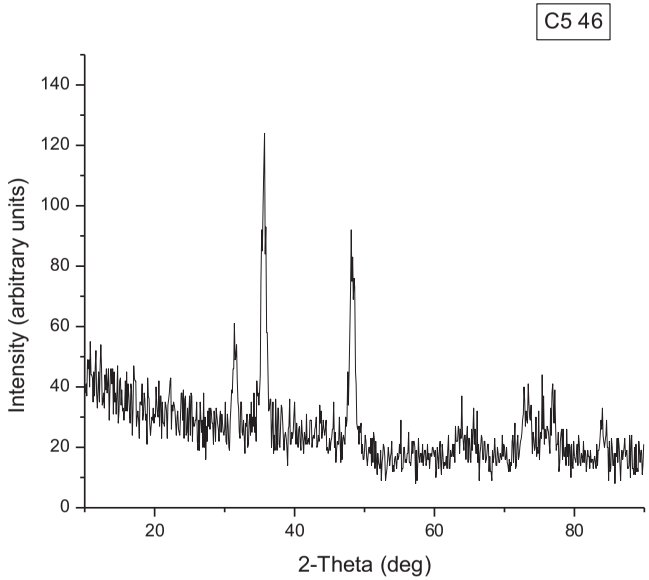
C5 46
Intensity (arbitrary units)
2-Theta (deg)
0
20
40
60
80
100
120
140
20
40
60
80

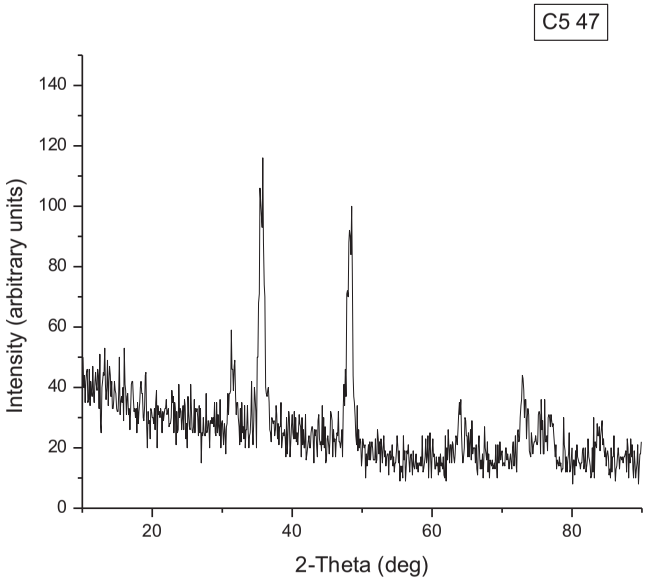
C5 47
Intensity (arbitrary units)
2-Theta (deg)
0
20
40
60
80
100
120
140
20
40
60
80

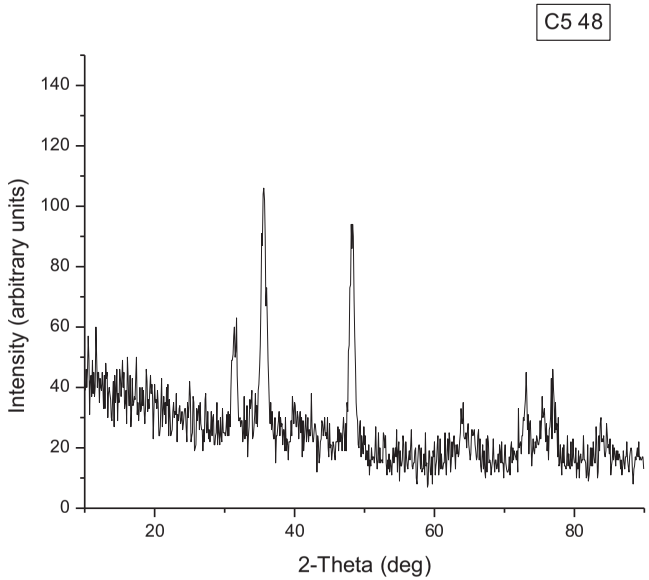
C5 48
Intensity (arbitrary units)
2-Theta (deg)
0
20
40
60
80
100
120
140
20
40
60
80

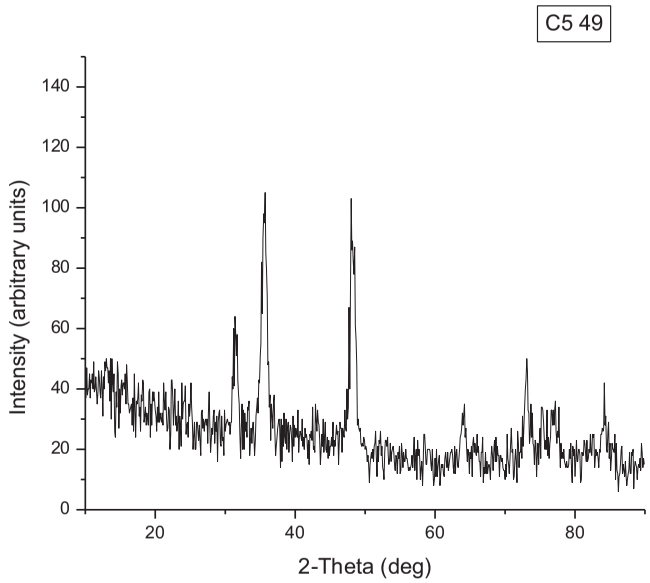
C5 49
Intensity (arbitrary units)
2-Theta (deg)
0
20
40
60
80
100
120
140
20
40
60
80